Alma Mater Studiorum – Università di Bologna

DOTTORATO DI RICERCA IN

Chimica

Ciclo 32°

Settore Concorsuale: 03/B1

Settore Scientifico Disciplinare: CHIM/03

HIERARCHICALLY ORGANIZED CHITIN-BASED MATRICES

Presentata da: **Devis Montroni**

Coordinatore Dottorato **Supervisore**

Prof.ssa Domenica Tonelli **Prof. Giuseppe Falini**

Esame finale anno 2020

Logic will get you from A to B.

Imagination will take you everywhere.

I would like to dedicate this thesis to my dad.

Table of contents

Abbreviations

AFM	=	atomic force microscopy
ATR	=	attenuated total reflectance
bicine	=	N,N-bis(2-hydroxyethyl)glycine
bis-TRIS	=	2,2-bis(hydroxymethyl)-2,2′,2″-nitrilotriethanol
CBD	=	chitin-binding domain
cryo-TEM	=	cryo-transmission electron microscopy
CW	=	Calcofluor White
DA	=	degree of acetylation
DOPA	=	dihydroxyphenylalanine
D-R	=	Dubinin Radushkevich (isotherm model)
DSC	=	differential scanning calorimetry
EDS	=	energy-dispersive X-ray spectroscopy
EDTA	=	ethylenediaminetetraacetic acid
EosY	=	Eosin Y
FTIR	=	Fourier transform infrared spectroscopy
IS	=	internal shell
MB	=	Methylene Blue
NMR	=	nuclear magnetic resonance
PBS	=	phosphate-buffered saline
SDS-PAGE	=	sodium dodecyl sulfate – polyacrylamide gel electrophoresis
SEM	=	scanning electron microscopy
TGA	=	thermogravimetric analysis
TRIS	=	tris(hydroxymethyl)aminomethane
XRD	=	X-ray diffraction
β-CnFs	=	β-chitin nano-fibrils

Chapter 1:
Introduction

1. Chitin

Biopolymers are polymers produced by living organisms. They include well-known examples as proteins and deoxyribonucleic acid (DNA). Despite the colossal importance of these two categories of biopolymers, the ones which people are more used to deal with are polysaccharides, such as starch, cellulose, or chitin.

Cellulose represents the most abundant biopolymer on earth, about 1.5 x 10^{12} tons of the total annual biomass production.[1] Chitin, on the other hand, has been estimated to have an annual production of about 10^{6} - 10^{10} tons.[2][3][4] Anyway, the overall view changes drastically if we think about the number of species synthetizing these polymers (Figure 1).

Figure 1: In the center a cake diagram reporting the distribution of species producing chitin, cellulose, or none of them. A few examples of representative organisms producing chitin are illustrated.

According to the International Institute for Species Exploration (2011)[5] over 70 % of the known species produce chitin (> 70 % of them are insects, and > 90 % belong to the animal kingdom) while about 15 % of them produce cellulose (> 95 % of them belong to the plant kingdom).

Despite the huge biomass of cellulose, chitin is still the most diffused biopolymer on earth and can be found in a limitless number of different morphologies and textures. From fungi to arthropods, chitin is present mainly with structural or protective purposes but has also been observed having a crucial role in photonic or mineralized structures.

1.1. Composition and crystal structure

Chitin, β(1,4)-linked N-acetyl-D-glucosamine polymer, is a polysaccharide. Its monomer is the N-acetyl-D-glucosamine, but usually few glucosamine residues (< 5 mol.%) are usually commonly present in natural chitin (Figure 2).

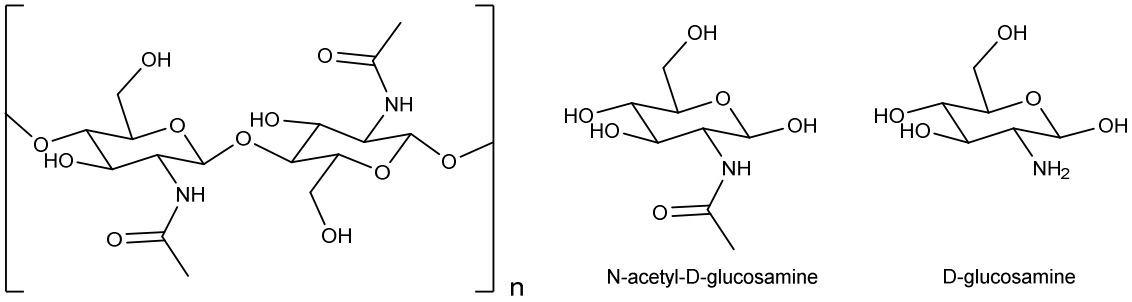

Figure 2: On the right, the structure of a chitin chain. On the center, the structures of N-acetyl-D-glucosamine, the monomer of chitin, and on the left D-glucosamine, the monomer of chitosan.

As many natural polymers, as cellulose, chitin occurs in three different polymorphs: α-chitin, β-chitin, and γ-chitin.

The former, α-chitin, is the most common polymorph in nature. It can be found in arthropods exoskeleton or in sponges and is characterized by an antiparallel packing of its polymeric chains. In this polymorph chitin has an orthorhombic unit cell with a $P2_12_12_1$ space group and its crystal parameter are: a = 4.71 Å, b = 18.78 Å, and c = 10.33 Å.[6] Its unit cell contains disaccharide sections of the two chains passing through the center and corner of the ab projection.[7]

On the other hand, β-chitin is less common than α-chitin. It presents a parallel packing of the polymer chains and it can be found in calcifying organisms (ex. bivalves, foraminifers,

diatoms, etc.) guiding the calcification process, or in internal skeletal structures of squids and cuttlefishes. The unit cell of β-chitin is monoclinic with a $P2_1$ space group and the following cell parameters: a = 4.85 Å, b = 9.26 Å, c = 10.38 Å, and γ = 97.5°. The unit cell contains two sugar residues related by the twofold screw axis.[8]

The latter, γ-chitin, is poorly diffused and can be mainly found in peritrophic membranes of mollusks and insects, or in cocoons. This polymorph has been poorly studied and is mainly associated with α-chitin. It is characterized by two chains antiparallel and one parallel.

Observing the bc projections in Figure 3 is clear that along the b direction, the cell parameter of α-chitin is close to twice that of β-chitin, whereas the c parameter is unaltered. In both structures, in the ab projection the chitin chains are organized in sheets where they are tightly held by a number of intra-sheet hydrogen bonds. This network, dominated by the rather strong C=O···H-N hydrogen bonds, maintains the chains at a precise distance of about 4.7 Å along the a axis. In α-chitin, some inter-sheet hydrogen bonds along the b parameter of the unit cell are present, involving the association of the hydroxymethyl groups of adjacent chains. Such a feature is not found in the structure of β-chitin, which is therefore more susceptible than α-chitin to intra-crystalline swelling.[9]

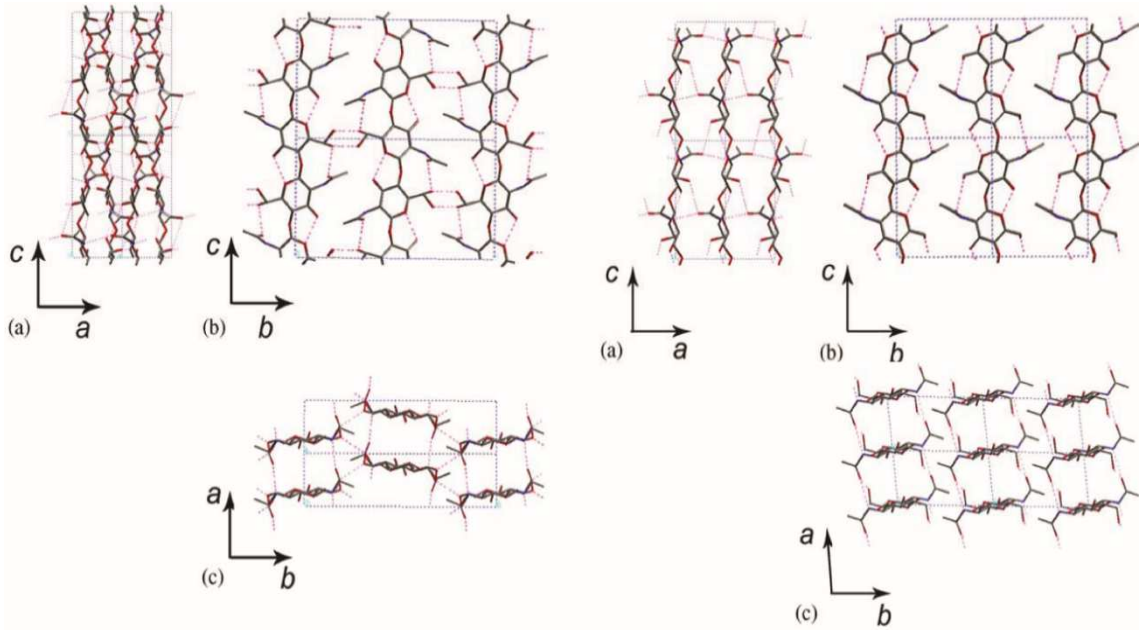

Figure 3: On the right, the crystal structure of α-chitin. On the left, the crystal structure of anhydrous β-chitin. Different projections along the crystallographic axes are reported for each polymorph: (a) ac projection; (b) bc projection; (c) ab projection. Figure from Rinaudo e al. (2006).[9]

Interconversion between polymorphs has been observed only from β-chitin and γ-chitin to α-chitin. This interconversion occurs in highly alkaline (> 7.5 M NaOH)[10] or acidic conditions (> 8 M HCl)[11] for β-chitin. γ-chitin was observed converting in α-chitin by treating it in saturated lithium thiocyanate solutions at room temperature.[12] Both the polymorph also re-precipitate as α-chitin when a complete solubilization of the polymer was observed.[13] This unidirectional conversion is probably due to a higher stability of α-chitin due to its inter-molecular network of hydrogen bonds.

1.2. Properties of chitin

Despite the relatively simple chemical structure, chitin exhibits some interesting properties that allowed this polymer to be applied in many different fields.[14] In fact, pure chitin is:
i) transparent, due to the absence of functional groups absorbing visible light; ii) biocompatible, being based on a polysaccharide which evolved to be inside living organisms;[15] iii) biodegradable, existing many different enzymes able to hydrolyze chitin;[16] iv) mechanically resistant; v) mildly antimicrobial.[17][18]

Among biological polymers, the α-chitin crystal possesses one of the highest axial moduli. This value range on tens of GPa, being reported by Ogawa et al. 2011 as 60 GPa[19] and by Vincent et al. (2004) as 150 GPa.[20] The actual mechanical properties of chitin as material, however, depend on the specific processed form of the material.[15] For example, chitin from various sources was found to exhibit elastic moduli ranging between 1.1 to 2.9 GPa by tensile testing, in the dry state, and 0.3 to 0.6 GPa in the wet state.[21]

Due to a lack of hydrogen bonding, β-chitin presents lower mechanical properties compared to α-chitin. Fan et al (2012)[22] reported different film casting for α-chitin and compared it with β-chitin obtaining Young's modulus of about 5 GPa for the former and 1 GPa for the latter. The mechanical properties highlight why in nature α-chitin is usually found where extreme hardness is required, while β- and γ-chitins provide toughness, flexibility, and mobility, and may have physiological functions other than supports, such as control of electrolytes and transport of polyanion.[23]

1.3. Differences between chitin and chitosan

The difference between chitin and chitosan is not well defined in the literature and those two compounds are frequently considered the same thing. The degree of acetylation (DA) has a crucial effect on chitin properties. As discussed, the amide group has an important

role in hydrogen bond formation in the crystal structure. Decreasing the DA chitin properties change and this new compound is called chitosan. Formally, chitin turns into chitosan when the DA is below 30% and the polymer starts to be soluble in mild acid environments.

The main difference between those two forms is in their solubility. Chitin lack in solubility so strong polar solvents (such as N,N-dimethylacetamide with LiCl 5 wt.%, or pure hexafluoroisopropanol) or warm highly acid treatments (which usually rely on hydrolysis) are necessary for the solubilization. Chitosan, on the other hand, is easily soluble in acetic acid 3 vol.%. This different behavior is easily explained considering that chitosan, mainly formed of D-glucosamine (Figure 2), presents a high number of positive charges on the free amine groups (pK_a ~ 6.3) in an acid environment.[24]

Nishino et al. (1998) measured the elastic modulus of crystal regions in α-chitin and chitosan, 41 GPa and 65 GPa respectively at 20°C.[25] Despite the higher modulus, chitosan samples are generally less crystalline than chitin samples[26][27] and tend to form less organized fibrils.[27] These are the reasons why at the macroscale chitin frequently overpass chitosan's mechanical properties. Ferreira et al. (2009) reported a Young's modulus of about 2 GPa for a pure chitosan film, derived from α-chitin, which is lower than the 5 GPa reported by Fan et al (2012)[22] for α-chitin. Anyway, chitosan enhanced solubility in acid conditions decreases its mechanical properties moving to acid pH. In fact, Tanabe et al. (2002) measured a Young's modulus of 1.3 GPa at pH 8.9 but were not able to measure the sample at pH 6.3 due to an increase of the swelling and a consequent loss of the mechanical resistance.[28]

Finally, another difference between chitin and chitosan is their antimicrobial activity. This property is stronger in chitosan, which also exhibited a mild antifungal ability, rather than in chitin. Three antibacterial mechanisms have been proposed: i) the ionic surface interaction resulting in cell wall leakage; ii) the inhibition of the mRNA and protein synthesis via the penetration of chitosan into the nuclei of the microorganisms; iii) the formation of an external barrier, chelating metals and provoking the suppression of essential nutrients to microbial growth. All these mechanisms are favored by a higher solubility and consequently a higher bioavailability. In fact, chitin/chitosan antimicrobial activity was observed increasing with the decreasing of the DA and the shortening of the polymeric chains, increasing the charge and solubility of the polymer.[17][29][30]

1.4. Applications

The applications of chitin have been deeply investigated using this biopolymer in a wide range of different scientific fields.

The most common application for chitin, considering its mechanical properties and biocompatibility, has been in producing biomaterials for mechanical resistant grafts, as for tendon or bones. Pure chitin has been widely tested for cell culture and regenerative medicine.[15] In Abe et al. (2002) a pure 3D porous chitin scaffold was used for the culture of chondrocytes and promoted the formation of an abundant extracellular matrix.[31] Chitin has also been observed to promote positively calcium mineralization processes, hence, it has been widely applied for bone regeneration. Labelling studies showed that the chitinous matrix not only promoted the osteoblasts to proliferate, but also recruited the ingrowth of surrounding tissues.[32] Many different blends with other materials have been studied for analog application. Some examples comprehend both natural materials, as collagen[33][34] or fibroin,[35] and synthetic ones, as poly(ε-caprolactone)[36] or bioactive ceramics.[37]

Chitin crystallites, sometimes named nano-whiskers, present usually a high aspect ratio and elastic modulus.[38] Those fibrillar crystals have been widely applied as additive to increase the stiffness of different materials,[39][40][41] such as hydrogels.[42][43][44]

Due to its biocompatibility, biodegradability, transparency, and gas and water permeation chitin have also been proposed for, edible and non-edible, food packaging.[45][46] Many of those studies mostly focused on chitosan or chitin/chitosan blends, which could also rely on good antimicrobial and antifungal abilities.[47] Moreover, chitin has also been applied as fiber dietary additive.[45]

The transparency of chitin has been exploited in producing optically transparent material for future application as corneal implant, biocompatible optics, or as material for traditional optics.[48][49] As an example, Huang et al. (2013) used a chitin/silk fibroin blend to produce a diffracting grating by replica molting.[35]

Chitin also exhibited high adsorption properties for both dyes and metals, being suitable in water remediation.[50][51][52] It was observed by Filipkowska et al. (2004) to be able to absorb 205 $mg \cdot g^{-1}$ of Blue D-5RN at pH 3.[53] Glutaraldehyde cross linked chitosan beads where also tested on Cd solutions and the adsorption capacity of a 1 mm bead was 518 $mg \cdot g^{-1}$ at pH 6.5.[54] Pure chitin has been reported to adsorb cadmium and lead on its surface from seawater. [55]

Chitin chemical structure presents different functional groups. Along the years literature has presented many different protocols to selectively functionalize those groups. This led to a wide range of new functional materials derived from chitin, which further expanded the chitin's range of application. This further development of chitin-based materials will be discussed in chapter 4.

1.5. Commercial sources of chitin

Chitin is a commercially available chemical, sometimes having different DA and molecular weight. Despite that, many research groups prefer to purify their own chitin from natural matrices to get a more customized and characterized starting material. Despite the wide range of natural matrices containing chitin, this polymer is usually produced from easily available discard of fisheries and alimentary industries. In fact, most of α-chitin in literature comes from crustacean exoskeleton (crabs and shrimps), while β-chitin is mostly obtained from squid pens.

1.5.1. α-chitin: crustacean exoskeleton

Crustaceans used for chitin extraction are usually crabs[56] or shrimps[57] of commercial interest. The exoskeleton of these animals is mainly composed of three different components: chitin (14-27 wt.% in crabs, 13-15 wt.% in shrimps),[58] calcium carbonate (~70 wt.% in crabs), and the remaining is mostly proteins.[59] This matrix in the animal has a role of protection, muscles anchoring, structural support to the animal's soft tissues, and de-hydration prevention.

In crustaceans the exoskeleton is usually divided in two regions. The outermost region is the epicuticle, a thin waxy waterproof layer. Beneath the epicuticle is the procuticle, the main structural part, which is primarily designed to resist mechanical loads. The procuticle is further divided into two parts, the exocuticle (outer) and the endocuticle (inner), which have similar composition and structure. The endocuticle makes up around 90 vol.% of the exoskeleton. At the molecular level, there are long-chain polysaccharide chitins that form fibrils, ~3 nm in diameter and ~300 nm in length. The fibrils are wrapped with proteins and assemble into fibers of about 60 nm in diameter.[60] These fibers further assemble into bundles. The bundles then arrange themselves parallel to each other and form horizontal planes. These planes are stacked in a helicoid fashion, creating a twisted plywood structure. A stack of layers that have completed a 180° rotation is referred to as a Bouligand

structure.[61] These structures repeat to form the exocuticle and endocuticle.[62] The same Bouligand structure is also characteristic of collagen networks in compact bone, cellulose fibers in plant cell walls, and other fibrous materials.[63] In crab exoskeletons, the minerals are in the form of calcite or amorphous calcium carbonate, deposited within the chitin–protein matrix.[64]

Chitin extraction in crustaceans is usually articulated in two[65][57][66] or three steps:[67] 1) demineralization using a concentrated acid solution; 2) de-proteination using a boiling NaOH solution; 3) de-pigmentation using oxidant as sodium hypochlorite or hydrogen peroxide. Even if this methodology is the most commonly used, other methods have been reported in literature, such as microbial fermentation[68] or using 1-ethyl-3-methyl-imidazolium acetate.[69]

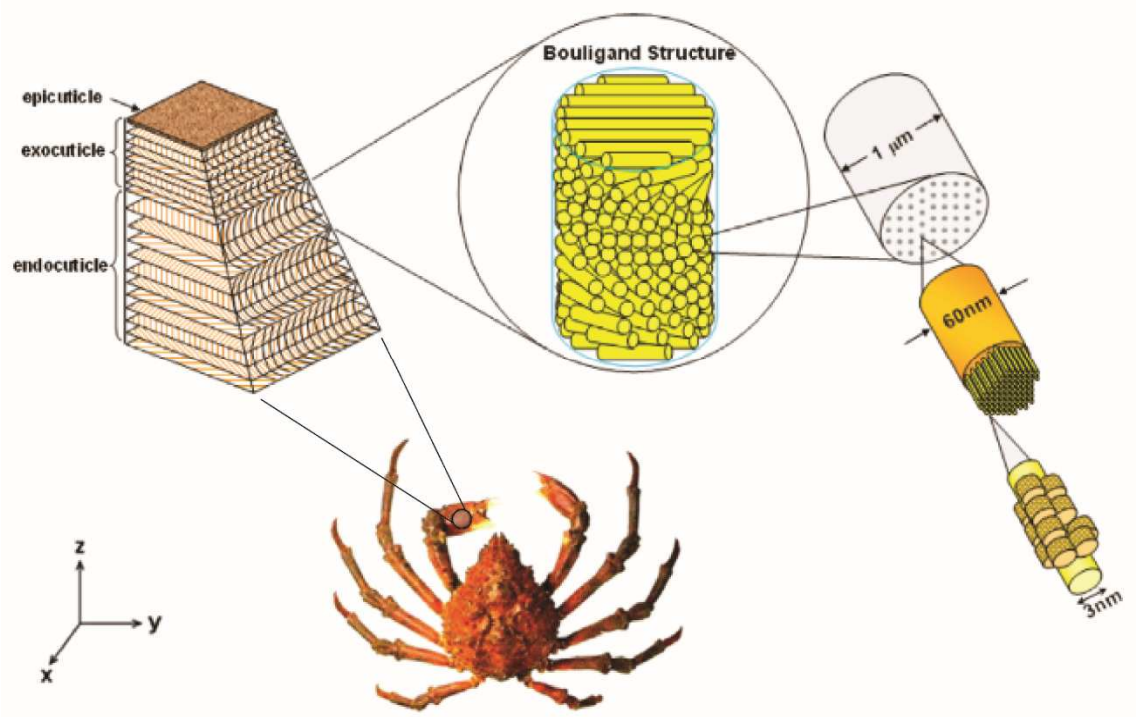

Figure 4: Hierarchical structure of the exoskeleton of sheep crab, Loxorhynchus grandis. Chitin fibrils (~3 nm in diameter) wrapped with proteins form a fiber of ~60 nm in diameter. Fibers further assemble into bundles, which form horizontal planes (x–y plane) superposed in a helicoid stacking along the z-axis, creating a twisted plywood structure (180° rotation). Figure from Chen et al. (2008).[60]

1.5.2. β-chitin: squid pen

The β-chitin polymorph, as told, is a bit more uncommon compared to α-chitin and can be found in the shell of many mollusks. The most abundant and cheap source of this chitin is the commercially available pen, or gladius, of squids. In fact, the gladius is a feather-shaped internal vestigial shell that supports the squid's mantle and serves as a site for muscle attachment.[70][71] Depending on where in the world the study takes place different species are used. In Europe, the most common squid genus used is the *Loligo*.

Yang et al. (2014) reported the structure of the gladius of two different squid species, *Sepioteuthis lessoniana* and *Uroteuthis chinensis*.[72] The gladii showed a hierarchical, self-similar structure with highly anisotropic fibers of different size oriented along the long axis of the gladius as reported in Figure 5. The fibrillar structure was observed using atomic force microscopy (AFM) and scanning electron microscopy (SEM) measurements, fibers with diameters of 500 μm, 100 μm, 10 μm, 2 μm, and 0.2 μm were observed. The molecular structure, determined using X-ray diffraction (XRD), showed chitin nano-crystallites of β-chitin wrapped in a protein layer, resulting in β-chitin nano-fibrils. About 100 of these nano-fibrils are necessary to form a 0.2 μm fiber. In these fibrils, about 90% of the α-coils of the proteins and β-chitin crystallites are oriented along the pen long axis, indicating a strong correlation between the macroscale structure and molecular orientation.

The organization of the squid pen of *Loligo vulgaris* was mildly studied by Hunt and Sheriff (1990) using transmission electron microscopy (TEM) and XRD. As reported by Yang, they also observed a protein wrapped nano-fibrillar structure of 22 nm in thickness, reported as a black and white striated structure observed using TEM. As before, the fibrils were oriented parallel to the direction of the major axis of the pen and the chitin fibers. Differently, the chitin fibrils are not hierarchically organized in bundles but are laid down in sheets which were theorized to produce an irregular Bouligand structure, as reported in arthropods.[73] This last hypothesis is rather improbable comparing this genus pen structure with other genera.

Considering the almost binary composition of this matrix, chitin is usually purified with a single de-proteination step using warm alkaline conditions, as reported in the step 2 for α-chitin.[74][75][76]

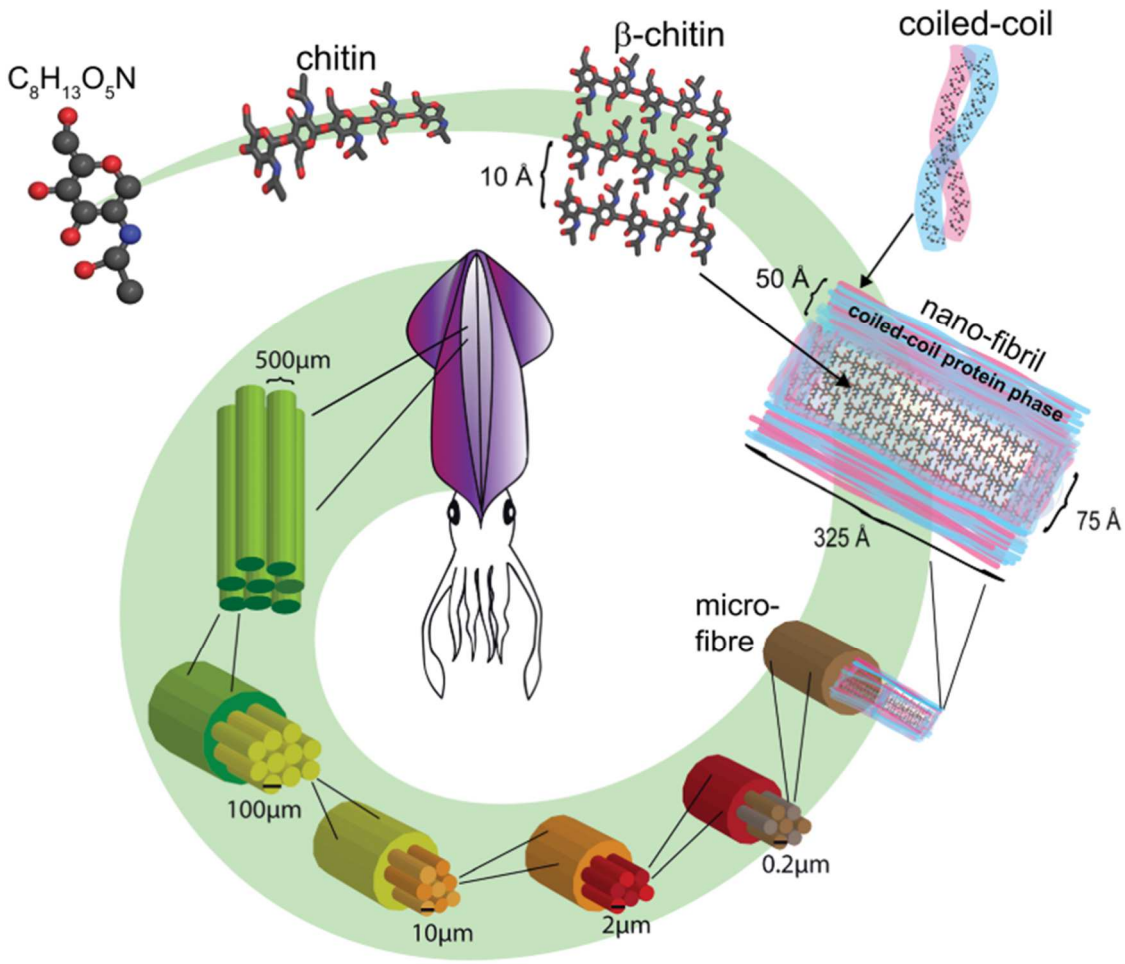

Figure 5: Hierarchy of the main structural levels in the squid gladius: β-chitin crystallites wrapped in a protein layer form the so-called nano-fibrils, which are the building blocks of 0.2 µm sized micro-fibers. These fibers aggregate into 2 µm, 10 µm, 100 µm and 500 µm thick fibers, which eventually form the squid gladius. Figure from Yang et al. (2014).[72]

2. Structure and morphology influence on the material's properties

The chemical structure of a molecule is crucial to define its properties and possible applications. In addition, organized materials can have properties depending on their structure and their combined effect with other structural components, as in self-assembled and composite materials. These scenarios are widely common in nature where evolution led to highly organized materials, usually composites.

As discussed at the beginning of the introduction, chitin is the most diffused structural biopolymer in nature[5] and is found in an enormous variety of different morphologies. Its different organizations lead to different properties of the matrix as light interference, control of crack propagation, high mechanical resistance, etc. Some examples of these organized structures have been reported in mollusks, the squid pen, and arthropod, crustacean exoskeleton, in this chapter section 1.5. Afterwards, a deeper analysis of other chitin-based highly organized natural matrices.

2.1. Chitin in nature's architecture

2.1.1. Structural material: Sponges

Despite the wide diffusion of chitin along the different animal phyla, chitin in Porifera was discovered only in 2007 by investigating the internal proteinaceous skeleton of two demosponges (*Aplysina sp*. and *Verongula gigantea*).[77] This discovery was quite important in the evolutionary point of view considering that Porifera are one of the most ancient phylum in the animal kingdom. Immediately after this discovery, Ehrlich and co-workers published the first report showing that α-chitin is an endogenous material within the siliceous skeletons of the glass sponge *Farrea occa,* Figure 6.[78] Underlying the siliceous structure the study showed a three dimensional chitinous matrix with an overall shape closely resemble the shape of the integer sponge skeleton. At the nanoscale a layered structure is present.

It was hypothesized that chitin may be part of a very old template system involved in biosilicification phenomena; which was established long before the origin of glass sponges in the Cambrian period. Chitin implication in biosilicification was, anyway, not surprising considering the wide influence that this biopolymer has on biomineralization processes, especially in calcification.[79][80][81]

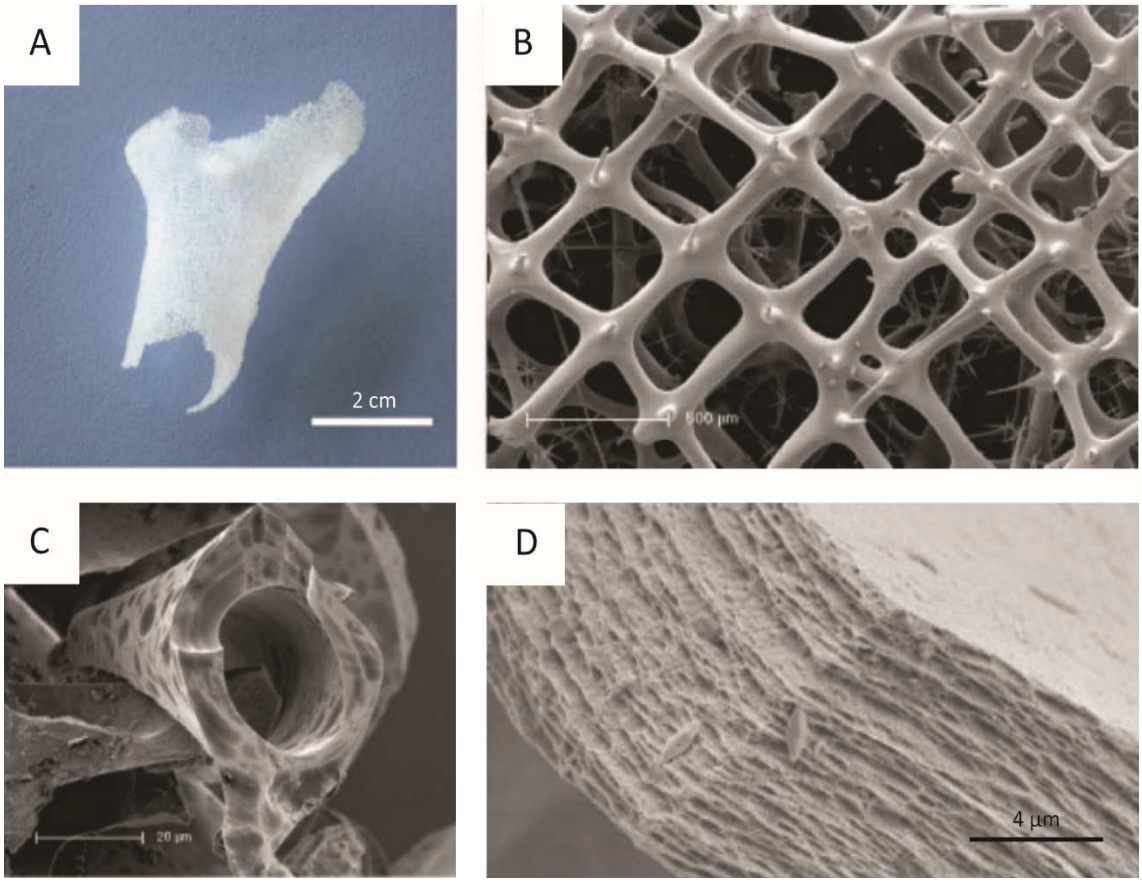

Figure 6: Picture (A) and SEM image (B) of Farrea occa siliceous tissue-free skeleton. (C) SEM image of the alkali resistant material of Farrea occa skeleton which (D) shows a multilayered structure. Images from Ehlrich et at. (2007).[78]

In 2009, Brunner et al.[82] discovered that chitin-based scaffolds are an integral part of skeletons from the marine demosponge *Ianthella basta*. This study showed how marine sponges can produce unique, chitin-based, highly organized two-dimensional networks composed of cross-linked fibers of approximately 40–100 nm in diameter. These fibers consist of loosely packed chitin; with rough, deeply fissured surfaces, as can be observed in Figure 7. The study showed how in the native sponge skeleton, proteins and bromotyrosine-related compounds are intercalated into the chitin-based scaffold and cross-linked with the chitin, preventing it from forming unperturbed crystalline chitin.[82][83] In 2013, chitin was reported in the skeletal structure of fresh water sponges responsible of the adhesion to the substrate, the holdfast, the sponges studied where *Lubomirskia baicalensis*[84] and *Spongilla lacustris*.[85] These were the first reports showing how chitin plays a crucial role in the adhesion of sponges to rocky substrates.

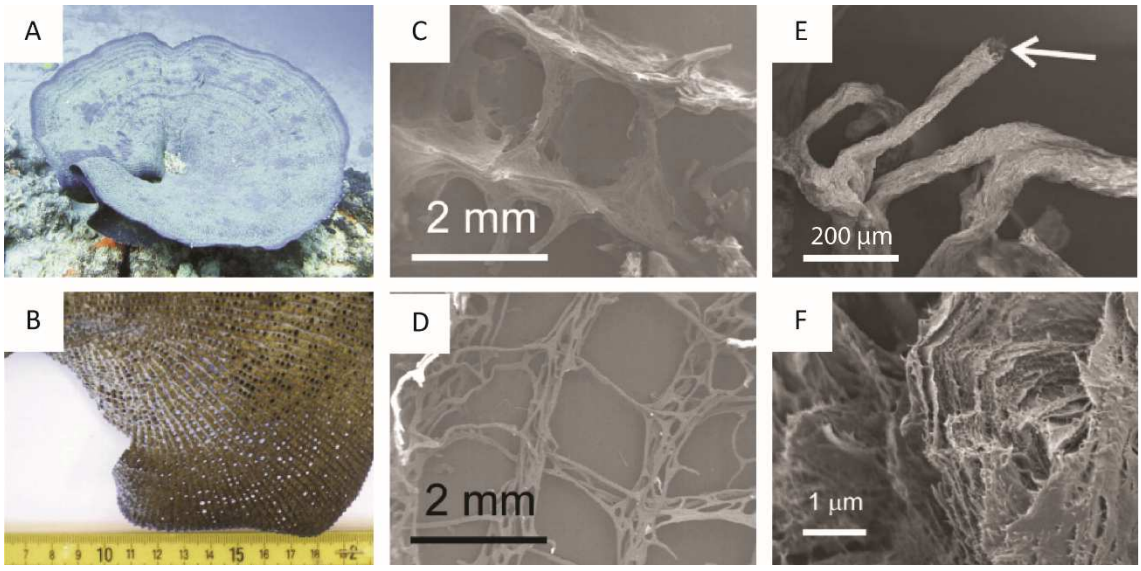

Figure 7: (A) Underwater photograph of a living marine demosponge Ianthella basta. The diameter of the sponge corresponds to about 1 m. (B) Photographs of the freeze-dried I. basta skeleton. (C) SEM images of a freeze-dried I. basta skeleton sample and of (D) an isolated scaffold after alkaline treatment. SEM images showing the (E) micro- and (F) nano-organization of a selected chitin fiber from the I. basta skeleton after alkaline treatment. Images from Brunner et al. (2009).[82]

Chitin in Porifera is a crucial example on how chitin evolved very early in life history as a structural material. Along this long evolution lifespan this biopolymer was also deeply involved in the control of the deposition of bioinorganic structural materials, as silicon and calcium based ones, establishing itself as one of the most diffused and crucial component of an enormous variety of natural matrices.

2.1.2. Mechanical properties: The stomatopod's dactyl club

The stomatopods are a group of marine crustaceans of about 15 cm of length. In stomatopods, the terminal segment of the second pair of thoracic appendages is a heavily mineralized club used to smash their prey. At the macroscale, the club comprises the two terminal segments, the propodus and the dactyl (Figure 8, A to D). This hammer-like structure can inflict considerable damage even to heavily mineralized biological structures (as shells, exoskeletons, skulls of fish, and occasionally fisherman).[86] As described by Patek et al. (2005),[87] these formidable structures are capable of accelerations to 10400 g and speeds of 23 $m \cdot s^{-1}$ from a stationary position. Their rapid strike can generate cavitation bubbles, which collapse producing high stresses at the contact point with the target, in addition to the instantaneous forces of ≥ 700 N resulting from the direct impact. Despite these large loads, the dactyl clubs are extremely damage tolerant and can withstand

thousands of highly energetic blows before being replaced during periodic molting events.[88]

Weaver et al. (2012) reported a detailed study on the structure, composition and mechanical properties of the dactyl club of *Odontodactylus scyllarus*,[89] a common reef-associated stomatopod from the tropical Indo-Pacific.[87]

Nanoindentation and energy-dispersive spectroscopy (EDS) measurements (Figure 8, F and G) of sectioned clubs reveal a distinct correlation between the extent of mineralization and their corresponding mechanical properties. Different mineral compositions were reported for these areas gradually moving from a hard hydroxyapatite impact region (Young's modulus of 65-70 GPa) to an amorphous carbon- and magnesium-rich periodic region (dry Young's modulus of 10-25 GPa). Further analysis of the impact region using synchrotron mapping data revealed that the hydroxyapatite crystallites exhibit a preferred orientation with the (002) lattice planes oriented parallel to the impact surface.

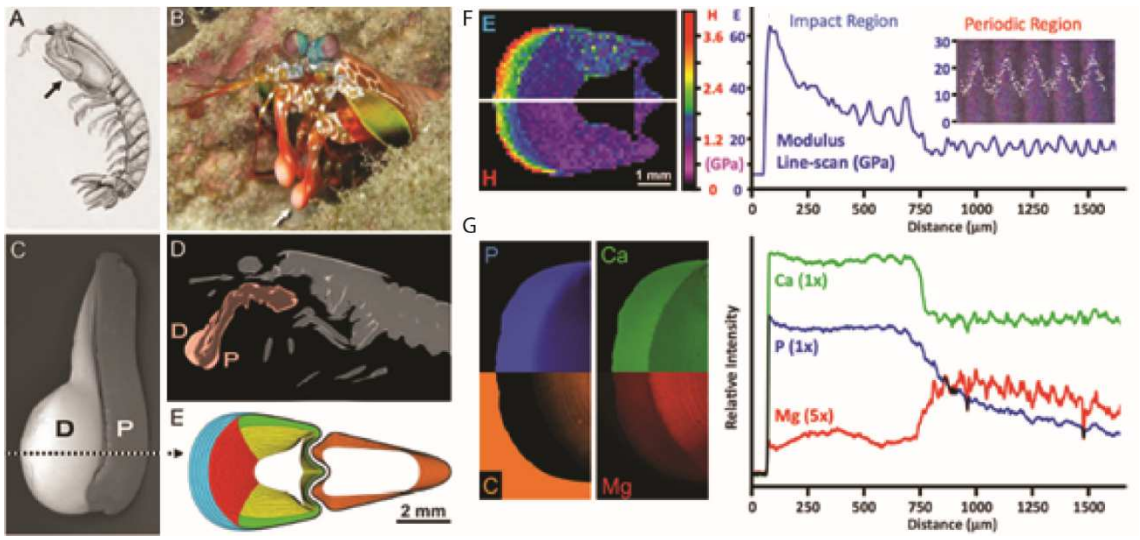

Figure 8: (A) A generalized stomatopod body plan and (B) a view of the anterior end of O. scyllarus. (C) Backscattered scanning electron micrograph of the club's external morphology [dactyl (D) and propodus (P) segments] and (D) a longitudinal section through the anterior half of a specimen, revealing their differences in electron density. (E) Cross-sectional analysis of the club illustrates the three distinct structural domains: (i) The impact region (blue), (ii) the periodic region [subdivided into: medial (red) and lateral (yellow)], and (iii) the striated region (green). The periodic region of the propodus is shown in orange. (F) Large-area nanoindentation [elastic modulus (E) and hardness (H)] map of the dactyl club and a corresponding line scan, including a high resolution plot through five superlayers; periodicity: ~75 µm overlayed on a corresponding micrograph. (G) EDS maps and line scans showing the non-uniform elemental distributions in the periodic and impact regions (Mg data were expanded by a factor of 5). Figure from Weaver et al. (2012).[89]

Underlying the mineral phases a chitinous matrix is observed. This matrix exhibits a Bouligand structure (Figure 9) with layers that decrease in thickness from the club exterior to the interior in a linear fashion and the superlayers that follow the club's contours.

A hard outermost layer is a structure widely employed for mechanically active[90] or protective[91] hard tissues. In addition to this first line of defense, a computational study showed how the club's microstructural complexity imparts the club with several mechanisms against catastrophic failure. Although internal cracks are suggested to be likely to nucleate beneath the impact region, the chitin helicoidal architecture provides several toughening mechanisms that hinder the catastrophic propagation of such cracks. Weaver et al. demonstrated that the tendency of cracks is in fact to nest volumetrically within the periodic region between the chitin fibers. In three dimensions, this can be represented as a helicoidal fracture pattern propagating between layers, with a rotating crack front that remains parallel to the fibers without severing them, which results in the distinctive double spiral-like motif shown in Figure 9, G and H. One key implication is that this pattern creates a much larger surface area per unit crack length in the main direction of propagation, hence amplifying the total energy dissipated during impact and crack propagation, a behavior that has also been observed in engineered helicoidal composites.[92] Moreover, when a crack deviates from its helicoidal path and propagates straight into neighboring layers, it encounters an elastic modulus oscillation due to their anisotropic stiffness. As shown by Fratzl et al.,[93] this oscillation provides an additional protection against damage. These results suggest that crack propagation across layers is hampered by the modulus oscillation, which improves the damage tolerance with an efficiency that depends on the crack propagation direction relative to the chitin fiber orientation, as can be observed in the micro-cracks in Figure 9 C.

A final protective mechanism against catastrophic fracture is provided by the sharp transition between the impact surface and the bulk of the impact region. If a crack approaches the impact surface, it encounters an elastic modulus mismatch which deflects the cracks at the interface. Such a mechanism has important implications, because the crack-tip stress amplification is greatly reduced when debonding occurs.[94] Charge-contrast scanning electron micrographs indicated that cracks remain mostly contained within the periodic region, with evidence of deflection within the impact region, implying that this effect successfully prevents cracks from reaching the club's outer surface.

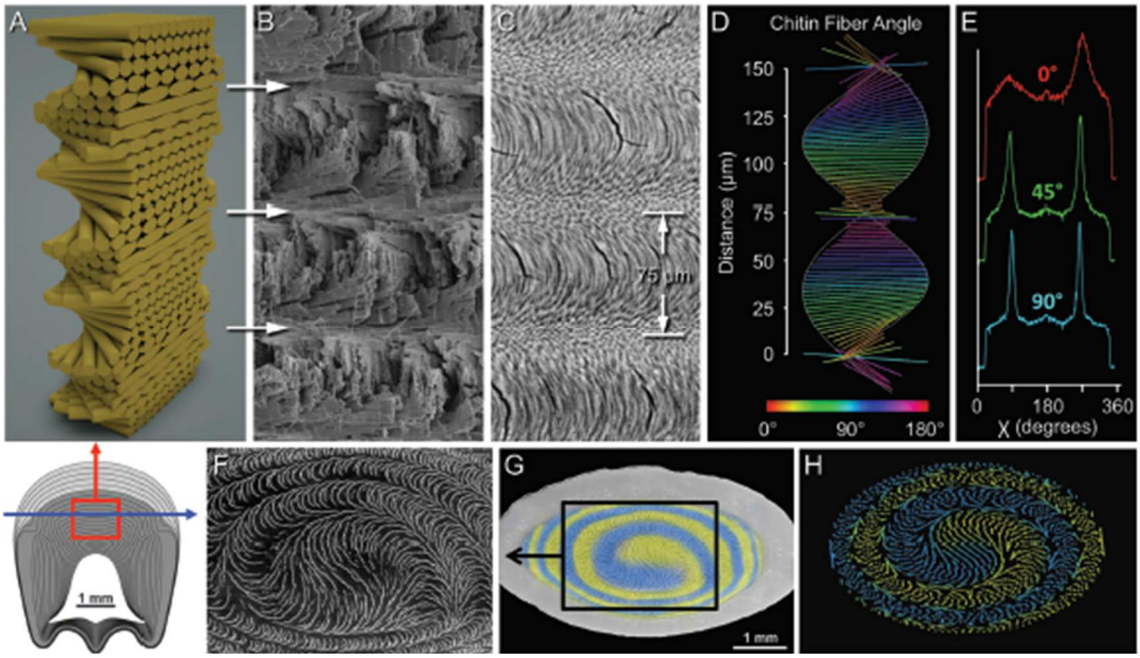

Figure 9: Comparisons between a generalized 3D model of a helicoid (A) with an SEM fractograph (B) and a polished surface from a transverse cross section (C) (with periodicity: ~75 µm). (D) A visualization of the chitin fiber orientations from the x-ray scattering analysis of 92 separate diffractograms obtained through two superlayers. (E) Three representative c plots of the α-chitin (110) reflection used to calculate fiber angles. A charge contrast scanning electron micrograph from a damaged coronal cross section (F) with false color (G) and a model of a helicoidal slice (H), which accurately reproduces the fracture patterns. Figure from Weaver et al. (2012).[89]

In conclusion, the stomatopod's dactyl club combination of structure and composition permits the infliction of strong impacts while simultaneously minimizing internal damage within the club. This structure is a perfect example of how a structure can control and manipulate the mechanical stress diffusion in a matrix.

2.1.3. Photonic structure: A deep look into insect's bright colorations

Among the different chitin-based matrices in nature, photonic matrices are surely the most beautiful. A photonic crystal is a periodic structure that can affect light motion due to the dual effect of medium/material refractive index and distances in the material periodicity, the wavelength reflected is usually angle dependent. In nature these effects can be widely found among insects, such as in the iridescence of beetles or butterfly's bright colored wings, where the effect arises from composite materials of chitin and proteins.

The wings of the butterflies of the genus *Morpho*, typical of Central and South America, are one of the most studied examples in nature of photonic structure. Their wings display a

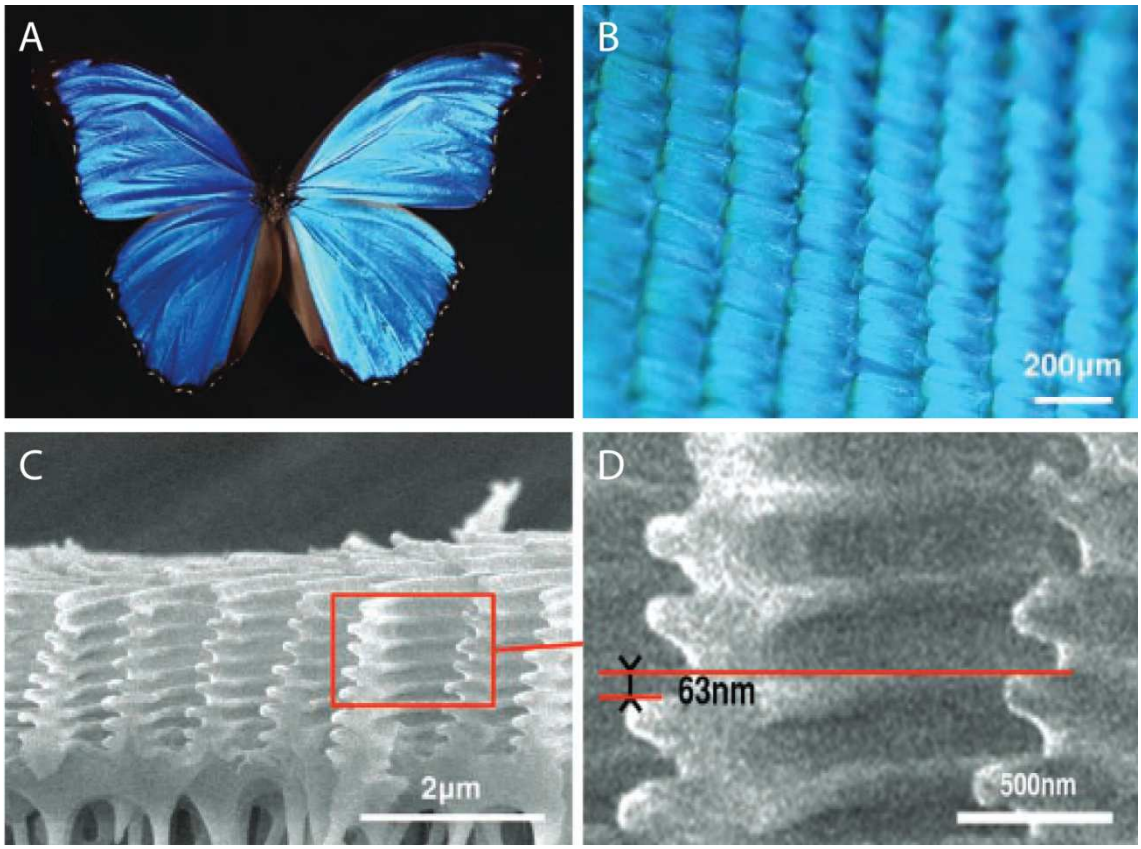

Figure 10: (A) Image of a Morpho didius and (B) optical microscope image of its wing, displaying many localized glints rather than a uniformly specular reflection. (C) Cross-sectional SEM image of the multilayered ridges on the dorsal ground scale of a Morpho didius butterfly. The red rectangle indicates the region shown in more detail in (D). (D) A close-up view of the ridges, showing a vertical offset of 63 nm between two neighboring ridges. Figure from Chung et al. (2012).[95]

bright blue coloration that arises from chitinous Christmas tree structures on the scales of their wings, see Figure 10.[95] These structures all have similar shapes, and are placed on the wing scales with a high packing density, leading to the high reflectivity. At the same time, the exact spatial locations of the structures, both along and perpendicularly to the surface of the scale, are disordered on the subwavelength level such that each ridge contributes individually to interference instead of forming a continuous multilayer.[95] This, together with their narrow width, their random variations in the exact shape, and pigment in the scales, causes the *Morpho* butterfly wings to exhibit not only interference,[96] but also diffraction,[96][97] scattering, and even pigment-induced absorption,[98] which all work together to produce the paradox of brilliant iridescence of *Morpho* butterflies.

Another uncommon example of a photonic structure can be found in *Chrysina resplendens* (Figure 11), a scarab beetle from Central America. It exhibits a peculiar metallic

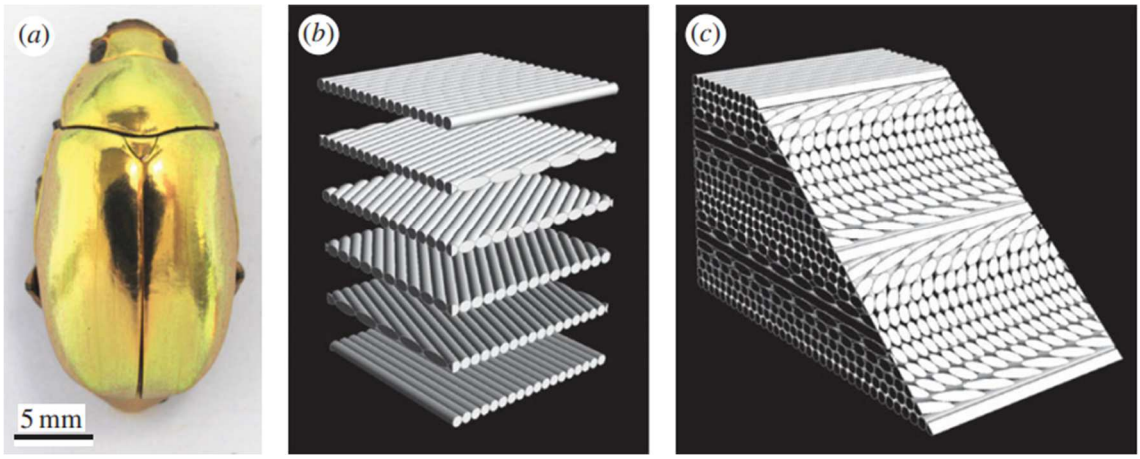

Figure 11: (a) Dorsal view of C. resplendens. (b) An exploded (c) and assembled view of the helicoidal Bouligand structure. Figure from Finlayson et al. (2017).[100]

coloration. Such a color cannot be obtained by using pigments as it involves a broad reflection over a wide angular range. The exoskeleton structures responsible for this effect have been identified as a Bouligand structure[99] that acts as a two dimensional photonic crystal. Below this structure, another layer act as retarder, a component able to invert light polarization. Finlayson et al. report that the combination of these two structures allow the insect to reflect both L- and R-handed circular polarized light.[100] Moreover, the inhomogeneity in thickness over the filament plane and the chirping of the planes allows reflecting light over a broad range of the visible spectrum being also less directionally dependent. The broader the range of bandwidths, the closer to pure gold the cuticle appears.

2.2. Learning from nature: the bioinspired approach

In section 2.1 are reported just a few examples on how nature has shaped chitin to get materials with very different applications, used as inspiration to invent and improve technologies all over the world. In fact, natural structures born as a solution to specific problems and their refinement has occurred over millions of years.

The need of exploiting nature's knowledge is the base of biomimicry or biotemplate approaches, which aims to replicate the designs of biological materials. In the last tens of years, another approach has widely diffused: the bioinspired one. This novel approach aims to improve modeling and simulation of the biological system to attain a better understanding of the nature's critical structural features to obtain bioinspired designs.

Bioinspired research can be seen as a return to the classical origins of science. It is a field based on observing the remarkable functions that characterize living organisms, and trying to abstract and imitate those functions.

Of course, the bioinspired approach needs a quite deep understanding of the natural system itself increasing the need for basic research. A few examples of bioinspired technologies are reported in the next sections.

2.2.1. Adhesion: Gecko foot

Climbing presents a significant challenge for an adhesive; it requires both strong attachment and easy rapid removal. Conventional pressure-sensitive adhesives are either strong and difficult to remove (e.g. duct tape), or weak and easy to remove (e.g. sticky notes). The gecko is able to easily climb on walls thanks to an adhesive system that differs dramatically from conventional adhesives. [101] Gecko's toes have angled arrays of branched hair-like setae, each 30-130 µm long, that divide into hundreds of projections terminating in 0.2-0.5 µm spatula-shaped structures[102] formed of keratin (Figure 12).

Autumn et al. (2000) discovered that the adhesion in isolated setae requires a small push perpendicular to the surface, followed by a small parallel drag. Dragging setae in shear pulls the spatula in tension resulting in large friction and adhesion forces. When properly oriented, preloaded and dragged, a single seta can generate 200 µN in shear and 40 µN in adhesion, over three orders of magnitude more than that required to hold the animal's body weight. All 6.5 million setae on the toes of one gecko attached simultaneously could lift 133 kg. Given the surprisingly large attachment forces generated by their setae, it is remarkable that geckos can detach their feet in just 15 ms with no measurable detachment forces. This easy detachment is due to the shape of the setae tips, which, if pulled at the right angle, can be easily detached from the surface.

The single setae only rely on van der Waals interactions.[103] This implies that the remarkable adhesive properties of gecko setae are merely a result of the size and shape of the tips, and are not strongly affected by surface chemistry, allowing the gecko to adhere on any surface. Moreover, the setae were reported to have self-cleaning ability due to an energetic disequilibrium between the adhesive forces attracting a dirt particle to the surface and those attracting the same particle to one or more setae.[104]

This unique system has inspired many different approaches.[105][106][107]

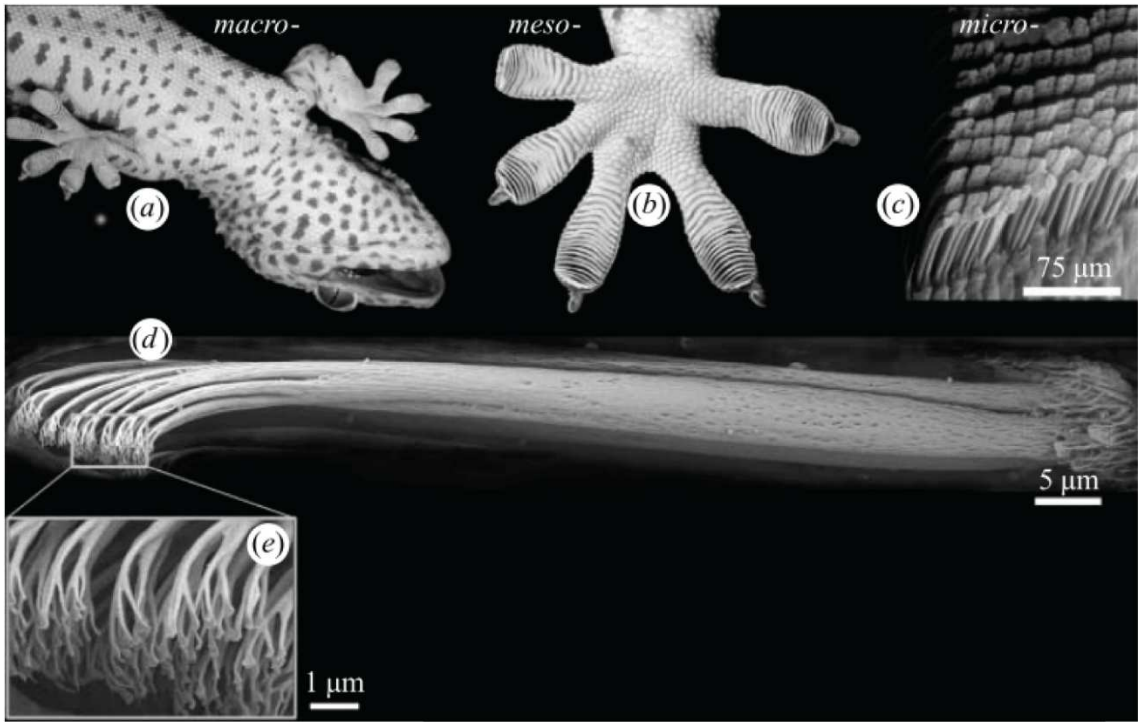

Figure 12: Structural hierarchy of the gecko adhesive system. (a) Ventral view of a Gekko gecko climbing a vertical glass surface. (b) Ventral view of the foot of the gecko, showing a mesoscale array of seta-bearing scansors. (c) Microscale array of setae are arranged in a nearly grid-like pattern on the ventral surface of each scansor. Each diamond-shaped structure is the branched end of a group of four setae clustered together in a tetrad. (d) Cryo-SEM image of a single seta with (e) nanoscale array of hundreds of spatular tips. Figure from Autumn et al. (2008).[101]

Geim et al. (2003)[106] proposed two examples of polyimide hairs microfabricated using electron-beam lithography and dry etching in oxygen plasma, Figure 13 A-B. Their results indicate that the microfabricated adhesive makes use of both capillary and van der Waals forces. The average force of a single hair was found to be ≈70 nN and 1 cm^2 patch was able to support 3 N, which is comparable to the estimated adhesive force of 10 $N \cdot cm^{-2}$ for gecko. Despite that, in 2007 a macroscopic array of vertically aligned multi-walled carbon nanotubes developed by Qu et al. set a new record of 11.7 $N \cdot cm^{-2}$ obtaining a semiconducting dry adhesives, Figure 13 C-D.[107]

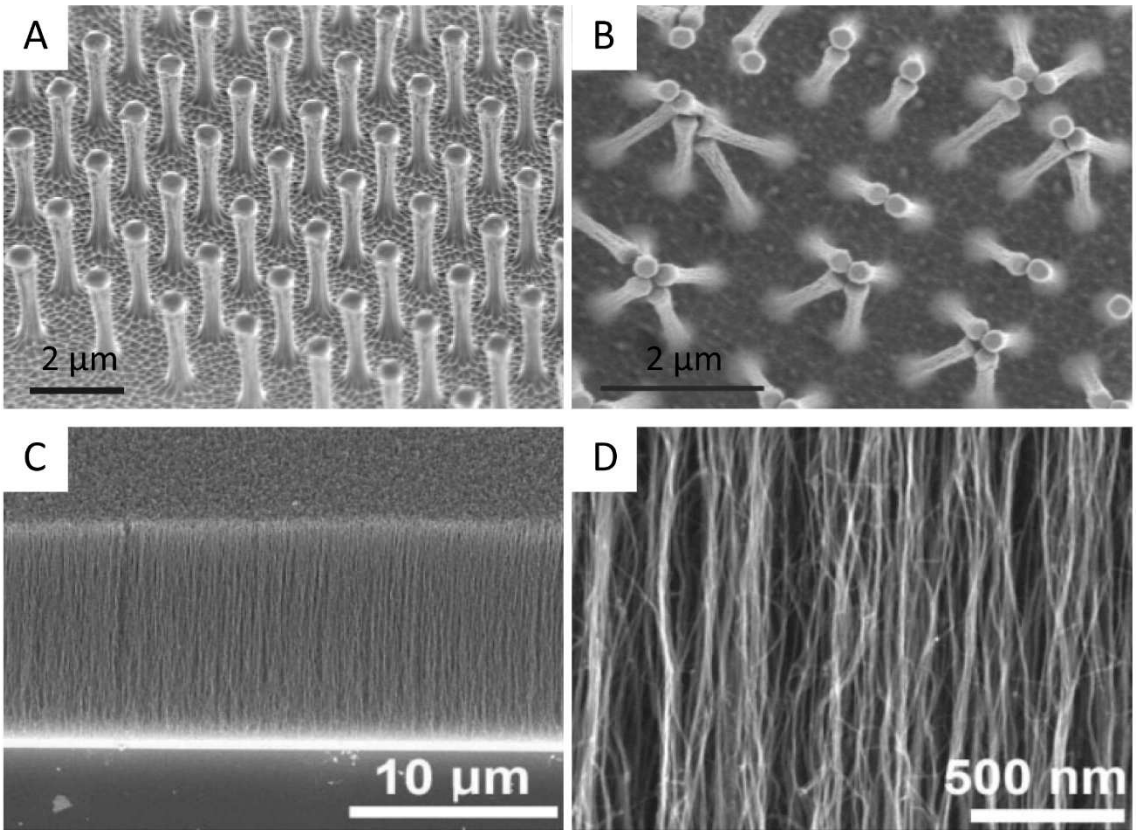

Figure 13: (A-B) Geim et al. arrays of polyimide hairs, (A) was later used to evaluate macroscopic adhesive properties of the mimetic material. The bunching observable in (B) was found to be one of the mechanisms responsible for the reduction of adhesive strength of the artificial hair.[106] *(C-D) SEM images of the aligned multi-walled carbon nanotubes by Qu et al. (2007).*[107]

2.2.2. Light interference: Chameleon's skin

One of the most surprising structural adaptation in nature is definitely the chameleon skin, able to change color on animal necessity. Teyssier et al. (2015)[108] found that the panther chameleons' (*Furcifer pardalis*) color-shifting ability is due to the active tuning of a lattice of guanine nano-crystals within a superficial thick layer of dermal cells called iridophores, Figure 14. The deeper population of iridophores with larger crystals reflects a substantial proportion of sunlight, especially in the near-infrared range. The iridophores in this layer contain small close-packed guanine crystals, with a diameter of 130 ± 20 nm, organized in a triangular lattice. The guanine crystals have a high refractive index of 1.83, while the cytoplasm has a low refractive index of 1.33, and together they form a photonic crystal structure. The TEM images of *F. pardalis* samples of blue or green skin and images of yellow or white skin of the same individuals showed that the distance among guanine crystals was on average 30 % smaller in the resting than in the excited skin. In these samples the crystal

size in surface iridophores did not vary. The organization of iridophores into two superposed layers constitutes an evolutionary novelty for chameleons, which allows some species to combine efficient camouflage with a spectacular display, while potentially providing passive thermal protection.

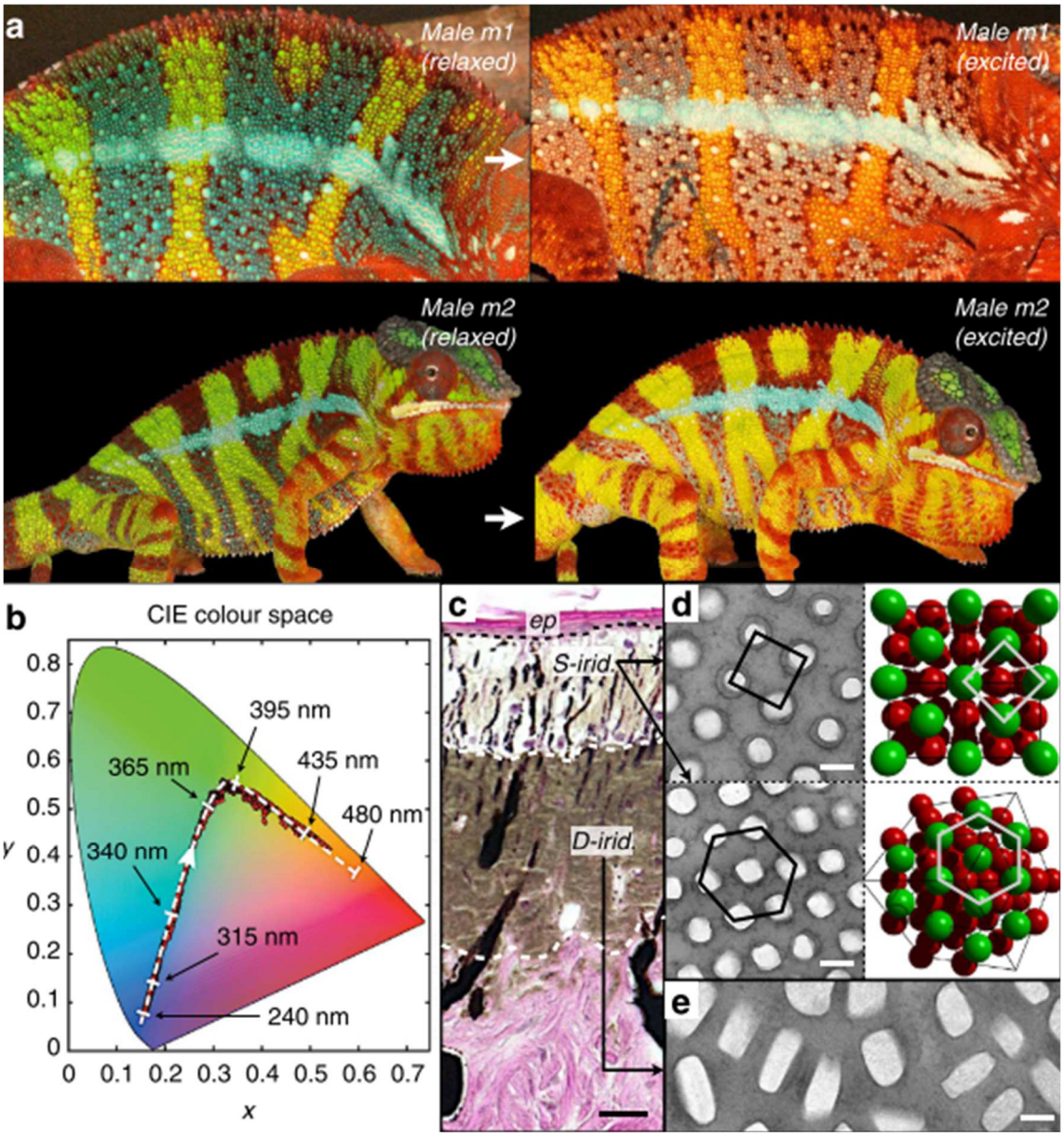

Figure 14: (a) Reversible color change is shown for two males (m1 and m2). (b) Red dots: time evolution in the CIE chromaticity chart of a third male with green skin in a high-resolution video; dashed white line: optical response in numerical simulations using a face-centred cubic lattice of guanine crystals with lattice parameter indicated with black arrows. (c) Haematoxylin and eosin staining of a cross-section of white skin showing the epidermis (ep) and the two thick layers of iridophores. (d-e) TEM images of guanine nanocrystals in D- and S-iridophores in the excited state. Scale bars, 20 µm (c); 200 nm (d,e). Figure from Teyssier et al. (2015).[108]

Kolle and co-workers[109] developed a simple strategy for measuring sub-bandage pressure reported in Figure 15. They integrated stretchable optomechanical fibers, inspired by chameleon skin, into elastic bandages. These fibers are made of polydimethylsiloxane (refractive index, n ≈ 1.41) and polystyrene-polyisoprene triblock copolymer (n ≈ 1.55). Specifically, these fibers possess an elastomeric photonic multilayer cladding that surrounds an extruded stretchable core filament. When stretched, the distances in the multilayer change leading to a change in coloration. Those fibers can sustain repetitive strains of over 100 %, and respond to deformation with a predictable and reversible color variation. Integrated into elastic textiles, which apply pressure as a function of their strain, these fibers can provide instantaneous and localized pressure feedback. These colorimetric fiber sensors are well suited for medical textiles, athletic apparel, and other smart wearable technologies, especially when repetitive, large deformations are required.

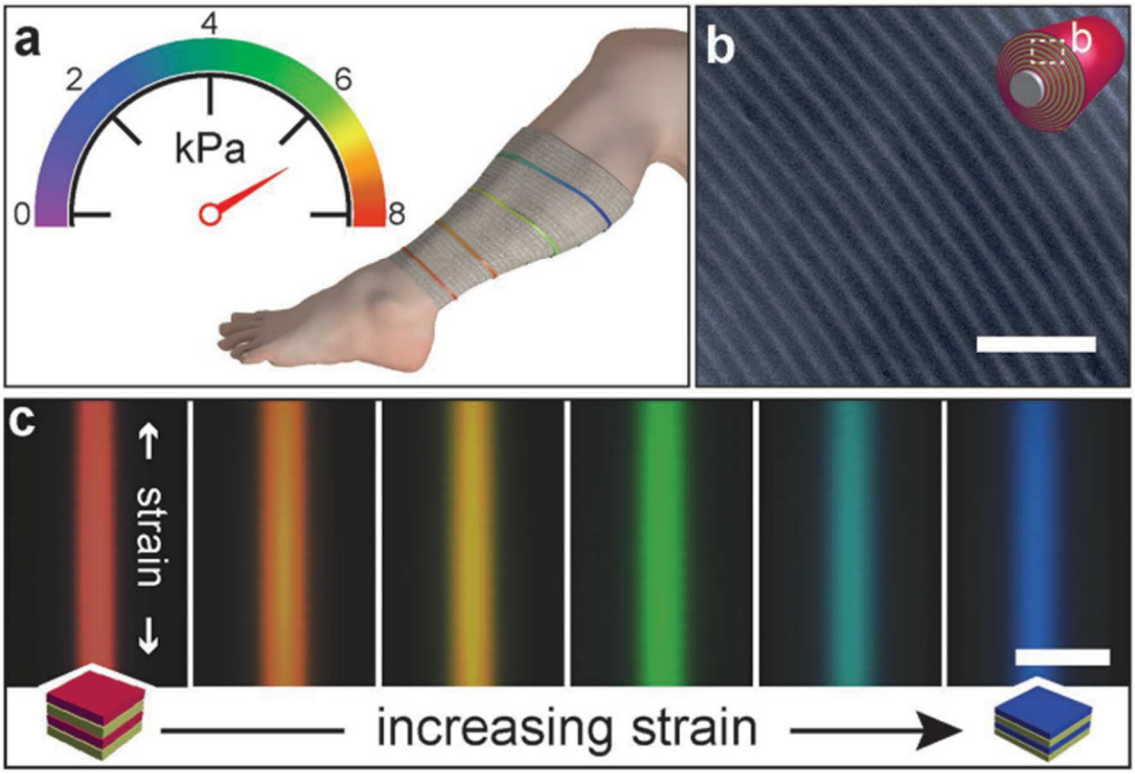

Figure 15: a) Depiction of the pro-posed use of fibers as colorimetric sub-bandage pressure indicators in compression therapy. b) Scanning electron microscopy image of a cross- section of a multilayer cladding, showing its distinct radial periodicity. Scale bar 2 µm. c) A series of optical micrographs showing the vivid, strain-dependent color of a fiber that is colored red when no strain is applied and changes as the strain increases and the layer period decreases. The direction of the applied strain is marked in the first image. Scale bar 100 µm. Figure from Sandt et al. (2018).[109]

2.2.3. Mechanical resistance: Nacre

Biomineralized structures have been a huge source of inspiration in both understanding how to synthetically control mineral deposition and how to achieve better properties inspiring to their nano-structure.

Among the huge variety of mineralized matrices (bones, teeth, horns, antlers, shells, etc.), nacre earned a central attention due to its specific nanostructure and composition. In fact, nacre is actually a composite between calcium carbonate and different biomacromolecules that both contribute to increase its properties and control mineral deposition. Nacre is mainly found in the inner layer of many mollusk shells and is composed of polygonal aragonitic tablets, about 5–15 µm in diameter.[110] These tables are arranged in continuous parallel lamellae, typically around 0.5 µm thick, separated by thin sheets of organic matrix creating a "brick wall" like structure.[111] These organic layers both direct crystal nucleation and growth and prevents crack propagation due to an oscillating Young's modulus (similarly as in the stomatopod dactyl club).[112]

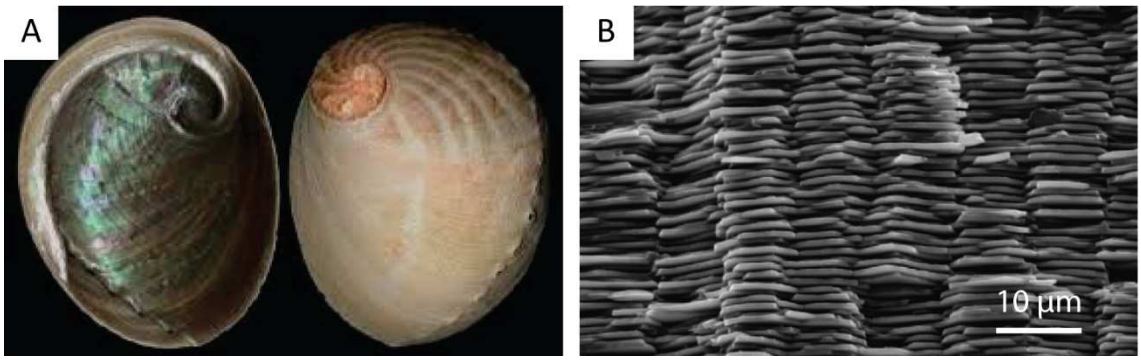

Figure 16: (A) Image of the shell of Haliotis laevigata where the iridescent internal nacre can be seen on the left. (B) Section of the SEM nacre layer, image from Tushtev et al. (2007).[112]

Das et al. (2015) reported the synthesis of a nacre bioinspired composite of polyvinylalcohol coated nanoclay platelets.[113] The study shows the relationships among structure formation, nano-structuration, deformation mechanisms, and mechanical properties as a function of nanoclay aspect ratio. They showed how highly ordered, large-scale nacre-mimetics obtained from low aspect ratio nano-platelets show pronounced inelastic deformation with very high toughness (Young's modulus of 40 GPa compared to natural nacre 70 GPa). On the other hand, the materials formed by large nano-platelets exhibit high stiffness and strength (200 MPa of max stress, which is almost three times that of nacre).

These results were previously only reachable by highly cross-linked materials. Moreover, the material obtained was glass-like transparent and an excellent gas barrier.

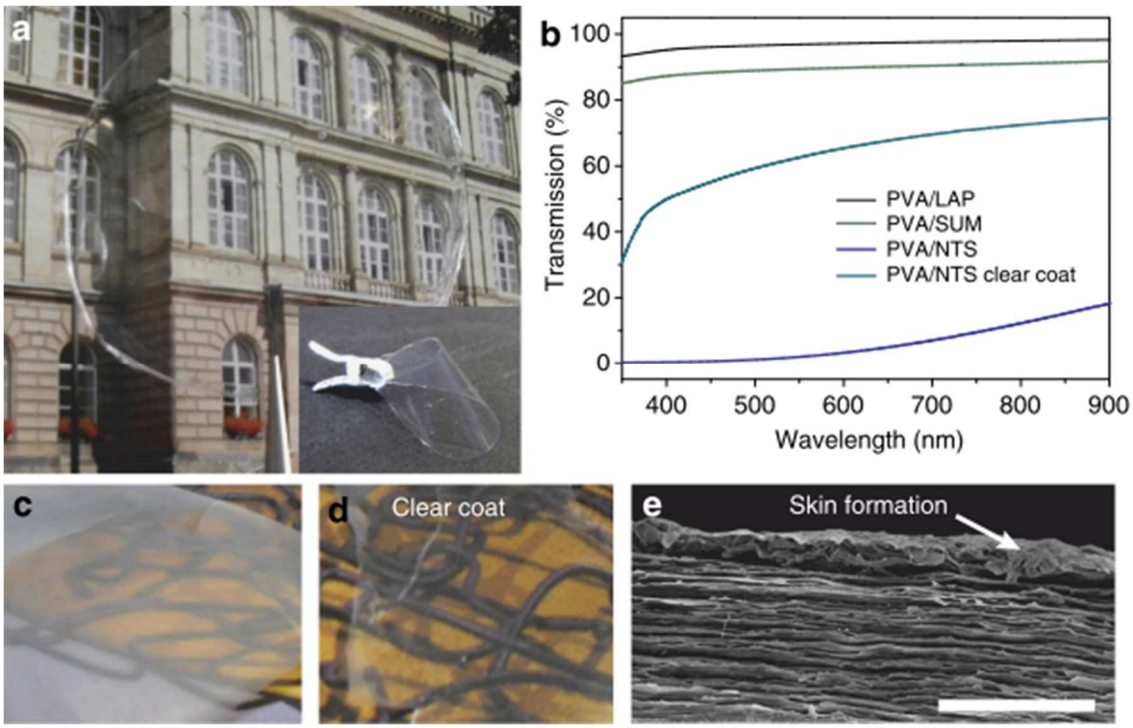

Figure 17: (a) Photographs of an almost fully transparent polyvinylalcohol coated nanoclay (PVA/LAP) film. (b) Transparency by UV-Visible spectroscopy (normalized to 25 mm thickness). (c,d) Nacre-mimetics with larger nanoclay (PVA/NTS) show translucency, but require a clear-coat matching the refractive index of the nacre-mimetics closely to become almost transparent. (e) SEM of a PVA/NTS nacre-mimetic (scale bar, 5mm). Figure from Das et al. (2015).[113]

3. Aim of the thesis

As described along this chapter chitin is a widespread material in nature whose properties have been observed vary depending on its morphology, texture, and overall structure. The bioinspired approach, as much as many other approaches, has given a huge contribution to science using the knowledge derived from the understanding of nature's phenomena. This thesis aims to study chitin at different levels of organization. To do that, the project is articulated in three main topics, which will be discussed each in a different chapter.

The first of these chapters will discuss the use of a bottom-up approach to study chitin self-assembly *in vitro* and its interaction with other biomacromolecules. As discussed chitin is a biopolymer that can be found in very organized matrices but how animals are able to achieve these structures is mostly unknown. New insight on how this process take place could one day help developing new methods to control the morphology of other polymers.

The second topic will examine organized chitin-based matrices in nature, in both *Ariolimax californicus* and *Loligo vulgaris*, in order to gain new information on natural structures. These information might one day be applied in new bioinspired approaches.

In the last one, a top-up approach will be used to exploit natural hierarchically organized chitinous matrices to obtain organized functional material. In this last chapter, the squid pen of *Loligo vulgaris* will be used as proof of concept for this new approach.

In conclusion, this thesis aims to exploit chitin diversity along nature as a source of new knowledge to drive future studies, especially in bioinspired materials.

4. References

[1] D. Klemm, B. Heublein, H. P. Fink, A. Bohn, *Angew. Chemie - Int. Ed.* **2005**, *44*, 3358.

[2] C. Jeuniaux, M. F. Voss-Foucart, *Biochem. Syst. Ecol.* **1991**, *19*, 347.

[3] N. O. Keyhani, S. Roseman, *Biochim. Biophys. Acta - Gen. Subj.* **1999**, *1473*, 108.

[4] V. S. Yeul, S. S. Rayalu, *J. Polym. Environ.* **2013**, *21*, 606.

[5] International Institute for Species Exploration, State of Observed Species **2011**.

[6] P. Sikorski, R. Hori, M. Wada, *Biomacromolecules* **2009**, *10*, 1100.

[7] R. Minke, J. Blackwell, *J. Mol. Biol.* **1978**, *120*, 167.

[8] K. H. Gardner, J. Blackwell, *Biopolymers* **1975**, *14*, 1581.

[9] M. Rinaudo, *Prog. Polym. Sci.* **2006**, *31*, 603.

[10] Y. Noishiki, H. Takami, Y. Nishiyama, M. Wada, S. Okada, S. Kuga, *Biomacromolecules* **2003**, *4*, 896.

[11] Y. Saito, J. L. Putaux, T. Okano, F. Gaill, H. Chanzy, *Macromolecules* **1997**, *30*, 3867.

[12] K. M. Rudall, W. Kenchington, *Biol. Rev.* **1973**, *49*, 597.

[13] M. Rolandi, R. Rolandi, **2014**, *207*, 216.

[14] E. Khor, *Chitin: fulfilling a biomaterials promise*; Elsevier, 2014.

[15] A. C. A. Wan, B. C. U. Tai, *Biotechnol. Adv.* **2013**, *31*, 1776.

[16] H. Merzendorfer, L. Zimoch, *J. Exp. Biol.* **2003**, *206*, 4393.

[17] M. S. Benhabiles, R. Salah, H. Lounici, N. Drouiche, M. F. A. Goosen, N. Mameri, *Food Hydrocoll.* **2012**, *29*, 48.

[18] M. M. G. Fouda, R. Hrdina, R. M. Abdel-Rahman, A. Y. Soliman, F. K. Mohamed, A. M. Abdel-Mohsen, K. Mohsin, T. D. Pinto, *Int. J. Biol. Macromol.* **2015**, *80*, 107.

[19] Y. Ogawa, R. Hori, U. J. Kim, M. Wada, *Carbohydr. Polym.* **2011**, *83*, 1213.

[20] J. F. V. Vincent, U. G. K. Wegst, *Arthropod Struct. Dev.* **2004**, *33*, 187.

[21] H. R. Hepburn, I. Joffe, N. Green, K. J. Nelson, *Comp. Biochem. Physiol.* **1975**, *50A*, 551.

[22] Y. Fan, H. Fukuzumi, T. Saito, A. Isogai, *Int. J. Biol. Macromol.* **2012**, *50*, 69.

[23] K. M. Rudall, *Symp. Soc. Exp. Biol.* **1955**, *49*.

[24] H. El Harmoudi, L. El Gaini, E. Daoudi, M. Rhazi, Y. Boughaleb, M. A. El Mhammedi, A. Migalska-zalas, M. Bakasse, *Opt. Mater. (Amst).* **2014**, *36*, 1471.

[25] T. Nishino, R. Matsui, K. Nakamae, *J. Polym. Sci. Part B Polym. Phys.* **1999**, *37*, 1191.

[26] D. Montroni, S. Fermani, K. Morellato, G. Torri, A. Naggi, L. Cristofolini, G. Falini, *Carbohydr. Polym.* **2019**, *207*, 26.

[27] K. Zhang, A. Geissler, S. Fischer, E. Brendler, E. Bäücker, *J. Phys. Chem. B* **2012**, *116*, 4584.

[28] T. Tanabe, N. Okitsu, A. Tachibana, K. Yamauchi, **2002**, *23*, 817.

[29] G. Tsai, W. Su, H. Chen, C. Pan, *Fish. Sci.* **2002**, *68*, 170.

[30] Y. Andres, L. Giraud, C. Gerente, P. Le Cloirec, *Environ. Technol.* **2007**, *28*, 1357.

[31] M. Abe, M. Takahashi, S. Tokura, H. Tamura, A. Nagano, *Tissue Eng.* **2004**, *10*, 585.

[32] Z. Ge, S. Baguenard, L. Yong, A. Wee, E. Khor, *Biomaterials* **2004**, *25*, 1049.

[33] S. B. Lee, Y. H. Kim, M. S. Chong, Y. M. Lee, *Biomaterials* **2004**, *25*, 2309.

[34] X. Li, Q. Feng, X. Liu, W. Dong, F. Cui, *Biomaterials* **2006**, *27*, 1917.

[35] J. Jin, P. Hassanzadeh, G. Perotto, W. Sun, M. A. Brenckle, D. Kaplan, F. G. Omenetto, M. Rolandi, *Adv. Mater.* **2013**, *25*, 4482.

[36] R. Arun Kumar, A. Sivashanmugam, S. Deepthi, S. Iseki, K. P. Chennazhi, S. V. Nair, R. Jayakumar, *ACS Appl. Mater. Interfaces* **2015**, *7*, 9399.

[37] M. Peter, P. T. Sudheesh Kumar, N. S. Binulal, S. V. Nair, H. Tamura, R. Jayakumar, *Carbohydr. Polym.* **2009**, *78*, 926.

[38] M. Mincea, A. Negrulescu, V. Ostafe, *Rev. Adv. Mater. Sci.* **2012**, *30*, 225.

[39] K. G. Nair, A. Dufresne, *Biomacromolecules* **2003**, *4*, 657.

[40] X. Li, Q. Feng, F. Cui, *Mater. Sci. Eng. C* **2006**, *26*, 716.

[41] P. Hariraksapitak, P. Supaphol, *J. Appl. Polym. Sci.* **2010**, *117*, 3406.

[42] J. Araki, Y. Yamanaka, K. Ohkawa, *Polym. J.* **2012**, *44*, 713.

[43] P. Hassanzadeh, M. Kazemzadeh-Narbat, R. Rosenzweig, X. Zhang, A. Khademhosseini, N. Annabi, M. Rolandi, *J. Mater. Chem. B* **2016**, *4*, 2539.

[44] Y. Huang, M. Yao, X. Zheng, X. Liang, X. Su, Y. Zhang, A. Lu, L. Zhang, *Biomacromolecules* **2015**, *16*, 3499.

[45] E. Agulló, M. S. Rodríguez, V. Ramos, L. Albertengo, *Macromol. Biosci.* **2003**, *3*, 521.

[46] P. C. Srinivasa, R. N. Tharanathan, *Food Rev. Int.* **2007**, *23*, 53.

[47] F. S. Kittur, K. R. Kumar, R. N. Tharanathan, *Z. Leb. Unters Forsch A* **1998**, *206*, 44.

[48] S. Ifuku, A. Ikuta, M. Egusa, H. Kaminaka, H. Izawa, M. Morimoto, H. Saimoto, *Carbohydr. Polym.* **2013**, *98*, 1198.

[49] M. I. Shams, S. Ifuku, M. Nogi, T. Oku, H. Yano, *Appl Phys A* **2011**, *102*, 325.

[50] L. N. Daubert, R. A. Brennan, *Environ. Eng. Sci.* **2007**, *24*, 1475.

[51] A. Bhatnagar, M. Sillanpää, *Adv. Colloid Interface Sci.* **2009**, *152*, 26.

[52] P. A. Felse, T. Panda, *Bioprocess Eng.* **1999**, *20*, 505.

[53] U. Filipkowska, E. Klimiuk, S. Kuś, **2004**, *13*, 653.

[54] G. L. Rorrer, T. Y. Hsien, J. D. Way, *Ind. Eng. Chem. Res.* **1993**, *32*, 2170.

[55] M. Gonzalez-Davila, J. M. Santana-Casiano, F. J. Millero, *J. Colloid Interface Sci.* **1990**, *137*, 102.

[56] F. Burrows, C. Louime, M. Abazinge, O. Onokpise, *Am. Eurasian J. Agric. Environ. Sci* **2007**, *2*, 103.

[57] A. Rajalakshmi, N. Krithiga, A. Jayachitra, *Middle-East J. Sci. Res.* **2013**, *16*, 1446.

[58] H. K. No, S. P. Meyers, K. S. Lee, *J. Agric. Food Chem.* **1989**, *37*, 575.

[59] F. Boßelmann, P. Romano, H. Fabritius, D. Raabe, M. Epple, *Thermochim. Acta* **2007**, *463*, 65.

[60] P. Y. Chen, A. Y. M. Lin, J. McKittrick, M. A. Meyers, *Acta Biomater.* **2008**, *4*, 587.

[61] D. Raabe, P. Romano, C. Sachs, H. Fabritius, A. Al-Sawalmih, S. B. Yi, G. Servos, H. G. Hartwig, *Mater. Sci. Eng. A* **2006**, *421*, 143.

[62] M. M. Giraud-Guille, *Tissue Cell* **1984**, *16*, 75.

[63] M.-M. Giraud-Giuille, *Curr. Opin. Solid State Mater. Sci.* **1998**, *3*, 221.

[64] H. A. Lowenstam, *Science (80-.).* **1981**, *211*, 1126.

[65] Y. S. Puvvada, S. Vankayalapati, S. Sukhavasi, *Int. Curr. Pharm. J.* **2012**, *1*, 258.

[66] A. Percot, C. Viton, A. Domard, *Biomacromolecules* **2003**, *4*, 12.

[67] S. Ifuku, M. Nogi, K. Abe, M. Yoshioka, M. Morimoto, H. Saimoto, H. Yano, *Biomacromolecules* **2009**, *10*, 1584.

[68] Y. Xu, C. Gallert, J. Winter, *Appl. Microbiol. Biotechnol.* **2008**, *79*, 687.

[69] Y. Qin, X. Lu, N. Sun, R. D. Rogers, *Green Chem.* **2010**, *12*, 968.

[70] A. I. Arkhipkin, V. A. Bizikov, D. Fuchs, *Deep. Res. I* **2012**, *61*, 109.

[71] J. A. A. Perez, R. K. O. Dor, P. Beck, E. G. Dawe, *Can. J. Fish. Aquat. Sci.* **1996**, *53*, 2837.

[72] F. C. Yang, R. D. Peters, H. Dies, M. C. Rheinstädter, *Soft Matter* **2014**, *10*, 5541.

[73] S. Hunt, A. El Sherief, *Tissue Cell* **1990**, *22*, 191.

[74] A. Ianiro, M. Giosia, S. Fermani, C. Samorì, M. Barbalinardo, F. Valle, G. Pellegrini, F. Biscarini, F. Zerbetto, M. Calvaresi, G. Falini, *Mar. Drugs* **2014**, *12*, 5979.

[75] R. L. Lavall, O. B. G. Assis, S. P. Campana-Filho, *Bioresour. Technol.* **2007**, *98*, 2465.

[76] A. Chandumpai, N. Singhpibulporn, D. Faroongsarng, P. Sornprasit, *Carbohydr. Polym.* **2004**, *58*, 467.

[77] H. Ehrlich, M. Maldonado, K. Spindler, C. Eckert, T. Hanke, R. Born, C. Goebel, P. Simon, S. Heinemann, H. Worch, *J. Exp. Zool. (Mol Dev Evol)* **2007**, *308B*, 347.

[78] H. Ehrlich, M. Krautter, T. Hanke, P. Simon, C. Knieb, S. Heinemann, H. Worch, *J. Exp. Zool. (Mol Dev Evol)* **2007**, *308B*, 473.

[79] S. Weiner, L. Addadi, *Annu. Rev. Mater. Res.* **2011**, *41*, 21.

[80] I. M. Weiss, V. Schönitzer, *J. Struct. Biol.* **2006**, *153*, 264.

[81] G. Falini, S. Weiner, L. Addadi, *Calcif. Tissue Int.* **2003**, *72*, 548.

[82] E. Brunner, H. Ehrlich, P. Schupp, R. Hedrich, S. Hunoldt, M. Kammer, S. Machill, S. Paasch, V. V. Bazhenov, D. V. Kurek, T. Arnold, S. Brockmann, M. Ruhnow, R. Born, *J. Struct. Biol.* **2009**, *168*, 539.

[83] M. Wysokowski, I. Petrenko, A. L. Stelling, D. Stawski, T. Jesionowski, H. Ehrlich, *Polymers (Basel).* **2015**, *7*, 235.

[84] H. Ehrlich, O. V. Kaluzhnaya, M. V. Tsurkan, A. Ereskovsky, K. R. Tabachnick, M. Ilan, A. Stelling, R. Galli, O. V. Petrova, S. V. Nekipelov, V. N. Sivkov, D. Vyalikh, R. Born, T. Behm, A. Ehrlich, L. I. Chernogor, S. Belikov, D. Janussen, V. V. Bazhenov, G. Wörheide, *Proc. R. Soc. B Biol. Sci.* **2013**, *280*.

[85] H. Ehrlich, O. V. Kaluzhnaya, E. Brunner, M. V. Tsurkan, A. Ereskovsky, M. Ilan, K. R. Tabachnick, V. V. Bazhenov, S. Paasch, M. Kammer, R. Born, A. Stelling, R. Galli, S. Belikov, O. V. Petrova, V. V. Sivkov, D. Vyalikh, S. Hunoldt, G. Wörheide, *J. Struct. Biol.* **2013**, *183*, 474.

[86] T. Claverie, E. Chan, S. N. Patek, *Evolution (N. Y).* **2010**, *65*, 443.

[87] S. N. Patek, R. L. Caldwell, *J. Exp. Biol.* **2005**, *208*, 3655.

[88] M. L. Reaka, *J. Morphol.* **1975**, *146*, 55.

[89] J. C. Weaver, G. W. Milliron, A. Miserez, K. Evans-lutterodt, S. Herrera, I. Gallana, W. J. Mershon, B. Swanson, P. Zavattieri, E. Dimasi, D. Kisailus, *Science (80-.).* **2012**, *336*, 1275.

[90] J. C. Weaver, Q. Wang, A. Miserez, A. Tantuccio, R. Stromberg, K. N. Bozhilov, P. Maxwell, R. Nay, S. T. Heier, E. DiMasi, D. Kisailus, *Mater. Today* **2010**, *13*, 42.

[91] B. J. F. Bruet, J. Song, M. C. Boyce, C. Ortiz, *Nat. Mater.* **2008**, *7*, 748.

[92] T. Apichattrabrut, K. Ravi-Chandar, *Mech. Adv. Mater. Struct.* **2006**, *13*, 61.

[93] P. Fratzl, H. S. Gupta, F. D. Fischer, O. Kolednik, *Adv. Mater.* **2007**, *19*, 2657.

[94] K. S. Chan, M. Y. He, J. W. Hutchinson, *Mater. Sci. Eng. A* **1993**, *167*, 57.

[95] K. Chung, S. Yu, C. J. Heo, J. W. Shim, S. M. Yang, M. G. Han, H. S. Lee, Y. Jin, S. Y. Lee, N. Park, J. H. Shin, *Adv. Mater.* **2012**, *24*, 2375.

[96] S. Kinoshita, S. Yoshioka, K. Kawagoe, *Proc. R. Soc. B* **2002**, *269*, 1417.

[97] D. Zhu, S. Kinoshita, D. Cai, J. B. Cole, *Phys. Rev. E* **2009**, *80*, 1.

[98] P. Vukusic, J. R. Sambles, C. R. Lawrence, R. J. Wootton, *Proc. R. Soc. B* **1999**, *266*, 1403.

[99] S. Caveney, *Proc. R. Soc. London. B* **1971**, *178*, 205.

[100] E. D. Finlayson, L. T. McDonald, P. Vukusic, *J. R. Soc. Interface* **2017**, *14*.

[101] K. Autumn, N. Gravish, *Philos. Trans. R. Soc. A* **2008**, *366*, 1575.

[102] K. Autumn, Y. A. Liang, S. T. Hsieh, W. Zesch, W. P. Chan, T. W. Kenny, R. Fearing, R. J. Full, *Nature* **2000**, *405*, 681.

[103] K. Autumn, M. Sitti, Y. A. Liang, A. M. Peattie, W. R. Hansen, S. Sponberg, T. W. Kenny, R. Fearing, J. N. Israelachvili, R. J. Full, *PNAS* **2002**, *99*, 12252.

[104] W. R. Hansen, K. Autumn, *PNAS* **2005**, *102*, 385.

[105] T. S. Kustandi, V. D. Samper, D. K. Yi, W. S. Ng, P. Neuzil, W. Sun, *Adv. Funct. Mater.* **2007**, *17*, 2211.

[106] A. K. Geim, S. V. Dubonos, I. V. Grigorieva, K. S. Novoselov, A. A. Zhukov, S. Y. Shapoval, *Nat. Mater.* **2003**, *2*, 461.

[107] L. Qu, L. Dai, *Adv. Mater.* **2007**, *19*, 3844.

[108] J. Teyssier, S. V. Saenko, D. Van Der Marel, M. C. Milinkovitch, *Nat. Commun.* **2015**, *6*, 1.

[109] J. D. Sandt, M. Moudio, J. K. Clark, J. Hardin, C. Argenti, M. Carty, J. A. Lewis, M. Kolle, *Adv. Healthc. Mater.* **2018**, *7*, 1800293.

[110] N. Watabe, *J. Ultrastruct. Res.* **1965**, *12*, 351.

[111] F. Nudelman, B. A. Gotliv, L. Addadi, S. Weiner, *J. Struct. Biol.* **2006**, *153*, 176.

[112] K. Tushtev, M. Murck, G. Grathwohl, *Mater. Sci. Eng. C* **2008**, *28*, 1164.

[113] P. Das, J. M. Malho, K. Rahimi, F. H. Schacher, B. Wang, D. E. Demco, A. Walther, *Nat. Commun.* **2015**, *6*, 1.

Chapter 2:
Self-assembly of β-chitin nano-fibrils

1. Introduction

1.1. Self-assembled materials

The preparation of organized material is a challenging problem in chemistry and material science. Self-assembly is a process in which a disordered system forms an organized structure or pattern without external direction thanks to specific interactions among the components. Self-assembly is widely spread in nature, from molecular to cellular or tissue level, therefore, understanding life will require understanding self-assembly. The cell itself also offers countless examples of functional self-assembly that stimulate the design of non-living systems. Self-assembly is one of the few practical strategies for making ensembles of nanostructures and it has been frequently applied in material science to get micro- and macro-organized materials.

"Self-assembly" is not a formalized subject, and definitions of the term "self-assembly" seem to be limitlessly elastic. In 2002 Whitesides and Grzybowski limited the term to processes that i) involve pre-existing components (separate or distinct parts of a disordered structure), ii) are reversible, and iii) can be controlled by proper design of the components.[1] "Self-assembly" is thus not synonymous with "formation."

There are two main kinds of self-assembly: static and dynamic. Static self-assembly (Figure 18) involves systems that are at global or local equilibrium and do not dissipate energy. For example, molecular crystals are formed by static self-assembly. In static self-assembly, formation of the ordered structure may require energy (for example in the form of stirring), but once it is formed, it is stable. In dynamic self-assembly, the interactions responsible for the formation of structures or patterns between components only occur if the system is dissipating energy. The patterns formed by competition between reaction and diffusion in oscillating chemical reactions are simple examples while biological cells are much more complex ones.

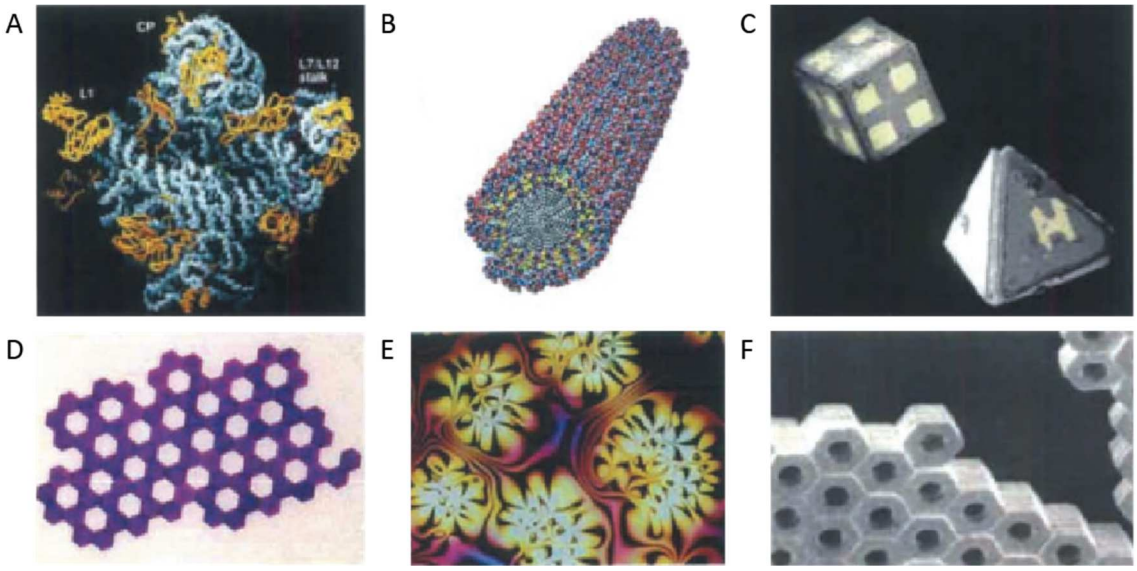

Figure 18: Examples of static self-assembly. (A) Crystal structure of a ribosome.[2] *(B) Self-assembled peptide amphiphile nanofibers.*[3] *(C) Micrometer-sized metallic polyhedra folded from planar substrates.*[4] *(D) An array of millimeter-sized polymeric plates assembled at a water/perfluorodecalin interface by capillary interactions. (E) Thin film of a nematic liquid crystal on an isotropic substrate. (F) A three-dimensional aggregate of micrometer plates assembled by capillary forces.*[5] *Figure from Whitesides and Grzybowski (2002).*[1]

1.2. Chitin biogenesis

Despite many studies have focused on chitin and a growing attention has been given to the characterization of natural chitin-based matrices, the chitin biogenesis process has not been completely understood.[6] Most studies have been focused on fungi, because of their fast growth, abundance, and "simple" unicellular structure.[7] In fungi the process has been observed to take place in three steps. First, the polymer is synthetized at the cytoplasmic-membrane interface of small vesicles where the chitin synthetases are bound. Those vesicles are less than 100 nm of diameter and are called chitosomes. Second, during the synthesis, the growing polymer is translocated across the cell membrane and released into the extracellular space (Figure 19 B). If the chitin synthetases are tightly packed on the membrane, the closely spaced chitin chains may crystallize outside the cell directly into nano-fibrils (as showed in Figure 19 C), otherwise single separate chains may be formed and be susceptible to further modifications. Third, the chitin self-assemble to form crystalline micro-fibers combining with other sugars, proteins, glycoproteins, and proteoglycans until reaching a final structure.[8]

On the other hand, chitin synthesis in arthropods appears to start from a lipid-linked intermediate, thus resembling the synthesis of glycoproteins, then, as in fungi, vesicles assemble and extrude the polymer outside the cell.[6][9]

Although many studies targeted the chitin synthase in insects,[10] gaining important information on the first two steps of the process, the route leading to complex macro-structures, such as arthropods' exoskeletons, or wings, remains almost unexplored. Similarly, in mollusks while a chitin synthase involved in shell formation was recently identified, its biosynthetic pathway and how it leads to complex 3D architectures are still unknown.[11][12]

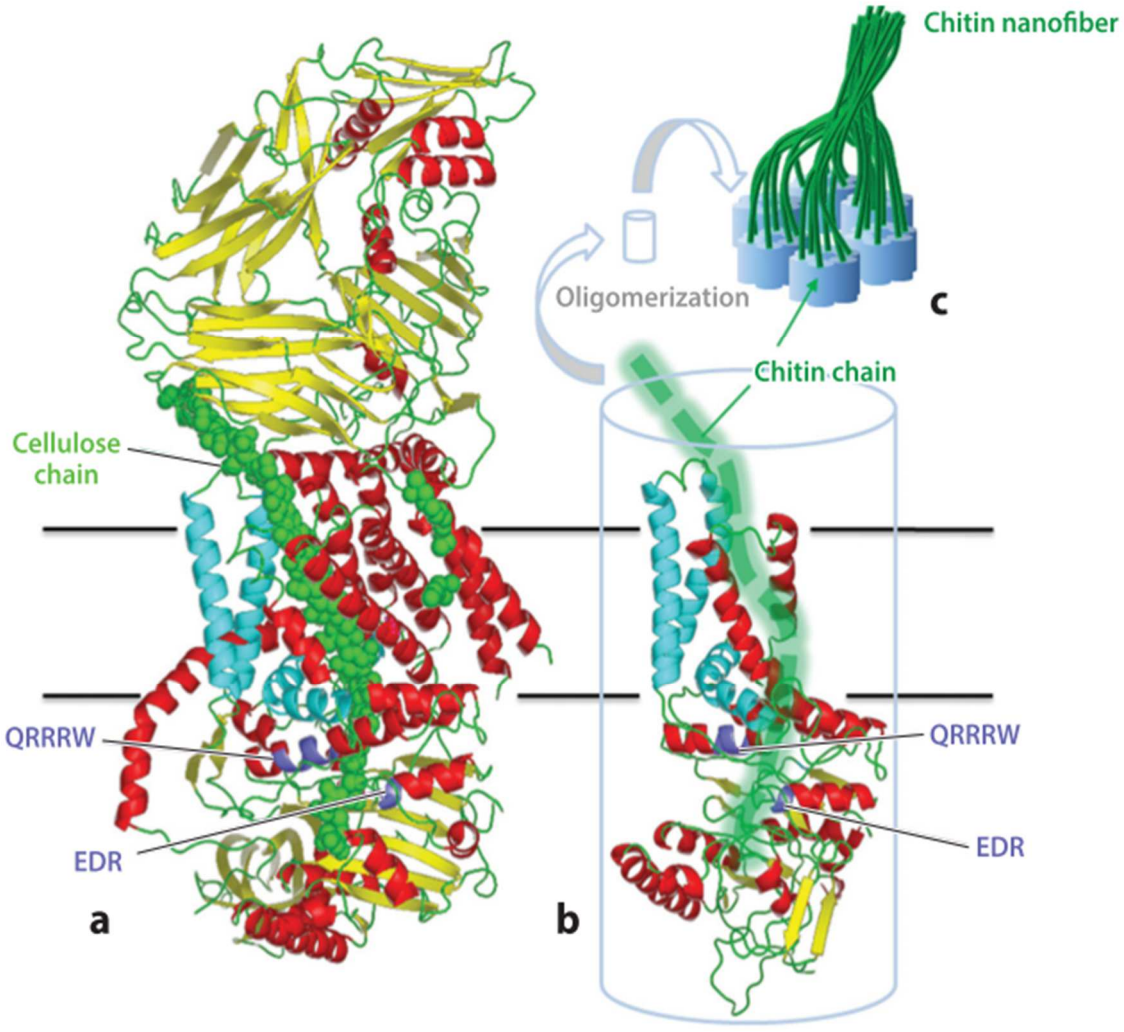

Figure 19: (a) Crystal structure of cellulose synthase from Rhodobacter sphaeroides. (b) Partial reconstruction of the structure of chitin synthase A from Tribolium castaneum. Green, cellulose/chitin; yellow, β-strands; red, α-helices; cyan, highly conserved α-helices; purple, catalytic site motifs. (c) Single catalytic chitin synthase units oligomerize to form multimeric complexes that pre-align sugar chains for nano-fibril formation. Figure from Zhu et al. (2016).[9]

1.3. Influence of molecules on self-assembly

Nature, chitin as a specific example, is a "living" proof on how the same molecule can self-assemble into different morphology depending on the molecules that are present in the system.

In vitro studies are probably one of the best ways to study the influence of different molecules on the self-assembly of a system, due to the possibility to easily isolate variables. This approach is commonly applied in biomineralization, where minerals have been crystalized in the presence of libraries of different molecules to understand their influence on the crystallization pathways (Figure 20). In chapter 3, a few examples of the influence of macromolecules on chitin self-assembly will be discussed in more details.

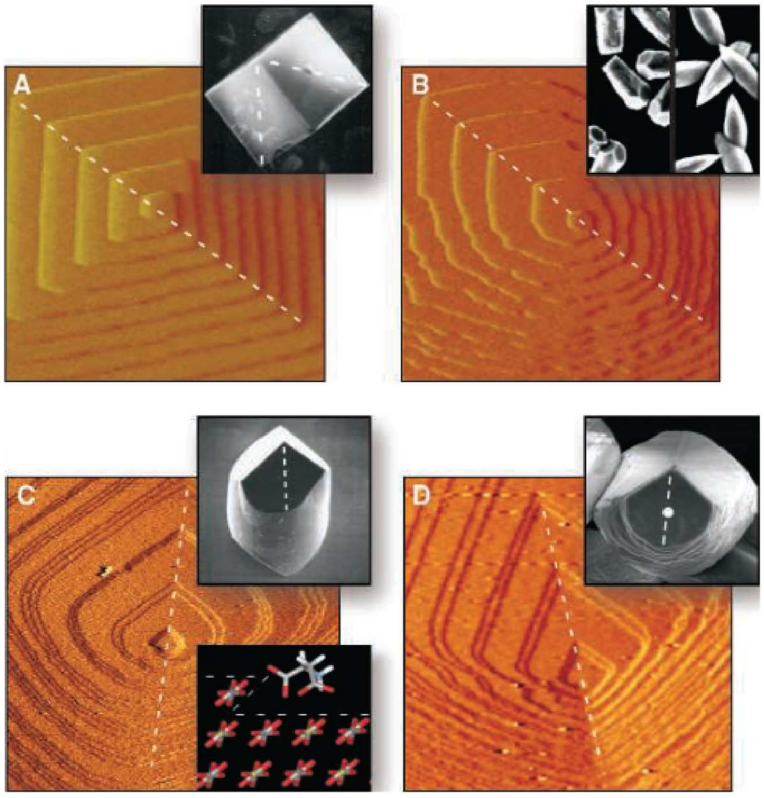

Figure 20: Studies of calcite show that changes in crystal shape are directly related to the modification of step morphology for a wide range of modifiers. Each panel shows an atomic force microscope image of growth hillocks (main image) and a scanning electron microscope image of the crystal shape (inset), with dashed lines to indicate the glide plane symmetry. (A) Pure calcite. (B) Calcite plus Mg^{2+}; inset shows crystals grown at Mg^{2+}:Ca^{2+} mole ratios of 1.5 (left) and 2.0 (right). (C) D-aspartic acid binding to a particular step on calcite. (D) Calcite plus AP8 protein extracted from abalone nacre. Figure from De Yoreo and Dove (2004).[13]

2. Aim of the study

As discussed in chapter 1, chitin is a widespread polymer in nature and biogenic chitin displays remarkable levels of organization that contribute to its material properties. Many studies aiming to synthetically replicate its structure and properties have been carried out.[14][15][16][17] Despite all those attempts, natural chitinous structures still outperform their synthetic analogues in many fields, as in mechanical performances,[18] or controlling crystal precipitation.[19][20][21] The different properties between the two chitins originate mainly from the precisely controlled hierarchical organization observed in the natural material, as opposed to synthetic ones.

In this chapter, the mechanism of β-chitin nano-fibrils assembly into micro-fibers in an aqueous solution will be investigated. β-chitin was selected instead of the more common α-chitin for two main reasons: i) its more opened and hydrated structure could be more easily dispersed in water, and ii) it could convert to α-chitin enabling us to study the best conditions for this phase transition. This study aims to obtain an *in vitro* system able to mimic the biological environment and be used in the future to study the influence of different molecules on chitin self-assembly. Chitin self-assembly is a biologically-relevant process, and its understanding will also help to describe the assembly mechanisms of other polysaccharide-based biopolymers that form highly ordered structures, such as cellulose. It may lead to new studies aiming to develop methods facilitating the synthesis of highly organized fibrous biomaterials from cheap sources, and the development of bionic approaches to biopolymers. Since this particular biopolymer is also present in pathogens, such as fungi, parasites, and pests, understanding the mechanisms of its supramolecular assembly can help with the development of new drugs targeting that process.

Successively, the system will be tested assembling chitin with collagen, another pH responsive biomacromolecule, in order to obtain an organized matrix for cell culture, reinforced with chitin. In fact, collagen exhibits huge biocompatibility and is commonly used in cell cultures and regenerative medicine. This study aims to understand how to optimize a chitin/collagen mixture to obtain an optimal cell growth.

3. Chitin nano-fibrils self-assembly

In this study, the self-assembly of β-chitin nano-fibrils (β-CnFs) in water was investigated. The fibrils were obtained as far as possible similar to their native state and the assembly was studied in water to mimic a biological environment.

3.1. Results

3.1.1. β-CnFs preparation and characterization

Squid pen is a natural matrix composed of proteins, about 60 wt.%, and β-chitin, about 40 wt.%, plus other minor components.[22][23] β-chitin was isolated from proteins using proteolytic enzymes at acidic and physiological pH, as shown in Figure 21 A. The de-proteination process was monitored by measuring the absorption of tryptophan residues at 280 nm (Figure 21 B). The spectra showed that this peak disappeared completely following the treatment, which confirmed the complete removal of proteins, at least those containing tryptophan residues.

Optical microscopy confirmed that acidic treatment at pH 3 after the de-proteination process caused the disaggregation of the β-chitin samples in β-CnFs (Figure 23). At a concentration of 0.5 mg.mL^{-1} or lower, only few disordered aggregates were present, which were not birefringent when viewed under polarized light. This indicates the absence of crystalline micro-fibers and that the β-CnFs were dispersed by the treatment at low pH. Indeed, atomic force microscopy (AFM) analysis on dry samples of β–CnFs at the same concentration revealed the presence of dispersed nanofibrils (Figure 21 C). Size measurements revealed two main groups of fibrils with different maximum average lengths, 160 ± 50 nm and 340 ± 150 nm respectively (Figure 22), and their height was (2.5 ± 0.3) nm; the latter value may be influenced by the applied load.[24] At a concentration of 1.0 mg mL^{-1}, on the other hand, few birefringent microfibers were still present (Figure 23). The XRD patterns reported in Figure 21 D showed that the chitin isolated using enzymatic digestion and the β-CnFs dispersion, all conserved the β-chitin structure. A shift of the (010) diffraction peak at a lower 2θ angle was observed in the purified β-chitin sample. This increment in the unit cell parameter was likely due to the hydration associated with the swelling observed in the de-proteination treatment.

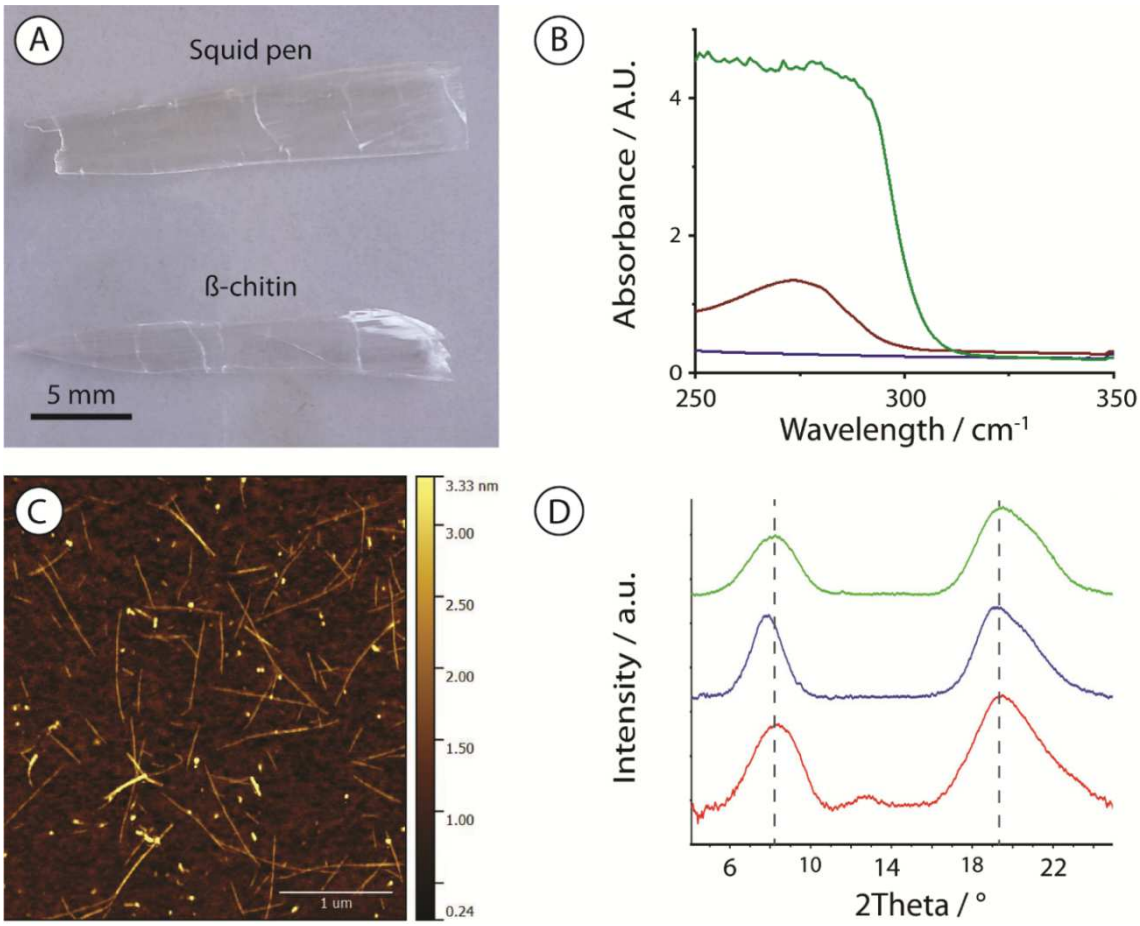

Figure 21: (A) A picture of a squid pen and the de-proteinized β-chitin. (B) The UV spectra of a squid pen (green), chitin after the first enzymatic treatment (brown), and purified β-chitin (blue). (C) AFM of the β-CnFs. (D) XRD of a squid pen (green), purified β-chitin (blue), and of a dried β-CnFs dispersion (red). The XRD patterns were shifted on y–axis for the sake of clearness. Figure from Montroni et al. (2019).[25]

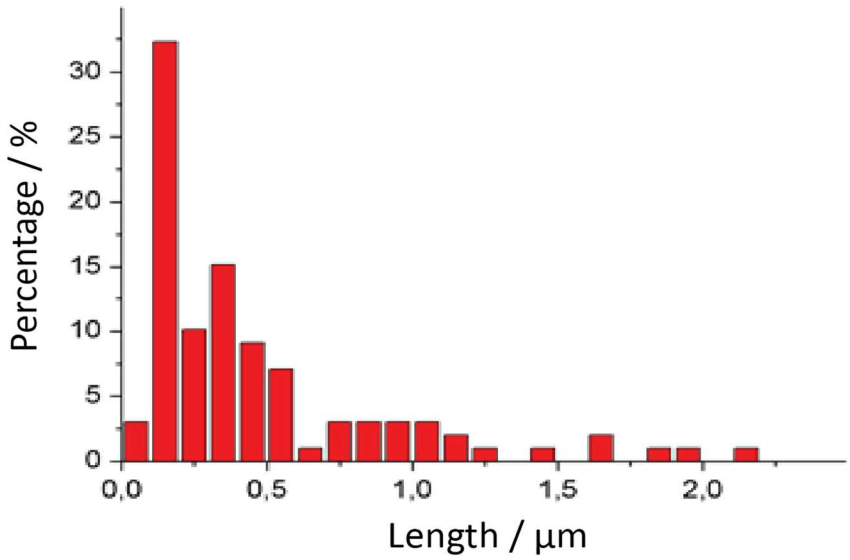

Figure 22: Distribution of the fibril length in a 0.5 mg·mL^{-1} obtained by end-to-end distance measured from an AFM image.

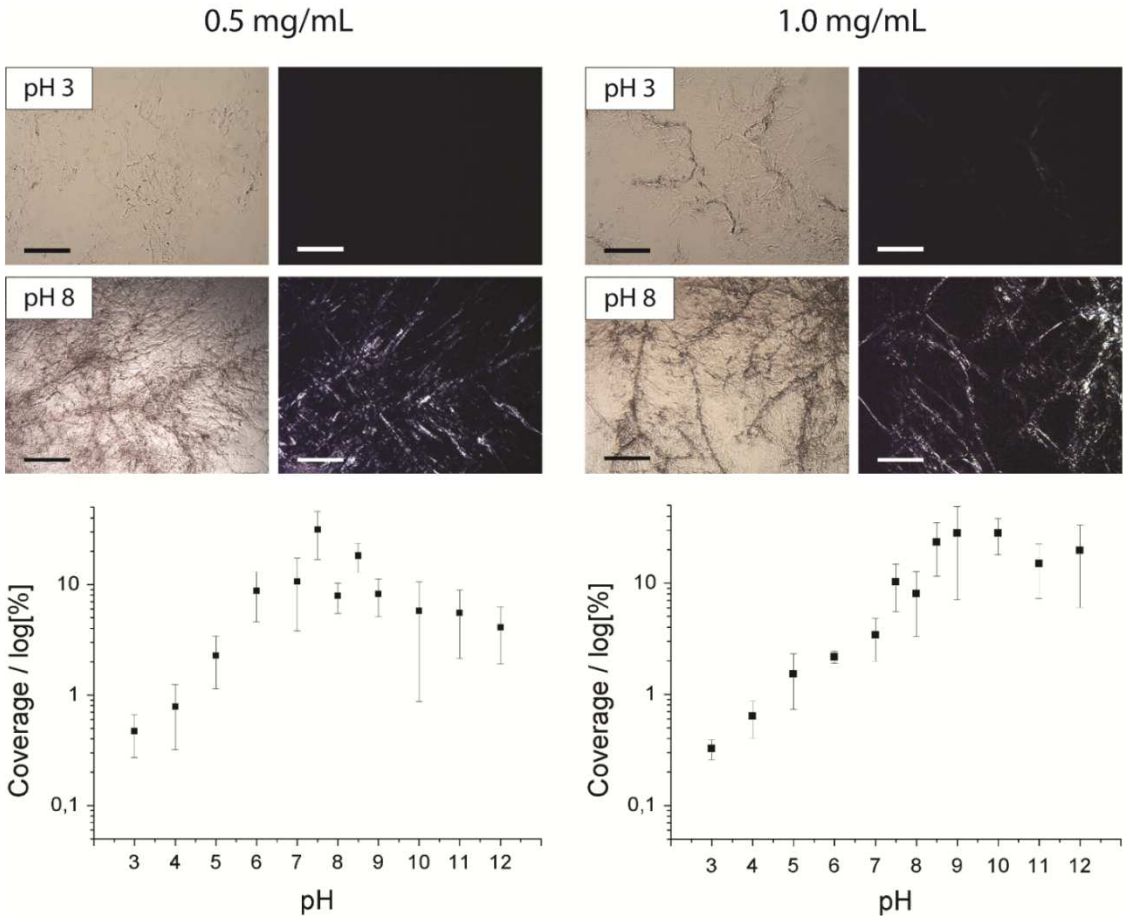

Figure 23: β-CnFs self-assembled at different conditions. On the left, β-CnFs assembled using a 0.5 mg·mL-1 dispersion. On the right, β-CnFs assembled using a 1.0 mg·mL-1 dispersion. For each concentration an optical image and one with cross-polarizers is reported at pH 3 and 8. Scale bars: 250 µm. Beneath each condition a graph with the fiber coverage at different pHs is shown. Figure from Montroni et al. (2019).[25]

Solid-state ^{13}C nuclear magnetic resonance (NMR) demonstrated that the preparation of β-CnFs did not result in the deacetylation of the chitin. The DA was above 95 % after the protease treatment, and remained above 93 % in the β-CnFs, after dispersion in acetic acid at pH 3 (Figure 24). It was not possible to determine the DA in the squid pen, due to the overlap of chitin and protein signals.

3.1.2. β-CnFs self-assembly

Since an acidic environment is required for a stable β-CnFs dispersion, we investigated the effect of pH in the self-assembly of the dispersed nanofibrils into microfibrils. This process was followed using the bright field and polarized light optical microscopy, whereby the presence of birefringent microfibers was confirmed. Two concentrations of β-CnFs were studied: 0.5 mg·mL^{-1}, and 1.0 mg·mL^{-1}. The lower concentration resulted in a homogeneous

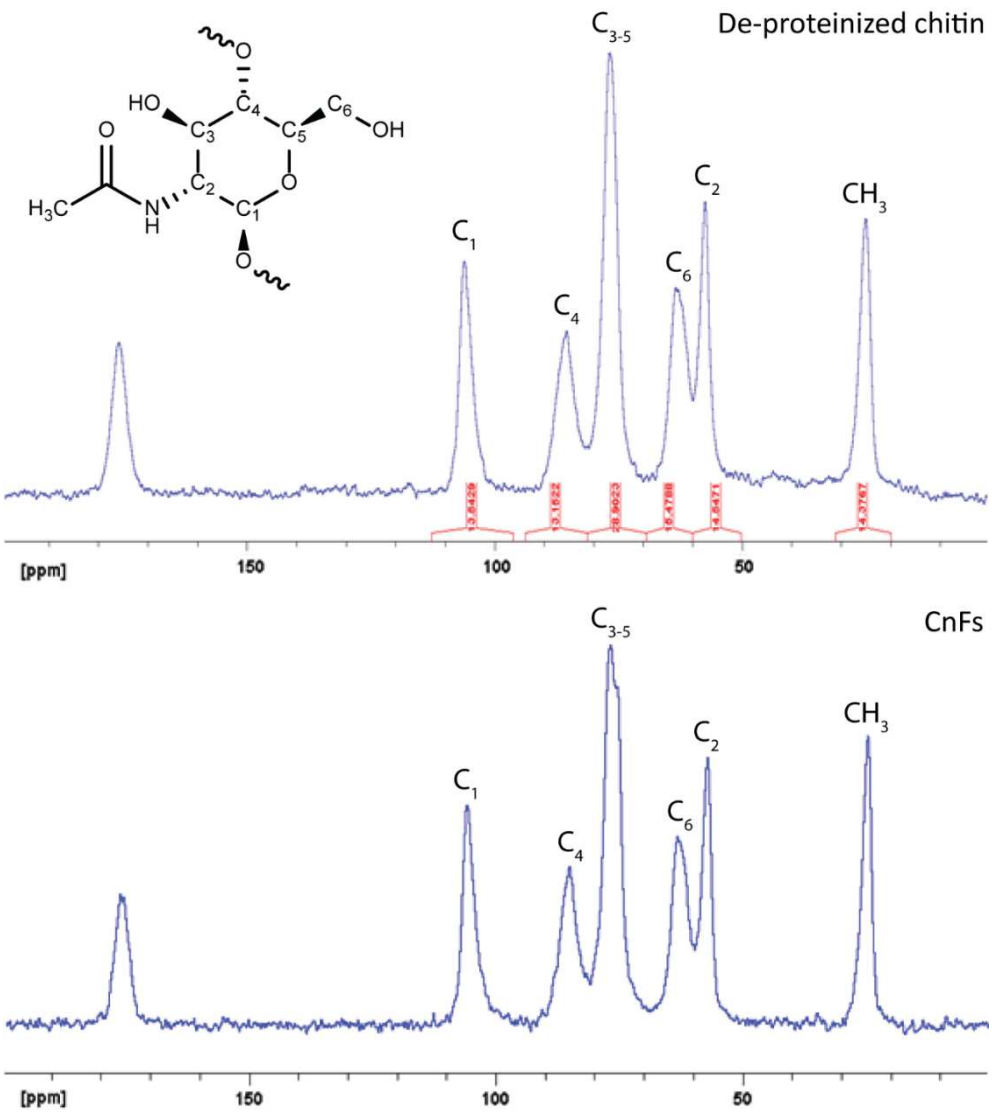

Figure 24: Cross polarization magic angle spinning NMR representative spectra of de-proteinized chitin and dried CnFs.

CnFs dispersion, and the higher one gave a mixture of CnFs and micrometric fibers that did not disassemble during the acidic treatment.

We quantified the fiber coverage at each of the pH conditions, as presented in Figure 23. The largest area coverage was observed between pH 7 and 8.5 for the 0.5 $mg \cdot mL^{-1}$ concentration. The higher concentration sample (1 $mg \cdot mL^{-1}$) showed similar coverage across all the investigated pH conditions above pH 8. At pH 8.5 the two concentrations studied showed a similar fiber coverage (Figure 23). The average thickness of the fibers at the two concentrations was also similar and not statistically different: 11 ± 2 µm for the 0.5

mg·mL^{-1} dispersion, and 13 ± 3 µm for the 1 mg·mL^{-1} dispersion (T-test, p = 0.05, v > 150). The maximum thickness of the fibers was 18 µm and 15 µm in the 1.0 mg·mL^{-1} and 0.5 mg·mL^{-1} dispersion, respectively. The length was not quantified because of the high degree of entanglement and cross-linking present, as can be observed in Figure 23.

X-ray diffraction (XRD) analysis confirmed that chitin was present as the β-chitin polymorph in all of the assembled fibers, except that at pH 12. At pH 12 a reduction of the unit cell parameters, which is in agreement with a β- to α-chitin transition, was detected in the XRD pattern. As shown in Figure 25, such transition was not visible using Fourier-transform infrared spectroscopy (FTIR) analysis, which showed only the absorption bands originating from the β-chitin polymorph.

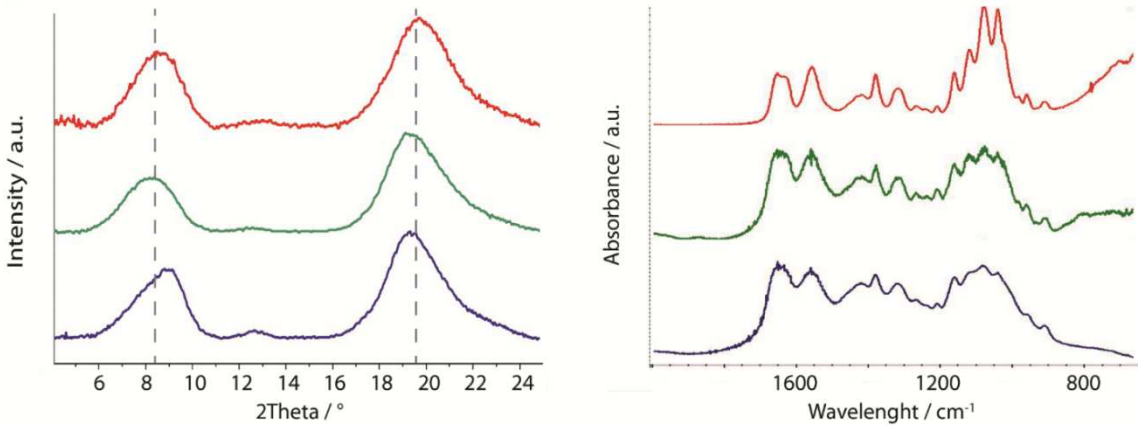

Figure 25: XRD patterns, on the left, and FTIR spectra, on the right, recorded for β-CnFs assembled at pH 3 (red), 8 (green), and 12 (blue). Figure from Montroni et al. (2019).[25]

The kinetics of β-CnFs self-assembly at pH 3, 8, and 12 were studied for an aging time from 10 min to 72 hours using the 0.5 mg·mL^{-1} β-CnFs dispersion, Figure 26. This particular concentration was selected because it allowed a better evaluation of the self-assembly process due to the absence of starting microfibers. pH 3 was selected as the most unfavorable condition for self-assembly. The kinetics at pH 8 was investigated since at this pH the higher density of assembled micro-fibers was observed. The experiments at pH 12 were carried out to investigate when the reduction of the unit cell parameters occur. At pH 3 few aggregation processes were observed. After 72 hours, only few non-birefringent fibers that were several micrometers in length were present. In the β-CnFs dispersion at pH 8, on the other hand, birefringent micrometric fibers were observed in less than 10 minutes. Those fibers continued to grow, mostly in length, until growth termination was

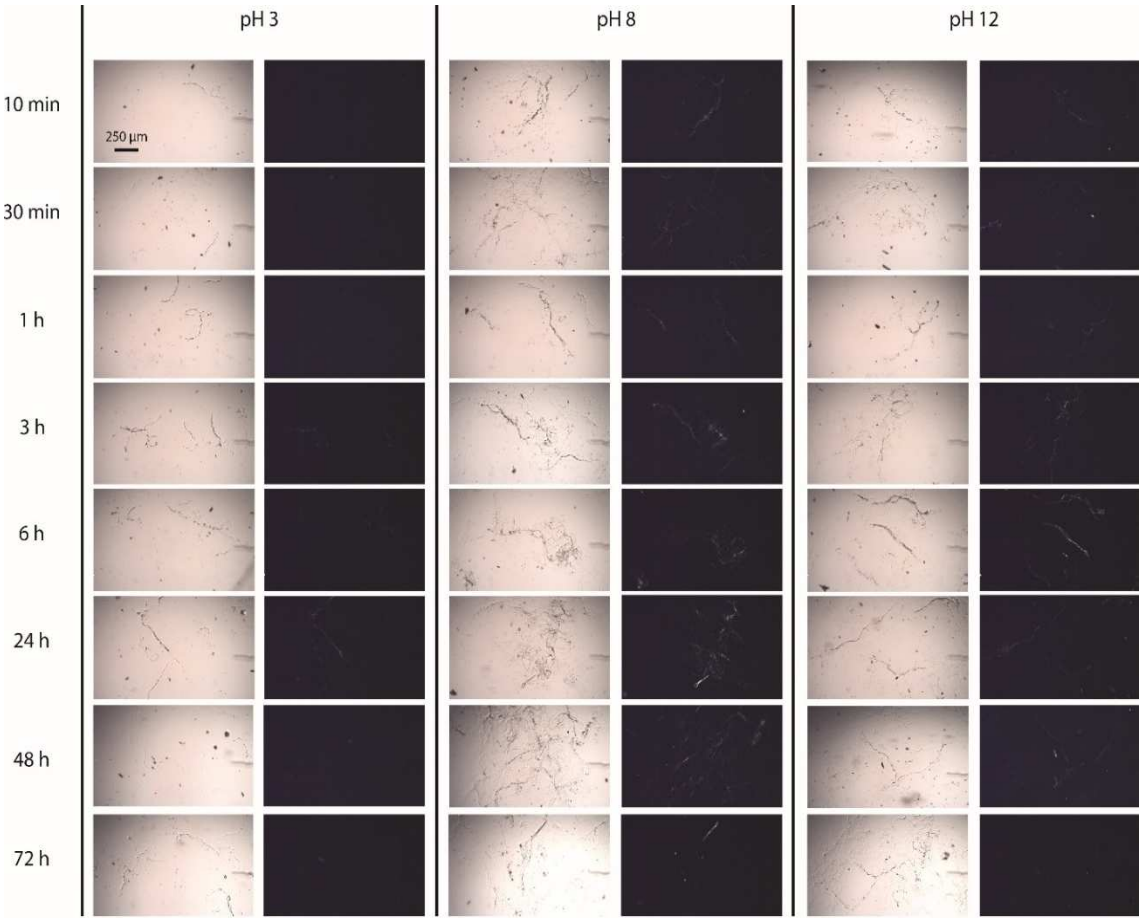

Figure 26: β-CnFs self-assembled at pH 3, 8, and 12 observed at different time points analyzed using optic microscopy and polarized light microscopy. A 0.5 mg·mL^{-1} β-CnFs was used. For each optical image the respective one with cross-polars is shown on the right.

observed between 24 and 48 hours. At pH 12, first micro-fiber appeared after 10 min and the low birefringent micro-fibers growth process was terminated after less than 6 hours. XRD patterns indicated that the reduction of the unit cell parameters occurred in less than 10 minutes, before the self-assembly process started, Figure 27.

Finally, the pH screening revealed a big increment in the microfiber density while transitioning from pH 4 to pH 5. The kinetic study showed that the assembly was less favored at a more acidic pH value.

The optical microscopy data provided information about the assembly of the chitin nanofibers at the micrometer scale. To gain a mechanistic understanding of this process at the nanometer scale, cryo-TEM was used. The study was performed on the 0.5 mg·mL^{-1} solution, considering the undesired micro-fibers presence observed in the higher concentration sample (1 mg·mL^{-1}). As shown in Figure 28, the assembly occurred in three different steps. Initially, isolated nano-fibrils of 6.4 ± 0.7 nm in diameter and about 100 nm

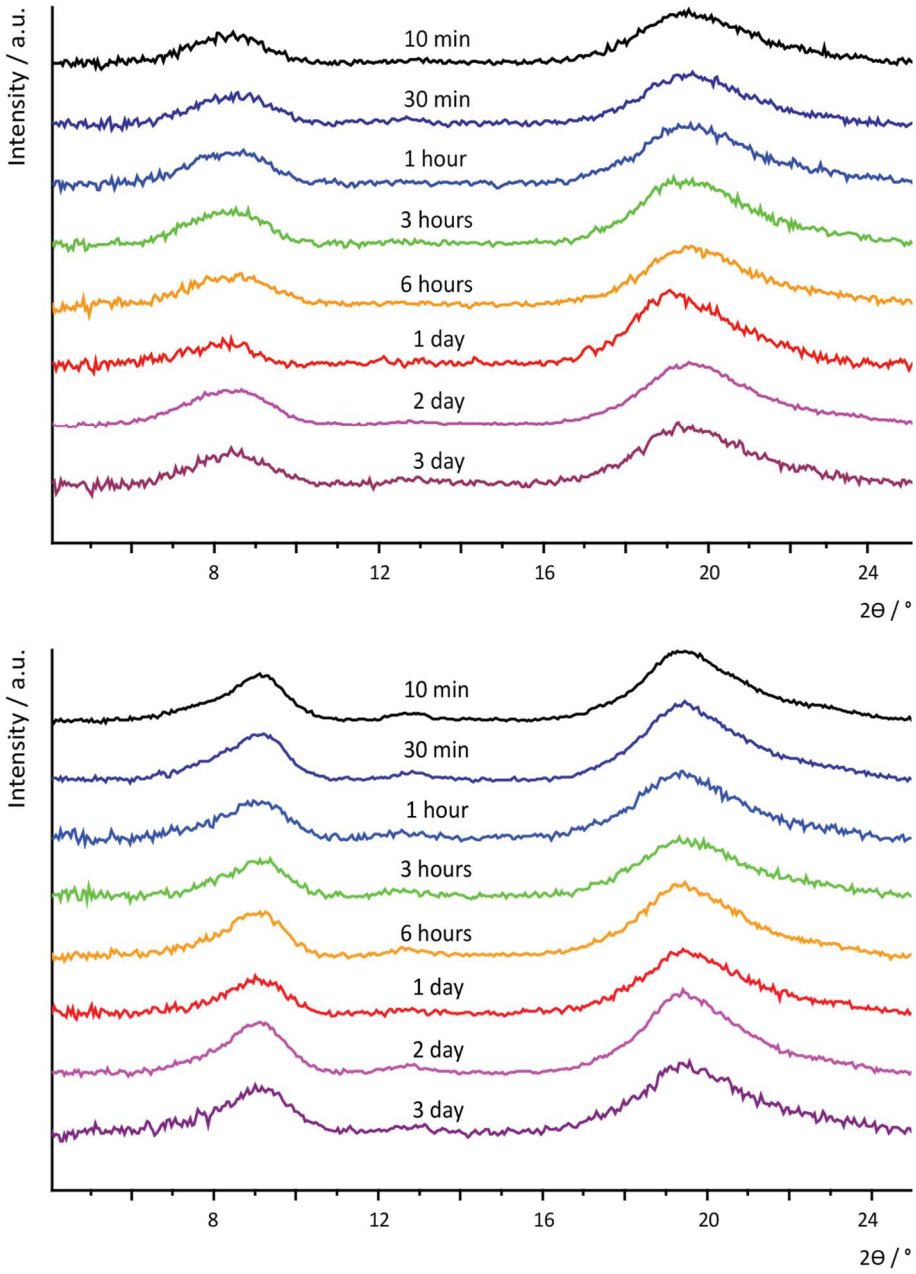

Figure 27: Time-resolved XRD patterns of the 0.5 mg·mL^{-1} β-CnFs dispersions self-assembling at pH 8 (top) and pH 12 (bottom).

in length were present, apparently not interacting with each other (Figure 28 A). 30 seconds after the pH increment the fibrils were observed increasing their length to several hundreds of nanometers, with a diameter of 6.9 ± 0.7 nm (Figure 28 B). Those longer fibrils did not show a significant difference in diameter considering the instrument resolution. At 3.5 minutes the fibrils underwent lateral aggregation, forming thicker and loosely organized bundles (Figure 28 C-D). Further self-assembly after longer periods could not be visualized due to the increasing fibers thickness, which eventually prevented electron transmission.

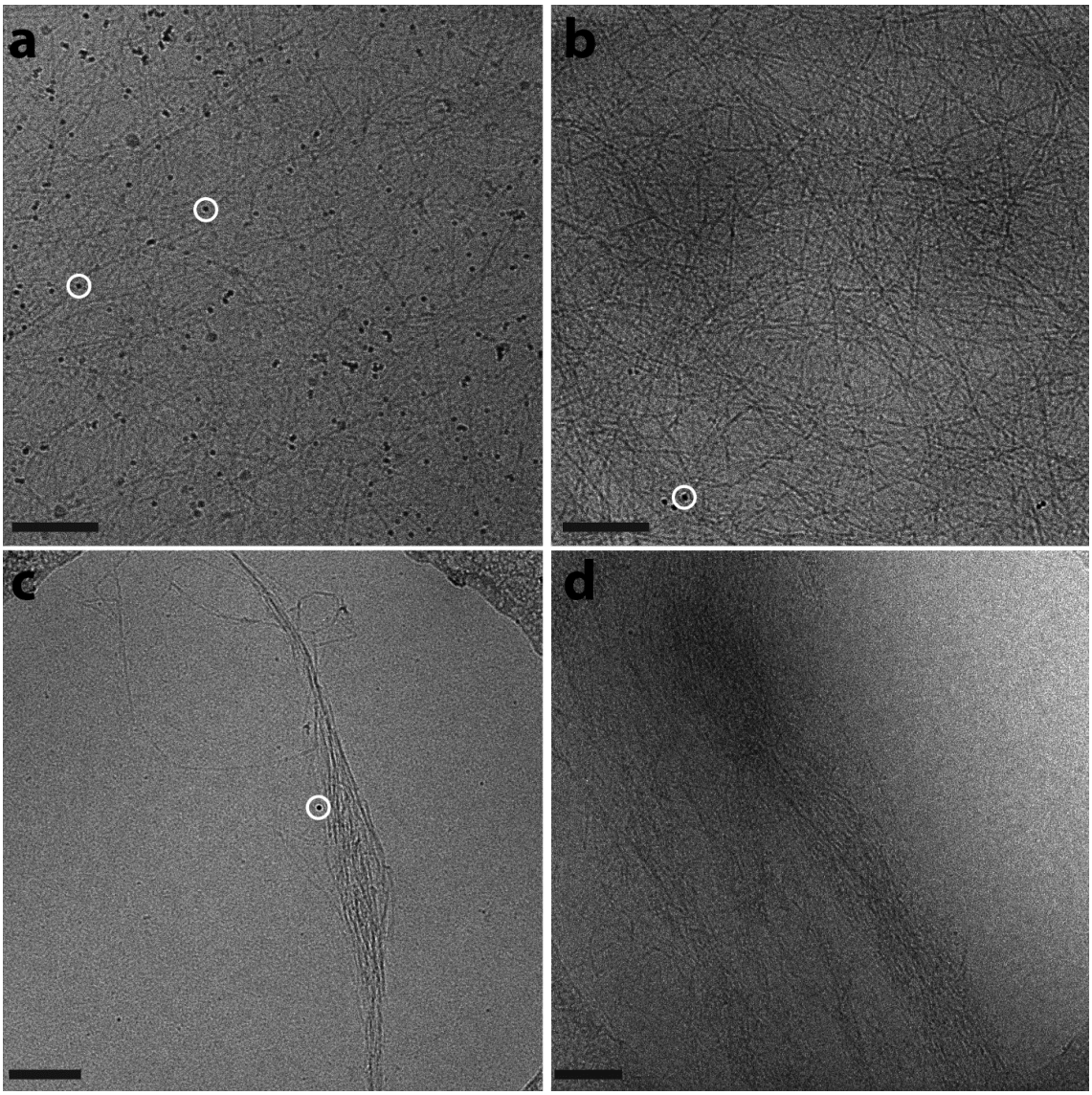

Figure 28: Cryo-TEM images of CnFs self-assembled at pH 8. The four different stages of the assembly process are reported: a) at the start of the self-assembly, b-d) different stages observed after 30 seconds. White circles on a-c: 10 nm gold nanoparticles used as fiducial markers. Scale bars: 200 nm. Figure from Montroni et al. (2019).[25]

3.2. Discussion

3.2.1. β-CnFs preparation and characterization

This research aimed to investigate the self-assembly process of β-CnFs in their native aqueous environments. To achieve this goal the first objective was to produce β-CnFs while avoiding the degradation or deacetylation of the N-acetyl glucosamine residues. For this reason, a mixture of proteolytic enzymes was used, as opposed to the harsh alkaline treatments at high temperatures usually reported in literature.[22]

Although proteolytic enzymes promote degradation of squid pen's proteins at physiological pH, usually they do not diffuse into the structure. Because chitin swells at acidic pH values[26],[27], pepsin – optimally active at acidic pH – was used. Under these conditions the enzyme diffused into the squid pen and catalyzed the degradation of the proteins in the whole material. Such a swelling, crucial for the enzyme diffusion, was preserved by keeping the pen hydrated during the trypsin enzymatic peptides hydrolysis at physiological pH. Subsequently, β-CnFs were obtained in a mild acidic environment exploiting the friction forces induced by the mechanical mixing. In this way, the β-chitin films disassembled to β-CnFs. The fibrils obtained showed a diameter of 6.4 ± 0.7 nm, when observed in the hydrate state using cryo-TEM, and one of 2.5 ± 0.3 nm, when observed dry using AFM. It is possible that the dehydration of the nanofibers for AFM measurements resulted in the shrinkage of the structure, hence the difference in the diameter obtained from the two techniques. Alternatively, it is also possible that the load applied during the AFM measurement resulted in the compression of the nano-fibril and hence a smaller diameter.

It is important to note that the disaggregation of the squid pen into β-CnFs under acidic conditions was only possible after proteinase treatment. Similarly, digestion of the chitin using chitinase was only possible after the squid pen was deproteinated. These results suggest that proteins in the squid pen may have a protective role against chitin disassembly, and biodegradation in physiological condition.

In natural matrices chitin is not completely acetylated[28],[29] and the amino groups of the deacetylated chitin units are hypothesized to covalently bind proteins. The chitin obtained from the proteolytic enzyme digestion had a DA above 95 %. The free amino groups were protonated during the acidic disassembly of chitin favoring its disaggregation by electrostatic repulsions. In another study, reported in chapter 4, chitin with lower DA, obtained from alkaline treatments, were observed to disaggregate in the same experimental conditions as used here. Interesting, no disaggregation was reported for DA below 83 % and above 55 %.[30] Considering the high DA and the insolubility of more deacetylated chitins, we estimate that the disaggregation observed was due partially to charge repulsion and mostly to a swelling of the regions between the crystal domains due to the squid pen structural organization, visible by the swelling of the material. As a result, mechanical stirring forces cause the dispersion of nano-fibrils.

This observation would explain why nano-fibrils and not single molecules were obtained, why the disassembly kinetic was so slow, and why the disassembly worked only under the strong mechanical action of the stirring bar (only a strong swelling was observed without stirring). Anyway, the ≤ 7 % of positive charges present in the CnFs at pH 3 had probably the role to stabilize the fibril dispersion, which were stable even in long-term storage.

3.2.2. β-CnFs self-assembly

The choice of β-CnFs as starting material to investigate the self-assembly has been guided by two main reasons: (i) when single polymeric chains are used they always assemble in α-chitin;[31] (ii) in biological systems the interaction of chitin with other molecules, as proteins, occurs when chitin is already assembled in nano-fibrils.[32][33][34][35]

The β-CnFs self-assembly was induced by increasing the pH. The pH controlled self-assembly of materials in biological systems has been already observed in other bio-macromolecules,[36][37][38] and is relevant in the biomineralization of biominerals.[39][40] In this context the identification of the pH value at which the self-assembly occurs can provide information on the features of the biological site where the assembly takes place.

The results of the present study of β-CnFs self-assembly provided at least four novel pieces of information. First, pH 7-8.5 is the optimal range for the formation of the micro-fibers starting from the 0.5 mg·mL^{-1} β-CnFs homogeneous dispersion. Interestingly, this pH range includes physiological pHs,[41],[42] and that of seawater, which ranges between 8.0 and 8.2.[38],[43] This result shows how chitin assembly can occur compatibly inside the living organism, as in cephalopods internal skeletal matrices,[32][44] or as an external process. This last possibility includes processes where the pH is that of sea water, as in marine calcifying organisms,[45][46] and processes where the pH is defined by the fluids secreted by the animal, as for terrestrial insects' exoskeletons. Moreover, these pH values are relevant in the precipitation process of calcium carbonate, a mineral that is commonly associated to chitin in calcified tissues.[47][48] In the pH range 7-8.5 the deposition of calcium carbonate almost does not occur, while it takes place at pH ≥ 8.5. This indicates that the assembly of β-CnFs to form β-chitin fibers occurs before the precipitation of calcium carbonate takes place. This hypothesis is in agreement with the current model of preformed organic matrix guiding the textural organization of calcium carbonate crystals.[49]

A second finding is the polymorphic stability of the β-CnFs even at pH 12, as deductible from the combination of the FTIR and XRD data. They show that only a unit cell parameter

contraction occurs (from 10.24 ± 0.06 Å to 9.8 ± 0.1 Å for the (010) signal). It is reported that the β- to α-chitin transition occurs at room temperature in very alkaline ($[OH^-]$ > 10 M)[50] or acidic ($[H_3O^+]$ > 7 M)[26][27] solutions, or in non-aqueous solvents[31] and that this process always occurred after a disassembly to single molecules and a successive reassembly.[30] It could be speculated that the contraction of the unit cell might be an initial step for a structural β- to α-chitin re-organization that does not affect the polymorphism of the β-CnFs.

The third point is related to the extent of the self-assembly as a function of the β-CnFs concentration. Despite the fiber's thickness, evaluated at pH 8.5, was not significantly different for the two concentrations, the maximum fiber's thickness in the 1.0 $mg \cdot mL^{-1}$ concentration is higher than the 0.5 $mg \cdot mL^{-1}$ one (about 18 µm and 15 µm respectively). Qualitatively the 1.0 $mg \cdot mL^{-1}$ concentration showed also longer fibers compared to the 0.5 $mg \cdot mL^{-1}$ one. These observations do not fit just with the doubling of the concentration. It has to be considered that in the 1.0 $mg \cdot mL^{-1}$ β-CnFs heterogeneous dispersion some micro-fibers were still present from the disassembly process. These fibers could act as a template for the β-CnFs assembling. This possibility is intriguing because in living organisms chitin deposition can occur also on previously assembled fibers. Moreover, despite showing shorter and thinner final β-chitin fibers, the lower concentration exhibited a comparable coverage in the image analysis, meaning that more fibers nucleated in the process. This result, combined with the two different pH range of preferred self-assembly, may indicate the fibers' preference to nucleate in the pH range between 7 and 8.5 and to grow at pH over 8.5.

The last finding comes from the analyses of the cryo-TEM observations. The β-CnFs were observed to assemble in three distinct steps: i) increase their length, ii) assemble in 1D organized bundle, and iii) assemble in bundles of bundles until getting their final dimension. It was not possible to detect a relevant increment in the fibrils thickness in the first step. However, during their growth the β-CnFs started aggregating laterally as well, forming loosely packed bundles. In nature chitin fibrils are frequently wrapped in a protein folder, as in insect cuticle,[44][45] nacre organic matrix,[33] or in the squid pen.[32][51] Our observations indicate that these proteins play a crucial role in the perfectly registered chitin self-assembly. Alternatively, the disordered assembly could have resulted from the rapid change of the environment. Since the presence of buffer molecules can affect β-CnFs

nucleation and aggregation, the chemical system was kept as simple as possible, controlling the pH only by adding an acid or a base.

It could be argued that the self-assembly of the nano-fibrils was caused by the deprotonation of the primary amines in the deacetylated monomers once the pH was raised above the pK_a of the amino groups (about 6.3[52][53][54][55]), effectively eliminating the electrostatic repulsion between nanofibrils. Here, we note that the DA of the β-CnF dispersion was ≥ 93 %. We hypothesize that these charged units play an important role in the stability of the nano-fibrils in water, that their deprotonation was the first trigger for chitin assembly, and might be directly involved in the kinetic of the process. Considering, however, that only ≤ 7 % of the monomeric units were deacetylated, it is likely that deprotonation is not enough to drive the self-assembly, and that other forms of intermolecular interactions are also involved. Indeed, if the self-assembly was only caused by the deprotonation of the amino groups, one would expect the aggregation of the nanofibrils to occur at pHs closer to 6.3, where already less than 3.5 % (50 % of the amino groups) of the chitin units are charged, rather than 8. The slight decrease in the coverage for the 0.5 $mg \cdot mL^{-1}$ dispersion at pH over 8.5 also would not be expected.

These results show a propensity for the β-CnFs to aggregate in large 1D organized structures (micrometric in diameter and millimetric in length) despite their non-specific interactions. We speculate that in living organisms proteins provide a greater control over the chitin fibrils self-assembly process (especially in lateral packing), and direct their growth towards organized macro-structures.

3.3. Conclusion

The aim of this research was to study the self-assembly of β-CnFs into β-chitin fibers in aqueous environments. Our first objective was to design an experimental system where chitin would exhibit features as close to the natural material as possible, and would be able to self-assemble. This goal was achieved by preparing stable dispersions in acidic conditions of β-CnFs from the squid pen β-chitin. Self-assembly process was triggered by increasing the pH of those dispersions to mild basic values whereby the kinetics of that process was regulated by the adjustment of the starting pH.

The main discoveries, on β-CnFs self-assembly to fibers, utilizing this system have been:

1) The nucleation β-CnFs is favored around pH 8, which is very close to both physiological, and seawater pHs;
2) The β-CnFs maintain the β-polymorph for the whole process, showing a shrinkage of the unit cell parameter at basic pH;
3) The self-assembly of β-CnFs is favored on previously grown fibers;
4) The β-CnFs grow preferentially at pH above 8.5 up to a maximum value in thickness.

The β-CnFs self-assembly observation by cryo-TEM showed a three-step process. Firstly the β-CnFs self-assembled and increased their length, and then formed bundles that finally aggregated into fibers until they reached macroscopic dimensions. Besides these important and novel information, the β-CnFs water dispersions represent an adaptable and flexible platform to study chitin self-assembly and chitin interaction with structural chitin-binding proteins, as much as any other chitin-interacting molecule.

3.4. Materials and methods

Materials All reagents and solvents were purchased from Sigma Aldrich and utilized without any further purification. Squid pens from *Loligo vulgaris* were collected from a local market. Once hydrated, the lateral blades were isolated, cleaned with distilled water and ethanol 70 vol.%, and then stored dry.

Squid pen de-proteination The β-chitin from the squid pen was purified from proteins by soaking about 1 g of the previously washed squid pens in 100 mL of a pH 2 HCl solution containing 20 mg of pepsin (an aspartic protease).[56] The solution was placed on a rocking table for 24 h at 37 °C. After this first de-proteination, the squid pens were collected and washed carefully with distilled water. The wet squid pens were then re-immersed in 100 mL of a 100 mM phosphate buffer solution at pH 7.6 containing 20 mg of trypsin (a serine protease).[57] As in the previous step, the solution was placed on a rocking table at 37 °C for 24 h. The removal of proteins from the pen was evaluated by the disappearance of UV absorption peaks originating from tryptophan residues and observed at 280 nm using a Varian Cary 300 Bio spectrophotometer.

β-Chitin nano-fibrils preparation A homogeneous dispersion of β-CnFs was obtained by placing 50 or 100 mg of protein-free β-chitin, cut into about 0.5 cm^2 square pieces, in 100 mL of an acetic acid solution at pH 3.[58] The solution was stirred vigorously for 72 h at room temperature. At the end of the process, a dispersion of CnFs was obtained. The dispersion was transparent, stable (for over 6 months), homogeneous, and highly viscous.

β-Chitin nano-fibrils self-assembly β-CnFs self-assembly was induced by changing the pH of 5 mL of freshly prepared (less than 24 h from preparation) β-CnFs dispersion. The pH change was induced using NaOH 1 M and measured using a pH-meter BASIC 20 (pH ± 0.01) by Crison Instruments coupled with a HI1048 pH electrode (Hanna Instruments). The pH-meter was calibrated daily. The solutions were left for 24 h at room temperature (25 °C) without any stirring. The morphological analysis were performed without any further purification of the mixture. For structural analyses, the samples assembled were frozen with liquid nitrogen and lyophilized using a FreeZone® 1 (Labconco Corp., Kansas City, MO, US). The obtained material was then dispersed in 10 mL of Pre-milliQ water and centrifuged

at 2000 g for 5 minutes. After that, the solution was disposed and the process was repeated two more times. Finally, the fibers were lyophilized for the last time upon freezing with liquid nitrogen.

β-Chitin nano-fibrils self-assembly kinetics The self-assembly of β-CnFs was investigated as a function of time in a 0.5 mg mL^{-1} β-CnFs dispersions. 45 mL of freshly prepared dispersion (always less than 24 h from preparation) were adjusted to different pH values in a test tube. At any reported time the solution was mildly stirred and 5 mL of dispersion were isolated, observed with an optical microscope, frozen using liquid nitrogen, and lyophilized. The obtained material was dispersed in 10 mL of Pre-milliQ water and centrifuged at 2000 g for 5 minutes, after that the solvent was disposed and the process repeated two more times. Finally, the fibers were lyophilized again upon freezing with liquid nitrogen.

Optical microscopy observations Optical microscopy images were collected using a SM-LUX POL microscope equipped with a 5.0 MP Moticam 5 camera. Right after the end of the assembly process the sample was stirred, a drop of sample was collected and placed on a microscope slide, covered with a cover slip, and observed immediately.
Cross-polarized light images were used to carry out the fibers area unit coverage analysis. All images were collected using the same gain and exposition time. Each sample was screened to record a complete map of the glass slide and 12 images with no common areas, and with the higher surface covered were analyzed. Optical microscopy images were processed using Gwyddion, an open access software originally developed for the analysis of Scanning Probe Microscopy images but here used to have a quantitative evaluation of the material adsorbed onto the surface. Briefly, the chitin fibers present on the surface were detected by setting an intensity threshold (constant throughout all the images) and then the coverage was measured as the ratio between the covered and the total area.

Electron and probe microscopy imaging Samples for AFM imaging were prepared by depositing 10 µL of the chitin material from the 0.5 mg·mL^{-1} β-CnFs dispersion on a mica surface and gently drying them with a nitrogen flow.[59] The AFM used was an AFM Multimode VIII controlled by the Nanoscope V electronic software package (Bruker, Santa Barbara, CA, US). The microscope was operated in the ScanAsyst mode and the cantilevers

were ScanAsyst with an elastic constant of 0.40 N m^{-1}. The length and height of the nano-fibrils were measured by analyzing AFM images with Gwyddion. The fibrils present on the surface were isolated from the background by selecting an appropriate threshold, and the height was measured as the maximum height with respect to the sample surface. The length was measured as the end-to-end distance. Considering that fibrils' persistence length was longer than their actual length this value was a good approximation of their contour length.

Cryo-TEM imaging was carried out using a FEI Tecnai F20 transmission electron microscope equipped with a Schottky field emission gun and operated at 200 keV. For sample preparation, cryo-TEM grids (R2/2 200 µm mesh Au/C, Quantifoil Micro Tools Gmbh) were plasma-treated using a Quorumtech Q150T Glow Discharge system for 45 seconds. Aliquots of 3 µl of the aqueous mixture containing the fibrils/fibers, right after the assembly time considered, were applied to the cryo-TEM grids. Samples were then vitrified in liquid ethane using the FEI Vitrobot (Mk IV) plunge freezer and loaded to a Gatan cryo-holder cooled to 77 K with liquid nitrogen. Images were recorded on an 8k x 8k CMOS TVIPS F816 camera.

Structural analysis FTIR spectra were collected using a Nicolet IS10 spectrophotometer. Omnic software (Thermo Electron Corp., Woburn, MA) was used for data processing and baseline correction. The samples were prepared as KBr pellets and the sample concentration was 2 wt.%. The spectra were obtained with 4 cm^{-1} resolution and 64 scans. XRD patterns were collected using a PanAnalytical X'Pert Pro diffractometer equipped with multi array X'Celerator detector using Cu Kα radiation generated at 40 kV and 40 mA (λ = 1.54056 Å). The diffraction patterns were collected in the 2θ range between 4° and 25° with a step size (Δ2θ) of 0.05° and a counting time of 100 s. Each pattern collection was repeated at least twice on different samples.

Determination of the degree of acetylation The DA of the chitin was determined using solid-state NMR. The NMR experiments were performed on a Bruker Advance spectrometer operating at the frequency of 300 MHz for proton (equipped with a 4 mm MAS BB probe) using the combined techniques of cross-polarization and magic angle spinning. Field strengths corresponding to 90° pulses of 4.5 µs were used for the matched spinlock cross-

polarization transfer ^{1}H to ^{13}C. The contact time was 1 ms, and the recycle delay 10 s. A typical number of 500–3000 scans were acquired for each spectrum. The chemical shifts were externally referred by setting the carbonyl resonance of glycine to 176.03 ppm. Glycine full width at half-height better than 27 Hz. The spinning speed was set at 8000 Hz for all samples. The signals assignment, reported in Figure 24, was done according to literature.[60] The DA was calculated as ratio between the CH_3 signal of the acetyl and the average signal of the six carbons of the ring, as follows: $DA = \{I_{CH3} / [(I_{C1} + I_{C2} + I_{C3} + I_{C4} + I_{C5} + I_{C6}) / 6] \} *100$.[60]

4. Self-assembly of chitin nanofibrils and collagen

4.2. Results

The assembly of chitin, as discussed in section 3 of this chapter, is different depending on the pH where it takes place. At pH 3 no assembly was observed, leading to a disorganized mass of fibrils. At pH 8 the best condition for chitin assembly occurs, leading to about ten micron thick fibers.

In this study, a 1 $mg \cdot mL^{-1}$ chitin nano-fibril dispersion was mixed with a collagen solution of the same concentration to obtain mixtures with different mass ratio. The 1 $mg \cdot mL^{-1}$ concentration was chosen for its tendency to giving longer fibers and for practical reasons. A type I collagen from bovine Achilles tendon was used in this study. The different chitin/collagen mass ratio investigated are reported in Table 1.

Table 1: Composition of the different chitin/collagen samples.

Sample name	Chitin / wt.%	Collagen / wt.%
C100	100	0
C75	75	25
C50	50	50
C25	25	75
C00	0	100

The assembly was studied 24 h after inducing the assembly by increasing the pH of the solution, being both chitin and collagen pH responsive.

As can be observed in Figure 29 neither chitin nor collagen formed fibers at pH 3. Contrary, at pH 8 both chitin and collagen appear to assemble; chitin assembled in long highly birefringent fibers, while collagen formed thicker less birefringent fibers. The fiber dimension along the samples was coherent with the increment in collagen content, moving from thinner chitin fibers to thicker collagen fibers. Despite that, the birefringence was not as linear, being C25 and C75 lower birefringent compared to the other samples.

The samples were examined using FTIR and XRD to evaluate the interaction between the two phases composing the materials.

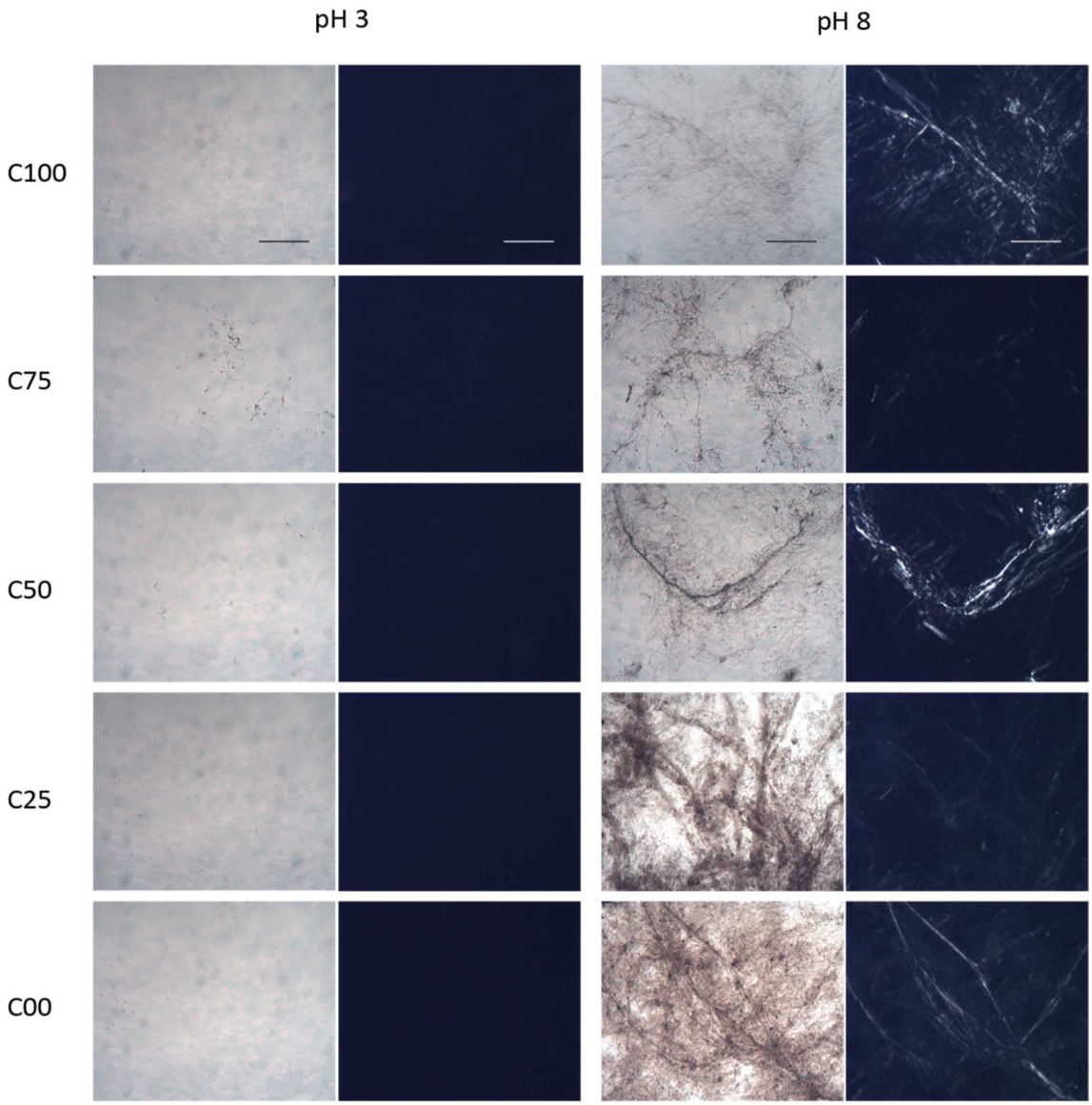

Figure 29: Optical microscopy images of the chitin/collagen mixtures at different pHs. For each condition an optical image and one with cross-polarizers are reported. Scale bar 300 µm.

The attenuated total reflectance (ATR) FTIR spectra of the different composites did not show differences depending on the pH of the assembly, Figure 30. Moving from C100 to C00 an increase in the relative intensity of the collagen signals was observed along with a decrease of the chitin ones. The collagen and chitin peaks showed no shifts.

The XRD (Figure 31) patterns showed a peak at 8.4° and one at 19.5° for pure chitin at pH 3 and 8. Pure collagen (C00) had a peak at 7.6° and a broad signal at about 20°. At both the pHs the 8.4° chitin signal and the 7.6° peak of the collagen appeared to coexist in the spectra of samples having a dual composition, being one overlapped to the other. The 19.5° chitin signal, instead, got broader increasing the collagen amount until it completely

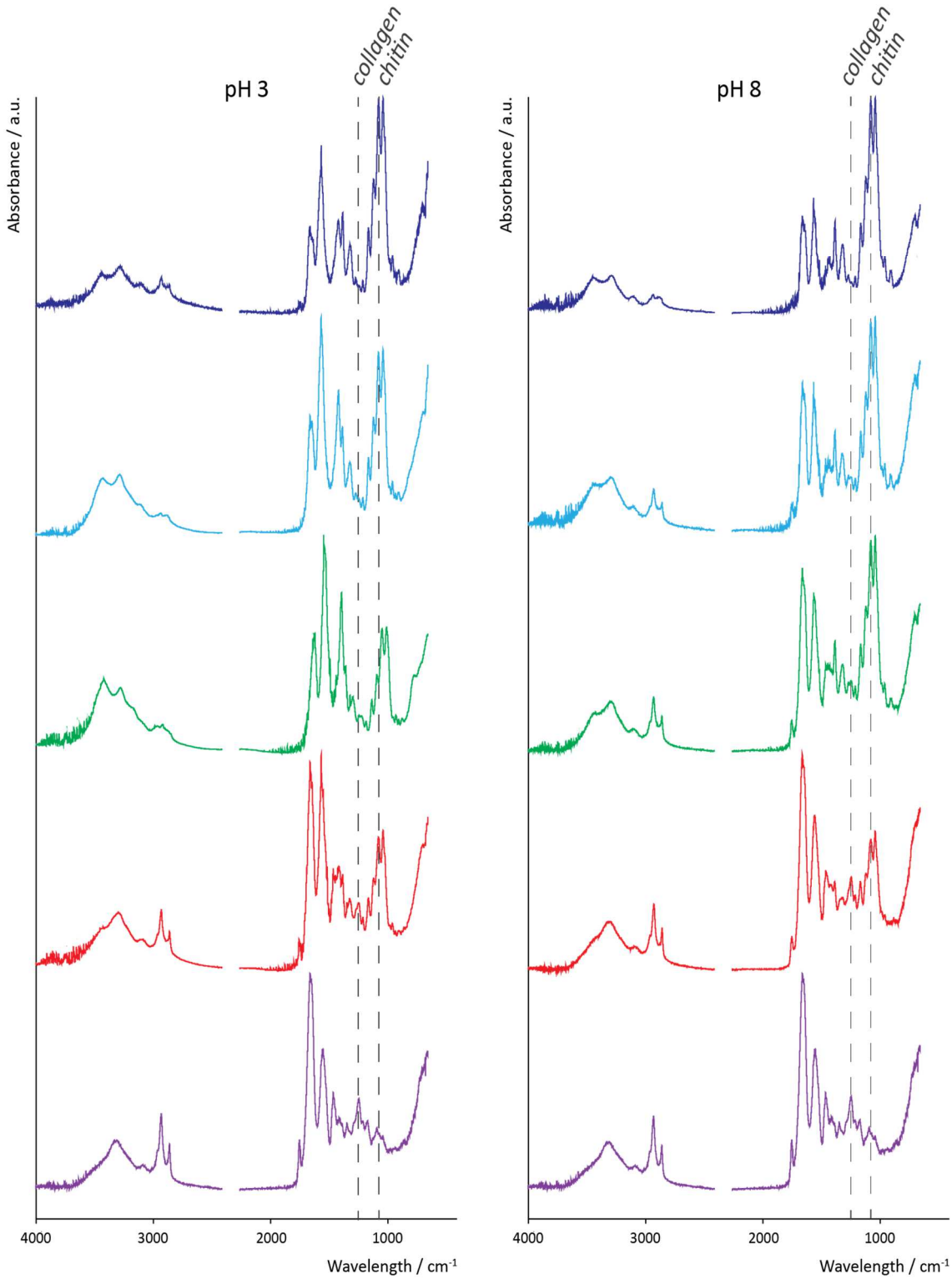

Figure 30: ATR-FTIR spectra of the chitin/collagen mixtures assembled at different pHs using the collagen with telopeptides. In blue the C100, in cyan C75, in green C50, in red C25, and in violet C00. In grey two typical signal of chitin (1071 cm^{-1}, CO stretching) and collagen (1235 cm^{-1}, amide III) are marked showing how the difference in relative intensity change increasing their relative amount. The spectral range occupied by the CO_2 signal was deleted.

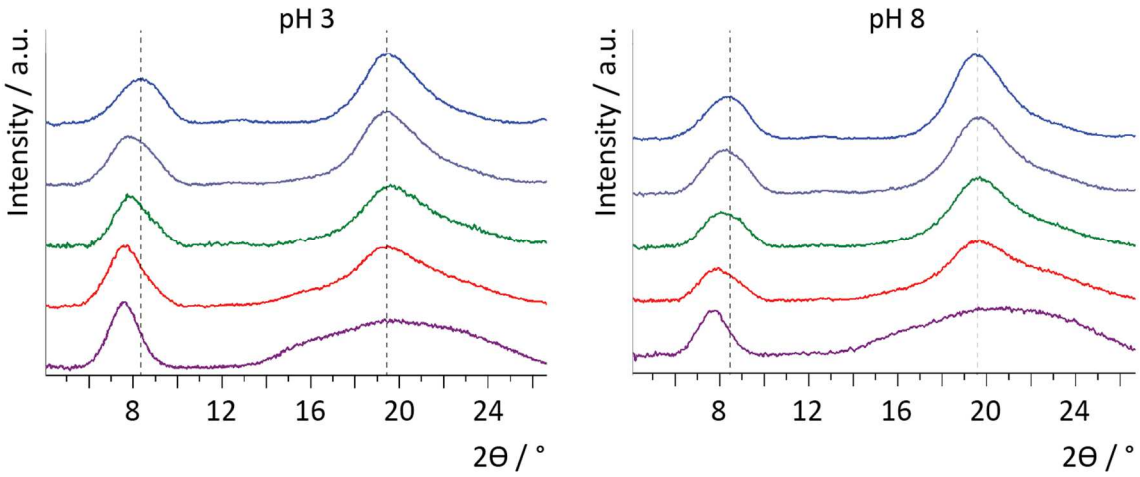

Figure 31: X-ray diffraction pattern of the chitin/collagen mixtures assembled at pH 3 and 8. In blue the C100, in cyan C75, in green C50, in red C25, and in violet C00.

interconverts in the broad collagen signal. Observing the relative intensity of the peaks, more intense signals can be observed for collagen at pH 3 and for chitin at pH 8.

The viability of fibroblast at 24 h, 48 h, and 72 h was tested for this set of samples, as reported in Figure 32. The results reported are normalized on the viability at 24 h for the C00 sample. Compared to a control sample without any matrix the cell viability was slightly higher using collagen assembled at pH 8 rather than the one at pH 3 (105 ± 4 % and 98 ± 6 % respectively). The results using the matrices prepared at pH 3 showed an increment in viability increasing the collagen amount at 24 h, being C100 the one with the lowest viability (42 ± 7 %). At 48 h an increment in viability of about 25-30 % was observed in all the samples except C25. Passing from 48 h to 72 h the highest increment, of 10-15 %, in viability was observed for C25, C75, and C100; the pure collagen sample, instead, increased of 4 ± 4 % being probably close to a plateau. The differences in cell viability are reported in Figure 33. As absolute value, the samples C25, C50, and C75 showed a similar viability at 72 h, between 110 % and 120 %, while the pure collagen matrix was 132 ± 2 %. The samples assembled at pH 8 showed a quite different trend. At 24 h all the samples except the pure collagen showed a comparable viability, between 74 and 85 %. At 48 h an increment of 20-25 % in viability was observed in C00, C25, and C50; C100 showed instead a decrement of 6 ± 3 %. Passing from 48 h to 72 h no increment in viability was observed with only C25 being almost stable at the 48 h value. As for pH 3, the differences in cell viability are reported in Figure 33. Comparing the results of the two sets the pH 3 samples showed generally better results and a positive trend in viability while the one assembled at pH 8

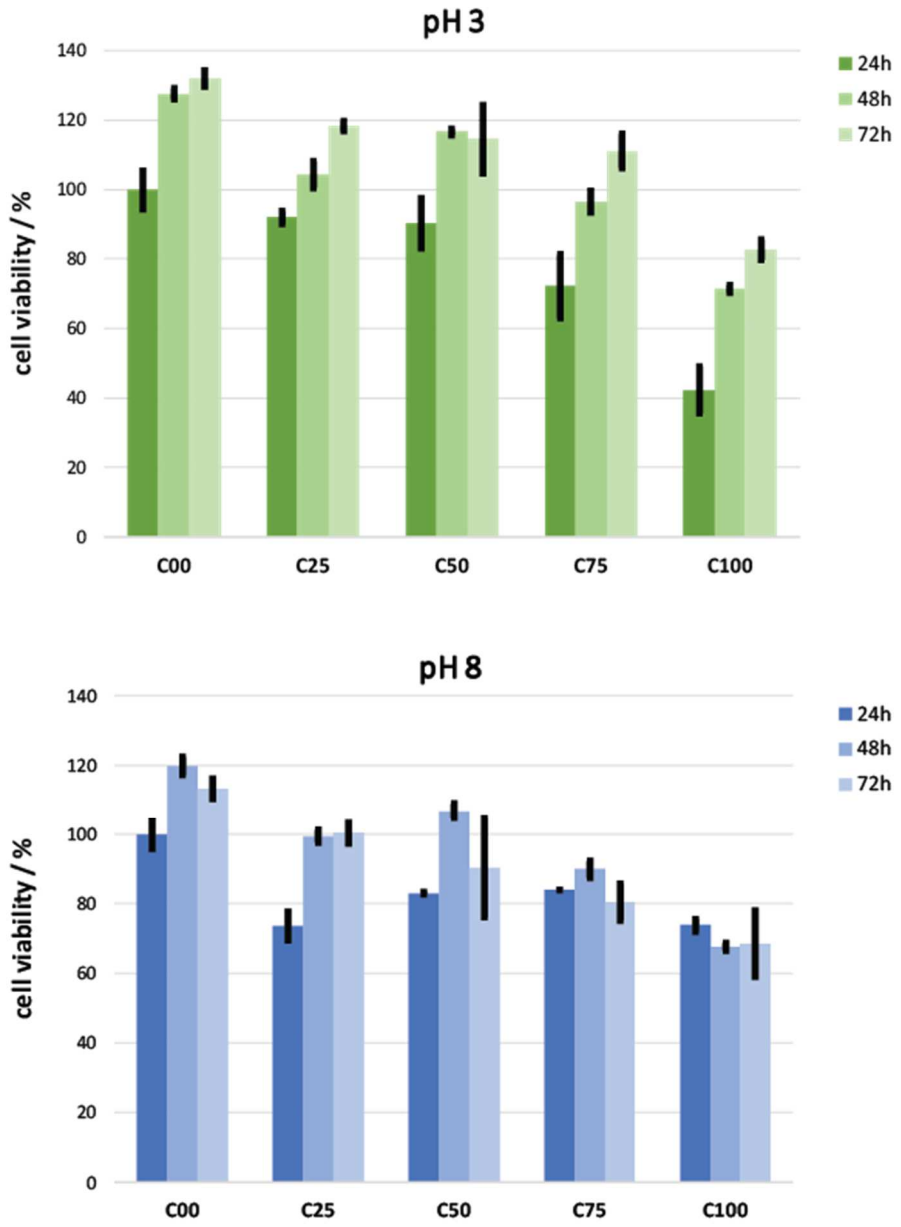

Figure 32: Cell viability of fibroblasts at 24 h, 48 h, and 72 h in the presence of the samples prepared at pH 3 and 8. For each sample set the results are normalized on the viability at 24 h for the C00 sample.

gave better results only at 24 h; in fact, all the results at 72 h are better using samples treated at pH 3.

4.3. Discussion

This study has two primary aims i) study the assembly of two pH responsive macromolecules together, and ii) define how to increase the cell viability in a composite chitin/collagen material. This second target is quite intriguing considering chitin mechanical

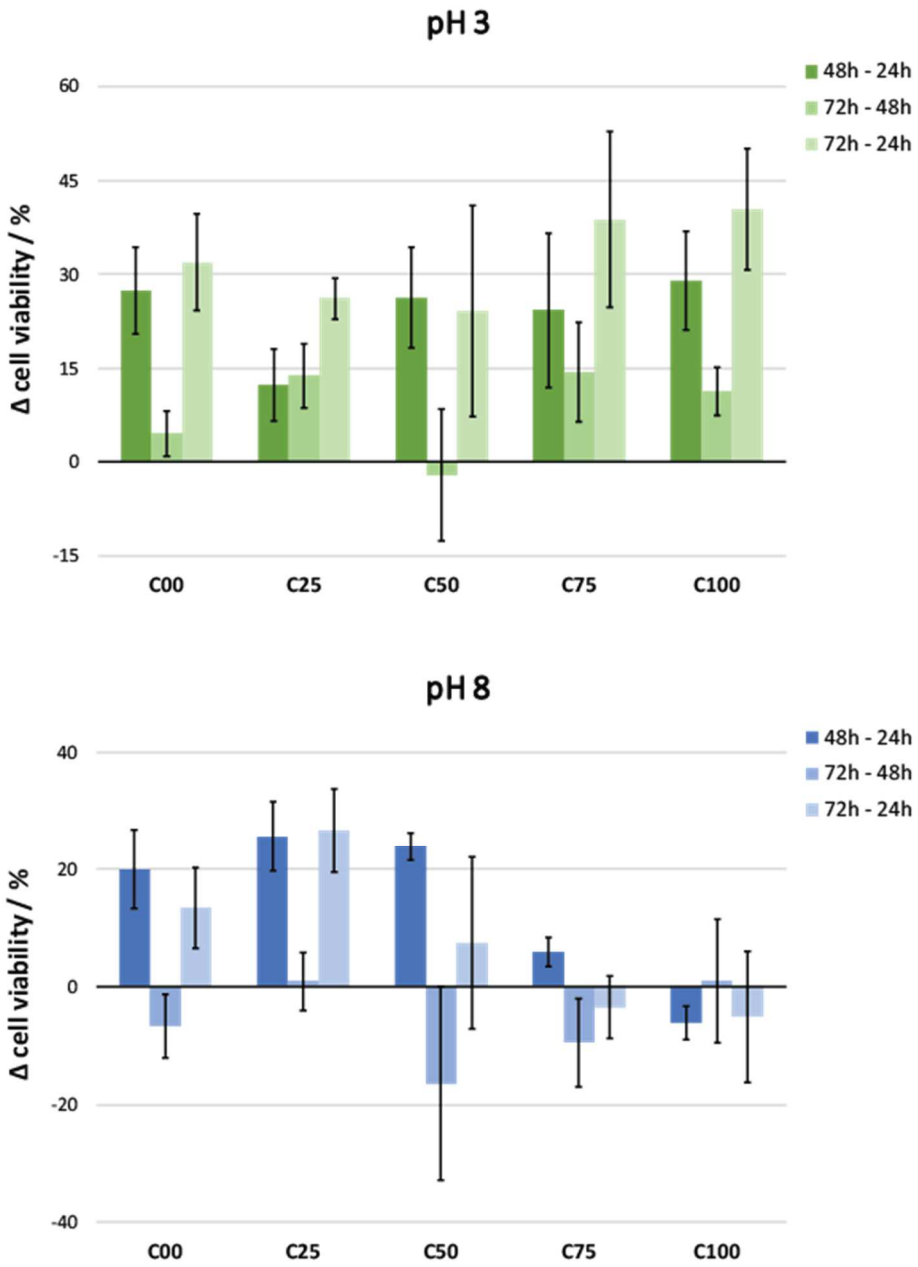

Figure 33: Difference in cell viability between the times studied.

resistance and collagen high biocompatibility. In fact, this composite has been widely applied in literature, especially in bone regeneration due to the positive influence of these two biomacromolecules on biomineralization.[61][61][62][63]

Two different pHs were studied, 3 and 8, after 24 h. As expected from the previous study on chitin and what reported in the literature for collagen, both the macromolecules did not assemble at pH 3. A proper assembly was obtained at pH 8, especially for chitin as shown by the relative intensities of the XRD diffraction peaks moving from pH 3 to pH 8.

After being assembled the fibers shifted from chitin- to collagen-like morphology increasing the relative amount of the components. Despite the linear interconversion in morphology,

C25 and C75 showed a lower birefringence than the other samples. FTIR, and XRD images showed how chitin and collagen assembled separately in distinct domains. Considering that, this low degree of order in C25 and C75 might be due to the low amount of chitin and collagen respectively, which are not enough to properly aggregate in big ordered unit and interfere in the proper assembly of the major component.

Despite the absence of co-assembly, the agglomeration of collagen and the chitin fibers observed in the optical images imply some sort or interaction between the two components. Chitin and collagen could interact by non-specific or weak interactions, which allow the collagen to nucleate its fibers on the surface of chitinous domain but are too weak to drive a co-assembly of the two components. The assembly was carried out without any stirring so we assumed mechanical entanglement was not the reason driving this sample homogeneity.

The cell culture in the presence of the matrices showed how assembled matrices have a positive influence on cell viability in short term while after three days they all appeared to have a negative effect. The only exception was observed using the C25 sample were a stabilization of the viability was observed, even if it is possible this trend will be negative too increasing the time of exposure of the cells. On the other hand, the samples treated at pH 3 all show positive effects reaching, in 72 h, higher values of viability than the highest observed for the corresponding sample at pH 8. This difference might be due to a higher homogeneity of the pH 3 samples or their higher surface area and swelling, being obtained by simple compression of a lyophilized material. These differences could allow a better development of the cells in the matrix. This effect was also observed in pure collagen samples, supporting the hypothesis of the exposed surface.

Among the pH 3 treated samples a higher increment in viability was observed increasing the chitin amount, as reported in Figure 33. Moreover, collagen-rich samples seemed to be closer in reaching a plateau compared to chitin-rich samples, still presenting a good increment in viability between 48 h and 72 h. Observing the samples at pH 8 this trend is totally opposite, having a decrement in viability increasing the chitin amount, except for sample C25. Probably the chitin domains cover the collagen ones limiting the collagen surface exposed.

Observing the overall picture emerging from these data, chitin and collagen appear to weakly interact one with the other, leading to separate assembly and a final material

homogeneous at the micro scale. This final material is more crystalline in the chitin domains and presents a higher order in the pure samples and when the composition is about 50-50 of each component. The assembled material showed a better influence on the cell viability in short term but have negative effects in longer exposure. The anisotropic material, instead, has a positive influence on the cell viability also in long exposure. This influence is more emphasized when a higher amount of chitin is present, even if in absolute values collagen shows better results.

4.4. Conclusion

In this study β-CnFs and collagen were assembled increasing the pH from 3 to 8. The results showed how weak interactions between the two components did not allow a co-assembly of the building blocks. Anyway, it led to the formation of a micro-homogenous biomaterial with distinct chitin and collagen domains. As proof of concept, this study confirms how the CnF dispersion is a proper system to study the assembly of pH responsive molecules with chitin.

The set of new materials obtained was also tested to understand the influence of composition and assembly on fibroblast cell viability. The results showed how assembly represents a favorable feature in the short term, while it is disadvantageous in long term. This has been mainly imputed to a lack of collagenous exposed surface, especially in chitin-rich samples. The not assembled materials, in fact, exhibited an increment in cell viability along the time. Contrary to the assembled condition, disorganized samples showed a higher increment in cell viability when a higher amount of chitin is used. Basing on these results, the most interesting materials are C75 (75 % chitin, 25 % collagen) among the not assembled samples (kept at pH 3) and C25 (25 % chitin and 75 % collagen) among the assembled samples (assembled at pH 8). In fact, both the samples are composite materials having advantages due to their dual composition. The first one showed a cell viability at 72 h comparable to all the other composites studied (about 111 %, compared to 132 % in pure collagen) but showed the highest increment in cell viability along the time (~40 % compared to ~25 % in the other composite and ~30 % for pure collagen). The second, instead, represents the highest amount of chitin tested that can be used to maintain a high biocompatibility (~100 % compared to ~113 % of pure collagen) and a proper increment in cell viability along the time (~27 % compared to ~13 % of pure collagen).

The novelty exposed in this study will be useful in future studies where structure and composition of chitin/collagen blend have to be exploited. Moreover, the development of a biocompatible route to obtain a micro-homogenous blend, obtained by self-assembly of two distinct pH-responsive biomacromolecules, might find application in the synthesis of new materials for medical applications.

4.5. Materials and methods

Materials All reagents and solvents were purchased from Sigma Aldrich and utilized without any further purification. Squid pens from *Loligo vulgaris* were collected from a local market. Once hydrated, the lateral blades were isolated, cleaned with distilled water and ethanol 70 vol.%, and then stored dry.

β-Chitin nano-fibrils preparation The 1 mg·mL^{-1} β-chitin nano-fibrils dispersion was prepared according to what reported in section 3.4 in this chapter.

Collagen solution preparation The 1 mg·mL^{-1} collagen solution was prepared by adding 200 mg of collagen in 40 mL of acetic acid pH 3. The solution was stirred overnight and then centrifuge 2000 g for 5 min. After centrifugation the solution was collected and the pellet was dispersed in 20 mL of solvent and sonicated for 20 min at 40 % of the maximum amplitude using a probe tip sonicator (Hielsher UP200St, 200 W, 26 kHz), refrigerating with a water bath. The solution was centrifuged again collecting the liquid phase with the previous one. The sonication and centrifugation steps were repeated once again. The remaining pellet (usually about 5 - 20 mg) was dried, weighted, and disposed. Basing on the weight of collagen in the pellet the solution collected along the different steps was diluted to get a 1 mg·mL^{-1} final concentration of collagen.

β-Chitin nano-fibrils self-assembly The chitin/collagen mixtures were prepared mixing 1 mg·mL^{-1} chitin and 1 mg·mL^{-1} collagen, both in acetic acid pH 3, in the different ratios studied. Self-assembly was induced by changing the pH of 20 mL of the solutions. The pH change was induced using NaOH 10 M and measured using a pH-meter BASIC 20 (pH ± 0.01) by Crison Instruments coupled with a HI1048 pH electrode (Hanna Instruments). The pH-meter was calibrated daily. The solutions were left for 24 hours at room temperature (25 °C) without any stirring. The morphological analyses were performed without any further purification of the mixtures. The samples assembled were then frozen with liquid nitrogen and lyophilized using a FreeZone® 1 (Labconco Corp., Kansas City, MO, US). The obtained material was compacted to obtain a film, washed with distilled water, and dried between two glass slides in a desiccator.

Optical microscopy observations Optical microscopy images were collected using a SM-LUX POL microscope equipped with a 5.0 MP Moticam 5 camera. Right after the end of the assembly process the sample was stirred, a drop of sample was collected and placed on a microscope slide, covered with a cover slip, and observed immediately.

Structural analysis FTIR spectra were collected using a Nicolet IS10 spectrophotometer. Omnic software (Thermo Electron Corp., Woburn, MA) was used for data processing. The samples were analyzed by ATR with 2 cm^{-1} resolution and 70 scans using a germanium crystal.

XRD patterns were collected using a PanAnalytical X'Pert Pro diffractometer equipped with multi array X'Celerator detector using Cu Kα radiation generated at 40 kV and 40 mA (λ = 1.54056 Å). The diffraction patterns were collected in the 2θ range between 4° and 25° with a step size (Δ2θ) of 0.05° and a counting time of 100 s. Each pattern collection was repeated at least twice on different samples.

Cell cultures Mouse embryonic fibroblast (NIH-3T3) cells were cultured under standard conditions in the DMEM medium, supplemented with 10 % (v/v) FBS, 2 mM L-glutamine, 0.1 mM MEM Non-Essential Amino Acids (NEAA), 100 $U \cdot mL^{-1}$ penicillin and 100 $U \cdot mL^{-1}$ streptomycin in a humidified incubator set at 37 °C with 5 % CO_2. Cells were seeded on samples at a density of 10^5 $cells \cdot cm^2$.

Cells viability test using a resazurin reduction assay Cell viability was determined by resazurin reduction assay; the reagent is an oxidized form of the redox indicator that is blue in colour and non-fluorescent. When incubated with viable cells, the reagent is reduced and it changes its colour from blue to red becoming fluorescent. Briefly, cells were seeded on samples with complete medium. After incubation times, the resazurin reagent was added directly to the culture medium with 10 % volume of medium contained in each sample and incubated for 4 h at 37 °C with 5 % CO_2. Subsequently, aliquots from each sample were transferred to a 96 multiwell plate for fluorescence measurement at λ_{exc} 560 nm and λ_{em} 590 nm (Thermo Scientific Varioskan Flash Multimode Reader). A negative control of only medium without cells was included to determine the background signal along with a positive control of 100 % reduced resazurin reagent without cells.

5. References

[1] G. M. Whitesides, B. Grzybowski, *Science (80-.).* **2002**, *295*, 2418.

[2] P. Nissen, J. Hansen, N. Ban, P. B. Moore, T. A. Steitz, *Science (80-.).* **2000**, *289*, 920.

[3] T. J. Mitchison, J. C. Biol, J. F. Kelleher, S. J. Atkinson, T. D. Pollard, J. C. Biol, J. D. Hartgerink, E. Beniash, S. I. Stupp, *Science (80-.).* **2001**, *294*, 1684.

[4] D. H. Gracias, V. Kavthekar, J. C. Love, K. E. Paul, G. M. Whitesides, *Adv. Mater.* **2002**, *14*, 235.

[5] T. D. Clark, J. Tien, D. C. Duffy, K. E. Paul, G. M. Whitesides, *J. Am. Chem. Soc.* **2001**, *123*, 7677.

[6] M. Mulisch, *Eur. J. Protistol.* **1993**, *29*, 1.

[7] S. Bartnicki-Garcia, G. Skjak-Brsek, T. Anthonsen, P. Sandford, In *The biochemical cytology of chitin and chitosan synthesis in fungi*; London and New York, 1989; pp. 23–35.

[8] N. S. Gupta, *Chitin Formation and Diagenesis*; Editor, S., Ed.

[9] K. Y. Zhu, H. Merzendorfer, W. Zhang, J. Zhang, S. Muthukrishnan, *Annu. Rev. Entomol.* **2016**, *61*, 177.

[10] H. Merzendorfer, *J. Comp. Physiol. B* **2006**, *176*, 1.

[11] I. M. Weiss, V. Schönitzer, N. Eichner, M. Sumper, *FEBS Lett.* **2006**, *580*, 1846.

[12] I. M. Weiss, F. Lüke, N. Eichner, C. Guth, H. Clausen-Schaumann, *J. Struct. Biol.* **2013**, *183*, 216.

[13] J. J. De Yoreo, P. M. Dove, *Science (80-.).* **2004**, *306*, 1301.

[14] M. Wysokowski, I. Petrenko, A. L. Stelling, D. Stawski, T. Jesionowski, H. Ehrlich, *Polymers (Basel).* **2015**, *7*, 235.

[15] J. Wu, J. C. Meredith, *ACS Macro Lett.* **2014**, *3*, 185.

[16] C. Zhong, A. Cooper, A. Kapetanovic, Z. Fang, M. Zhang, M. Rolandi, *Soft Matter* **2010**, *6*, 5298.

[17] J. Jin, P. Hassanzadeh, G. Perotto, W. Sun, M. A. Brenckle, D. Kaplan, F. G. Omenetto, M. Rolandi, *Adv. Mater.* **2013**, *25*, 4482.

[18] J. D. Fox, R. Capadona, P. D. Marasco, S. J. Rowan, *J. Am. Chem. Soc.* **2013**, *135*, 5167.

[19] G. Falini, S. Fermani, A. Ripamonti, **2002**, *91*, 475.

[20] G. Falini, M. Reggi, S. Fermani, F. Sparla, S. Goffredo, Z. Dubinsky, O. Levi, Y. Dauphin,

J. P. Cuif, *J. Struct. Biol.* **2013**, *183*, 226.

[21] S. Goffredo, P. Vergni, M. Reggi, E. Caroselli, F. Sparla, O. Levy, Z. Dubinsky, G. Falini, *PLoS One* **2011**, *6*, 1.

[22] A. Ianiro, M. Giosia, S. Fermani, C. Samorì, M. Barbalinardo, F. Valle, G. Pellegrini, F. Biscarini, F. Zerbetto, M. Calvaresi, G. Falini, *Mar. Drugs* **2014**, *12*, 5979.

[23] A. Chandumpai, N. Singhpibulporn, D. Faroongsarng, P. Sornprasit, *Carbohydr. Polym.* **2004**, *58*, 467.

[24] D. Iannazzo, A. Mazzaglia, A. Scala, A. Pistone, S. Galvagno, M. Lanza, C. Riccucci, G. M. Ingo, I. Colao, M. T. Sciortino, F. Valle, A. Piperno, G. Grassi, *Colloids Surfaces B Biointerfaces* **2014**, *123*, 264.

[25] D. Montroni, B. Marzec, F. Valle, F. Nudelman, G. Falini, *Biomacromolecules* **2019**, *20*, 2421.

[26] Y. Saito, T. Okano, F. Gaill, H. Chanzy, J.-L. Putaux, *Int. J. Biol. Macromol.* **2000**, *28*, 81.

[27] Y. Saito, J. L. Putaux, T. Okano, F. Gaill, H. Chanzy, *Macromolecules* **1997**, *30*, 3867.

[28] R. Hackman, *Aust. J. Biol. Sci.* **1960**, 568.

[29] A. Gottschalk, W. H. Murphy, E. R. B. Graham, *Nature* **1962**, *4833*, 1051.

[30] D. Montroni, S. Fermani, K. Morellato, G. Torri, A. Naggi, L. Cristofolini, G. Falini, *Carbohydr. Polym.* **2019**, *207*, 26.

[31] M. Rolandi, R. Rolandi, **2014**, *207*, 216.

[32] F. C. Yang, R. D. Peters, H. Dies, M. C. Rheinstädter, *Soft Matter* **2014**, *10*, 5541.

[33] I. M. Weiss, C. Renner, M. G. Strigl, M. Fritz, *Chem. Mater.* **2002**, *14*, 3252.

[34] J. Blackwell, M. A. Weih, *J. Mol. Biol.* **1980**, *137*, 49.

[35] A. C. Neville, B. M. Luke, *Tissue Cell* **1969**, *1*, 689.

[36] F. Z. Cui, Y. Li, J. Ge, *Mater. Sci. Eng. R Reports* **2007**, *57*, 1.

[37] G. Askarieh, M. Hedhammar, K. Nordling, A. Saenz, C. Casals, A. Rising, J. Johansson, S. D. Knight, *Nature* **2010**, *465*, 236.

[38] T. Priemel, E. Degtyar, M. N. Dean, M. J. Harrington, *Nat. Commun.* **2017**, *8*, 14539.

[39] F. Hammes, W. Verstraete, *Rev. Environ. Sci. Biotechnol.* **2002**, *1*, 3.

[40] J.-H. Bradt, M. Mertig, A. Teresiak, W. Pompe, *Chem. Mater.* **1999**, *11*, 2694.

[41] W. F. Boron, P. De Weer, *J. Gen. Physiol.* **1976**, *67*, 91.

[42] J. R. Casey, S. Grinstein, J. Orlowski, *Nat. Rev. Mol. Cell Biol.* **2010**, *11*, 50.

[43] D. Clark, M. Lamare, M. Barker, *Mar. Biol.* **2009**, *156*, 1125.

[44] M. Florek, E. Fornal, P. Gómez-Romero, E. Zieba, W. Paszkowicz, J. Lekki, J. Nowak, A. Kuczumow, *Mater. Sci. Eng. C* **2009**, *29*, 1220.

[45] N. Kröger, *Science (80-.).* **2009**, *325*, 1351.

[46] G. Fu, S. Valiyaveettil, B. Wopenka, D. E. Morse, *Biomacromolecules* **2005**, *6*, 1289.

[47] A. Mikkelsen, S. B. Engelsen, H. C. B. Hansen, O. Larsen, L. H. Skibsted, *J. Cryst. Growth* **1997**, *177*, 125.

[48] G. Falini, S. Weiner, L. Addadi, *Calcif. Tissue Int.* **2003**, *72*, 548.

[49] S. Weiner, L. Addadi, *Annu. Rev. Mater. Res.* **2011**, *41*, 21.

[50] Y. Noishiki, H. Takami, Y. Nishiyama, M. Wada, S. Okada, S. Kuga, *Biomacromolecules* **2003**, *4*, 896.

[51] S. Hunt, A. El Sherief, *Tissue Cell* **1990**, *22*, 191.

[52] J. LI, J.-F. REVOL, R. H. MARCHESSAULT, *J. Colloid Interface Sci.* **1996**, *183*, 365.

[53] H. El Harmoudi, L. El Gaini, E. Daoudi, M. Rhazi, Y. Boughaleb, M. A. El Mhammedi, A. Migalska-zalas, M. Bakasse, *Opt. Mater. (Amst).* **2014**, *36*, 1471.

[54] R. A. A. Muzzarelli, *C. Cell. mol. life sci.* **1997**, *53*, 131.

[55] S. Prefecture, *Text. Res. J.* **2004**, *74*, 34.

[56] B. M. Dunn, *Chem. Rev.* **2002**, *102*, 4431.

[57] E. S. Radisky, J. M. Lee, C.-J. K. Lu, D. E. Koshland, *PNAS* **2006**, *103*, 6835.

[58] Y. Fan, T. Saito, A. Isogai, *Biomacromolecules* **2008**, *9*, 1919.

[59] A. Antosova, Z. Gazova, D. Fedunova, E. Valusova, E. Bystrenova, F. Valle, Z. Daxnerova, F. Biscarini, M. Antalik, *Mater. Sci. Eng. C* **2012**, *32*, 2529.

[60] L. Heux, J. Brugnerotto, J. Desbriéres, M. F. Versali, M. Rinaudo, *Biomacromolecules* **2000**, *1*, 746.

[61] S. B. Lee, Y. H. Kim, M. S. Chong, Y. M. Lee, *Biomaterials* **2004**, *25*, 2309.

[62] X. Li, Q. Feng, X. Liu, W. Dong, F. Cui, *Biomaterials* **2006**, *27*, 1917.

[63] X. Li, Q. Feng, W. Wang, F. Cui, *J. Biomed. Mater. Res. - Part B Appl. Biomater.* **2006**, *77*, 219.

Chapter 3:
Natural chitin-based matrices

1. Introduction

Technological innovations have had a great boost from basic research, as mentioned in chapter 1. The results obtained are a growing reason that spur science to deep into nature's secrets. As mentioned, chitin-based matrices are a pool of knowledge where crucial information could arise from different aspects, as how:

- proteins interact with chitin;
- chitinous matrices can direct biomineralization;
- structure and morphology influence the properties of materials.

1.1. Chitin-binding proteins

As discussed in chapters 1 and 2, chitin-based matrices are made up of crystalline nano-fibrils typically embedded in a protein matrix.[1][2][3][4][5]

Biochemical studies on proteins associated with chitin from a wide variety of arthropod cuticles identified a conserved chitin-binding domain (CBD) of 35-36 residues in a 65 residues sequence, called Rebers & Riddiford consensus sequence (RR).[6] Comparing different cuticular proteins two different families of RR where identified; RR-1 is present in soft cuticles (flexible, relatively unsclerotized regions such as caterpillar abdomens or intersegmental membranes), RR-2 is present in hard cuticles (rigid head capsules or lepidopteran wings).[7] This difference arises from an N-terminal hydrophilic region, well conserved in RR-2, which also presents more histidine residues involved in sclerotization processes. Homology modeling suggested that the preferred tertiary structure of RR in cuticular proteins is an antiparallel β-sheet structure in a half β-barrel structure, Figure 34. In this configuration, aromatic residues face the internal β-barrel surface and are expected to interact with the chitin crystal.[8]

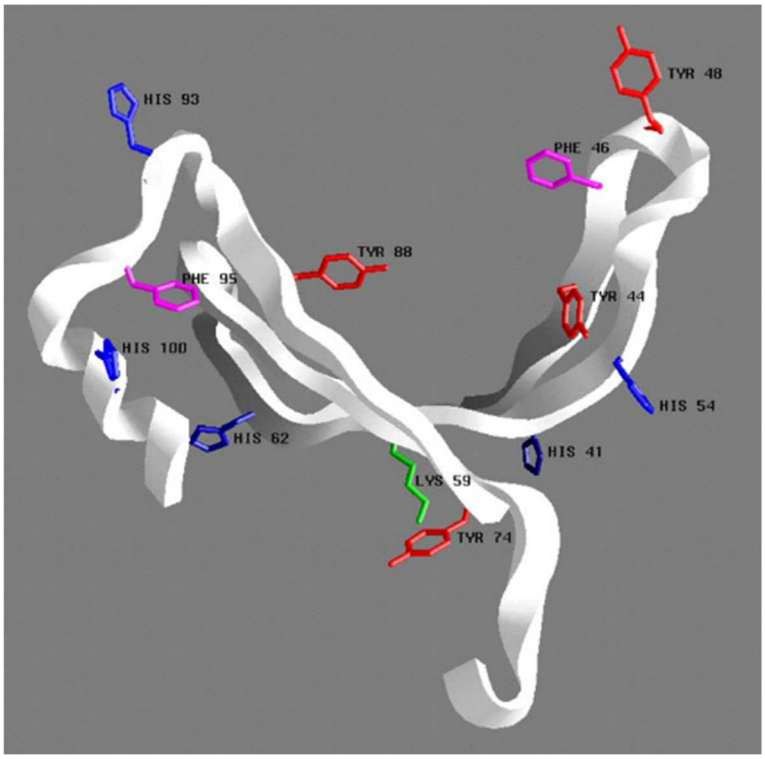

Figure 34: A ribbon model of hard-cuticle protein structure. The side chains of several aromatic residues are shown as ''ball and sticks''. The model structure has a ''cleft'' full of aromatic residues, which form a ''flat'' surface of aromatic rings (upper side), ideally suited for cuticle protein–chitin chain interactions, and an outer surface (lower side) which should be important for protein–protein interactions in the cuticle. Also, the model provides for the right positioning of histidine residues, so that these histidines might participate in cuticle sclerotization. Figure from Iconomidou et al. (2005).[8]

Another group of proteins presents a different CBD.[9][10] Some examples of this group are chitinases,[11][12] chitin synthases,[12] or peritrophic membrane proteins. This CBD has a similar structure in arthropods and plants, being probably a result of convergent evolution. This domain presents aromatic residues, crucial for chitin binding too, but they have been found in lower numbers. Contrary to the RR consensus, this CBD is kept folded by disulfide bonds (usually three for insects,[13][14] and four for plants[15][16]), as reported in Figure 35. These disulfide bonds are essential for the correct folding of the binding sites and a drastic drop in the binding capability was observed after their reduction.[17][18]

CBDs are highly selective for chitin, sometimes even at the level of different polymorphs.[19] It is common for structural proteins to present many CBDs in their sequence,[14] Shi & al. (2009) reported a protein with even 19 CBDs.[20]

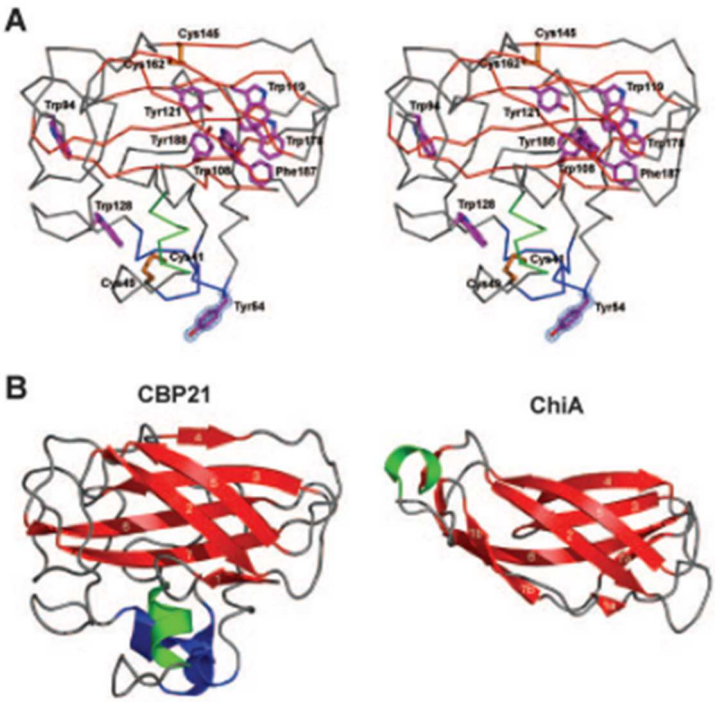

Figure 35: (A) Carbon trace of a chitin binding protein from Serratia marcescens shown in stereo. Conserved aromatic amino acids are shown as sticks. Disulfide bridges are shown as orange sticks. (B) The same structure showing the secondary structure of the protein. Figure from Vaaje-Kolstad et al. (2005).[9]

To date, only a few studies have been carried out on how these proteins have a crucial role in governing chitin fibrils self-assembly and ultrastructural organization,[21][22] and in the properties of different chitin matrices.[2][23][24] Chaudari et al. (2011) studied the influence of a protein called Knickkopf in the molting process of the insect *Tribolium castaneum*. This protein has a crucial role in protecting the chitin of the new cuticle from the chitinase degrading the old cuticle; it also have an influence in organizing the new cuticle chitin into laminae. Knickkopf down-regulation resulted in chitinase-dependent loss of chitin, severe molting defects, and lethality at all developmental stages.

Another example is TcCPR27 (RR-2), a protein essential for maintaining the rigidity of the elytra of *T. castaneum*.[25] Even though the inhibition of TcCPR27 did not eliminate structural features in the elytra, the elytra were wrinkled and did not expand properly.

Basing on the few examples reported, chitin binding proteins might one day be a major source of information for bioinspired control over polymer assembly or to project building blocks for new composite materials.

1.2. Chitin in biomineralization

Biomineralization is the process by which living organisms produce minerals. This field has been explored to understand how organisms precisely control inorganic crystal's nucleation, growth, morphology, and polymorphism.[26]

Among the mineralized matrices, mollusk' shells[27][28] have been deeply investigated to understand their control over calcium carbonate deposition. Those works observed how this control is due to a highly organized organic matrix interacting with the crystals.[29][30] These organic phases are frequently multicomponent structures made of β-chitin[31] and proteins. Each component shows different effects that drives mineral deposition. In nacre, for example, the a-axis of the aragonite tablets was observed to grow parallel to the β-chitin fibril-axis, while chitin layers were observed to limit nacre tablets vertical growth.[32] On the other hand, the proteic composition is widely diversified, but frequently two main components are present, silk fibroin-like proteins[33][34] and acidic residue-rich proteins.[35] The latter seems to be responsible for the polymorph control of the crystal.[26] These components collaborate to get the fine final control over the crystals.

Mineralized structures have a fundamental structural or protective purpose. Despite this advantages, slugs lost their external shell during their evolutionary path,[36][37] probably to adapt to a lower calcium environment. Anyway, some slugs still maintain a vestigial thin internal shell (IS). The role of this IS still has to be defined, some hypotheses assume its implication in mechanical protection, protection from parasites,[38] and calcium storage.[39] In 1969, the internal shell of *Ariolimax columbianus* has been observed calcify or decalcify depending on the slug's diet or ovulation, as shown in Figure 36.[39] For example, a calcium-rich diet was observed to induce calcification of the IS in the slugs while a decalcification was observed when eggs, which require a high amount of calcium, where produced. These observations led to the hypothesis that the main role of this IS might be calcium storage.

This vestigial shell is just one of the examples of matrices that could be investigated to better understand how to create substrates able to control crystal growth. As a specific example, a better understanding of the calcium storage ability of this matrix might unveil new information for dynamic inorganic systems development.

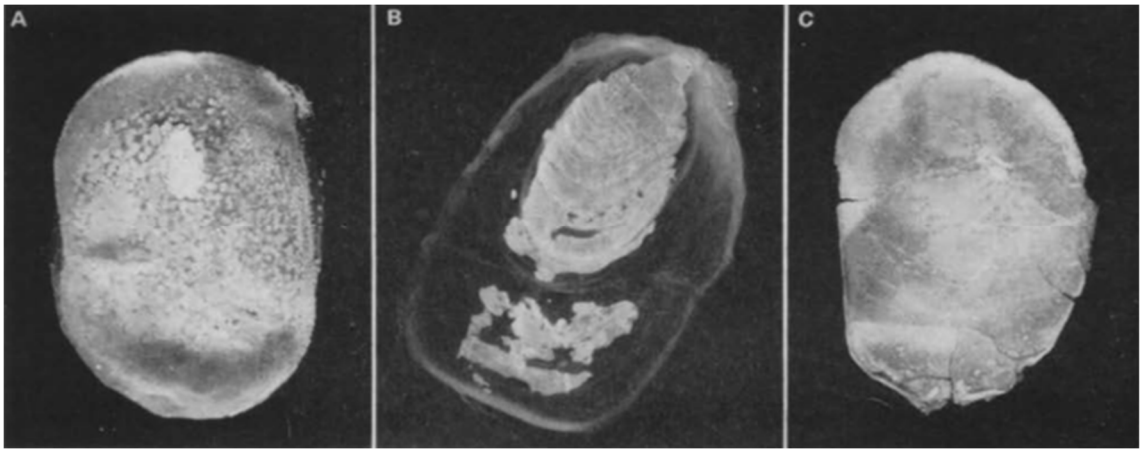

Figure 36: Internal shells of Ariolimax columbianus at different stages of nutrition and breeding. (A) Shell from the slug, fresh from the field. (B) Shell from the slug after egg-laying. (C) Shell from the slug fed on a calcium-rich diet for 10 days in the laboratory. Figure from Meenakshi and Scheer (1970).[39]

1.3. Matrices in the buccal mass of Gastropods

Among the natural matrices, the ones correlated to feeding are quite intriguing when we think about the forces involved in this process. Feeding is essential to the life of any organism and involves many biomaterials of interest including apatite from human teeth[40] and the chiton's tooth, which is the hardest known biological material.[41] Mollusks, except bivalves, start processing their food with the buccal mass, an apparatus similar in function to the human mouth, Figure 37.[42][43] The buccal mass contains three acellular components: the radula, the odontophore, and the jaw. The radula is a flexible chitinous membrane with tooth-like structures, called denticles, arranged in transverse and longitudinal rows.[44] The odontophore, on the other hand, is a cartilaginous structure that supports the radula.[45][46] The radula and the odontophore have a complex tissue organization which allows motion[47] and stems from their biogenesis.[48][49] The third component, the jaw, is a chitin-reinforced part of the foregut cuticle, which is located opposite the radula.[50] When a slug feeds on leaves, a leaf is squeezed in between the jaw and the radula, and the radula cuts off pieces of the food.[51]

In many different mollusk species, the radula is the most studied matrix of the buccal mass structures.[52][53][54][55][56][57][58][59][60] The radula's composition and morphology, which is used in taxonomy,[53][54][55] varies widely between species depending on feeding habits. For example, the radula of a limpet that scrapes hard surfaces to collect algae has 2-6 large hard cusps biomineralized with iron.[56] In chitons, with similar eating habits, the posterior

region of the tooth is instead made of a "softer" material such as apatite (Figure 38).[58] In the radula of the mainly omnivorous slugs of the genus *Ariolimax*, dozens of denticles, that do not contain iron, are present as an adaptation to a softer food.[54][55] In the genera *Haliotis*,[59][60] *Lacuna,*[61] or *Littoraria*[62] radular morphology responds to changes in the diet. Similarly, the jaw is smaller in purely carnivorous mollusks than in herbivorous species.[51] Although the jaw has an important role during the feeding process, its structure has been investigated at the micro-scale only externally for taxonomic observations.[50][54][63] The odontophore has been described as a "cartilaginous structure",[46][48][51] and researches have focused on investigation on its external tissues, which are involved in both the feeding motion and biogenesis of the radula.

The radula has been widely investigated to understand its control over biomineralization processes and to understand how to get mechanical resistant materials. On the other hand, jaw and odontophore have never been investigated with this purpose and might led to new materials for compression resistance and to interface hard and soft tissues.

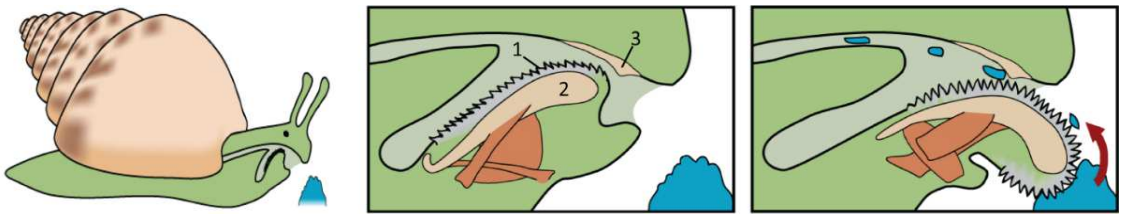

Figure 37: Schematic representation of the buccal mass of a snail while rest and feeding. (1) The radula. (2) The odontophore. (3) The jaw.

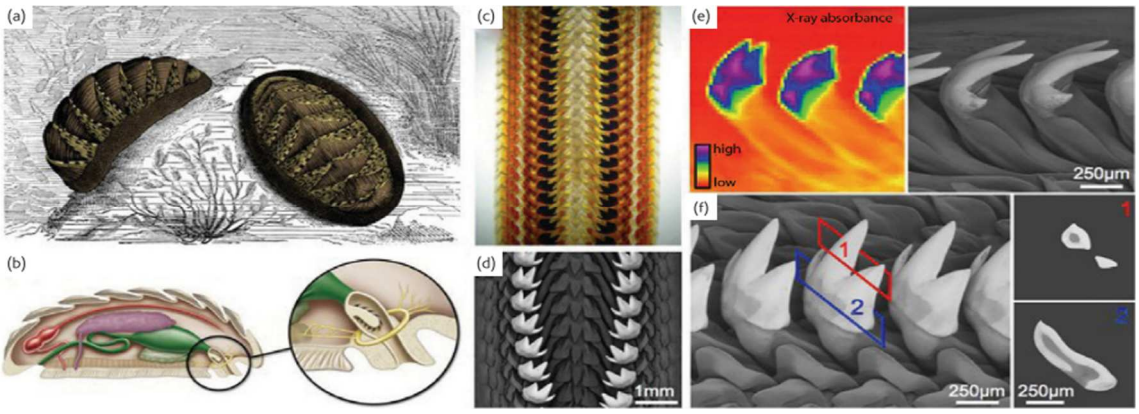

Figure 38: (a) External and (b) internal anatomy of a representative chiton showing the location of the radula. Details of the anterior region of the radula from (c-f) C. stelleri. (c) Optical, (d) backscattered SEM imaging, and (e) XRD studies reveal the nature of the electron density distribution of the tricuspid tooth caps. Cross-sectional studies through the mature teeth from C. stelleri (f 1,2) reveal a concentric biphasic structure. Figure from Weaver et al. (2010).[41]

2. Aim of the chapter

This chapter is articulated in three projects aiming to study three different aspects of natural chitinous matrices and collect information that could be used in future bioinspired studies.

The first aims to characterize the influence of the structural proteins on the mechanical properties of a chitin-based composite material, the gladius of the squid *Loligo vulgaris*.[2][64] The knowledge from this research is of potential interest for understanding the biosynthesis and structure-function relationship of chitin-based composites, and for the design of new materials.[65][66]

The second and third projects both study matrices in *Ariolimax californicus,* a terrestrial slug endemic to western North America and commonly known as banana slugs.
The second project studies morphology, crystal phase, and composition of the IS of *A. californicus*. Contrary to external shells, ISs have been only superficially characterized and, to our knowledge, the only morphological description reported in literature is from 1984, where *Limax maximus* was examined.[37] New information on this matrix would lead to a better understanding on how this IS controls the dynamic equilibrium of calcification and decalcification required in calcium storage.

In the third project, the structure and material composition of the acellular components of *A. californicus* buccal mass - radula, jaw, and odontophore - were investigated. Up to now, there is relatively little information on these components, especially in the buccal mass of terrestrial slugs, or slugs that eat relatively soft food. A better understanding of the structure and composition of the buccal mass may provide insights in how the jaw, radula, and odontophore have evolved into a perfectly working system able to cut food and handle strong stresses while interfacing with soft tissues.

3. Influence of structural proteins on the mechanical properties of the gladius of Loligo vulgaris

3.1. Results

3.1.1. Characterization of squid pen extracted proteins

To extract the proteins from the squid pen a denaturing aqueous solution (Mix. 24h) containing 8 M urea, 4 vol.% mercaptoethanol, and 1 mM ethylenediaminetetraacetic acid (EDTA) was used at room temperature for 24 h. The extracted proteins were stable in the denaturing solution but precipitated upon dialysis against a 50 mM tris-(hydroxymethyl)aminomethane (TRIS) buffer at pH 7.4. The amino acid composition (Table 2) of this extract shows a low amount of cysteine (1.1 mol.%), and is rich in glycine (13.7 mol.%), alanine (13.5 mol.%), proline (11.5 mol.%) and histidine (9.0 mol.%). The sodium dodecyl sulfate – polyacrylamide gel electrophoresis (SDS-PAGE) analyses revealed the same protein bands from the precipitated proteins and the protein remained in solution (Figure 39). Four strong bands between 30 and 45 kDa plus three weak bands at about 97 kDa, 25 kDa, and 20 kDa were stained. The protein precipitate was also analyzed using FTIR spectroscopy (Figure 40). All the typical absorption bands of proteins were observed: amide A (3290 cm^{-1}), amide I (1655 cm^{-1}), amide II (1521 cm^{-1}), and amide III (1235 cm^{-1}). Other weak absorption bands related to side-chain amino acid vibration modes were also observed, no absorption bands that could be related to phosphorylation or glycosylation were detected.[67][68][35]

When the extraction of the proteins was carried out using the single components of the denaturing solution the SDS-PAGE showed no bands for 1 mM EDTA and 4 vol.% mercaptoethanol, and only a weak band at about 45 kDa for 8 M urea. When the denaturing solution was used again on the matrices treated using the Mix. 24h (Mix. 48 h) a slightly different pattern of bands was observed with respect to that observed using the Mix. 24 h (Figure 40). Increasing the amount of solution loaded in the gel other less intense bands appeared (Figure 41). Those bands were efficiently extracted using the mixture for 24 h, but a less intense signal of those bands was also detected after 48 h. Moreover, the urea 8 M treatment extracted selectively those bands.

Table 2: Amino acid composition of the Mix 24h protein extract dialyzed against water and lyophilized.

Residue	**mol %**
Ala	13.5
Arg	1.6
Asx	8.6
Cys	-
Cys-Cys	1.1
Glx	4.4
Gly	13.7
His	9.0
Ile	3.1
Leu	5.9
Lys	3.0
Met	-
Phe	2.3
Pro	11.5
Ser	3.4
Thr	3.6
Trp	-
Tyr	6.7
Val	8.5

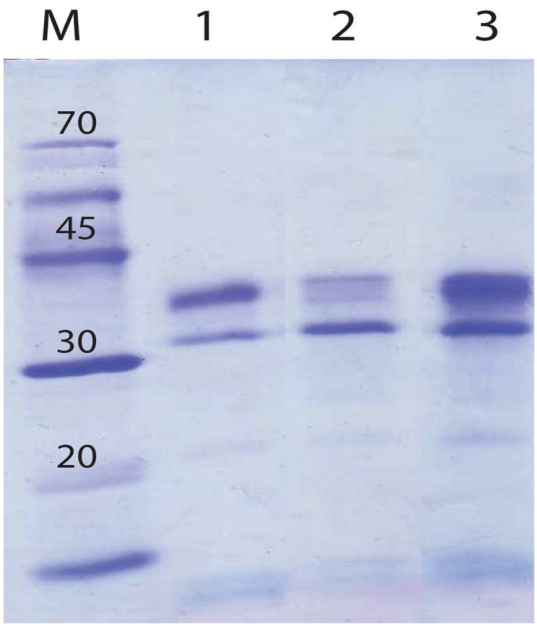

Figure 39: SDS-PAGE from the Mix. 24h solution (3), the protein precipitate obtained after dialysis (2), and the dialysis solution (1). (M) shows the references for the molecular weight in kDa.

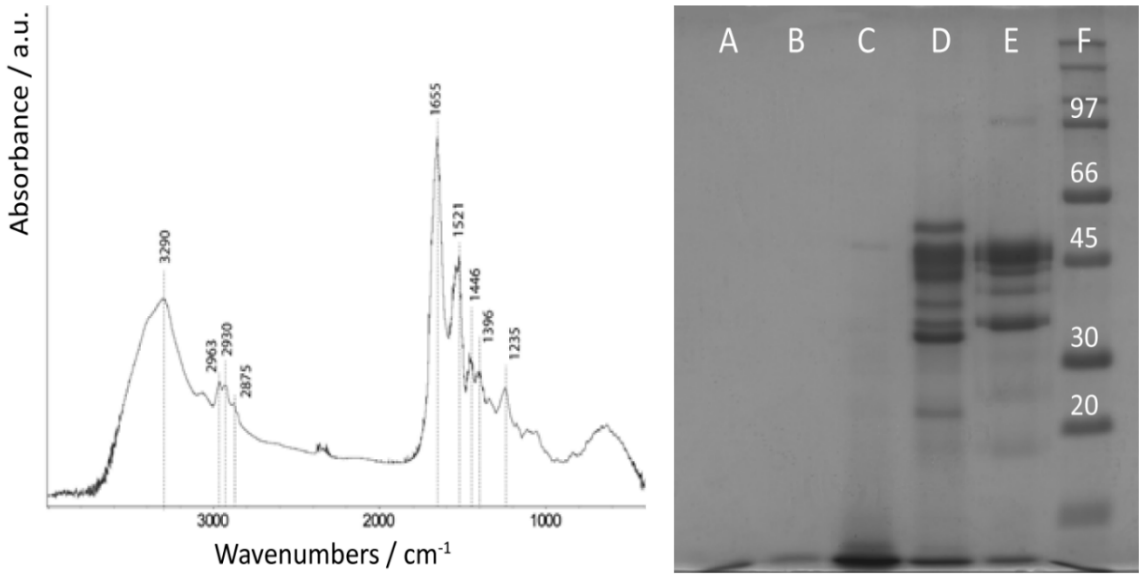

Figure 40: (left) FTIR spectrum of the proteins extracted from the squid pen using the Mix. 24h. The main absorption bands of proteins are labelled. (right) SDS-PAGE from the extracting solution: (A) 1 mM EDTA; (B) 4 vol.% mercaptoethanol; (C) 8 M urea; (D), Mix. 24h, and (E) Mix. 48h. (F) References for the molecular weight reported in kDa. 25 µL of each sample were loaded in the SDS-PAGE, except for Mix. 24h were only 2 µL were loaded.

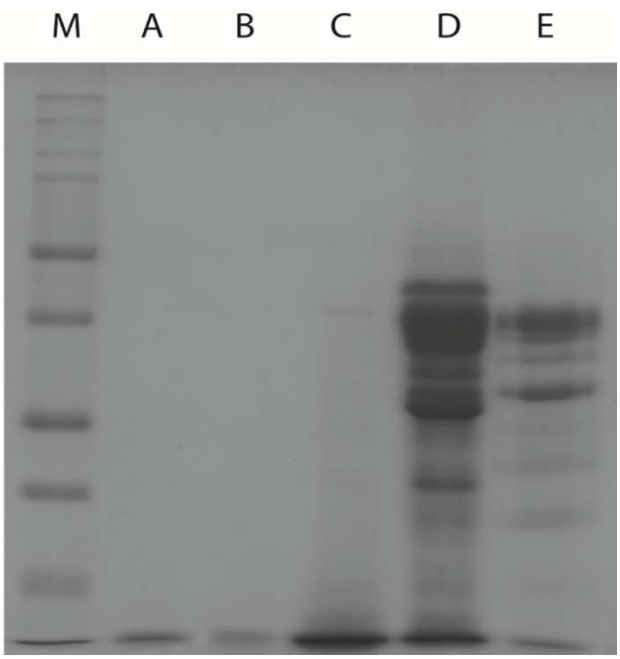

Figure 41: SDS-PAGE from the extracting solution injecting more material in the gel: (A) 1 mM EDTA; (B) 4 vol.% mercaptoethanol; (C) 8 M urea; (D), Mix. 24h, and (E) Mix. 48h. (M) References for the molecular weight is the same as in Figure 39. 32 µL of each sample were loaded in the SDS-PAGE, except for Mix. 24h were only 12 µL were loaded.

3.1.2. Structural characterization of treated squid pen

The quantification of squid pen degree of de-proteination, which was carried out by gravimetric measurement, indicated that no molecules were removed from the squid pen after treatment with a 1 mM EDTA or 4 vol.% mercaptoethanol solution (Table 3). The sample treated with the 8 M urea solution lost about 6 wt.%, while those treated in Mix. 24h or Mix. 48h lost about 40 wt.% and 50 wt.%, respectively. The treatment of the squid pen with a proteolytic mixture of enzymes or with a 1 M NaOH solution lead to a weight loss of about 40 wt.% and 60 wt.%, respectively (Table 3).

The 1 M NaOH and enzymatically treated samples, being protein-free, were analyzed by solid state NMR spectroscopy to determine the DA that was 89 ± 1 % and above 93 %, respectively.

The samples were also characterized by UV-Vis and FTIR spectroscopy and the results are shown in Figure 42 and Figure 43.

Table 3: Summary of the compositional, swelling, and mechanical properties of squid pen treated samples. Maximum stress (σ_{max}), maximum strain (ε_{max}), and Young modulus (E).

	weight loss / %	swelling / %	σ_{max} / MPa	ε_{max} / %	E / MPa
Squid pen	0*	199 ± 2	40 ± 9	1.2 ± 0.4	4000 ± 1000
1 mM EDTA	0 ± 3	212 ± 21	30 ± 10	0.99 ± 0.06	4000 ± 1000
4 vol.% Merc.	0 ± 2	260 ± 20	17 ± 8	1.8 ± 0.5	900 ± 300
8 M Urea	6.3 ± 0.4	220 ± 20	30 ± 10	1.6 ± 0.6	2400 ± 400
Mix. 24h	40 ± 9	800 ± 100	11 ± 3	5 ± 2	380 ± 80
Mix. 48h	52 ± 3	800 ± 100	6 ± 2	4 ± 2	300 ± 100
Enzymes	41 ± 9	760 ± 50	5 ± 1	3.9 ± 0.6	190 ± 50
1 M NaOH	60.1 ± 0.9	450 ± 20	7 ± 2	4.3 ± 0.5	330 ± 90
1 M NaOH dry	60.1 ± 0.9	340 ± 10	16 ± 2	11 ± 4	250 ± 40

* Squid pen was the reference weight.

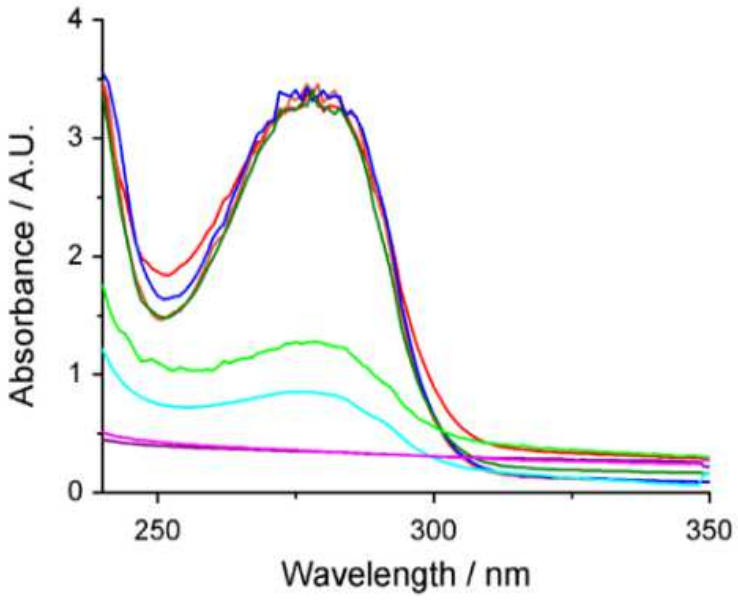

Figure 42: UV-Vis spectra of the different samples after chemical or enzymatic treatments. In red the squid pen, in orange the 1 mM EDTA treated sample, in blue the 4 vol.% mercaptoethanol treated sample, in dark green the 8 M urea treated sample, in light green the Mix. 24h sample, in light blue the Mix. 48h sample, in pink the enzyme treated sample, and in violet the 1 M NaOH treated sample.

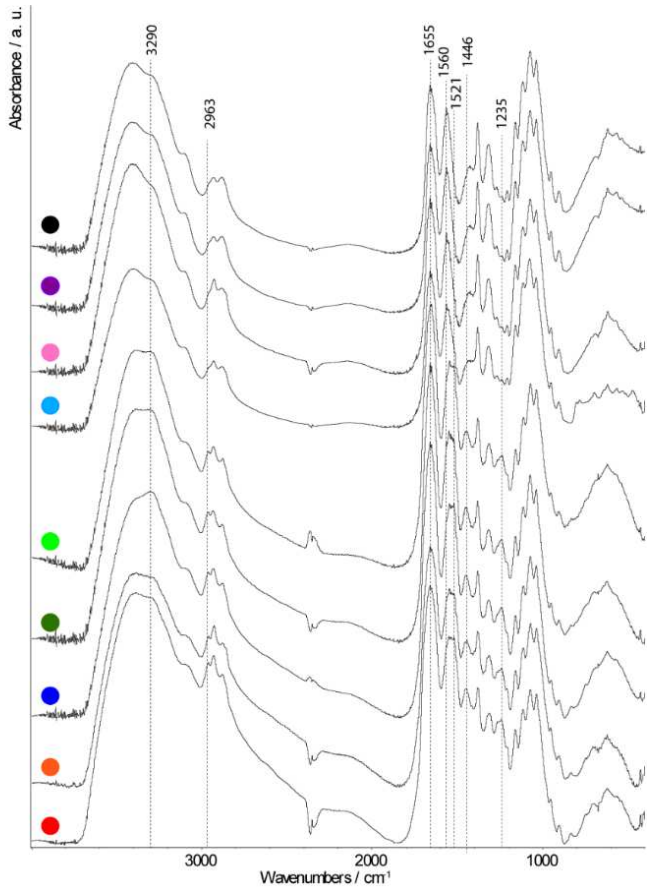

Figure 43: FTIR spectra of the different samples after chemical or enzymatic treatments. The different samples are labeled by a colored circle. In red the squid pen, in orange the 1 mM EDTA treated sample, in blue the 4 vol.% mercaptoethanol treated sample, in dark green the 8 M urea treated sample, in light green the Mix. 24h sample, in light blue the Mix. 48h sample, in pink the enzyme treated sample, and in violet the 1 M NaOH treated sample.

The UV-Vis spectra (Figure 42) showed that the intensity of the tryptophan absorption band (280 nm)[69] does not change for the samples treated in an EDTA, mercaptoethanol, or urea solution with respect to that of the squid pen sample. This band decreased progressively for the sample treated with Mix. 24h and Mix. 48h solution, while for the samples treated in the enzyme or the alkaline solution was absent. The analysis of the FTIR spectra (Figure 43) showed that the typical protein absorption bands at 3290 cm^{-1} (amide A), 1650 cm^{-1} (amide I), 1520 cm^{-1}, and 1235 cm^{-1} (amide III) were present only in the samples treated with 1 mM EDTA, 4 vol.% mercaptoethanol, 8 M urea, and Mix. 24h. In addition to these absorption bands, other two bands at 2963 cm^{-1} and 1446 cm^{-1} were present only in the protein containing samples. The typical absorption bands of chitin were present in all samples.[70]

The squid pen sample showed a swelling of about 200 wt.%, a similar value was obtained for the samples treated in the 1 mM EDTA, 4 vol.% mercaptoethanol, or 8 M urea solution. The swelling increased to about 800 wt.% for the samples treated in Mix. 24h, Mix. 48h, or enzyme solution while it was of lower, around 450 wt.%, for the samples treated in 1 M NaOH solution. The Mix. 24h, Mix. 48h, or enzyme treated samples if subject to a drying and rehydration cycle recovered their swelling to intermediate levels between the squid pen and the NaOH treated sample (Table 4).

Table 4: Swelling of different samples after the synthesis and after a dehydration/rehydration cycle.

	Initial swelling	**After dehydration**
Enzymes tr.	760 ± 50	256 ± 6
Mix. 24h	800 ± 100	333 ± 5
Mix. 48h	800 ± 100	430 ± 50

SEM images of the cross-sections of the samples, reported in Figure 44, showed that the overall ultrastructural organization is conserved in all the samples. However, while in the samples containing the higher content of proteins the chitin matrix is embedded within the proteins, making the material of compact appearance, in the ones protein free, or almost, the layered chitin matrix is well visible. Similar information was obtained from the observation of the surface of the samples, where the rough protein coverage of the samples is reduced up to completely disappear in the almost protein free samples, leaving the smooth surface of the chitin matrix (Figure 45).

The synchrotron XRD images of the samples are reported in Figure 46. All the samples showed the typical periodicities of di-hydrated β-chitin at 10.7 and 4.4 Å along the equator direction and 5.1 Å, 3.3 Å and 2.55 Å along the meridian direction (Figure 47).[71] Additional diffraction peaks, typical of di-hydrated β-chitin were also observed in the samples with giving high diffraction intensities. Weak diffraction intensities were observed for the samples treated with 4 vol.% mercaptoethanol or enzyme solution. No evident diffraction peaks that could be associated with proteins were detected.

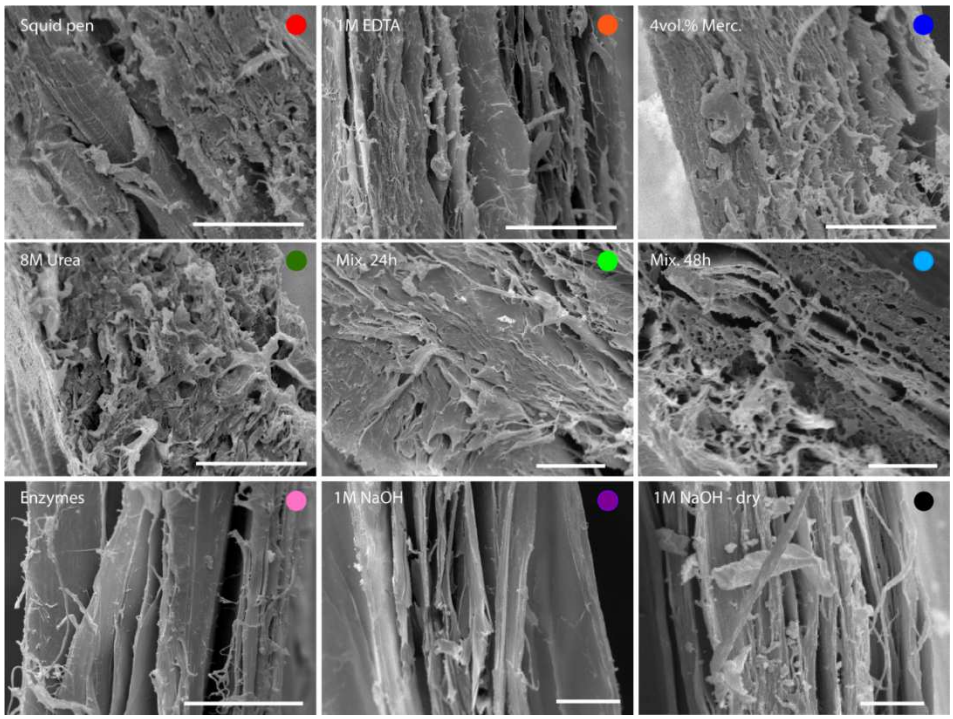

Figure 44: SEM images of cross section of the squid pen sample (red) and samples treated with EDTA (orange), mercaptoethanol (blue), urea (dark green), Mix. 24h (light green), Mix. 48h (light blue), enzymes (pink), alkaline (violet), and alkaline dried (black). Scale bar: 20 µm.

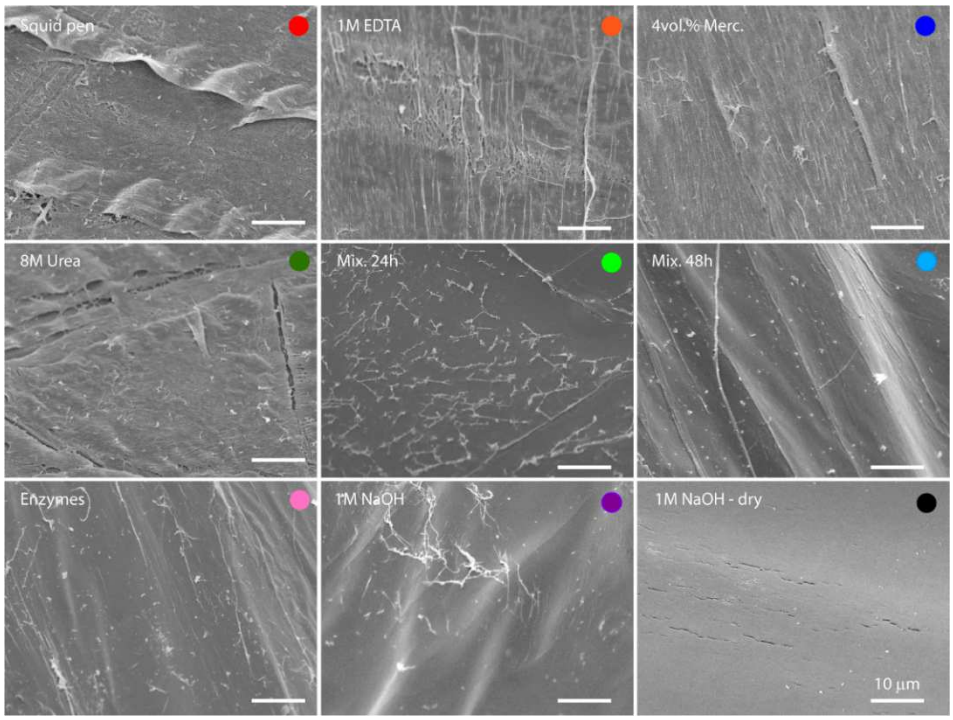

Figure 45: SEM images of the surface of the squid pen sample (red) and samples treated with EDTA (1 mM EDTA), mercaptoethanol (blue), urea (dark green), Mix. 24h (light green), Mix. 48h (light blue), enzymes (pink), alkaline (violet), and alkaline dried (black). Scale bar: 10 µm.

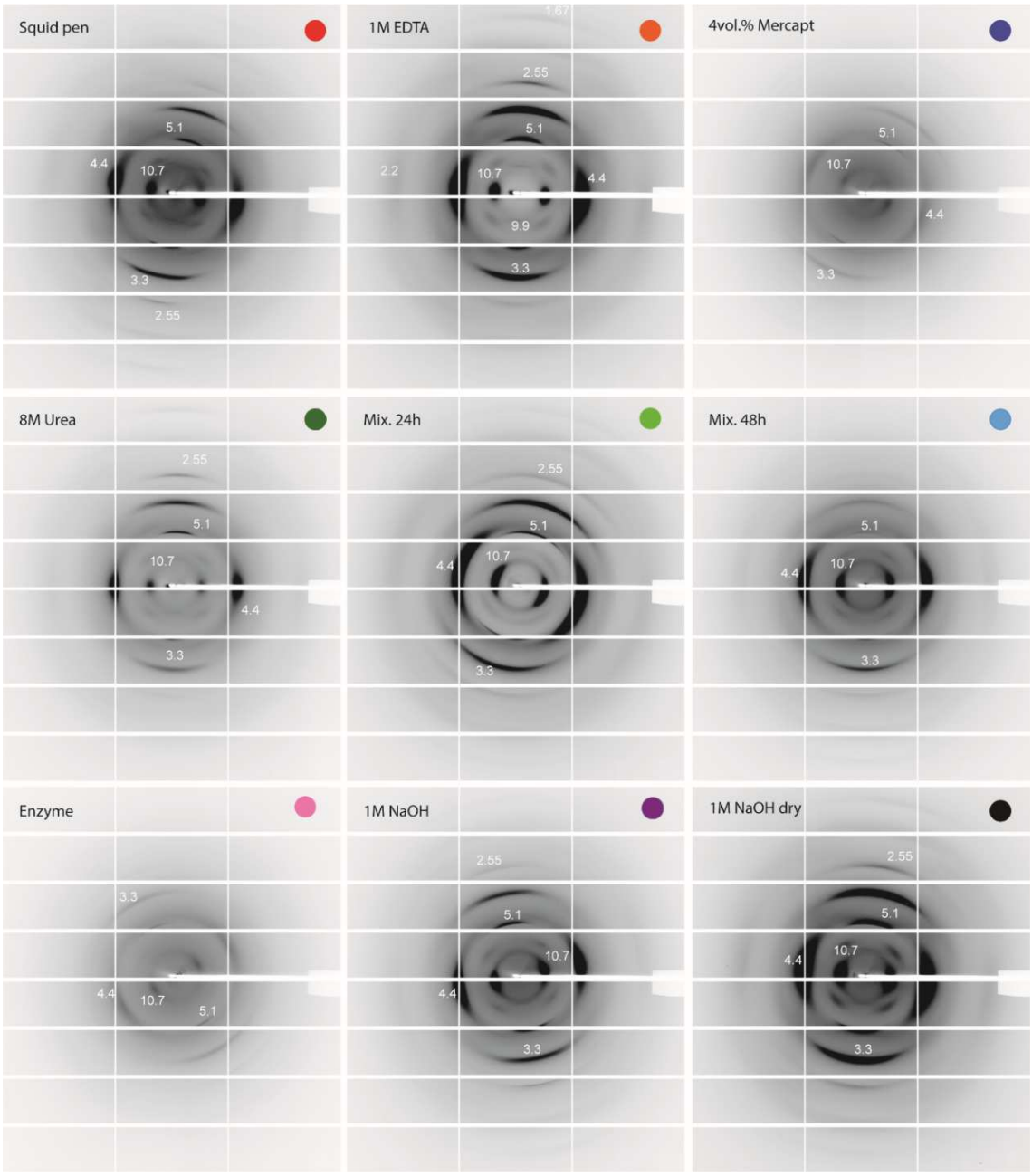

Figure 46: Synchrotron X-ray diffraction images of the squid pen sample (red) and of samples treated with: EDTA (orange), mercaptoethanol (blue), urea (dark green), Mix. 24h (light green), Mix. 48h (light blue), enzymes (pink), 1 M NaOH (violet), and 1 M NaOH dried (black).

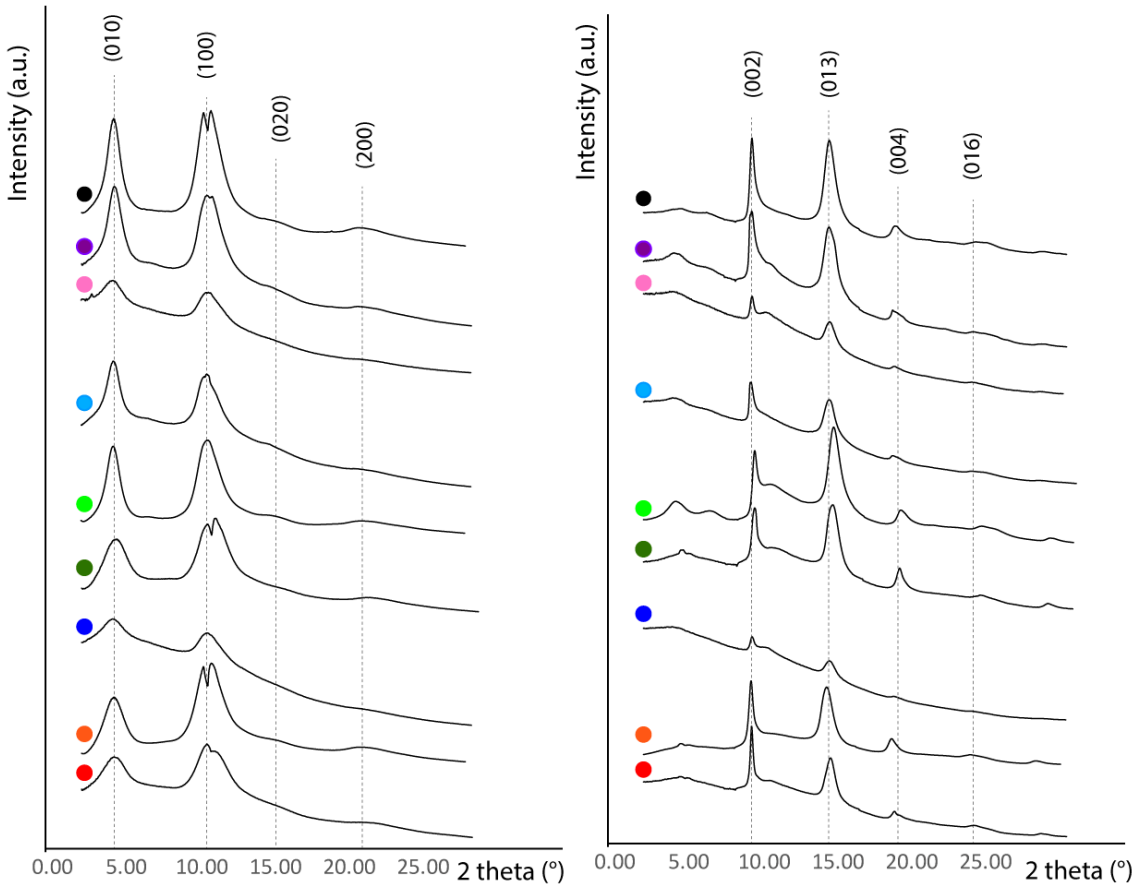

Figure 47: X-ray diffraction profiles along the equatorial (left) and meridional (right) direction of squid pen sample (red) and of samples treated with EDTA (1 mM EDTA), mercaptoethanol (blue), urea (dark green), Mix. 24h (light green), Mix. 48h (light blue), enzymes (pink), alkaline (violet), and alkaline dried (black). The Miller indices according to a monoclinic unit cell are reported.[72]

3.1.3. Mechanical characterization of treated squid pen

The mechanical properties of the samples were analyzed by uniaxial deformation tests. Slipping, early breakage, breakage at the grips, or inhomogeneity in data were not observed in the samples examined. The Young's modulus (E), maximum stress (σ_{max}), and maximum elongation (ε_{max}) that were calculated by the analysis of the stress–strain plots are summarized in Table 3 and plotted in Figure 48**.** These data show that the sample treated with 1 mM EDTA behaves as the pristine squid pen. The sample treated with 4 vol.% mercaptoethanol shows a reduction of E and σ_{max}, but did not change the ε_{max} with respect to the squid pen. The treatment with 8 M urea did not affect the ε_{max} and the σ_{max}, but reduced the E. The treatment with the Mix. 24h and Mix. 48h provoked a strong reduction of E and σ_{max} and an increase of ε_{max}. The treatment with enzymes was the most efficient in reducing E and σ_{max}, increasing ε_{max}. The sample treated with 1 M NaOH, Mix. 24h, Mix.

48h, and enzymes showed a similar E and ε_{max}, while σ_{max} was similar in the samples treated with NaOH, Mix. 48h, and enzymes.

When the sample treated with 1 M NaOH was first dried and then rehydrated showed an increase of the ε_{max} and σ_{max} with respect to the un-dried one, but did not change the E. The clustering of the results was checked using a T-test ($p = 0.05$, $\nu \geq 8$).

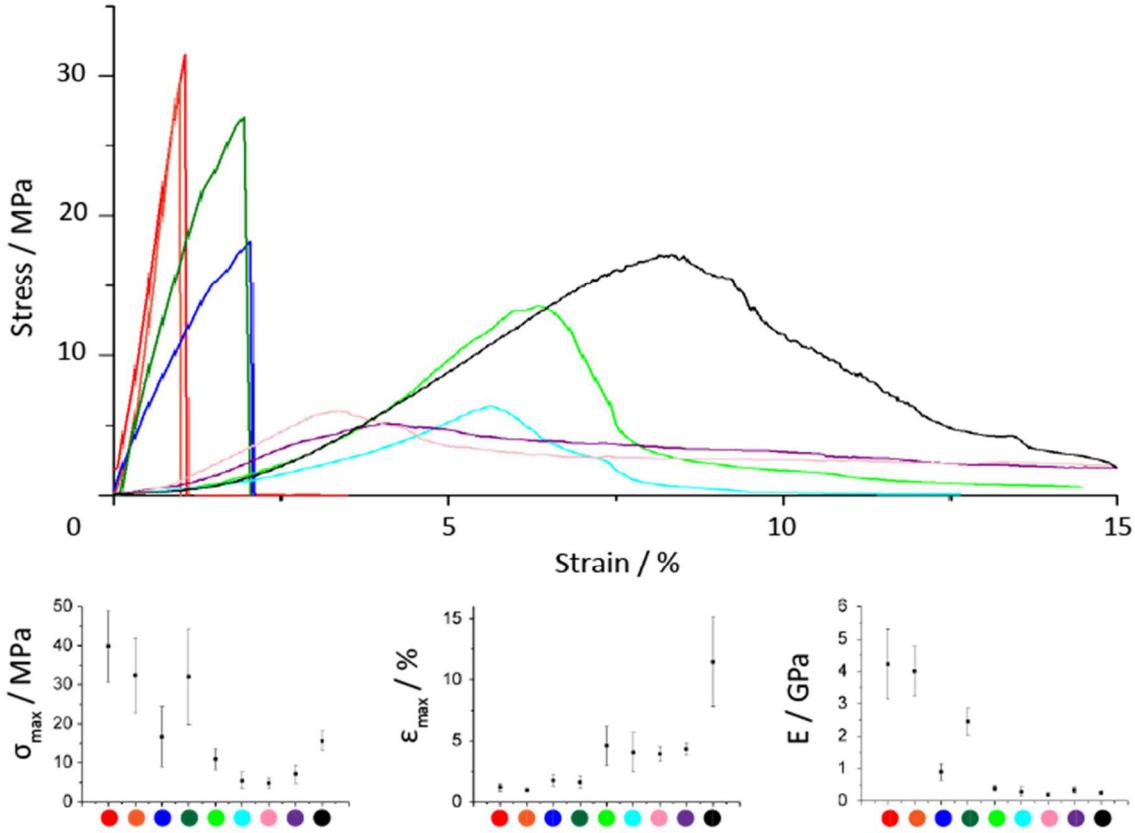

Figure 48: (above) Uniaxial traction profiles of the representative samples and (below) the mechanical parameters of uniaxial traction, maximum stress (σmax), maximum strain (εmax), and Young modulus (E). The data reported are relative to squid pen (red) samples and samples treated with 1 mM EDTA (orange), 4 vol.% mercaptoethanol (blue), 8 M urea (dark green), Mix. 24h (light green), Mix. 48h (light blue), enzymes (pink), 1 M NaOH (violet), and 1 M NaOH dried (black).

3.2. Discussion

The goal of this research is to investigate the role of proteins in determining the mechanical properties of natural chitin/protein composites. To our knowledge, no study has addressed this theme, despite the key role that these composites have in protecting organisms, and the number of organisms that use them. As model system squid pen was chosen because: (i) it is an examples of stiff bio-polymeric fibrous material, which have usually a Young's

modulus on the order of a few GPa and are not very extensible (ε_{max} < 20 %);[73] (ii) it is an almost pure binary chitin/protein composite; (iii) the proteins can be modified and/or removed without affecting the ultra-structure of the chitin matrix;[74] (iv) the structure of the chitin matrix has been deeply investigated;[2][74] (v) it is formed by aligned fibrils, so the uniaxial contribute of chitin is easy to identify; (vi) it is widely distributed, low cost, and commercially available.

The different chemical and enzymatic treatments were performed to change the structure or remove, partially or completely, the proteins present in the chitin matrix. Since the squid pen once was mineralized,[75] a way to modify the protein structure is to remove metal ions by chelating agents, EDTA.[76][77] Changes of the protein folding and interaction can be achieved by a denaturing agent (urea)[78][79] or a species able to reduce the disulfide bonds (mercaptoethanol).[80][81] A mixture of the above chemicals was used to extract proteins from matrices avoiding their primary structure degradation,[82][83] while the enzymatic[69] and alkaline treatments[74] are more efficient methods to remove by degradation the proteins from chitin samples. Successively the mechanical parameters of the samples were measured and compared with those of the native squid pen.

Urea was able to extract a small amount of proteins (about 6 wt.%) from the squid pen. This did not happen with the reductive treatment by mercaptoethanol or the removal of the metal ions by EDTA treatment. However, an efficient no-degradative time dependent removal of proteins from the squid pen was achieved when the chelating, denaturing, and reductive chemicals were used together (Mix. 24h and Mix. 48h). This suggests that the denaturating effect, and solubilization, of urea was efficient only when the disulfide bridge bonds (or eventually other oxidized chemical bonds reduced by mercaptoethanol) were broken by reduction.

The protein extract by Mix. 24h contained several proteins in a wide range of molecular weights, as shown by the SDS-PAGE data. The protein amino acid composition showed the presence of a low amount of cysteine, suggesting the formation of few disulfide bridges in key positions for the protein structure.

A relevant removal of the proteins from the squid pen was also achieved by enzymatic (41 wt.%) or alkaline treatment (60 wt.%). The alkaline treatment, being harsher than the enzymatic one, might have also provoked a loss of chitin material due to hydrolysis. In these samples no protein signals were detected in the UV-Vis and FTIR spectra, indicating a

complete de-proteination. The Mix. 24h and 48, instead, still showed a signal from protein residues suggesting that some proteins were covalently bonded to the chitinous matrix and unaffected by the mercaptoethanol reduction. This linkage might be amide moieties on the amino groups of chitin, as already reported in the literature for other composites.[84][85] They were cleaved only when alkaline or enzymatic treatment was used. Anyway, the chitin covalently linked protein matrix is a minor component in the pen composition.

All samples were further analyzed in their hydrated (or lyophilized) state, to preserve as much as possible their ultrastructure. The alkaline treated samples were additionally studied after drying and subsequent re-hydration, this was done to evaluate the properties of the pure chitin matrix once the fibrils were allowed to interact in dry conditions.

The results from the analyses of FTIR spectra and X-ray fiber diffraction patterns showed that the structure of the β-chitin matrix was preserved. Indeed, no differences were observed in the position of the X-ray diffraction peaks, and the position and profile of the chitin FTIR absorption bands.

The inter-fibril interactions should be controlled by the protein wrapping the chitin fibrils or by the interactions among the β-chitin fibrils when the proteins were removed. An intermedia scenario occurred when the proteins were partially removed. The inter-fibril interactions were estimated from the swelling data and the SEM observations. The swelling was not affected significantly (T-test, $p = 0.05$, $v \geq 3$) by the treatments with the EDTA or urea, suggesting that most of the inter-fibril interactions remained unchanged. This although some proteins (6 wt.%) were extracted by urea. The reductive breakage of the chemical bonds induced a slight increase of the swelling (~ 60 %) with respect to the one of the native pen, which became higher (~ 600 %) when most of the proteins were removed by the Mix. 24h, the Mix. 48 h, or the enzymatic treatment. The increase of the swelling was lower (~ 250 %) when the proteins were completely removed using the alkaline treatment, suggesting a higher interaction among the chitin fibrils.[69] All these observations were supported by the SEM observations on the sample's cross sections.

The mechanical properties of the squid pen samples were measured through uniaxial deformation along the pen main axis, since the material is highly anisotropic.[10] The removal of the salt bridges in the squid pen by chelation of the metal ions did not affect its mechanical properties. This may suggest that no structural salt bridges were present in the matrix, despite its vestigial role of shell.

The treatment with urea induced a decrease in the E (from 4 GPa to 2.4 GPa), even if it did not affect the swelling. The rupture of the chemical bonds by reduction caused a decrease of E (from 4 GPa to 0.9 GPa), as expected by the weaker inter-fibril interaction shown by the swelling data. The decrease in stiffness in the reduced samples might be due to two main contributes: i) the breaking of inter-protein disulfide bridges, which formed a cross-linked matrix where the chitin fibrils where embedded; ii) the breaking of structural disulfide bonds in the CBD which consequently decreases the protein-chitin interaction. In literature, the disulfide bridges in the CBD are reported as necessary for its correct folding, which is missing otherwise. This information was obtained through experiments with proteins in the solution.[17][18] In a solid and compact state, as in the matrix, the folding might be only partially affected by the disruption of the disulfide bonds leading to only a partial loss of binding. The urea treated samples might instead induce a loss of stiffness due to a potential denaturation of the structure at the inter-protein interface, creating a point of discontinuity in the structure. It is common for structural chitin-binding proteins to possess more than one CDB, so a single protein can bind more than one fibril. If that so, the denaturation would decrease the stiffness of the material due to an unfolding of the protein domain linking the CBDs.

The σ_{max} measurements showed a relevant reduction (from 40 MPa to 17 MPa) only when the disulfide bonds of the matrix were broken, or the CBD were unfolded, and the stress may act more on the single fibrils. The same order of magnitude of ε_{max} values suggested that this parameter was dependent more by the intra-features of the chitin fibrils than their inter-fibril interactions, and that the fibrils might undergo to a minimum sliding during the uniaxial deformation when the protein matrix is not removed.

The decrease of σ_{max} and E without an increase in the ε_{max} in the mercaptoethanol treated samples support the CBD unfolding hypothesis. In fact, in this scenario, the decrease in the binding between protein and chitin would imply a decrease in the first two parameters due to a lack of interaction without an increment in the elongation because of the loss of the CDB folding when the chitin fibril slide out of it. This would also explain why the combination with a reducing and a denaturing agent is necessary to undergo a proper protein removal.

The value of σ_{max} indicated that in the sample partially de-proteinized (Mix. 24h) the remaining proteins had interactions that affected the mechanical properties. Indeed, this

sample had a significantly higher value of σ_{max} with respect to the other protein free samples (T-test, $p = 0.05$, $\nu \geq 8$), but not of E and ε_{max}. However, these values of ε_{max} were significantly higher than that of the squid pen, indicated a sliding among fibrils, being the hindering effect of the proteins removed.

The enzymatic, the alkaline, and the Mix. 48h treated samples did not show significant differences in all their mechanical parameters, which could be due to the almost complete removal of the protein and the presence of the only almost pure chitin matrix. This suggests a convergent effect due to the lack of interactions between the chitin fibrils even at different degrees of swelling.

A significant increment in both σ_{max} and ε_{max} was observed in the alkaline treated samples once dehydrated and rehydrated. This extra step allowed the chitin fibrils to stack better generating stronger interactions, proving how the non-dehydrated alkaline treated sample had a lower interaction between the fibrils.

The presented considerations are supported by the data that the E of chitin nano-fibrils is more than 150 GPa.[86] This information agrees with the proposed general observation that the mechanical features of the samples are controlled by the inter-fibril interactions. Indeed, the ε_{max} values were low (1-5 %) and only in the sample of re-hydrated β-chitin reached the 11% value. Here, it can be supposed that since the chitin fibrils have a better stack, during the sliding, up to a certain extent, non-specific interaction points were broken and regenerated.

3.3. Conclusion

The squid pen of *Loligo vulgaris* is a chitin/protein natural composite that was used as a model system to study the influence of proteins on the mechanical properties. The latter was measured, together with other physical and structural properties, after modification of the inter- and intra-protein interactions or proteins removal from the squid pen. The treatment with a chelating agent did not modify the properties of the squid pen, meaning that no structural metal ions based bonds are present in the matrix. The use of the reducing agent mercaptoethanol showed how the squid pen properties widely rely on disulfide bonds, probably in both inter-protein interaction and CBD folding, to achieve its high E and σ_{max}. The overall analysis of the data from samples subject to different treatments allows concluding that the protein wrapping has a huge contribution in the E (> 90 %) and the σ_{max} (> 80 %) of the material. This is due to strong interactions that it establishes among the chitin fibrils avoiding their relative sliding. The data from dehydrated and rehydrated pure chitin samples showed that the chitin fibrils have a low interaction, highlighting as the protein matrix act as binder among the stiff chitin crystallites.

In conclusion, the proteins in the squid pen act as a stiff matrix that link crystalline chitin fibrils avoiding sliding, as would happen in a pure chitin material.

3.4. Materials and methods

Materials All reagents and solvents were purchased from Sigma Aldrich and utilized without any further purification. Squid pens from L. vulgaris were collected from a local market. Once hydrated, the lateral blades (Figure 49) were isolated, cleaned with abundant distilled water (carefully eliminating eventual residual tissues), ethanol 70 vol.%, distilled water to remove the ethanol, and then stored dry in a desiccator.

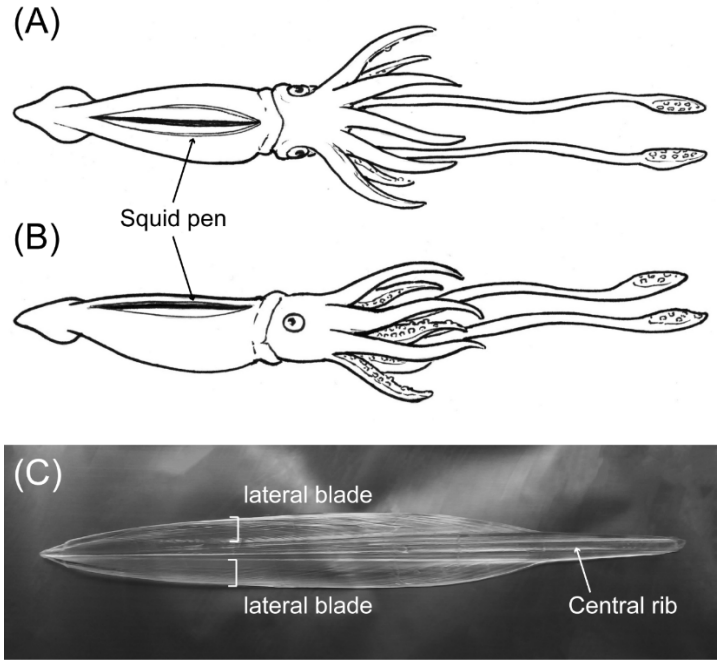

Figure 49: A schematic representation of a squid where the squid pen is illustrated even if, being an internal structure, is not visible from the outside of the animal. In (A) the squid is observed frontally while in (B) laterally. In (C) a camera picture of a squid pen.

Sample preparation All samples were prepared using the squid pens previously washed as described. The squid pens were set in a vial with a solution to get a squid pen/solution ratio of 10 mg·mL-1. The vial was then set on a rocking table for 24 h. The aqueous solvent tested were: 1) 1 mM EDTA; 2) 4 vol.% mercaptoethanol; 3) 8 M urea; 4) a solution with all the previous reported conditions, named Mix. All the solutions were shaken for 24 h except the Mix. that was also tested for 48 h, changing the solution after the first 24 h of treatment. After the different treatments, the samples were washed with water (using PremilliQ water for the samples treated with EDTA), left in water, and set on the rocking table for 15 minutes gently shaking the vials. After that, the solution was changed and the process repeated for a total of 6 times.

The alkaline treated samples,[74] instead, were obtained putting about 25 g of squid pen in 1 L of boiling 1 M NaOH solution, and stirring for 1 hour. Then, that solution was replaced with a fresh one and stirred under reflux for one hour more (counting the time from when the reflux restart). The obtained β-chitin was washed two times with a warm 1 M NaOH solution and then with distilled water until the washing water was neutral.
The enzyme treated samples were obtained as reported in chapter 2.[69] Briefly, the squid pens (1 g) were soaked in 100 mL of a pH 2 HCl solution containing 20 mg of pepsin (an aspartic protease). The mixture was placed on a rocking table for 24 h at 37 °C. After this first de-proteination, the squid pens were collected and washed carefully with distilled water. Then, the wet squid pens were soaked in 100 mL of a 100 mM phosphate buffer solution at pH 7.6 containing 20 mg of trypsin (a serine protease). As in the previous step, the mixture was placed on a rocking table at 37 °C for 24 hours. Finally, the samples then washed as previously reported. All the samples were stored in the water at 4 °C.

De-proteination weight lost and swelling measurements The measure of the chitin sample swelling in water was carried out first weighting a wet sample after the de-proteination, prior blotting it on a paper towel, and secondly weighting it after drying overnight in a desiccator under vacuum. The dry alkaline treated sample's swelling was measured weighting the dry sample before and after immersion for 24 hours in water. The weight loss due to de-proteination was determined by weighting the dry starting squid pens before and after the de-proteination process. Mass measurements were performed using a Sartorius CP225D (±0.01 mg) on at least 100 mg of initial dry sample. Both swelling and de-proteination weight lost measurements were performed at least on three independent samples.

Sodium dodecyl sulfate – polyacrylamide gel electrophoresis Polyacrylamide gel electrophoresis of SDS-denatured proteins was performed according to the description of Laemmli.[87] Protein samples were loaded on 12.5 % polyacrylamide gel and separated at a constant power of 120 V for about 90 min. The detection was performed using a staining solution with Coomassie Brilliant Blue R-250 (methanol 50 vol.%, acetic acid 10 vol.%, Coomassie Brilliant Blue R-250 0.25 wt.%). The excess of Coomassie was eliminated by washing with a de-staining solution (ethanol 25 vol.%, acetic acid 8 vol.% in water). Proteins

samples were prepared mixing different volumes of the sample with denaturating loading buffer (60 mM TRIS pH 6.8, SDS 2 wt.%, glycerol 10 vol.%, bromophenol blue 0.025 wt.%, and β-mercaptoethanol 2.5 vol.%). Samples were boiled 5 min before loading.

Amino acid analysis Amino Acid Analysis was performed in Xell (Germany) using a high-performance liquid chromatography (HPLC) system with an absorbance detector. A 6 M HCl solution was given to the dry sample and used for hydrolysis at 100 °C for 24 h. Then, sample was dried in vacuo over NaOH. The sample was resolved in 1 mL water, filtered and used for amino acid measurements. The depicted results were obtained by UHPLC-DAD on an Agilent 1290 system after the derivatization of amino groups. Two different System Suitability Tests (SSTs) were measured along with the samples to verify the calibration. Samples were measured in different dilutions. HCl hydrolysis converts of glutamine to glutamate and asparagine to aspartate.

Spectroscopic analyses UV-Vis spectra were collected between 240 and 450 nm with a 1 nm resolution, and an average time of 0.1 s using a Varian Cary 300 Bio spectrophotometer. FTIR spectra were collected using a Nicolet IS10 spectrophotometer. The samples were prepared as KBr disks and the sample concentration was about 2 wt.%. The spectra were obtained with 4 cm^{-1} resolution and 64 scans. Omnic software (Thermo Electron Corp., Woburn, MA) was used for data processing and baseline correction.

Scanning electron microscopy SEM images were acquired with a Philips SEM 515 using 15 eV. The wet samples were lyophilized, eventually cut with a scalpel to expose the section, glued on carbon tape, dried overnight in a desiccator, and coated with 20 nm of gold prior to image them.

Synchrotron X-ray diffraction analysis X-ray fiber diffraction patterns were collected at ID23 beamline, European Synchrotron Radiation Facility, Grenoble, France. Each frame was collected at the peak wavelength (0.87313 Å) using an exposure of 60 s. The X-ray diffraction patterns were analyzed using Fit2D software.

Uniaxial tensile test Monotonic uniaxial tensile tests were performed using a universal testing machine (Mod. 4465 with Series IX software, Instron) and dedicated grips. The tests were performed with an actuator speed of 5 mm·min^{-1} (resulting in a strain rate of about 0.3 %·sec^{-1}) at room temperature. Each wet sample was cut in a proper dimension using scissors before the de-proteination, maintained hydrated after the synthesis, and tested hydrated. The actual width and thickness of each hydrated sample were measured after the de-proteination using a SM-LUX POL microscope collecting images with a 5.0 MP digital camera (Motic Moticam 5+). The images were analyzed using ImageJ. Each sample was about 30 mm long, 5 mm wide, and 0.15-0.30 mm thick (the thickness varied between samples, because of the intrinsic variability of the initial biological samples). The samples were connected at the instrument, leaving a free length of 20 mm between the clamps. As the curves were rather linear until failure started, the following parameters could be calculated, taking into account the actual dimensions of each specimen:

- The Young modulus (E) of elasticity;
- The maximum stress (σ_{max}) and strain (ε_{max}).

At least five specimens were tested for each group.

4. Characterization of the internal shell of Ariolimax californicus

4.1. Results

The IS from *A. californicus* is a thin ovoid film, slightly concave ventrally. It is usually 13.7 ± 0.7 mm length and 8.0 ± 0.7 mm width in organisms of 10 ± 1 cm length. Anatomically, it is located inside the mantle right behind the kidney which is directly connected to the aorta, Figure 50 A-B and Figure 51 A.

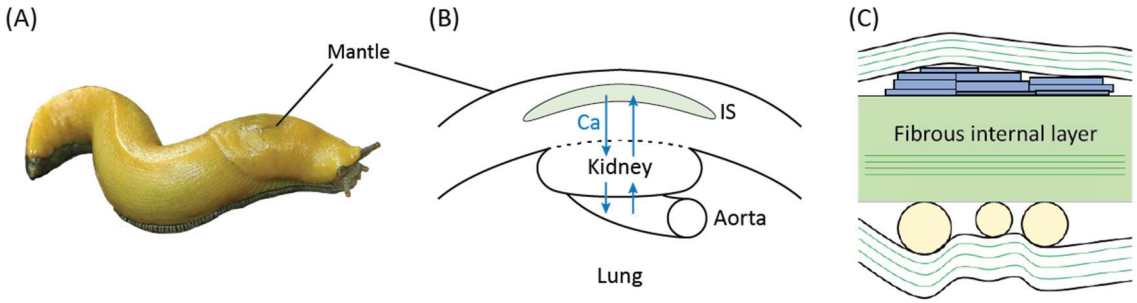

Figure 50: (A) A picture of A. californicus. (B) a schematic representation of the anatomical position of the IS. (C) A schematic representation of the section structure of the IS, as dark green lines are reported the chitin layers in the structure.

The observation of optical images of shells and shell's sections reveal the presence of three distinct layers in this matrix, a dense inner layer (about 50 - 100 µm) and two outer membranes (about 2 µm each) having gel features. The observation of the topography of the faces of the IS shows the presence of concentric lines (Figure 51 C). After a Calcofluor White (CW) staining, a stain specific for chitin, used to detect chitin presence, those concentric lines appeared to be composed of chitin, Figure 51D. As illustrated in Figure 51 E-F, a CW staining on an IS section showed how all the three layers of this matrix contained a substructure of parallel chitin-rich layers. Those layers appeared more concentrated in the dense inner layer than the external ones.

FTIR and XRD measures on a non-calcified sample showed only a clear β-chitin pattern (Figure 52). Despite that, after an overnight 1 M NaOH treatment at room temperature the dry sample lost 73 ± 5 wt.% and was stable for 24 h of additional treatment. The IS also showed a swelling of 550 ± 50 wt.%.

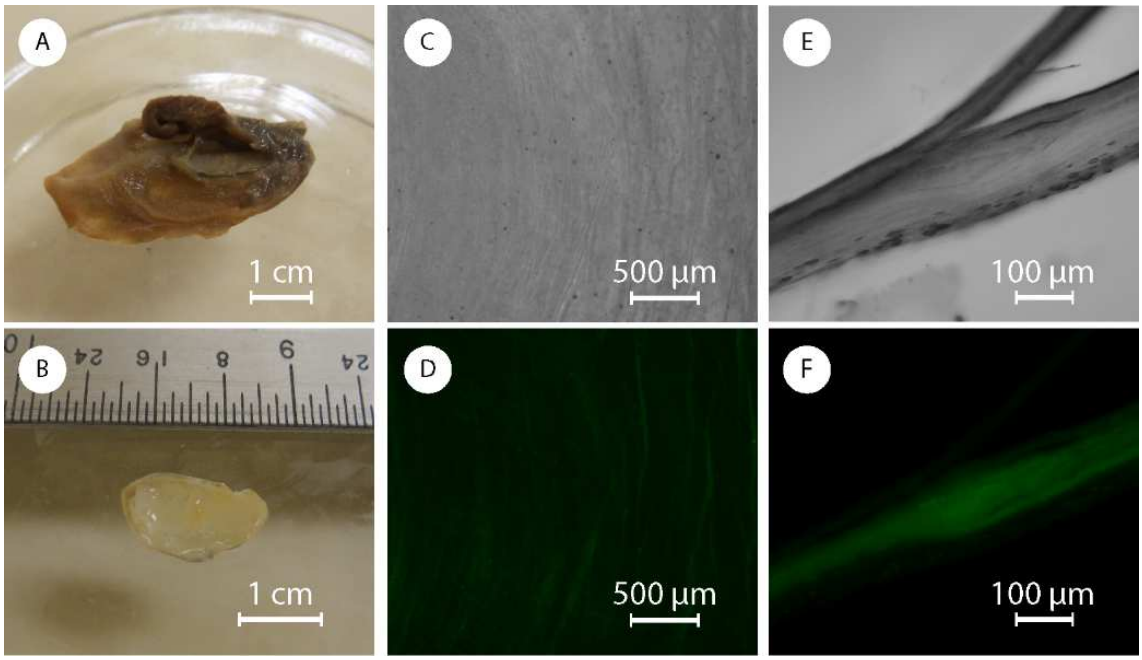

Figure 51: (A) Picture of a dissected mantle with an incision between the IS and the kidney. (B) Picture of an IS. IS sample stained with CW: (C and D) image of the surface, (E and F) image of a sagittal section. Both the images have been reported in optical microscopy and fluorescent microscopy.

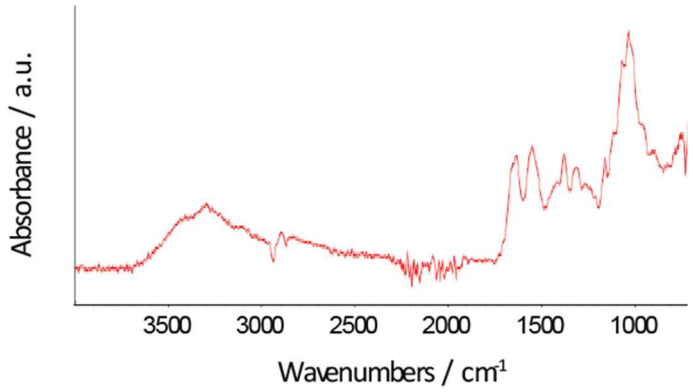

Figure 52: FTIR spectra of a decalcified internal shell, showing a typical pattern of β-chitin. A control sample for both chitin polymorphs is reported in Figure 59.

The IS was observed to be mineralized on both the faces of the shell between the outer membranes and the dense inner layer. The crystals on both the sides showed calcite signals in the XRD patterns and in the FTIR spectra (Figure 53), however the ventral face, the one exposed internally to the animal's body, showed additional FTIR signals that were associated to amorphous calcium phosphate. A sample among the biggest crystals present

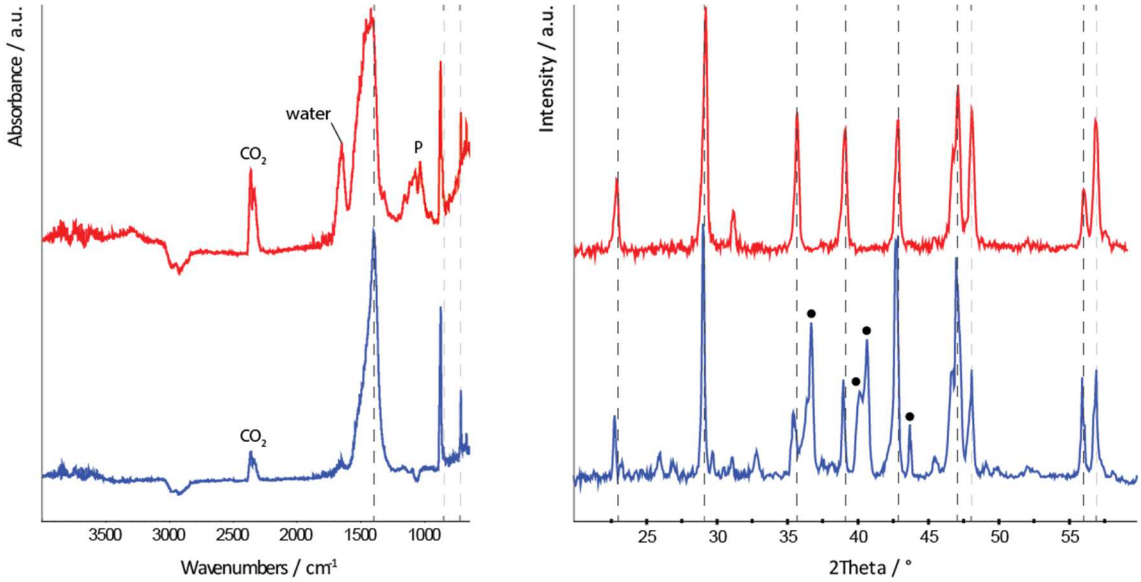

Figure 53: (on the left) FTIR and (on the right) XRD of the two crystalized faces of the IS (ventral face in red, dorsal face in blue). Calcite signals are marked with dotted lines, a black circle mark some signals due to the XRD holder, and in the FTIR some signals due to gasses are reported (except P, which might be due to a little amount of inorganic amorphous calcium phosphate).

on both faces was mechanically detached and analyzed by single crystals X-ray diffraction. The indexing of the diffraction spots produced the unit cell of calcite.

Optic and SEM observations of both faces of a calcified region of the IS show many morphological differences on the two faces. On the dorsal face, the one exposed externally to the animal's body, the membrane appears thinner and after dehydration collapses in a more compact material, Figure 54 C-D. Instead, on the ventral face the membrane appears thicker and collapses in a less compact structure, Figure 54 G-H. As reported in Figure 55, both the membranes appear formed of layered fibrous structure, Figure 55 C-D. Coherently with what observed with CW staining, the dense inner layer shows fibrous layers packed one on the other, Figure 55 B.

Along with two different membranes, two different crystal morphologies can be observed. On the dorsal face the crystals grow in a lamellar structure of variable layer thickness (380 ± 150 nm), Figure 54 A-B. Those crystals appear highly interconnected forming a single crystalline layer in highly crystalized ISs. The ventral face, Figure 54 E-F, shows instead spherulites of some tens of microns of diameter, those poly-crystalline aggregated appear mostly isolated and even in highly calcified IS regions is still possible to distinguish single aggregates.

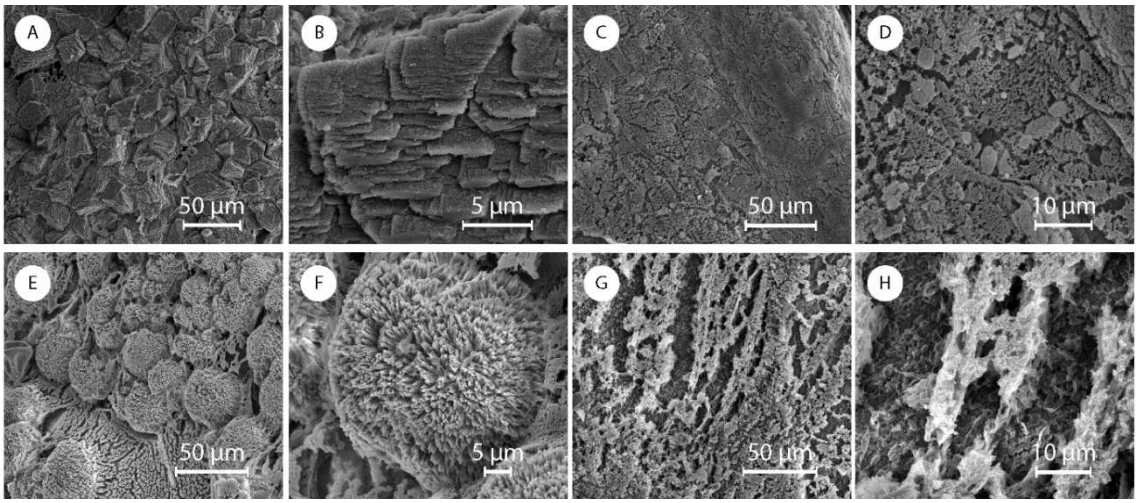

Figure 54: (A-D) SEM images of the dorsal face of the IS. (A and B) Images of a crystalized area. (C and D) Images of the membrane. (E-H) SEM images of the ventral face of the IS. (E and F) Images of a crystalized area. (G and H) Images of the membrane.

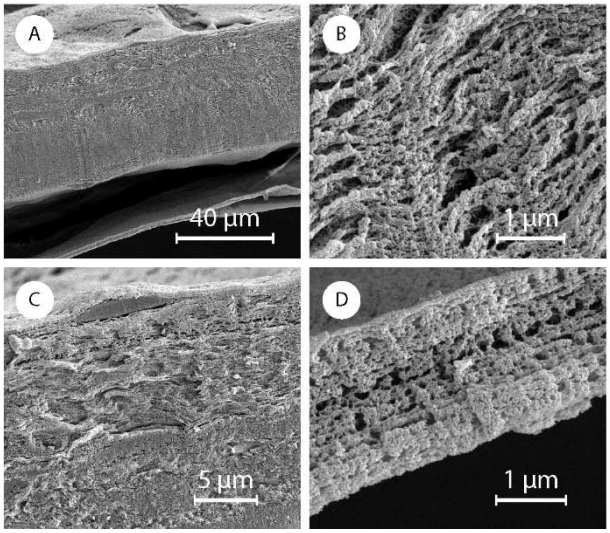

Figure 55: (A) SEM image of a fixed IS section with magnification on the (B) dense inner layer, (C) the dorsal membrane where a growing crystal can be observed, and (D) the ventral membrane.

An *in vitro* crystallization experiment was carried out using ISs decalcified using an acetate buffer at pH 4 overnight at 4 °C. At the end of the experiment the crystals were observed using SEM on both the faces of the IS and at the bottom of the same well to understand the influence of molecules released in the environment during the crystallization, Figure 56. Using a 10 mM concentration of calcium ions in solution a change in the morphology of the crystals was observed on two of the three edges of the crystals while no significant changes were observed on the crystals developed outside the IS. The crystals in the control experiment were about double the dimension of the crystals in the well with the IS. Using

an initial 100 mM concentration of calcium the morphology of the crystals on the two IS faces appeared rather altered compared to the control experiment. Despite the differences in morphology were analogue, the crystals on the dorsal face presented a less aligned development of their layers compared to the one on the ventral face. Both the faces presented a second morphological phase with a spherulite appearance that was not found in the control experiment or at the bottom of the well. Outside of the IS the crystals developed similarly as on the IS but with less marked morphological changes, a wrinkled surface was observed. In both the concentration studied the ventral face presented more crystals than the dorsal face and the crystals appeared to nucleate inside the matrix and then broke the external layer along their growth. This phenomenon is visible in the insight of the ventral face in the 10 mM condition where the external layer of the IS is still glued with the crystal. In the dorsal face image at 10 mM some breaking points in the membrane were crystals developed are visible.

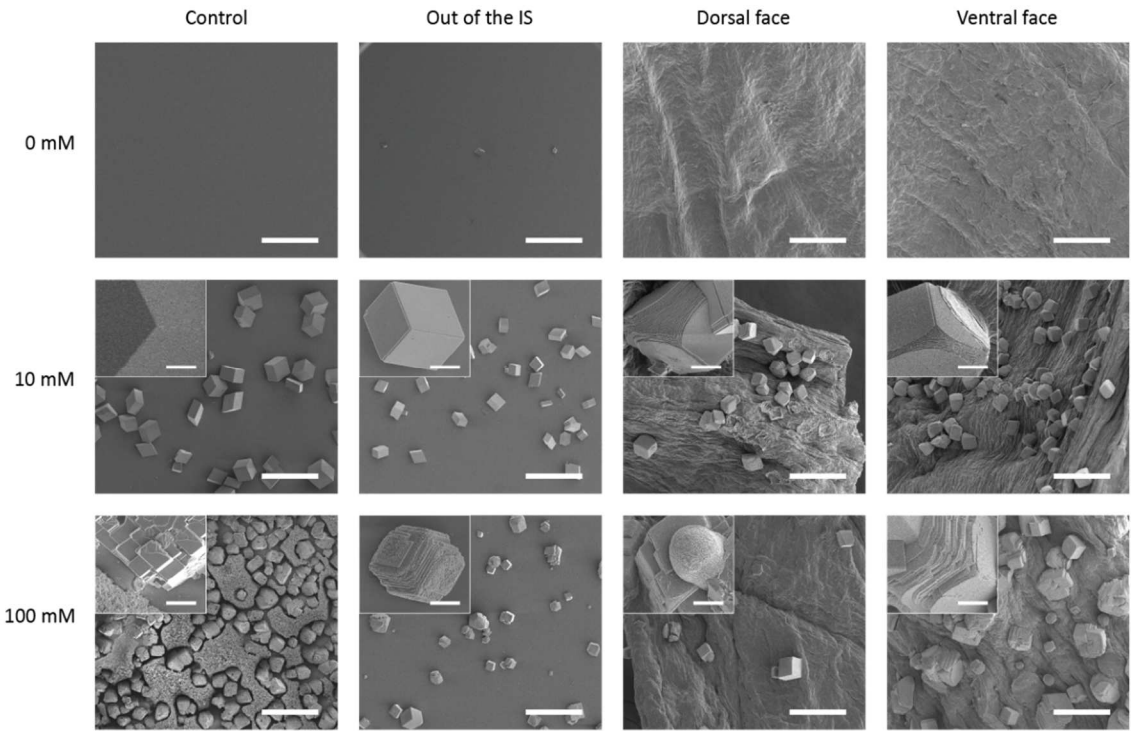

Figure 56: SEM images of the in vitro crystallization at different concentration of $CaCl_2$. For each condition the images were collected in a control experiment without IS, and in a well with an IS. In this last well the crystals were observed on the two faces and at the bottom of the well. For each condition presenting crystals a low magnification image (scale bar 200 µm) and a high magnification image (scale bar 10 µm) are reported.

4.2. Discussion

As reported by Meenakshi & Scheer in 1970,[39] *A. columbianus'* internal shell was observed to calcify and decalcify during the slug's life cycle. Based on this observation, this study proposes this matrix as a calcium storage system for the animal.

For an availability reason, this study was carried out on *A. californicus* that is genetically closely related and exhibits similar features. In this species the hypothesis that the IS works as a calcium storage structure finds a base on its anatomical position. The IS was observed to be located right behind the kidney, an organ strictly bounded to the aorta and related to excretion and blood filtration. The proximity of the IS may regulate the physiological equilibrium of calcium ions among the aorta, the kidney and the IS (Figure 50). The latter may act as calcium source or calcium storage substrate on the base of the animal needs.

The organic layers of the IS are mainly composted of materials removable by alkaline digestion (around 75 wt.%) and β-chitin. The presence of β-chitin has been widely observed in calcium carbonate tissues and thus can have a role in favoring the calcification of the IS. The β-chitin mapping with CW showed a concentric structure on the IS. Those lines are probably growing lines, showing how in each growth step a new layer of chitin is deposited. In an IS section chitin fibers are organized in parallel layers in the dense inner layer and in the two outer membranes. In the former, the fibers are densely packed and highly cross-linked as shown by the SEM observations. On the other hand, the membranes appear to be fibrous based too, but a low density of crosslinking is observed.

The calcite crystals show two complete different morphologies on the two IS faces: spherulites and lamellar crystals. This diversity leads to a difference in exposed surface. The lamellar morphology has a lower exposed surface due to its structure and the compact packing of the lamella. Contrary, the spherulites having a radial needle structure, expose a high surface even when densely packed. The little amount of calcium phosphate detected using FTIR spectroscopy might be due to a contamination of the matrix from the phosphate-buffered saline (PBS) treatment used to rehydrate the animal before dissection.

The *in vitro* crystallization experiment showed how the matrix is able to nucleate crystals right below the surface, presumably between the membrane and the internal layer. Looking the crystals at the bottom of the well, the influence of the matrix on the morphology was mainly due to the substrate and not to proteins released by it. It has to be considered that those might have been lost during the decalcification process. Those

proteins, anyway, might have a role in controlling the growth rate of crystals. In fact, those crystals presented dimensions similar to those on the IS but lower compared to the one in the control experiment. Moreover, the ventral phase appeared to nucleate more crystals compared to the dorsal one.

In the view of the starting hypothesis of this study is important to highlight that the spherulites are embedded in the thick, but sparse, gel matrix on the ventral face of the IS. These spherulites could act as a fast access calcium reserve, that quickly exchange calcium through the membrane, allowing the animal to access this reserve for daily life necessity. This hypothesis is also supported by the ability of that face to nucleate more crystals. Differently, on the other side the low exposed surface lamellar crystals are located in a relatively denser membrane, which probably allows a lower calcium ions trafficking and a lower nucleation density. Thus, it can be proposed that the calcium carbonate into this other face could act as a long term calcium reserve for slow, but high calcium demanding events, like egg deposition. The high density of lamellar morphology crystals may also guarantee a better protection for the animal, while not used as calcium reserve.

4.3. Conclusion

In this research morphological and compositional studies of the internal shell of *A. californicus* were performed. The results show how this matrix crystalizes calcite in two complete different morphologies on the two IS faces. On both faces the nucleation occurs at the interface between the dense inner layer and the outer membrane. The first one is a dense fibrous layer, probably responsible for the crystal nucleation control. The second one, instead, is in a fibrous gel state and is probably responsible of the morphology and growth control of the crystals.

The two crystals morphology have a very different exposed surface. We theorize that the two morphologies evolved one as a fast-access calcium reserve and the other as a slow-access calcium reserve.

The results reported are completely new on the topic background. The discovery of a bi-morphological dynamic biomineralized structure represents a novelty in biomineralization studies and opens an innovative aspect of the response of calcified tissues to the environment.

4.4. Materials and methods

Sample preparation The material used in this study was derived from a laboratory population of slugs collected at Purisima Redwoods, Half Moon Bay, CA. The slugs were maintained in the lab using a protocol previously described.[88] After natural death, we froze the animals for storage and future handling and kept them in a commercial freezer. We collected the IS by dissecting frozen animals after slowly rehydrating them in phosphate-buffered saline (PBS) at 4 °C overnight. Once collected the sample was rinsed with distilled water and stored in distilled water at 4 °C.

Swelling measures The sample swelling was measured weighting a pristine not calcified sample, then weighing it again after dehydration in a desiccator and again after 24 and 48 hours of rehydration in distilled water, prior blotting on filter paper. Every measure was performed three times. All the hydrated measures showed comparable weight.

Weight loss in NaOH An IS dried in a desiccator was weighted, then it was weighted again after soaking it in a freshly prepared NaOH 1 M solution after 24 h and 48 h, prior washing with distilled water and drying in a desiccator. Every measure was performed three times.

Fourier Transform Infrared measures FTIR spectra were recorded using a Bruker Vertex 70 FTIR spectrometer equipped with a diamond crystal ATR accessory. The spectra were collected in the 4000-400 cm^{-1} range with a 4 cm^{-1} resolution and analyzed using OPUS.

X-ray diffraction analysis XRD patterns were collected using a PanAnalytical X'Pert Pro equipped with X'Celerator detector powder diffractometer using Cu Kα radiation generated at 40 kV and 40 mA. The diffraction patterns were collected within the 2θ range from 4° to 25° with a step size (Δ2θ) of 0.05° and a counting time of 100 s. Single crystal data were collected at RT (300 K), on an Oxford XCalibur S CCD diffractometer equipped with a graphite monochromator (Mo–Kα radiation, λ = 0.71073 Å).

Optic and fluorescence microscopy Sample sections and the samples reported as fixed were treated with glutaraldehyde 2,5 vol.% in PBS at 4 °C for 16 hours, washed with PBS, eventually sectioned using a Leica CM3050S cryo-microtone in 50 µm sections embedding

them in O.C.T. Compound by Tissue-Tek, then washed with water and eventually stained before the analysis. CW staining was performed putting a drop of stain on the sample and a drop of KOH 10 wt.% on the sample, waiting 1 minute, and washing away the stain in excess with water. Optical images were acquired using a Keyence VHX-5000 microscope while fluorescence images were acquired using a Keyence BZ-X710. A green fluorescence protein filter was used on CW stained samples.

Scanning electron microscopy images All samples were treated with glutaraldehyde 2,5 vol.% in PBS at 4 °C for 16 hours, washed with PBS, eventually sectioned using a Leica CM3050S cryo-microtone in 50 µm sections embedding them in O.C.T. Compound by Tissue-Tek, then washed with water, fixed using an alcohol gradient (from 10 – 90 vol.% every 10 vol.%, then 95 vol.%, pure ethanol, and two times using pure methanol), critically point dry using methanol/carbon dioxide exchange, mounted on a SEM stub with a carbon tape, and coated with 20 nm of gold. SEM images were acquired using a FEI Quanta™ 3D.

In vitro crystallization experiment The experiments were carried out using a vapor diffusion technique. In this technique $CaCO_3$ formation is induces diffusing CO_2 in a closed environment by slow decomposition of $(NH_4)_2CO_3$. The IS used in this experiment were decalcified soaking them in an acetate buffer 50 mM at pH 4 overnight at 4 °C. Each IS was set vertical in a different well of a multiwell plate with 2 mL of $CaCl_2$ solution and a glass slide at the bottom. 0 mM, 10 mM, and 100 mM calcium concentration were tested in double along with a control experiment with no IS. The multiwell prepared was covered with alumina and each well was pierced once to allow vapor diffusion. The multiwell was then set in a desiccator with three Petri dishes of 5 cm of diameter full of i) $CaCl_2$ decahydrate, ii) $(NH_4)_2CO_3$, and iii) $CaSO_4$ anhydrous. The system was kept closed for 72 h. At the end of the experiment each IS and glass slide was washed three times with ethanol, two times with water, and again one more with ethanol before being prepared for SEM observation.

5. Characterization of acellular matrices in the buccal mass of *Ariolimax californicus*

5.1. Results

We dissected several different specimens of *A. californicus* (Figure 57 A) to analyze the anatomy of the buccal mass (Figure 57 B).

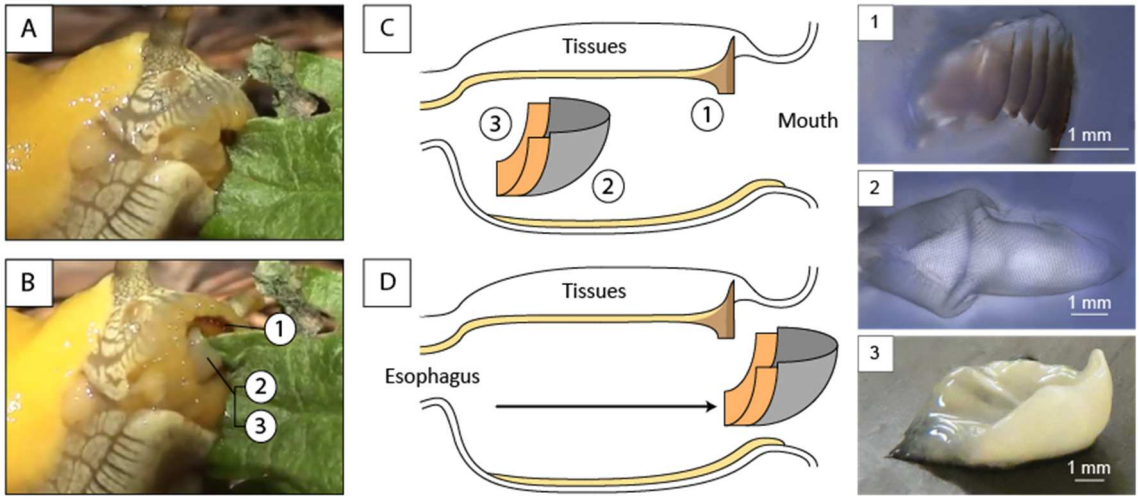

Figure 57: Representation of the acellular components in A. californicus buccal mass. (A-B) A picture of a banana slug, while approaching and biting a leaf, and (C-D) a schematic representation of the buccal mass in the same moments. In the scheme we reported the three structures (1) the jaw, shown in the scheme as the brown region while the foregut cuticle is shown in yellow; (2) the radula; (3) the odontophore, dissected out of the surrounding tissues.

In the buccal mass (Figure 57 B) the jaw, the radula, and the odontophore were identified. The jaw is an anterior stiff brown line of tooth-like structures located behind the upper lip and appeared directly connected with a tunnel-like structure, which covers most of the internal walls of the buccal mass and the esophagus (Figure 58 A-B) similarly to the peritrophic membrane of insects,[89] we will refer to this as the foregut cuticle. The jaw appeared to gradually convert into the foregut cuticle. In *A. californicus*, the radula appeared as a rectangular transparent membrane with a triangular end on the short edge below the odontophore, similarly to other mollusks like limpets[56] or chitons.[58] This transparent membrane carries many denticles on the outer face. In the dissection, we observed the radula lying on top of the odontophore. The odontophore is shaped as a distorted semi-hemisphere and is mostly covered by the radula. While the radula and the

jaw are relatively easily separated from the surrounding tissue, the odontophore was strongly connected to the tissue on the edges not covered by the radula (Figure 57 B). We qualitatively observed the jaw, radula, and odontophore working collectively in a living slug observing the slug while eating, Figure 57 A-D. During the feeding process, the radula and the odontophore form a structure that scrapes the food by sliding out of the buccal mass to grab a bite. The slug than pinches the food between the jaw and the radula allowing the radula to bite off smaller pieces of food.

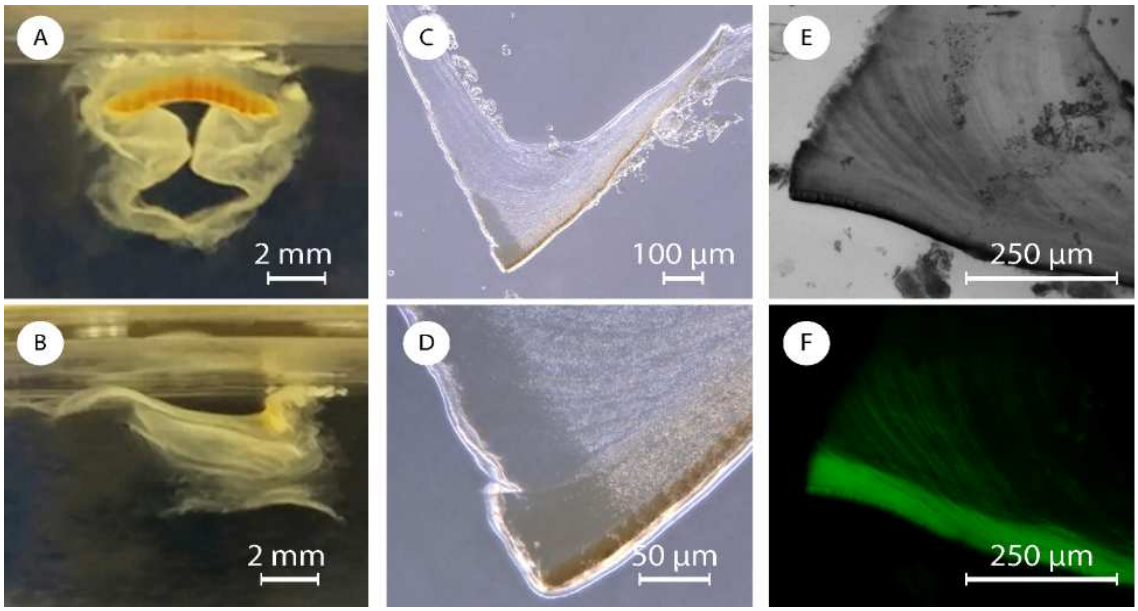

Figure 58: Picture of a jaw in water from the (A) frontal and (B) lateral point of view. (C and D) Optic images of a section of jaw at two different magnifications. Fluorescence microscopy images in (E) bright field and (F) dark field of a section of jaw stained with CW.

As part of a more in depth characterization of the jaw (Figure 57 C), from analysis of the FTIR spectra, we identified, chitin as a major component of the jaw and the foregut cuticle. The presence of chitin was also confirmed by staining with CW (Figure 58 E-F). In the FTIR spectra all the absorption bands observed were related to chitin's vibrational modes (Figure 59). These data did not allow us to precisely discriminate between α- or γ–chitin polymorphs[91][70] (the latter commonly observed in peritrophic membranes[89]). Chitin is white or colorless as a pure material, the jaw, however, is brown (Figure 60 A). This coloration might arise from pigmentation, sclerotization, mineralization, or be due to chitin-binding proteins. We performed an energy-dispersive X-ray spectroscopy (EDS) -SEM on the jaw and did not find any substantial quantities of minerals, such as iron oxide, which

may result in brown coloring. To identify the presence of sclerotization, which is usually due to the polymerization of catechols, we used the Arnow's assay, a colorimetric assay, which gave a negative result. Overnight HCl 1 M treatment or 2 hours in NaOH 2 M at 80 °C resulted in no color change suggesting that structural proteins, usually hydrolyzed in those harsh conditions, or acid soluble materials might not be responsible for the color.

In images of a longitudinal section (Figure 58 C-D) of the jaw, we found that the brown structure included a darker layer of 13.8 ± 0.6 µm, in the anterior region. This layer becomes lighter inside the tooth-like structure of the jaw and then gradually fades into the foregut cuticle. The SEM images shown in Figure 60 show the microstructures present in the jaw. The jaw corresponds to the area highlighted in Figure 60 B and is composed of irregular ovoid micro/nano-particles with a length along the longitudinal axis of 800 ± 300 nm. These particles are densely packed and connected by a network of nanofibrils. In the darker anterior layer the particles appear denser, larger, interconnected, and with few or no nanofibrils. This external layer is more homogeneous and we were not able to measure effectively the dimensions of the particles. To provide further insights on the nature of this coloration, we collected both back- and forward-scattering spectra in dark field and the results showed an asymmetrical peak between 400 and 850 nm with a maximum between 550 and 600 nm (Figure 61). Moreover, SEM observations of the jaw (Figure 60 A) showed parallel grooves, 41 ± 5 µm apart, starting after the tooth-like structure.

CW staining of chitin in a jaw section indicates the presence of a micrometric fibrous structure (Figure 58 E-F). In the jaw these fibers are initially parallel to the jaw's anterior layer (perpendicular to the long axis of the animal), this layer is observed as a dense fluorescent area, and then, while moving towards the esophagus, tend to bend. In the foregut cuticle, those fibers, still connected to the fibers in the jaw, are parallel to the internal wall of the buccal mass. Moving from the brown region, the jaw, to the white one, the foregut cuticle, along the internal wall of the buccal mass, we observed the nanoparticle structure gradually disappear until it is completely replaced by a randomly organized nanofibrous carpet, as can be observed in Figure 60 B-D. In Figure 60 C a sample crack showed an outer layer of random organized nanofibrils that come from a thicker internal layer of perpendicular nanofibrils.

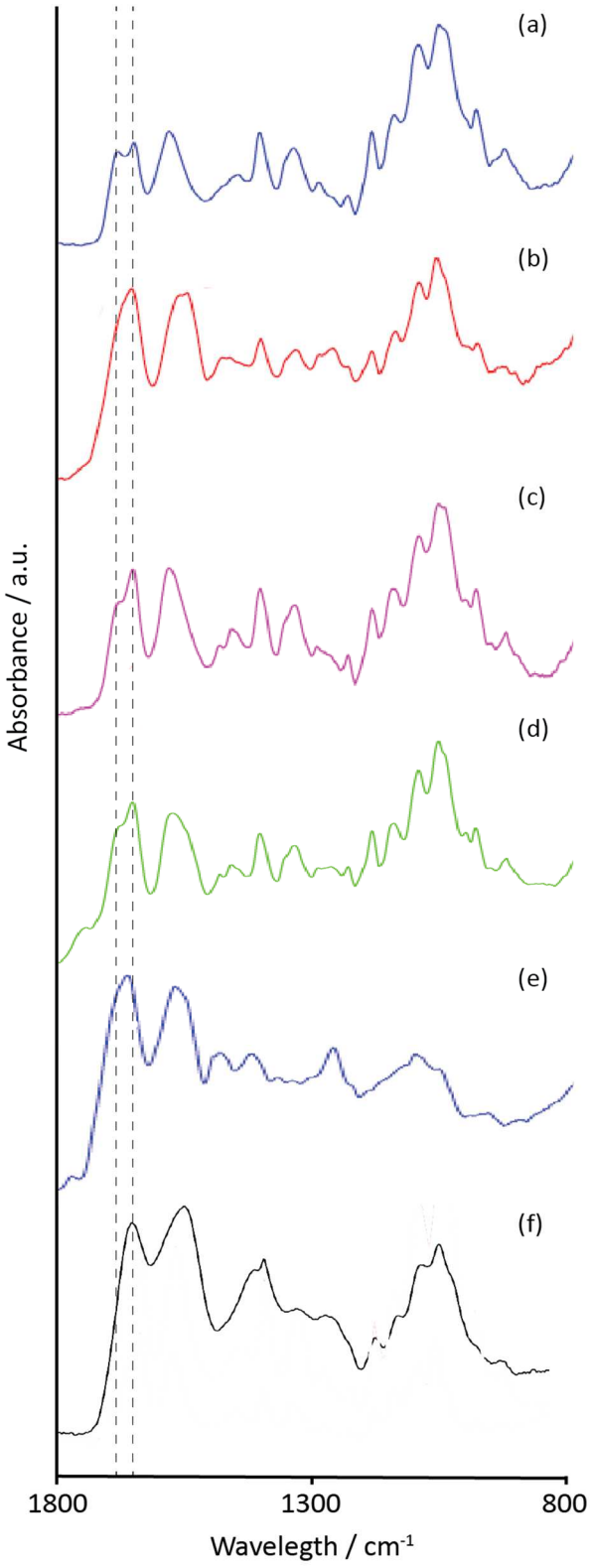

Figure 59: FTIR spectra of (a) α-chitin, (b) β-chitin, (c) the foregut cuticle, (d) the jaw, (e) the odontophore, and (f) the radula. The assignment of the absorption band was done according to literature.[70] *As can be observed, β- and α-chitin differ at the amide signal at ≈1600 cm*$^{-1}$*. The signal presents a single maximum in β-chitin and two maximums in α-chitin for the amide signal; in γ-chitin the two maximums appear of different intensity while usually in α-chitin they have comparable intensities.*[90]

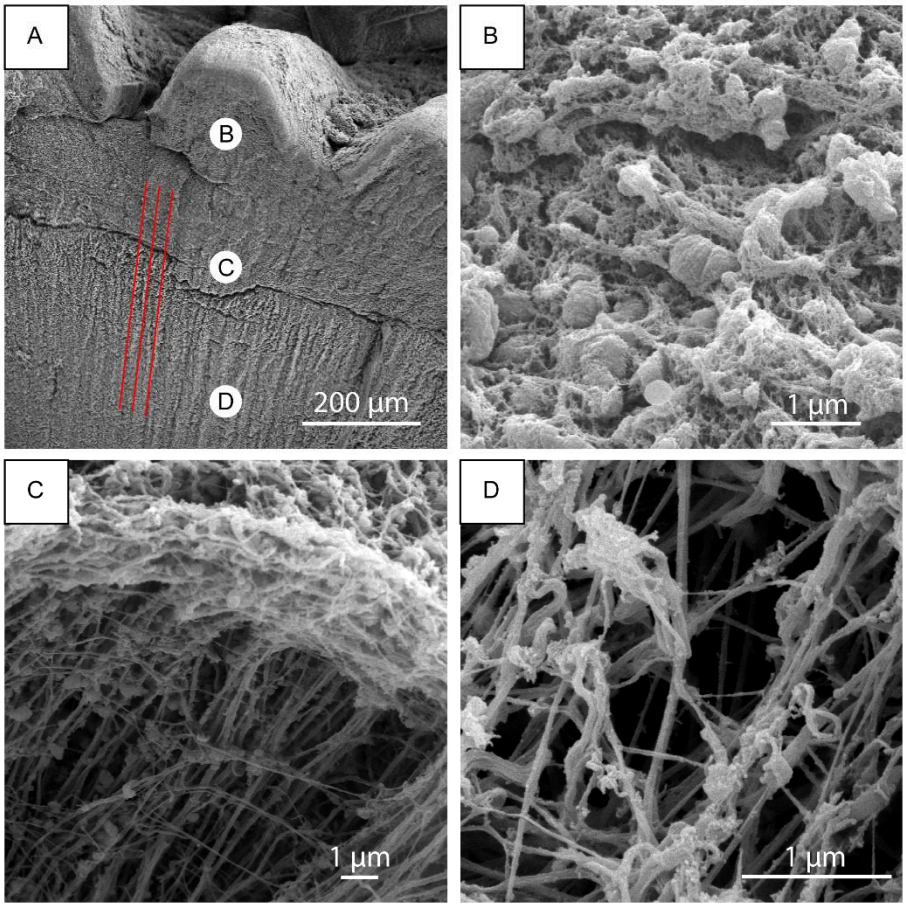

Figure 60: SEM analysis of a jaw. (A) SEM images of a jaw treated in NaOH 1 M; red lines highlight the parallel grooves observed in the foregut cuticle. (B) The nano-particles at a higher magnification, (C) a crack of the structure where the perpendicular nanofibers and few particles can be observed, and (D) the nanofibrous carpet

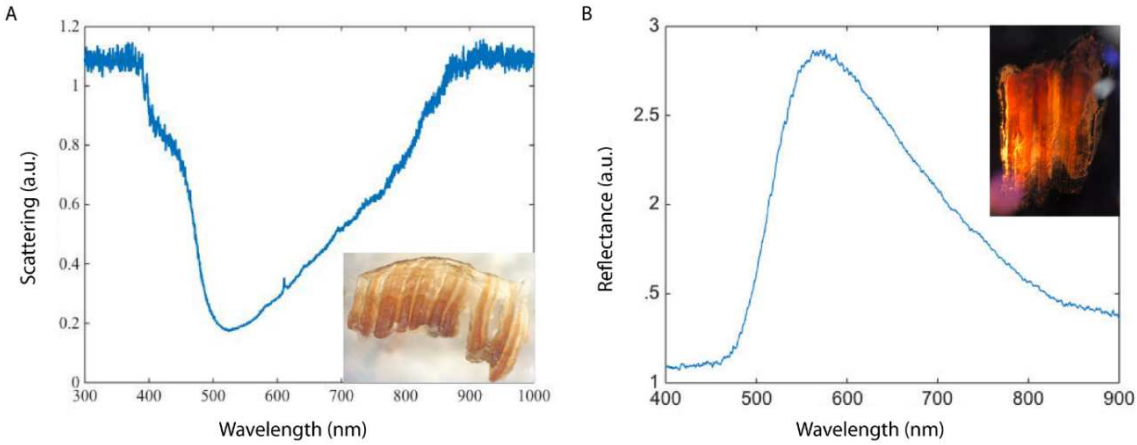

Figure 61: (A) Dark field back-scattering spectra and (B) dark field forward-scattering spectra of the jaw. For each condition, an image of the analyzed jaw is reported.

We then analyzed the structure and composition of the radula (Figure 57 D).

The radula is composed of hundreds of denticles packed in rows (~150 denticles per row). Radular ribbons are bilaterally symmetrical structures where the central tooth, called a rachidian tooth, is flanked by an equal number of teeth on each side. Because of this, denticles have different morphology depending on their position in the radula. Proceeding laterally from the rachidian tooth, denticles increase in aspect ratio (from 1.7 ± 0.3 to 2.9 ± 0.8), length (from 75 ± 9 µm to 93 ± 8 µm), and inclination relative to the membrane (from 37 ± 3 ° to 22 ± 1 °). In 1874, Binney[54] classified these denticles depending on their morphology into two groups: a) central denticles (Figure 62 A-C), with the rachidian tooth as a specific example, with lower aspect ratio and length, and higher inclination; and b) lateral denticles (Figure 62 E-G), exposed on the radula's sides, with higher aspect ratio and length, and lower inclination. The transition between the two types of denticles occurs gradually across ~10 denticles. FTIR and XRD analysis showed that the radula is mainly composed of β-chitin, Figure 59.[91] SEM and EDS-SEM analysis instead, highlighted the presence of a minor calcified mineralized phase only in the denticles with a calcium signal of about 10 wt.%. This mineral phase was not detectable using FTIR, XRD, or micro-Raman spectroscopy. In order to define the chitin micro-structure, we stained a longitudinal section of the radula with CW (Figure 63 A-B). The signal from CW indicated no chitin microstructure in the radula, and a more intense chitin signal was observed in the denticles compared to the membrane. The membrane is composed of an intricate network of nanofibrils with diameter of 300 ± 100 nm (Figure 63 C-D) arranged in layers (Figure 63 E-F). These nanofibrils, likely made of chitin, preferentially run longitudinally to the radula. An additional fibrous matrix between the larger fibers was dissolved after treatment in NaOH 1 M at room temperature suggesting that this matrix may be made of proteins. After a urea/hexafluoroisopropanol treatment to weaken the membrane, we collected individual denticles and imaged them with SEM. The central ones, Figure 62 C, did not show any specific anchoring feature. We measured the anterior to posterior distance of the base of these isolated central denticles to be 76 ± 4 µm. When assembled in the radula, the base is 55 ± 4 µm, indicating that there is a certain degree of overlap as sketched in Figure 62 D. Lateral denticles (Figure 62 G) had a different morphology with a hook on the anterior side of the denticle and a tiny posterior gap. Observation of some radula sections showed how

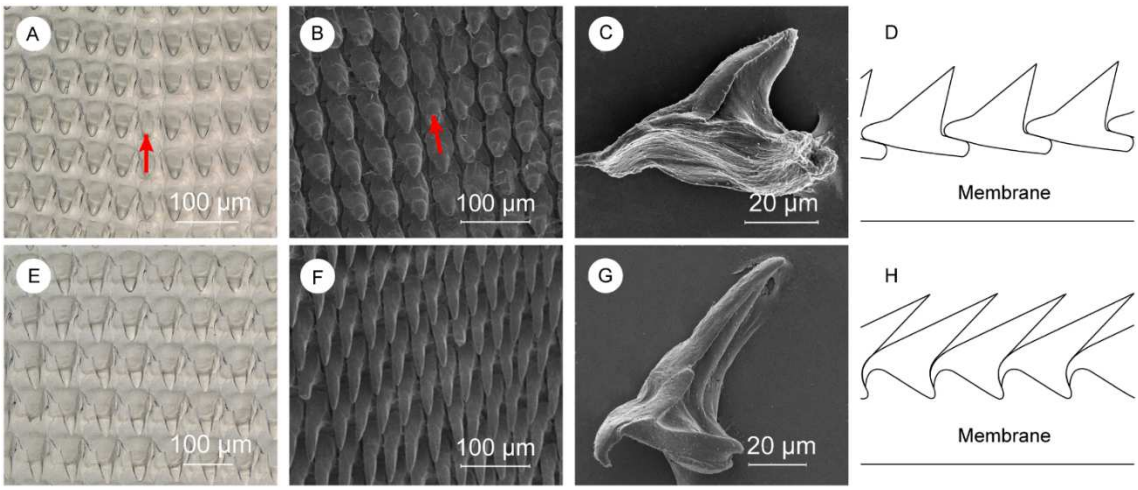

Figure 62: Description of central and lateral denticles. (A and E) Optical microscope images of central, and lateral denticles. SEM images of (B) central denticles, (F) lateral denticles, (C) a single central denticle still showing some fibrils on the base, and (G) a clean single lateral denticle. Schematic representation of the (D) central, and (H) lateral denticles' packing. Red arrows indicate the rachidian tooth where visible.

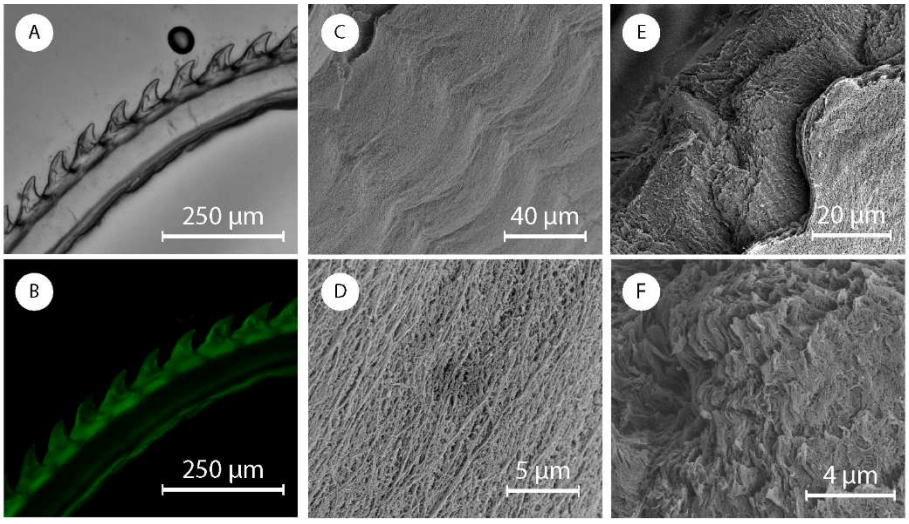

Figure 63: (A) Optical and (B) fluorescence microscope images of a radula longitudinal section. SEM images of (C and D) the radula membrane and of (E and F) a radula membrane section.

this hook perfectly fit the posterior side of the previous denticle (as sketched in Figure 62 H). In a similar way the hook probably fits in the posterior gap.

The end of the radula above the odontophore shows some rows of denticles with a completely different morphology (Figure 64 A-B). Those denticles are mainly fibrous, with fibers perpendicular to the surface of the denticle, while those in the base are mainly parallel to the membrane. Starting from the most proximal row, the denticles appear to become progressively more structured until they reach complete maturation. As reported

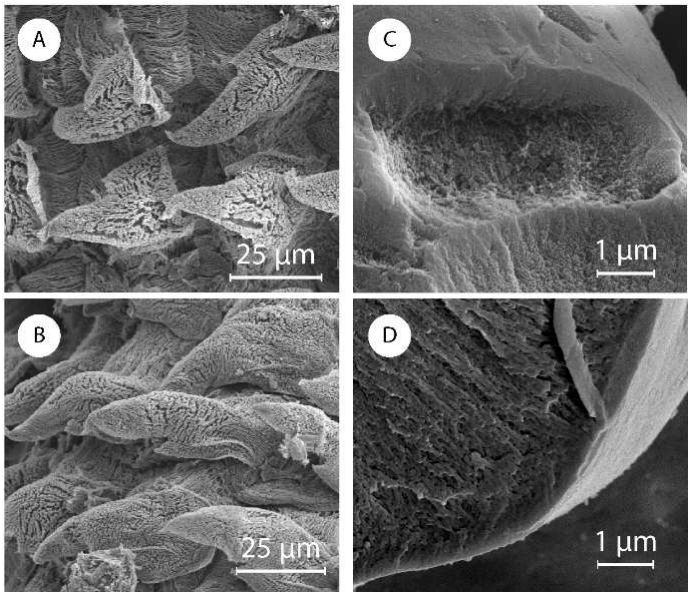

Figure 64: SEM images of immature (A) central and (B) lateral denticles. (C) SEM image of a broken mature etched denticle and of (D) a broken mature denticle.

for other species,[48][56] the rows of radular teeth are secreted at the proximal margin of the radula, becoming harder as they mature. The teeth then erode and shed at the distal portion of the radula with the radular ribbon advancing anteriorly to replace rows as they become worn.

CW staining indicated a high concentration of chitin in the denticles, while EDS showed the presence of calcium, but mineralized phases were not detected with standard techniques. We treated a radula in acetic acid pH 3 for 24 hours (Figure 64 C-D). After the treatment we observed no significant difference on the surface of the denticles. However, some broken denticles showed an external denser layer of 680 ± 90 nm, while the inside appeared as a tightly cross-linked network. An untreated control broken radular denticle showed the same external features with an internal phase that looked mineralized.

Finally, as reported in Figure 65, a membrane a few hundreds of microns thick, without denticles is present all along the edge of the radula, except where immature denticles were observed.

We then examined the odontophore (Figure 57 E).

The odontophore presents mainly protein absorption bands in the FTIR spectra, Figure 59. However, weak signals attributed to chitin, such as the asymmetric in-phase ring stretching mode, were also detected. This matrix dissolves completely in an aqueous solution of 1 M

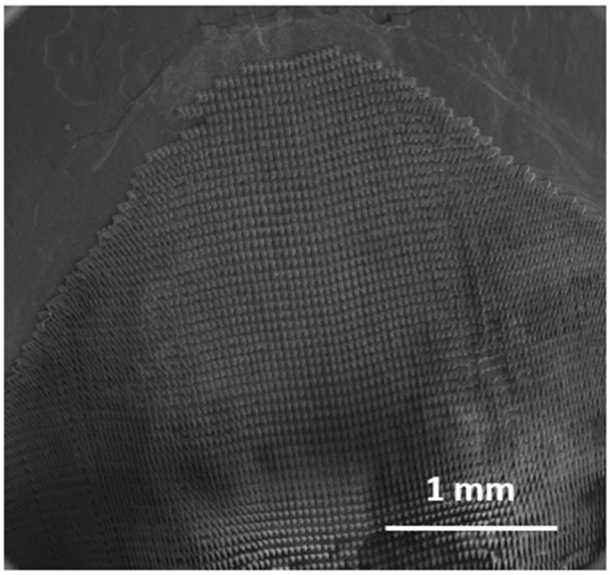

Figure 65: SEM image of the triangular distal end on the radula outer face and its denticle-free lateral membrane.

NaOH at room temperature, and we do not see any detectable chitin signal from CW staining, probably because of the high natural fluorescence of the matrix (Figure 66). Identifying the detailed protein composition of the odontophore will be part of future studies. Both in SEM and optical microscope images, the odontophore looked like a continuous single piece from the outside (Figure 67). The observation of sections, however, unveiled a dense outer layer with aligned perpendicular structures on the inside (Figure 66 and Figure 67). On a transverse section, Figure 66 A,D, we observed these structures to be straight lines in the front, and bend into arcs laterally, Figure 66 E-F. In Figure 66 G,J we show sagittal sections of the odontophore. In this plane of section we observed straight lines on the ventral region, Figure 66 I,L, gradually turning into triangles, Figure 66 H,K, at the dorsal end of the odontophore. With SEM those perpendicular structures appeared composed of ~10 µm thick fibers embedded and connected by layers (Figure 68). Both the fibers and the layers were composed of aligned nanofibrils. A coronal section showed those fibrils perpendicular to the section plane and still aligned, Figure 66 M-R.

We observed these perpendicular structures, composed of fibers, along all the transverse section of the odontophore. On the sagittal section, on the other hand, those structures were present only in part of it, being completely replaced by the dense outer layer in the ventral region of the odontophore, as can be seen in Figure 66 G,J. The dense outer layer

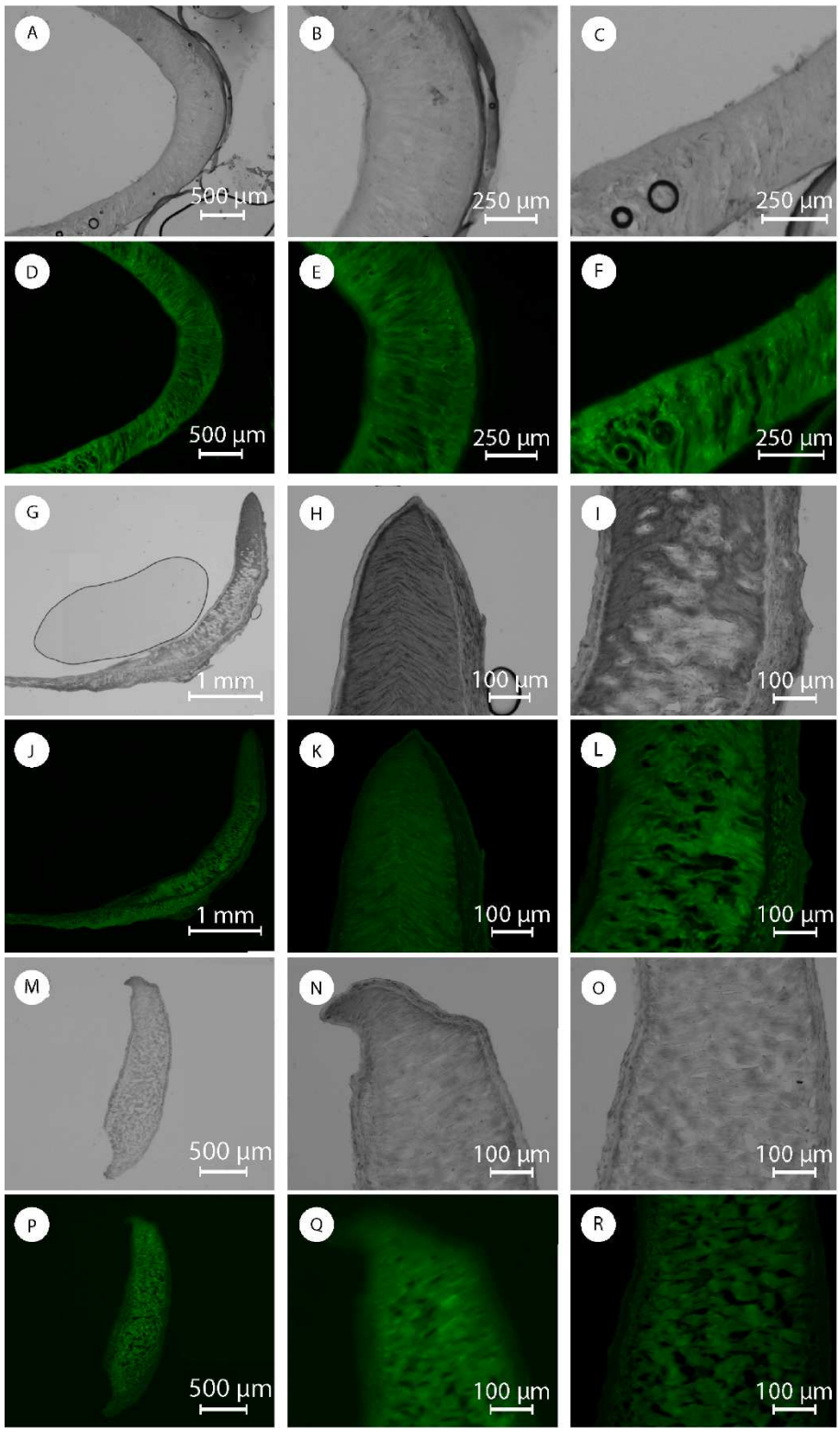

Figure 66: Optical and fluorescence images sections of the odontophore: (A and D) Transverse section, (B and E) anterior region in the transverse section, (C and F) posterior region in the transverse section; (G and J) Sagittal section, (H and K) dorsal sagittal region and (I and L) ventral sagittal region; (M and P) Coronal section, (N and Q) dorsal coronal region and (O and R) ventral coronal region.

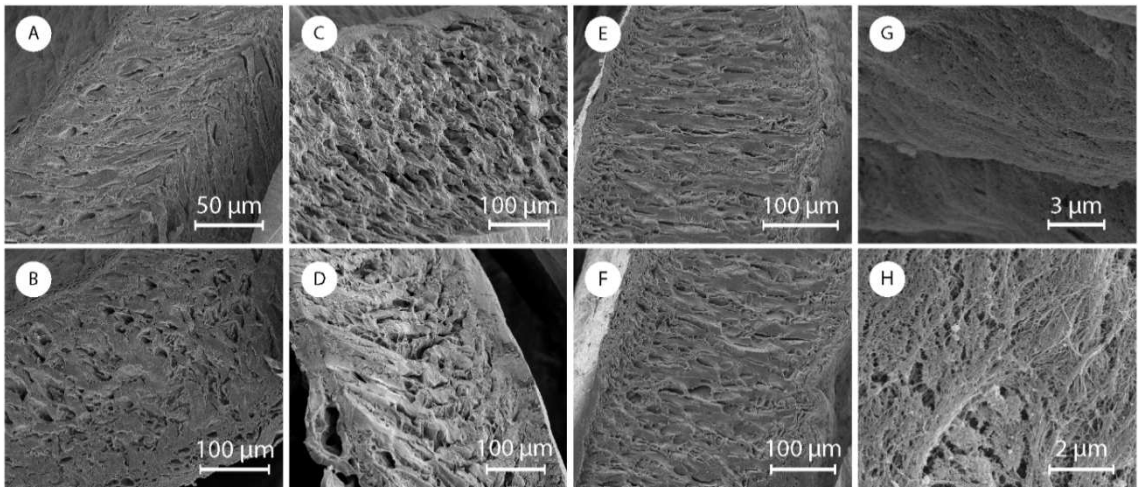

Figure 67: SEM image of fixed sections of the odontophore: (A) dorsal and (B) ventral sagittal section, (C) anterior and (D) posterior transversal section and (E) dorsal and (F) ventral coronal section. External surface of the odontophore, (G) inside and (H) outside the odontophore sphere.

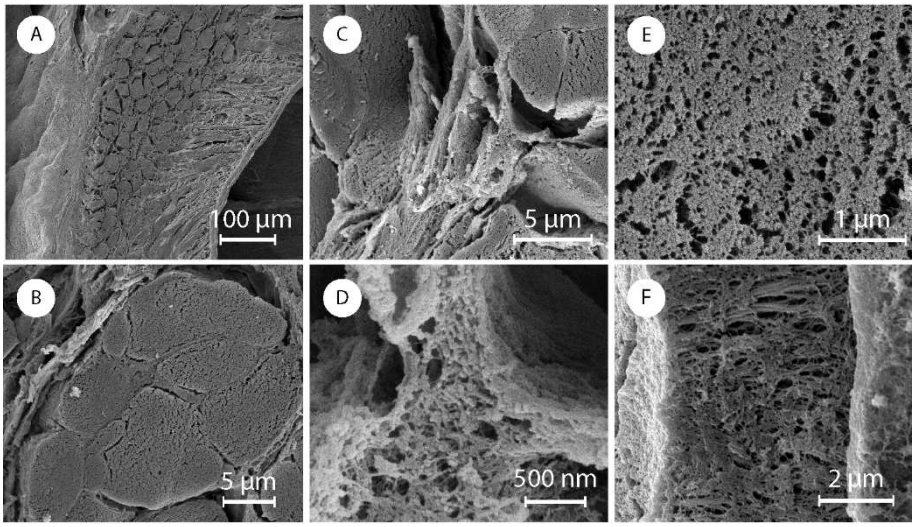

Figure 68: SEM image of a fixed section of the odontophore: (A) ventral coronal section, (B) a fiber perpendicular to the plane of section, (C and D) connecting matrix between the fibers, (E) frontal view of the fiber section and (F) lateral view of the micrometric fiber.

appeared thicker and composed of vertical, poorly fluorescent, fibrous structures. We observed thick, horizontal, highly fluorescent fibers only in the external wall (Figure 66 L). The external wall was thicker at the base, getting thinner moving up on the structure and from the anterior to the posterior regions. Its horizontal fibrous composition also seemed to decrease moving from the bottom to the top of the structure leaving space for the vertical fibrous structure. The internal wall, in contrast, maintained a constant thickness along the structure.

5.2. Discussion

We have characterized the structure and composition of several of the acellular components in the buccal mass of *A. californicus*, a banana slug. The buccal mass contains the jaw, the radula, and the odontophore as acellular structures. In the buccal mass the radula, supported by the odontophore, works against the anterior part of the jaw in order to cut pieces of food.

We observed that the jaw is directly linked to the foregut cuticle. These two are both made of chitin, but with different morphologies. In the foregut cuticle, perpendicular nanofibrils coil randomly and generate an intricate nanofibrous carpet. In this carpet we observed a sequence of parallel grooves posterior to the jaw. Those grooves have a spacing (41 ± 5 μm), comparable to that of the central denticles [lateral tip-tip distance (45 ± 4 μm)]. We theorize that the radula scrapes against the upper wall of the buccal mass. The protective purpose of the foregut cuticle is known in biology, but its structure has never been characterized. The chitin nanofiber network in the foregut cuticle protects the tissues from damage done by the denticles in the radula. Considering that a denticle's tip has a curvature radius of some microns, a randomly coiled nano-fibrous carpet is perceived by the denticle tip as a homogenous surface. Below this structure, the very organized perpendicular fibrils may act as mechanical shock absorbers to the impact of the radula on the tissues underneath.

The dense nanoparticle structure of the jaw, connected by fibrous crosslinks, resembles composite structures and may be responsible for the stiffness of the material. Moreover, the micro-fibrous packing observed from CW staining might contribute to connect the nanoparticles on a bigger scale, mechanically reinforcing the structure. Finally, the darker anterior layer morphology guarantees a homogenous surface for interaction with the denticle's tips, acting, probably, as a protective layer for the nanoparticles underneath. It is still premature to discuss the origin of the jaw coloration, but we may infer that the color gradient is strictly related to the nanoparticle presence, except in the very anterior layer, meaning that, it is directly associated with the interaction or composition of the nanoparticles.

The function of the radula is to bite off bits of food by working against the jaw. The observation of over 20 different radula samples showed that not one was ever missing one single denticle. Starting from this simple observation we assumed the denticles have a

strong anchoring to the membrane and a good ability to disperse mechanical stress that avoid denticles to be pulled out during the biting. The central denticles overlap part of the posterior base of the anterior denticle. Thanks to this interlocking, during biting each denticle compresses the anterior one against the membrane, diminishing the possibility that it will be dragged away. The lateral denticles, instead, have a hook structure that fits on the posterior wall of the anterior denticle. The radula assumes an arc conformation on the odontophore. Senseman[92] described movements of the radula during biting, in A. californicus, as being largely the result of the action of muscles attached to the odontophore. These muscles produce a cycle of events during a bite, which begins with the medial tooth being driven into the food substrate. This is followed by protraction of the radula out of the buccal cavity and onto the food, and then retraction of the radula into the buccal cavity, still moving in an anterior-dorsal arc. A bit of food is scooped out of the substrate during the retraction phase. The lateral denticles act as a serrated cutting tool as the radula moves into and through the surface of the food. Towards the end of the retraction process the lateral denticles scrape against the medial tooth. Senseman suggested that this last phase of biting is functionally equivalent to occlusion in vertebrate biting and serves to sever the bit of food cleanly from the substrate.[92] Therefore, the lateral denticles may also experience a lateral force during the cutting movement. A deeper interaction with the membrane, due to a higher surface of contact, and a partial lateral interlocking between the hook and the gap might be adaptations to face this lateral stress. Moreover, their high inclination may let them experience differently the force of food penetration that might be partially dissipated on the successive denticle.

The results suggested the denticles are mainly composed of organic material reinforced with an additional internal calcium phase, which was not detected as a mineral one by surface vibrational spectroscopies.

The network of radular membrane nanofibrils was mainly aligned longitudinally with the radula, probably to better resist to elongation. The alkaline resistance of those fibers supported the idea that they were chitin-based, with a protein interconnection among fibrils. The denticles have a high fiber content. Probably nanofibrils connect denticle and membrane generating linkages between those two structures. The layered structure observed in cross-sections of the membrane could provide the lower layers the possibility

to deform more than the ones interfacing the denticles. This would help interaction of the hard denticles with the soft tissues underneath.

The literature[48] on radula biogenesis and migration reports a tissue between the radular membrane and the odontophore. The role of this tissue is to anchor the radula and move it in order to expose new denticles during the lifespan of the animal. In this study we did not focus on cellular structures or tissues. Despite that, the existence of this tissue explains why we did not detect anchoring components between the radula membrane and the odontophore.

The odontophore works as support for the radula and is strongly linked to the surrounding tissues. As consequence of the strong relationship between odontophore and radula those structures are subjected to similar mechanical stresses.

Microscope images showed that this structure appeared as a continuous nano-fibrous surface from the outside. Observation of sections, on the other hand, showed a perpendicular fibrous structure with different curvatures inside, schematically represented in Figure 69. This morphology fits with a weakly flexible structure on the ventral sagittal region, which, thanks to its structure, became horizontally elastic (along the transverse plane of section) on the posterior transverse regions, and vertically elastic (along the sagittal plane of section) in the dorsal sagittal region. The perpendicular structures observed in the sections were made up of a single row of microfibers, aligned and connected with the others. A dense layer was observed to cover the whole structure and occupy the area of the odontophore, where the biogenesis and degradation of the radula takes place.

The odontophore's structure suggests that it would allow an elastic reaction to feeding stresses without excessive surface deformation, avoiding possible tissue damage. The vertical dimension of the jaw was about 800 µm. Comparing this with the odontophore, it shows that only the portion of the radula on the flexible dorsal sagittal region of the odontophore can get in contact with the jaw. At most, 15 denticle rows should be involved in this contact. From the observational evidence collected we could theorize the odontophore could be structurally programmed to drive a correct motion of the radula on the jaw and, meanwhile, dissipate gently the mechanical energy on the surrounding tissues.

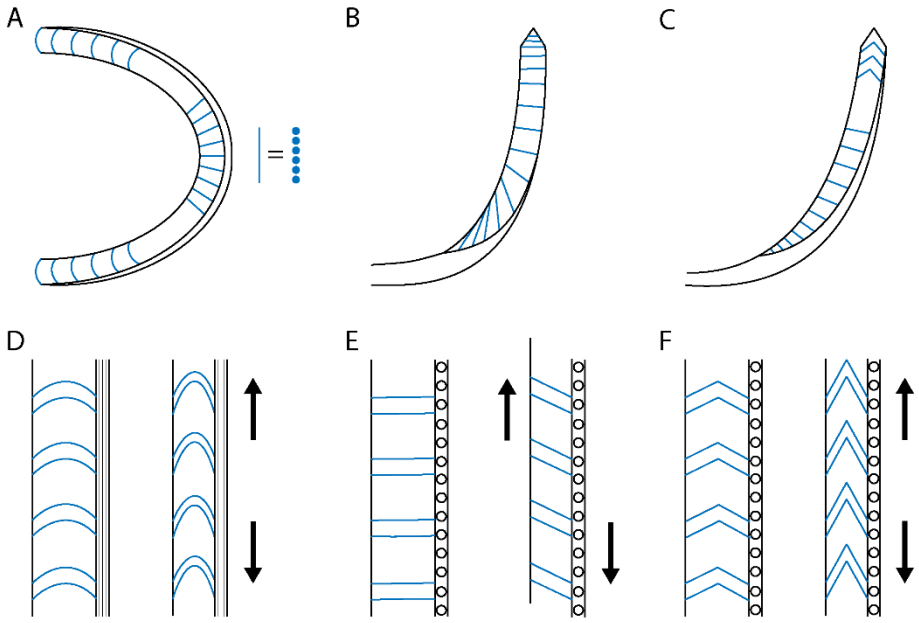

Figure 69: Schematic representation of the odontophore sections: (A) transverse section, (B) coronal section, and (C) sagittal section. Schematic representation of the elastic behavior on different position of the odontophore, the forces inducing the deformation are reported as arrows: (D) transversal posterior region, (E) ventral sagittal region, and (F) dorsal sagittal region.

It was not possible to study the mechanical properties of these matrices because their complex architecture and tiny structure would require uncommon set ups and a deeper knowledge on the mechanical behavior of materials. The investigation of these properties will be object to future studies in collaboration with a specialized engineering group.

5.3. Conclusion

In this work we performed an overall characterization of the three main acellular components in A. californicus's buccal mass. For the first time, we characterized the radula of an herbivorous terrestrial slug, and micro- and nano-structures in the jaw and odontophore. The results obtained showed a strong interaction among those structures In the feeding motion both the jaw and radula have a first contact between the compression-resistant nanostructured anterior layer of the jaw and the radula region located on the internal wall of the flexible dorsal region of the odontophore. Although not many rows of denticles are involved in the interaction, their strict interlocking allow them to efficiently disperse the force applied. We observed how both the denticles' packing and morphology, and the odontophore structure vary between the central and lateral regions, which are subjected to different forces. The odontophore's structure suggests it produces the correct motion of the radula on the jaw. It also seems to allow proper dispersal of the forces on the surrounding tissues without inducing external deformation that would damage the tissues between the radula and the odontophore. After the first contact between radula and jaw the radula gets in contact with the foregut cuticle, which appeared to be organized to protect the upper foregut.

5.4. Materials and methods

Sample collection The material used in this study was derived from a laboratory population of slugs collected at Purisima Redwoods, Half Moon Bay, CA. The slugs were maintained in the lab using a protocol previously described.[88] After natural death, we froze the animals for storage and future handling and kept them in a commercial freezer. We collected the three components of interest by dissecting frozen animals after slowly rehydrating them in PBS at 4 °C overnight. Then we cleaned the samples from residual tissues by shaking them in a TWEEN60 solution $5x10^{-2}$ M for 5 hours,[93] and then rinsing them with abundant water. We stored the clean samples in PBS at 4 °C.

Isolation of denticles We collected the radula's denticles by putting a radula sample in 500 µL of 8 M urea and shaking it for 24 hours to remove and/or denature the structural proteins in the membrane. Then we treated the radula in 2 mL of hexafluoroisopropanol, a chitin solvent used to soften the radula membrane, and shook it vigorously for 24 hours. We observed a suspension of denticles in solution after the treatment.

Optic, and fluorescent microscopy images We treated all the sample sections and the samples reported as "fixed" as follows: the sample was soaked in 2 mL of glutaraldehyde 2.5 vol.% in PBS at 4 °C for 16 hours, washed with PBS, and eventually sectioned using a Leica CM3050S cryo-microtone in 50 µm sections embedding it in O.C.T. Compound by Tissue-Tek, washed with water, and eventually stained before the analysis.
We acquired optical images using a Keyence VHX-5000 microscope and fluorescence images using a Keyence BZ-X710 with a green fluorescence protein filter on CW stained samples and odontophore's sections.

Scanning electron microscopy images and coupled analysis We fixed all the samples for SEM using an alcohol gradient (from 10 to 90 vol.% every 10 vol.%, then 95 vol.%, pure ethanol and two times with pure methanol), and critical point dried them using methanol/carbon dioxide exchange to preserve their morphology. We pre-treated the sample sections and the samples reported as "fixed" as previously reported in the optical microscopy section. We mounted all the samples on a SEM stub with carbon tape, and coated them with 20 nm of gold. We acquired SEM images using FEI Quanta™ 3D. In the

EDS we used an Octane Silicon Drift Detector coupled to a FEI Helios 600i Dual Beam FIB/SEM. We acquired the imaging at 1kV while for EDS we used an accelerator voltage of 20 keV.

Staining We performed the Arnow's assay[94][95] soaking in sequence a sample in 1) 100 µL of water, 2) 100 µL of HCl 0.5 M, 3) 100 µL of a solution obtained mixing 10 g of $NaNO_2$ and 10 g of Na_2MoO_4 in 100 mL of water, and finally in 4) 100 µL of NaOH 1M. We performed a control experiment without adding the sample. After 5 minutes an eventual color change from uncolored to red should occur in the presence of free catechols.
We highlighted the presence of chitin using CW, a polysaccharide specific stain. We set a drop of stain and then a drop of KOH 10% on the sample, waited 1 minute, and washed away the excess stain with water.

Fourier Transform Infrared analysis We recorded the FTIR spectra using a Bruker Vertex 70 FT-IR spectrometer equipped with a diamond crystal ATR accessory. The spectra were collected between 4000-400 cm^{-1} with a 4 cm^{-1} resolution and analyzed using OPUS.

Optical scattering analysis The optical scattering properties of chitin were studied with both optical reflection and a transmission-based dark-field microscope (Nikon). The optical spectra were taken using a highly sensitive spectrometer (Ocean Optics HR4000). The specimen was first placed on a glass microscope slide that was later mounted on the stage holder of the microscope. A 20x objective was used to collect the transmitted and reflected scattering signals. The measured scattering light spectra were normalized to the excitation light spectrum.

6. References

[1] J.-F. Revel, R. H. Marchessault, *Int. J. Biol. Macromol.* **1993**, *15*, 329.

[2] F. C. Yang, R. D. Peters, H. Dies, M. C. Rheinstädter, *Soft Matter* **2014**, *10*, 5541.

[3] I. M. Weiss, C. Renner, M. G. Strigl, M. Fritz, *Chem. Mater.* **2002**, *14*, 3252.

[4] J. Blackwell, M. A. Weih, *J. Mol. Biol.* **1980**, *137*, 49.

[5] A. C. Neville, B. M. Luke, *Tissue Cell* **1969**, *1*, 689.

[6] J. E. Rebers, J. H. Willis, *Insect Biochem. Mol. Biol.* **2001**, *31*, 1083.

[7] J. H. Willis, *Am. Zool.* **1999**, *39*, 600.

[8] V. A. Iconomidou, J. H. Willis, S. J. Hamodrakas, *Insect Biochem. Mol. Biol.* **2005**, *35*, 553.

[9] G. Vaaje-Kolstad, D. R. Houston, A. H. K. Riemen, V. G. H. Eijsink, D. M. F. Van Aalten, *J. Biol. Chem.* **2005**, *280*, 11313.

[10] T. Suetake, S. Tsuda, S. I. Kawabata, K. Miura, S. Iwanaga, K. Hikichi, K. Nitta, K. Kawano, *J. Biol. Chem.* **2000**, *275*, 17929.

[11] H. Merzendorfer, L. Zimoch, *J. Exp. Biol.* **2003**, *206*, 4393.

[12] R. Bolognesi, Y. Arakane, S. Muthukrishnan, K. J. Kramer, W. R. Terra, C. Ferreira, *Insect Biochem. Mol. Biol.* **2005**, *35*, 1249.

[13] Y. Arakane, Q. Zhu, M. Matsumiya, S. Muthukrishnan, K. J. Kramer, *Insect Biochem. Mol. Biol.* **2003**, *33*, 631.

[14] Z. Shen, M. Jacobs-Lorena, *J. Mol. Evol.* **1999**, *48*, 341.

[15] N. V. Raikhel, H. Lee, *Annu. Rev. Plant Mol. Biol.* **1993**, *44*, 591.

[16] H. T. Wright, G. Sandrasegaram, C. S. Wright, *J. Mol. Evol.* **1991**, *33*, 283.

[17] D. I. Svergun, A. Becirevic, H. Schrempf, M. H. J. Koch, G. Gruber, *Biochemistry* **2000**, *39*, 10677.

[18] Y. Takeshi, F. Gunki, *Biosci. Biotechnol. Biochem.* **1996**, *60*, 1081.

[19] L. Chamoy, M. Nicolaï, J. Ravaux, B. Quennedey, F. Gaill, J. Delachambre, *J. Biol. Chem.* **2001**, *276*, 8051.

[20] X. Shi, M. Chamankhah, S. Visal-Shah, S. M. Hemmingsen, M. Erlandson, L. Braun, M. Alting-Mees, G. G. Khachatourians, M. O'Grady, D. D. Hegedus, *Insect Biochem. Mol. Biol.* **2004**, *34*, 1101.

[21] S. S. Chaudhari, Y. Arakane, C. A. Specht, B. Moussian, D. L. Boyle, Y. Park, K. J.

Kramer, R. W. Beeman, S. Muthukrishnan, *Proc. Natl. Acad. Sci.* **2011**, *108*, 17028.

[22] K. Y. Zhu, H. Merzendorfer, W. Zhang, J. Zhang, S. Muthukrishnan, *Annu. Rev. Entomol.* **2016**, *61*, 177.

[23] D. Raabe, P. Romano, C. Sachs, H. Fabritius, A. Al-Sawalmih, S. B. Yi, G. Servos, H. G. Hartwig, *Mater. Sci. Eng. A* **2006**, *421*, 143.

[24] C. Valverde Serrano, H. Leemreize, B. Bar-On, F. G. Barth, P. Fratzl, E. Zolotoyabko, Y. Politi, *J. Struct. Biol.* **2016**, *193*, 124.

[25] M. Y. Noh, K. J. Kramer, S. Muthukrishnan, M. R. Kanost, R. W. Beeman, Y. Arakane, *Insect Biochem. Mol. Biol.* **2014**, *53*, 22.

[26] G. Falini, S. Albeck, S. Weiner, L. Addadi, *Science (80-.).* **1996**, *271*, 67.

[27] L. Addadi, D. Joester, F. Nudelman, S. Weiner, *Chem. - A Eur. J.* **2006**, *12*, 980.

[28] J. S. Evans, *Chem. Rev.* **2008**, *108*, 4455.

[29] G. Bevelander, H. Nakahara, *Calcif. Tissue Res.* **1969**, *3*, 84.

[30] F. Nudelman, B. A. Gotliv, L. Addadi, S. Weiner, *J. Struct. Biol.* **2006**, *153*, 176.

[31] E. C. Keene, J. S. Evans, L. A. Estroff, *Cryst. Growth Des.* **2010**, *10*, 1383.

[32] S. Weiner, Y. Talmon, W. Traub, *Int. J. Biol. Macromol.* **1983**, *5*, 325.

[33] Y. Levi-Kalisman, G. Falini, L. Addadi, S. Weiner, *J. Struct. Biol.* **2001**, *135*, 8.

[34] S. Weiner, W. Traubt, *FEBS Lett.* **1980**, *111*, 311.

[35] S. Michio, S. Kazuko, K. Toshihiro, Y. Yuya, N. Tatsuya, K. Takashi, N. Hiromichi, *Science (80-.).* **2009**, *325*, 1388.

[36] J. Fournié, M. Chétail, *Integr. Comp. Biol.* **1984**, *24*, 857.

[37] D. R. Furbish, W. J. Furbish, *J. Morphol.* **1984**, *180*, 195.

[38] R. G. Rae, J. F. Robertson, M. J. Wilson, *J. Invertebr. Pathol.* **2008**, *97*, 61.

[39] V. R. Meenakshi, B. T. Scheer, *Comp. Biochem. Physiol.* **1970**, *34*, 953.

[40] J. L. Cuy, A. B. Mann, K. J. Livi, M. F. Teaford, T. P. Weihs, *Arch. Oral Biol.* **2002**, *47*, 281.

[41] J. C. Weaver, Q. Wang, A. Miserez, A. Tantuccio, R. Stromberg, K. N. Bozhilov, P. Maxwell, R. Nay, S. T. Heier, E. DiMasi, D. Kisailus, *Mater. Today* **2010**, *13*, 42.

[42] A. Graham, *J. Zool.* **1973**, *169*, 317.

[43] I. Hurwitz, D. Neustadter, D. W. Morton, H. J. Chiel, A. J. Susswein, *J. Neurophysiol.* **1996**, *75*, 1309.

[44] P. Van Der Wal, *J. Ultrastruct. Mol. Struct. Res.* **1989**, *102*, 174.

[45] M. R. Carriker, J. G. Schaadt, V. Peters, *Mar. Biol.* **1974**, *25*, 63.

[46] N. W. Runham, C. J. Bailey, M. Carr, C. A. Evans, S. Malham, *Ecology* **1997**, *61*, 67.

[47] A. A. D. . Mc Clellan, *J. Exp. Biol.* **1982**, *98*, 195.

[48] U. Mackenstedt, K. Märkel, *Zoomorphology* **1987**, *107*, 209.

[49] K. Wolter, *J. Molluscan Stud.* **1992**, *58*, 245.

[50] E. Vortsepneva, D. Ivanov, G. Purschke, A. Tzetlin, *Zoomorphology* **2013**, *132*, 359.

[51] K. M. U. Mackenstedt, *The Biology of Terrestrial Molluscs*; 2001.

[52] M. Saunders, C. Kong, J. A. Shaw, D. J. Macey, P. L. Clode, *J. Struct. Biol.* **2009**, *167*, 55.

[53] J. Alvim, L. R. L. Simone, A. D. Pimenta, *J. Molluscan Stud.* **2014**, *80*, 604.

[54] W. G. Binney, **1875**, *27*, 140.

[55] W. G. Binney, *Acad. Nat. Sci.* **1874**, *26*, 33.

[56] E. D. Sone, S. Weiner, L. Addadi, *J. Struct. Biol.* **2007**, *158*, 428.

[57] G. Falini, M. Reggi, S. Fermani, F. Sparla, S. Goffredo, Z. Dubinsky, O. Levi, Y. Dauphin, J. P. Cuif, *J. Struct. Biol.* **2013**, *183*, 226.

[58] L. A. Evans, D. J. Macey, J. Webb, *Acta Zool.* **1992**, *51*, 78.

[59] T. Kawamura, R. D. Robertsand, Y. Yamashita, *Fish. Sci.* **2001**, *67*, 596.

[60] O. Toshihiro, K. Tomohiko, O. Satoshi, H. Toyomitsu, Y. Watanabe, *J. Shellfish Res.* **2004**, *23*, 1079.

[61] P. D. K., *The Veliger* **1998**, *41*, 201.

[62] D. G. Reid, Y. M. Mak, *J. Molluscan Stud.* **1999**, *65*, 355.

[63] W. G. Binney, *Proc. Acad. Nat. Sci. Philadelphia* **1876**, *28*, 183.

[64] A. Ianiro, M. Giosia, S. Fermani, C. Samorì, M. Barbalinardo, F. Valle, G. Pellegrini, F. Biscarini, F. Zerbetto, M. Calvaresi, G. Falini, *Mar. Drugs* **2014**, *12*, 5979.

[65] J. Huang, Y. Zhong, L. Zhang, J. Cai, *Adv. Funct. Mater.* **2017**, *27*, 1701100.

[66] M. Hong, G. Choi, J. Kim, J. Jang, B. Choi, J. Kim, S. Jeong, S. Leem, H. Kwon, H. Hwang, H. Im, J. Park, B. Bae, J. Jin, *Adv. Funct. Mater.* **2018**, *28*, 1870163.

[67] E. A. Pillar, R. Zhou, M. I. Guzman, *J. Phys. Chem.* **2015**, *119*, 10349.

[68] G. Fu, S. Valiyaveettil, B. Wopenka, D. E. Morse, *Biomacromolecules* **2005**, *6*, 1289.

[69] D. Montroni, B. Marzec, F. Valle, F. Nudelman, G. Falini, *Biomacromolecules* **2019**, *20*, 2421.

[70] R. H. Marchessault, F. G. Pearson, C. Y. Liang, *J. Polym. Sciece* **1960**, *43*, 101.

[71] K. H. Gardner, J. Blackwell, *Biopolymers* **1975**, *14*, 1581.

[72] K. Kobayashi, S. Kimura, E. Togawa, M. Wada, *Carbohydr. Polym.* **2010**, *79*, 882.

[73] M. Guthold, W. Liu, E. A. Sparks, L. M. Jawerth, L. Peng, M. Falvo, R. Superfine, R. R. Hantgan, S. T. Lord, *Cell Biochem. Biophys.* **2007**, *49*, 165.

[74] D. Montroni, S. Fermani, K. Morellato, G. Torri, A. Naggi, L. Cristofolini, G. Falini, *Carbohydr. Polym.* **2019**, *207*, 26.

[75] A. I. Arkhipkin, V. A. Bizikov, D. Fuchs, *Deep. Res. I* **2012**, *61*, 109.

[76] D. Montroni, C. Piccinetti, S. Fermani, M. Calvaresi, M. J. Harrington, G. Falini, *RSC Adv.* **2017**, *7*, 36605.

[77] D. Montroni, F. Valle, S. Rapino, S. Fermani, M. Calvaresi, M. J. Harrington, G. Falini, *ACS Biomater. Sci. Eng.* **2018**, *4*, 57.

[78] J. Bennion, V. Daggett, *PNAS* **2003**, *100*, 5142.

[79] C. N. Pace, In *Methods in enzymology*; 1986; Vol. 131, pp. 266–280.

[80] W. Konigsberg, In *Methods in Enzymology*; 1972; pp. 185–188.

[81] C. B. Anfinsen, E. Haber, *J. Biol. Chem.* **1961**, *236*, 1361.

[82] Y. Maeda, H. Koga, H. Yamada, T. Ueda, T. Imoto, *Protein Eng.* **1995**, *8*, 201.

[83] D. B. Pho, J. L. Bethune, **1972**, *47*, 419.

[84] A. Gottschalk, W. H. Murphy, E. R. B. Graham, *Nature* **1962**, *4833*, 1051.

[85] R. Hackman, *Aust. J. Biol. Sci.* **1960**, 568.

[86] J. F. V. Vincent, U. G. K. Wegst, *Arthropod Struct. Dev.* **2004**, *33*, 187.

[87] U. K. Laemelli, *Nature* **1970**, *227*, 680.

[88] J. L. Leonard, J. S. Pearse, A. B. Harper, *Invertebr. Reprod. Dev.* **2002**, *41*, 83.

[89] K. M. Rudall, W. Kenchington, *Biol.Rev.* **1973**, *49*, 591.

[90] M. Kaya, M. Mujtaba, H. Ehrlich, A. M. Salaberria, T. Baran, C. T. Amemiya, R. Galli, L. Akyuz, I. Sargin, J. Labidi, *Carbohydr. Polym.* **2017**, *176*, 177.

[91] M. K. Jang, B. G. Kong, Y. Il Jeong, C. H. Lee, J. W. Nah, *J. Polym. Sci. Part A Polym. Chem.* **2004**, *42*, 3423.

[92] D. M. Senseman, *Ph.D. Diss. Princet. Univ.* **1977**.

[93] T. W. Gilbert, T. L. Sellaro, S. F. Badylak, *Biomaterials* **2006**, *27*, 3675.

[94] X. Z. Gao, X. Wang, K. Zenger, *Int. J. Bio-Inspired Comput.* **2013**, *5*, 336.

[95] M. A., S. T., S. C., Z. W. F., W. H. J., *Science (80-.).* **2008**, *319*, 1816.

Chapter 4:
Functional chitin-based matrices

1. Introduction

The top-up approach is an uncommon method to exploit a system already organized. This approach is quite different from its relatives, the top-down and bottom-up approaches, which aim respectively to break down or build up a material starting respectively from an organized matrix of from its building blocks. This rather new approach aims to further improve an already organized matrix and introduce new level of complexity in its structure, without altering the previous ones. This approach allows combining the properties of the two levels of complexity in a new functional material.

1.1. Functional materials

The term functional materials generally refers to materials with particular native properties and functions of their own. From the chemical point of view, the easiest way to obtain a functional material is by functionalizing an existing material, frequently polymers, introducing properties related to the new group introduced.

As mentioned in chapter 1, chitin has been widely applied in chemistry as polymeric material and a multitude of different functionalization have been tested to introduce or enhance the material's properties (Figure 70).[1][2] In these studies chitosan was mainly involved, being the amino group a simple target for selective functionalization on the chitinous ring. Martin et al. (2002), functionalized the amino group of a chitosan scaffold with palmitoyl and the hydroxyl group in C_6 with glycol to obtain a hydrogel with controlled erosion as release system for the delivery of hydrophilic macromolecules.[3] Similarly, Mi et al. (2002) synthetized a porous scaffold for the immobilization of the indomethacin, a nonsteroidal anti-inflammatory drug, by introducing quaternary ammonium, octanoyl, and benzoyl groups along the chitosan backbone.[4] Functional chitosan-based materials have also been applied in catalysis. A copper complex involving the C_3-OH and C_2-NH_2 of the hexose ring was used for the oxidation of hydroquinones to quinones with oxygen. Many other complexes have been tested for as many reactions.[5] As last example, alkyl or

carboxymethyl groups have been used to increase the solubility of chitin and chitosan at neutral and alkaline pH values without affecting their characteristics; carboxymethyl derivatives have shown promise application in water remediation from metals, drug delivery, wound healing, anti-microbial, or as components in cosmetics and food.[6]

These are just a few examples of functional material derived from chitin showing the versatility a single polymer could gain by simple chemical functionalization

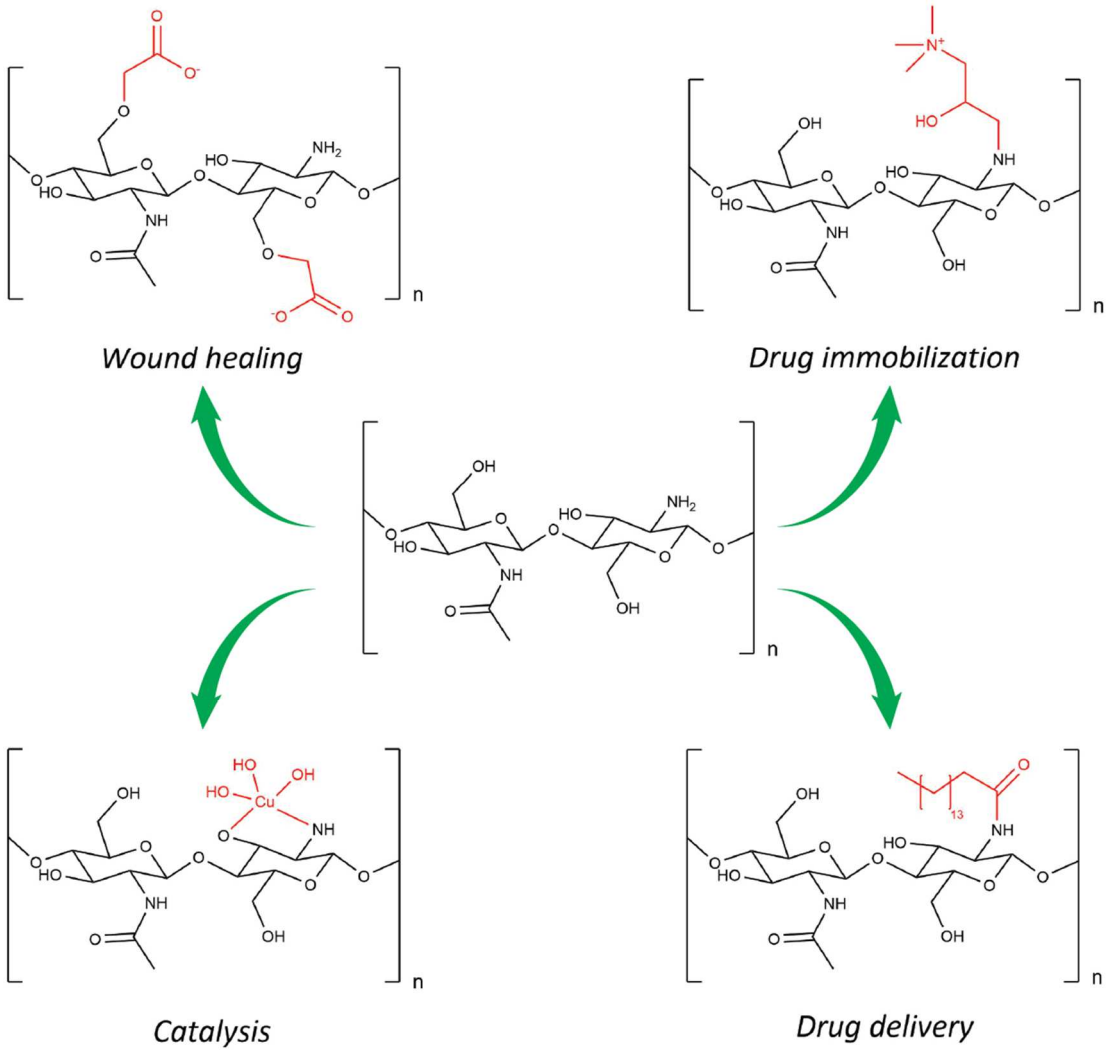

Figure 70: Examples of different functionalization on chitin/chitosan involving the hydroxyl and amino groups of the polymer to obtain different functional materials.

1.2. Catechols, from byssus to bioinspired

"Good things come in small packages" says the proverb. If this is true, the byssus might be one of the best examples at nature-science interface. The byssus is the proteic thread produced by mussels to anchor to a substrate and resist to currents and waves. It presents

catechol moieties, as 3,4-dihydroxyphenylalanine, responsible of the thread's mechanical and self-healing properties, and of the adhesive property of the thread to the substrate.[7][8][9][10] Since this discovery, catechols have been widely applied in materials with high mechanical[11][12] and adhesive properties,[13][14][15][16][17] especially in wet environments.[18][16][17] These applications are due to two important catechols' chemical properties: I) to chelate transition metals as bidentate ligands,[19][20][21][22] and, II) when oxidized to quinone, to crosslink covalently throw Michael addition reducing back to their dihydroxy state.[19][20][21][23][24] The catechol-functionalization have been also observed to highly increase the mucoadhesive property of materials.[25][24][26] Thanks to its enhanced mucoadhesive property and the high molecule absorption of these materials they found applications as biomaterials and drug delivery systems.[25][24][27][17] On the other hand, the metal-chelating ability of catechol-based matrices led to application in water remediation.[28] This chelating ability is also responsible for the self-healing properties of the byssus. In fact, along traction the catechol-metal bond acts as a sacrificial bond, avoiding initial critical damages, to reform after the stress. In 2017, Filippidi et al. developed an hydrogel inspired to byssus exhibiting analogue self-healing properties.[11]

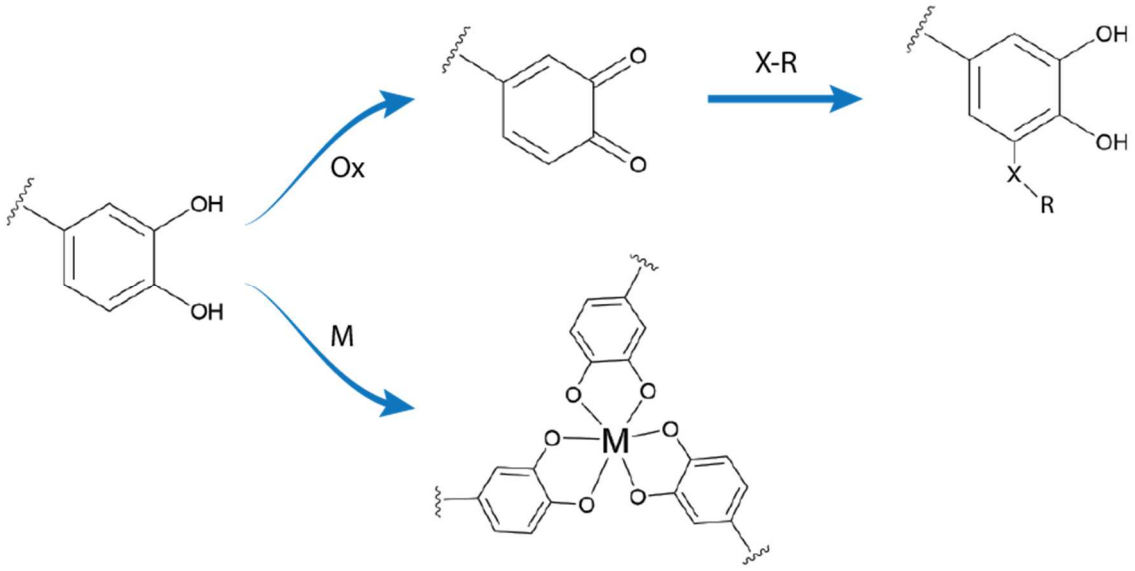

Figure 71: General reactions of crosslinking in catechols. M, is a generic transition metal (usually Fe or V). X, is a generic heteroatom (usually O, N, or S based groups).

2. Aim of the chapter

Ordered structures have been widely observed to have increased properties compared to their disordered or amorphous analogues. Properly organized structures have shown better mechanical properties [29] and biocompatibility[30] for example. Since chitin exhibits many different organized structures in nature it represents an important source of exploitable structures with diversified properties.

The aim of our study is to functionalize a hierarchically organized natural matrix, the gladius (or pen) of the squid *Loligo vulgaris*, with catechols to get a bioinspired hierarchically organized functional material. We decided to use this matrix because its relatively simple structure would have been easy to monitor and test.

Catechol-functionalized chitins have been widely studied in literature. Those materials are mainly referred to chitosan[31][15][26][27][16] more than chitin and usually led to gel,[20][25][27][16] due to the high water solubility of the functionalized polymer.[15] No work has been done on actual chitin (with a high DA), or on a hierarchically organized material.

The amino group of glucosamine units is a perfect target for a functionalization because de-acetylation mainly occurs in amorphous region, or on the fibril external surface. This should avoid the functionalization to perturb the material crystallinity and structure. A first study was performed to define how the DA affects the structural and mechanical properties of chitin/chitosan materials, while keeping the overall ultra-structure preserved at most.

The matrices obtained in this work represent a proof of concept that highly organized chitin matrices could be functionalized to get organized functional material. Moreover, the matrices obtained could easily find application in biomedical research and mechanics for wet environments, or even in drug delivery or water remediation.

3. Structured chitin matrices with different degree of acetylation

3.1. Results and discussion

β-chitin samples were purified from *L. vulgaris* squid pens using an alkaline treatment (1M NaOH), according to literature.[32][33][34] A yield of 41 ± 1 wt.%. was obtained, that despite the different fishing locations, confirmed that the chitin content is mainly related to the animal species.[35] Moreover, the extraction process of lipids and lipoproteins did not affect the final yield, as observed elsewhere.[36] Subsequently, that material (sample A) was used for the preparation of β-chitin samples having a lower DA, as reported in Table 5. The diverse chemical conditions were selected according to literature procedures.[32][33] Fresh 10 M NaOH was used in all the experiments, unless one case in which 5 M NaOH was used. Different treatment times at diverse temperatures were tested. The selection of the de-acetylation conditions was guided by the request to preserve as much as possible the microfibrillar organization of β-chitin samples. For this reason the reaction time was kept short (15 min), while the temperature was changed. Samples A and B, after the chemical treatment, preserved their pristine shape in wet and dry state. The other samples preserved it during the treatment, but upon pH neutralization/temperature decrease curled. The lower the DA observed, the more curled the samples were. The sample's DA was determined by NMR spectra and is reported in Table 5. DA was measured considering the relative integrals of methyl group compared to the carbon integrals of the polysaccharidic backbone. The non-separation at 77 ppm of the C_3 signal from the C_5 one indicates the non-transition of β- to α-chitin, even in the more intensely treated samples.[37]

Table 5: Synthetic conditions for the preparation of chitin samples having different degree of acetylation (DA), as determined by CP-MAS NMR.

Sample	DA / %	[NaOH] / M	Time / min	Temperature / °C
A	89	-	-	-
B	83	5	60	100
C	80	10	15	60
D	63	10	15	80
E	55	10	15	115
F	12	10	60	100

The reference sample, A, showed a DA equal to 89 %, accordingly to the literature data.[32] The samples B and C showed a similar DA, but they were obtained using different concentrations of NaOH. Samples D and E were treated for 15 min as sample C, but at higher temperatures, this provoked a reduction of the DA to 55 %. Sample F was obtained applying a treatment of 60 min in 10 M NaOH at 100 °C, and showed a DA of 12 %. Accordingly to the measured DA the samples A-E could be classified as chitin, while sample F was chitosan.[38][35]

The molecular weight of the polymer was measured using dynamic light scattering as reported by Terbojevich, Carraro, and Cosàni, (1988).[39] Samples A and B appeared to be over 500 KDa with a similar hydrodynamic radius. The insolubility of the other samples in N,N-dimethylacetamide (DMAA) and LiCl 5 wt.% did not allow the same study. The high molecular weight measured for both sample A and B let us assume a very mild chain shortening occurred during the purification process and the following treatment.

In Table 6 the qualitative solubility of the samples in DMAA and LiCl 5 wt.%, a typical solvent for chitin, and in acetic acid pH 3 in water, the most common solvent for chitosan, is reported. Samples C, D and E showed lower or none solubility in both the solvents.

SEM images of the cross-sections of the samples, reported in Figure 72, did not show relevant differences in the microfibrillar organization of the different samples. The only exception was sample F in which microfibrils were not observed. An analogous information was obtained from the observation of the surface of the samples (Figure 73).

Table 6: Solubility of the samples in two different solvents: i) 5% LiCl in N,N-dimethylacetamide (DMAA) and ii) acetic acid (AcOH) at pH 3 in water. The study was performed to achieve a 0.3 % w/w concentration of chitin/chitosan after stirring 24h. Conditions reported as part. sol. presented both solubilized and insolubilized matrix after 24 h.

Sample	DMAA, LiCl 5%	Water, AcOH pH 3
A	soluble	part. sol.
B	soluble	insoluble
C	insoluble	insoluble
D	insoluble	part. sol.
E	insoluble	part. sol.
F	insoluble	soluble

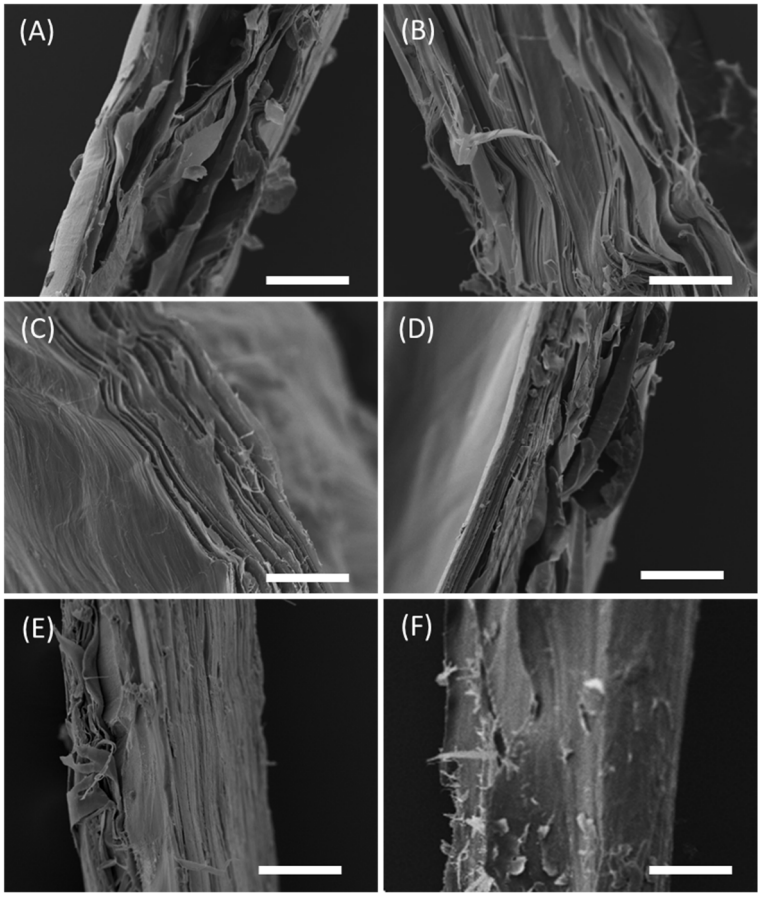

Figure 72: SEM images of the surface of the chitin/chitosan samples having differently chemically treated. They were labelled according to the nomenclature in Table 1. Scale bar: 50 mm.

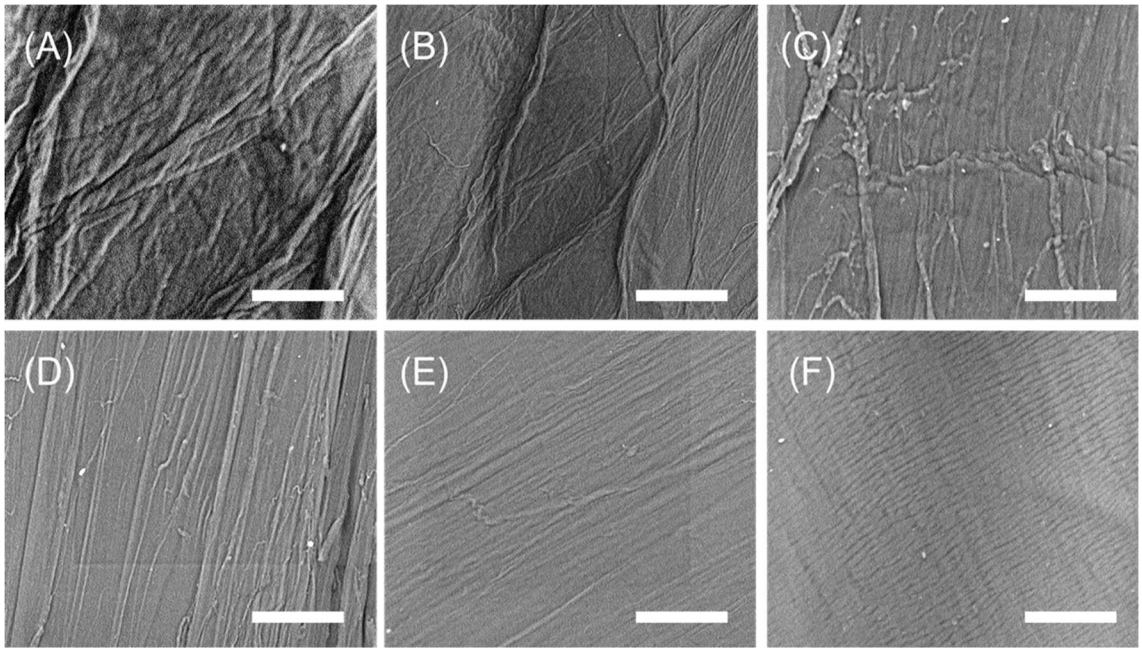

Figure 73: SEM images of the surface of the chitin samples having differently chemically treated. They were labelled according to the nomenclature in Table 1. Scale bar 20 mm.

The samples were characterized by thermal analyses. In the differential scanning calorimetry (DSC) measurements (Figure 74), an endothermic peak at around 70 °C was evident for samples A and B and appeared very broad for samples C-F, while an exothermic peak at around 300 °C was observed for all samples. The former might represent the dehydration of the samples, although the stepwise dehydration of crystalline β-chitin was not observed.[40] The second peak was attributed to the decomposition of amine groups[41] and its integration (Table 7) gave values of enthalpy that could be related to the DA. The latter was consistent with the one determined by NMR data.

The thermogravimetric analysis (TGA) profiles (Figure 75) showed for all sample a major weight loss in the range 290–350 °C with two contributes, one centered at about 300 °C and the other at about 340 °C (Table 7) and a minor one in the range 70 – 100 °C. The extens of the 290 – 350 °C weight loss are consistent with the DA of the samples (Table 7), being the first event related to the amino group pyrolysis. The 70 – 100 °C signal was attributed to dehydration.[41]

The FTIR spectra of the samples are illustrated in Figure 76 and the absorption bands were assigned as reported in Table 10. These spectra were not used for an estimation of the DA because the samples' wide DA range caused a change in the absorption of the diagnostic

Table 7: Summary of data from DSC and TGA analyses. The DSC profiles (Figure 74) show two peaks (I and II), for each of them the enthalpy and the temperature at the derivate maximum are reported. The TGA profiles (Figure 75) show three pyrolytic events (I-III), for each of them a weight loss is reported together with maximum temperature.

Sample	**DSC**				**TGA**		
	I ΔH / J·g^{-1}	I T / °C	II ΔH / J·g^{-1}	II T / °C	I (70-100) °C	II 300 °C	III 340 °C
A	263	78.4	31	325.6	4.0	-	58.8
B	145	78.3	25	306.9	4.1	-	58.9
C	-	-	160	296.3	7.3	13.9	41.1
D	-	-	185	296.2	7.6	22.0	29.9
E	-	-	262	305.4	7.4	25.8	15.1
F	-	-	333	301.8	7.3	45.5	-

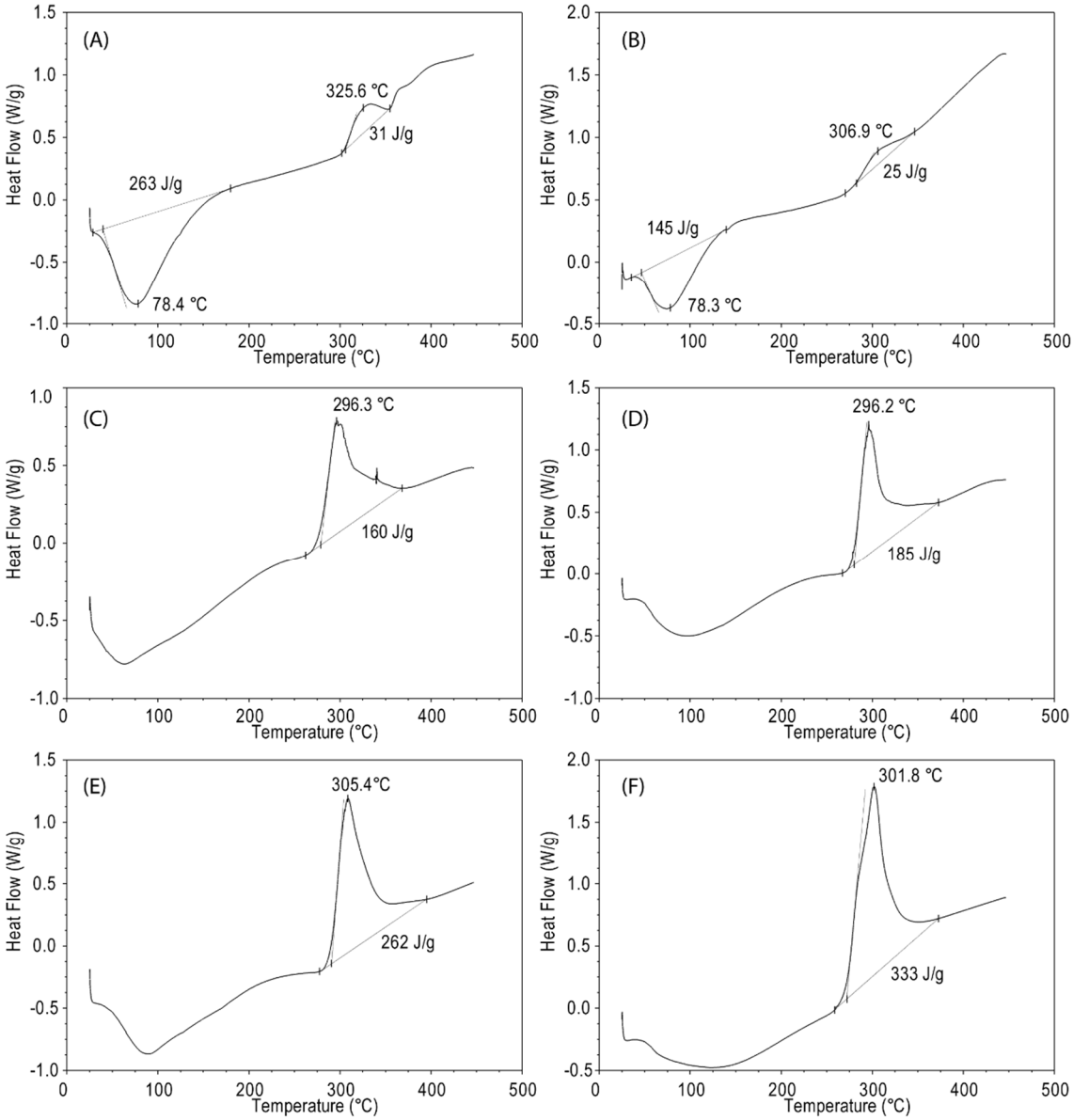

Figure 74: Differential scanning calorimetry profiles of the chitin samples having a different degree of acetylation. The main pyrolytic events are reported in Table 7.

bands. This change made it difficult to define a univocal set of reference bands.[42] The FTIR spectra were used to identify the chitin polymorph, being β-chitin characterized by one amide I band at 1656 cm^{-1}, while α-chitin shows two amide I absorption bands at 1660 and 1627 cm^{-1} that in samples with low crystallinity merge in one wide band.[43] Accordingly, the FTIR spectra indicate that all samples were β-chitin. Noishiki et al. (2003) reported that β-chitin converts into α-chitin when treated with a NaOH solution with a concentration higher than 7.5 M for 1 h, and as consequence of this, the microfibrillar organization totally collapsed.[44] Since the alkaline treatments used in this research were time shorter, the

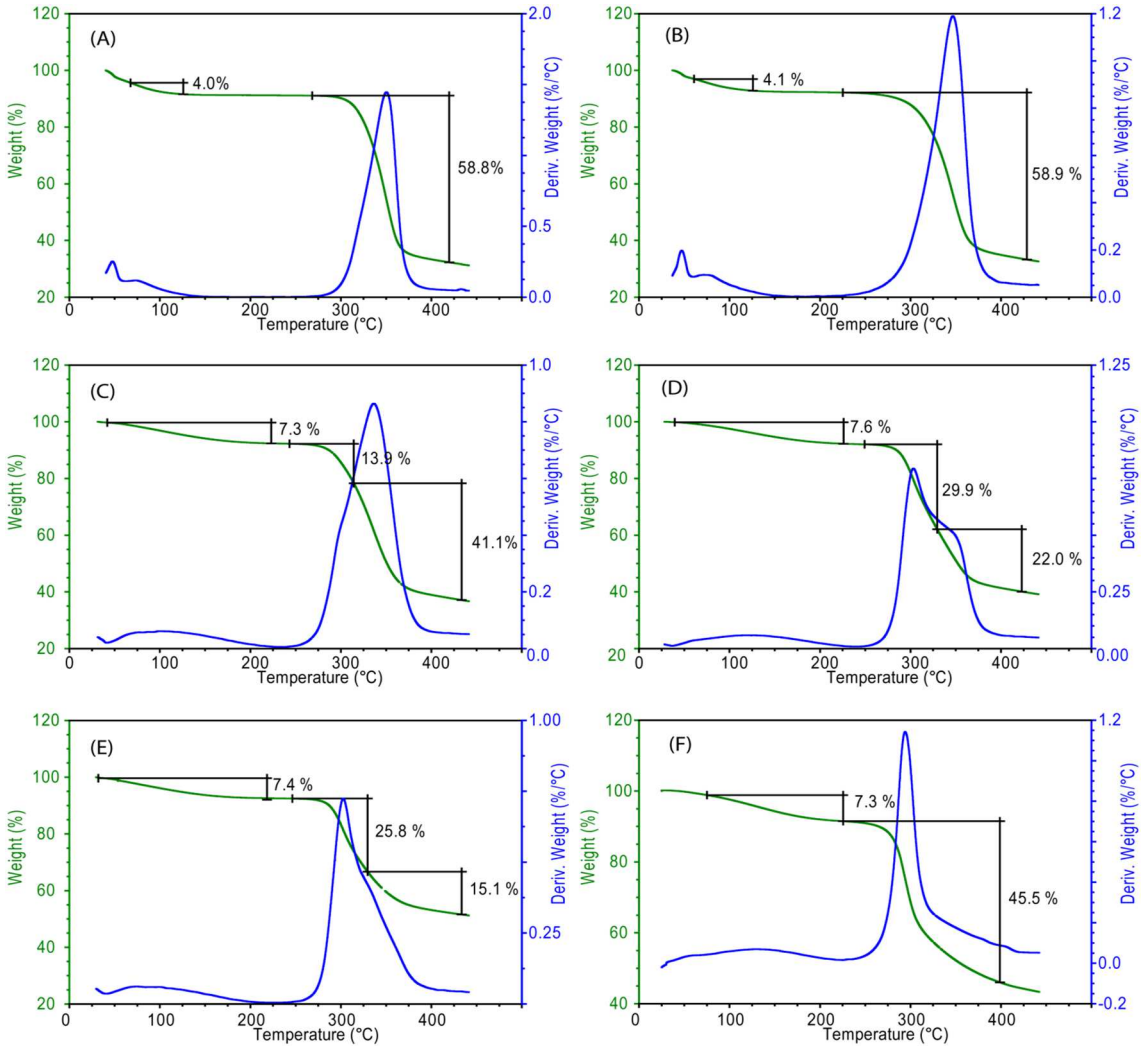

Figure 75: Thermogravimetric profiles of the chitin samples having a different degree of acetylation. The green line indicates the weight loss as a function of temperature. The blue line indicates the derivate of the weight loss over the temperature. The main pyrolytic events were established according to the derivate profile and are reported in Table 7.

polymorphic transition from β- to α-chitin was not observed, according to FTIR and NMR spectra.

The structural features of chitin samples were further investigated by the synchrotron source X-ray fiber diffraction images analyses (Figure 77). The diffraction intensity of the reflection from the samples treated with 10 M NaOH (C-F) was lower than that of the samples treated with 1 M (A) or 5 M NaOH (B) solutions. This observation suggests that in the sample C-F the crystalline regions were less than in the samples A and B.

The diffraction profiles along the 2Θ angle were obtained from the intensity integration of the images in Figure 77 and are reported in Figure 78. In addition, data from the analyses of the fiber diffraction images are summarized in Table 8. The samples A and B showed the

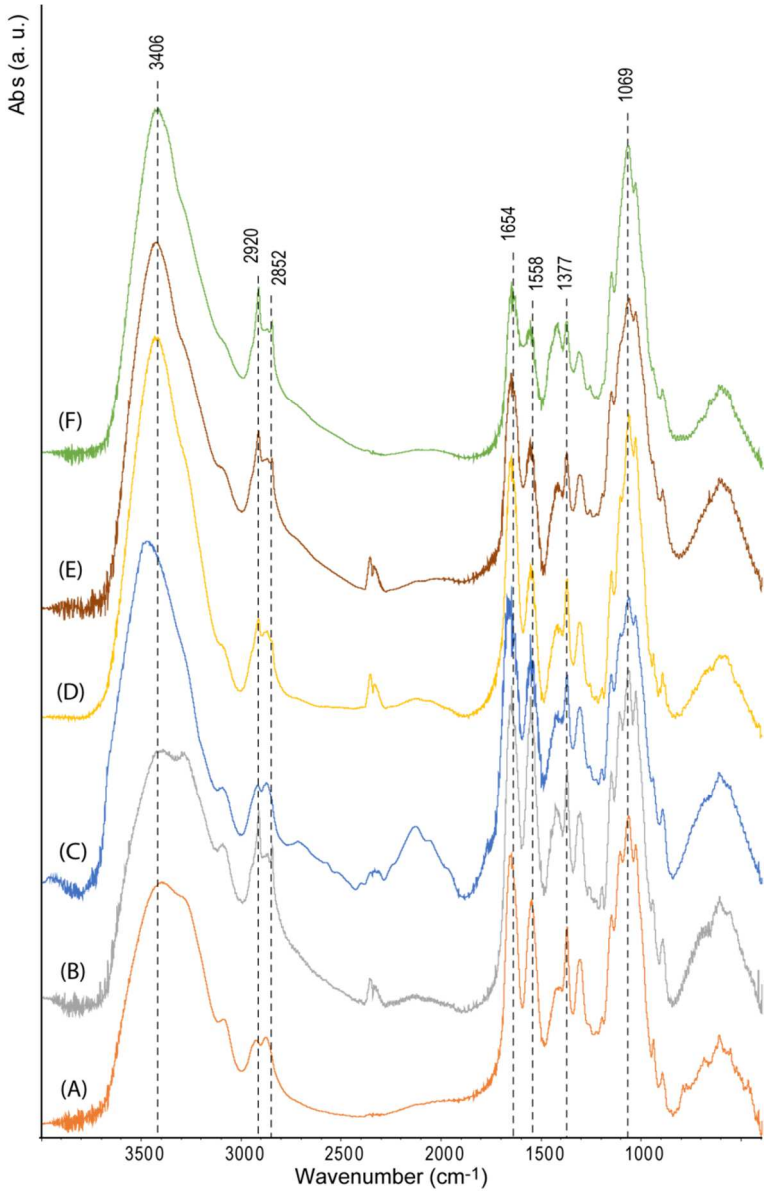

Figure 76: FTIR spectra of the different chitin/chitosan samples. The assignment of the absorption bands is reported in Table 10.

typical periodicities of di-hydrated β-chitin, d010 and d100 were equal to 10.85 and 4.66 Å, respectively.[45] Samples C and D showed diffraction peaks at about 9.6 and 4.5 Å. The sample E showed diffraction peaks having d010 equal to 9.80 and d100 equal to 4.45 Å, while the sample F showed only the diffraction peak d100 at 4.35 Å. The reduction of lattice parameters in samples C and D may suggest a polymorphic transition from β- to α-chitin, not observed in the FTIR and NMR data. Moreover, the preservation of the microfibrillar organization poses in favor of a β-chitin structure conservation.

The analysis of the angular spread of the meridional reflection (002) and of the equatorial

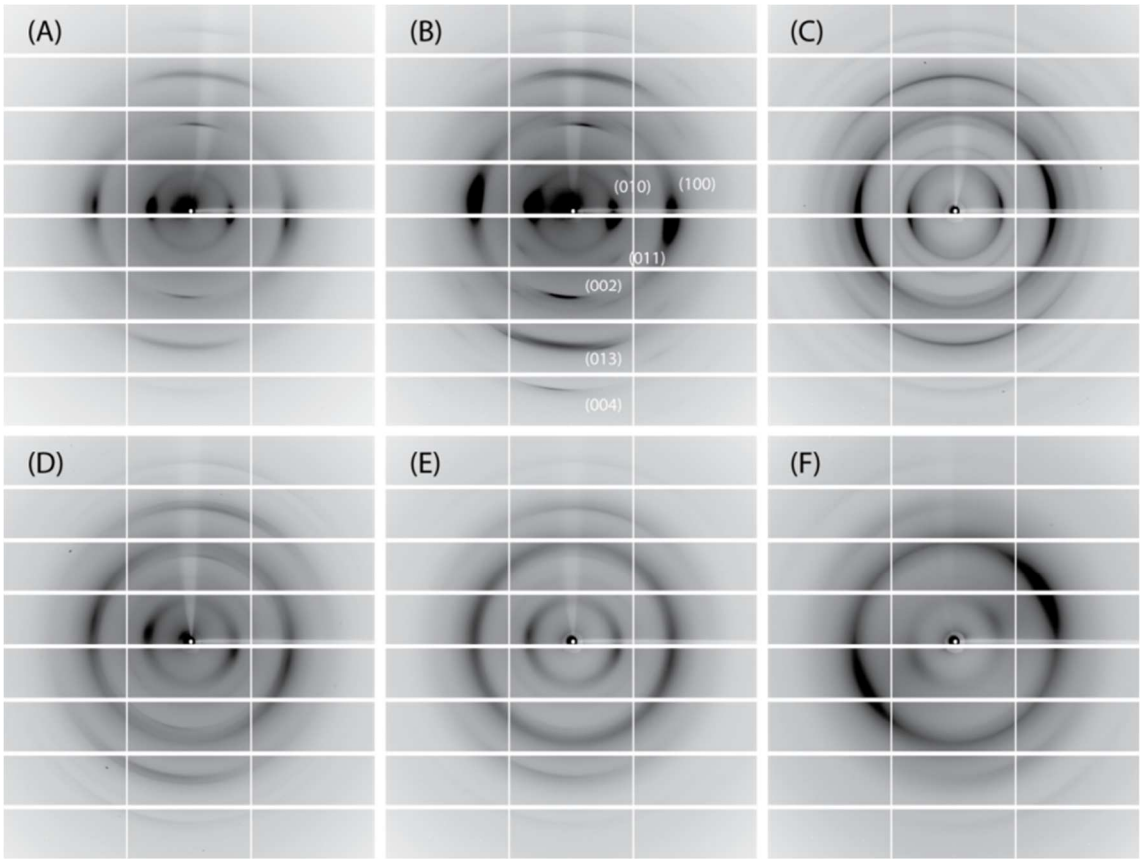

Figure 77: X-ray fiber diffraction images of chitin samples having different DA. The sample was mounted with a geometry having the X-ray beam normal to the fiber axis and parallel to the sample surface. The diffraction reflections were indexed according to the monoclinic unit cell for b-chitin.[45]

(100) one was used, together with the X-ray diffraction intensity ratio between the reflections (100) and (010) or (020), to evaluate the textural organization of the samples (Table 8). The results showed that the angular spreading of the fibers along the a-axis is more affected by the chemical treatment than the DA. In fact, an increase of the angular spreading was observed when 10 M NaOH solutions were used. Contrary, the angular spreading of fiber axis (c-axis) increased with the decrease of the DA. In addition to these observations, the intensity of the (010) and (100) reflections decreased with the DA. All this information can be rationalized considering that when a 10 M NaOH solution is used a partial swelling – disassembly – recasting process can occur. At this process is reasonably associated a molecular chain dis-alignment. This effect manifests more along the crystallographic direction in which the inter-chain interactions are weaker, i.e. the b-axis.[45] The inter-chain interactions along the a-axis and the c-axis are stronger, and accordingly the molecular chains preserve more their ordered assembly.

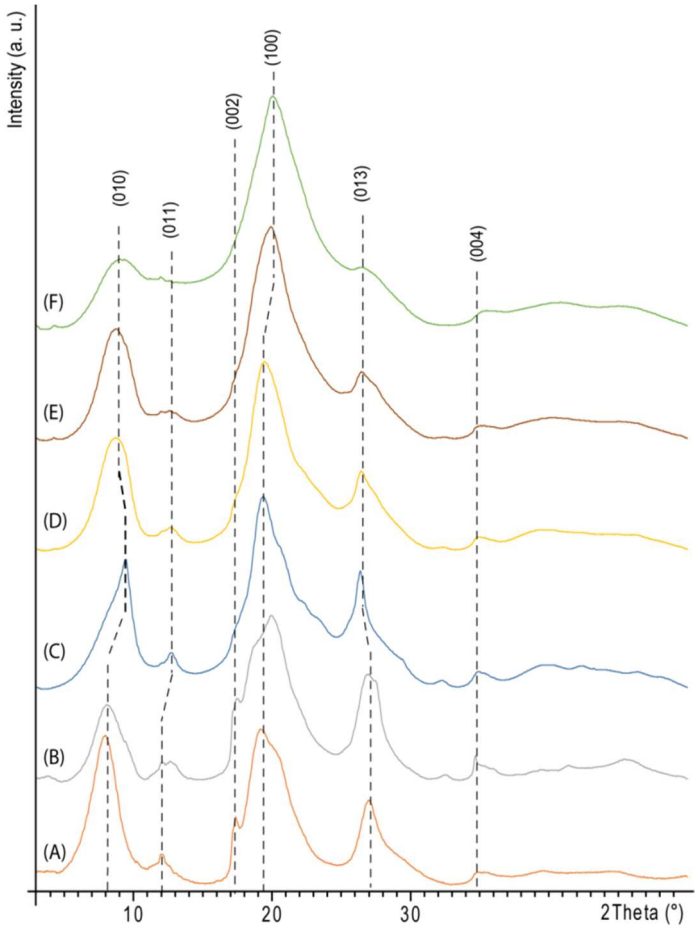

Figure 78: XRD pattern of chitin samples having different DA obtained carrying out integration of the diffracted intensity in the X-ray fiber diffraction images along the 2Θ angle. The diffraction peaks were indexed according to the monoclinic unit cell of β-chitin.[45]

Table 8: Analyses of the X-ray fiber diffraction images. The intensity ratio I010/I100 was evaluated from the maximum intensity of the reflections. The azimuthal angle full width half maximum (a.a. FWHM) was calculated from the X-ray diffraction analysis profile along the azimuthal angle corresponding at the reflection (002) and (100).

Sample	d_{010} / Å	d_{100} / Å	I_{010}/I_{100}	a.a.FWHM d_{002} / °	a.a.FWHM d_{100} / °
A	10.85	4.63	1.1	19	20
B	10.89	4.65	1.6	17	19
C	9.58	4.51	1.4	37	41
D	9.63	4.57	1.5	41	42
E	9.78	4.45	1.7	48	41
F[$]	9.78	4.36	2.8	-	44

[$] *This sample is chitosan obtained from β-chitin and in the X-ray fiber diffraction image does not show any orientation in the (002) reflection.*

Similar considerations can be derived from the analysis of the NMR spectra showing an enlargement of the C_1 and C_4 signals as the DA decreases to indicate a reduction in the sample crystallinity and a greater heterogeneity in the structure.[37]

In order to investigate the macroscale mechanical properties of these chitin samples, tensile tests were performed. The stress–strain curves showed relatively consistent trends for samples having different DA, with a rather linear trend until failure started, and a more or less pronounced post-yield deformation (Figure 79). Slipping, early breakage, breakage at the grips, or inhomogeneity in data were not observed. The samples A and B behaved similarly (stiffer than all the others, and with very limited plasticity) despite sample A was more acetylated than sample B. These samples showed significantly the same mechanical properties (T-test, p=0.05, v≥8). The latter had a DA similar to that of sample C, which showed a lower microfibrillar organization. Samples C, D and E showed stress–strain curves significantly equal between them (T-test, p=0.05, v≥8). Sample F, the one made of chitosan, had a different stress–strain curve compared to the others, with a more pronounced plastic behavior. This last sample showed anyway a significantly similar Young's modulus, E, and max stress, σ_{max} (T-test, p=0.05, v≥8), as samples C-E. The mechanical properties extracted from the stress–strain plots are summarized in Table 9 and some parameters have been plotted in Figure 80.

The DA had a highly significant effect on the E (one-way ANOVA, $p = 3 \cdot 10^{-9}$), on the yield stress, σ_{yield} ($p = 4 \cdot 10^{-5}$), on the σ_{max} ($p = 2 \cdot 10^{-4}$), on the work required to reach yield (p =

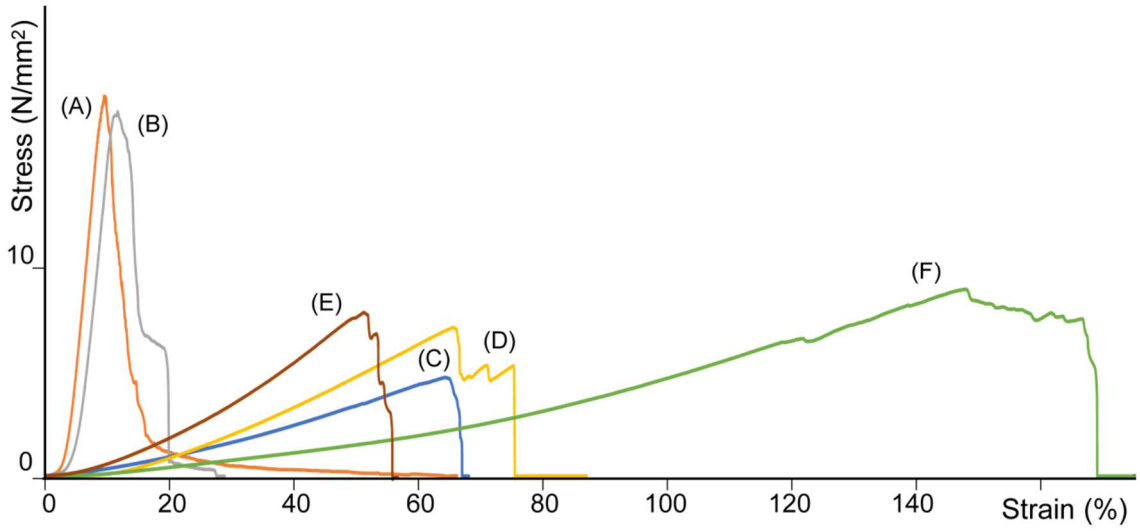

Figure 79: Typical stress-strain plots from the uniaxial tensile tests. One specimen for each group is shown; all the specimens from the same group exhibited similar trends.

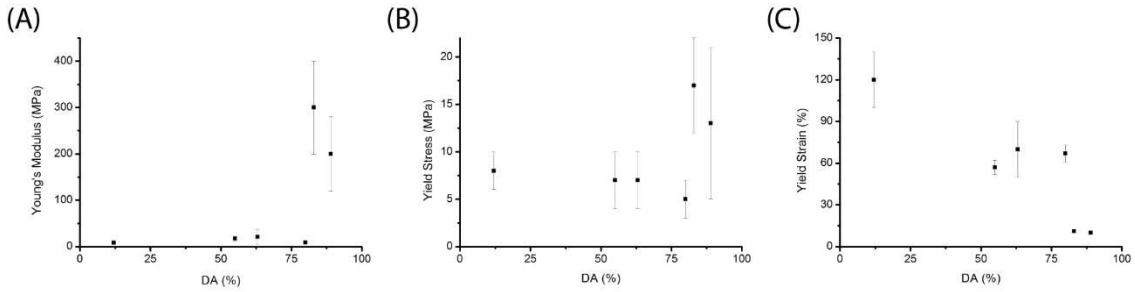

Figure 80: Plot of different mechanical parameters versus DA: Young's modulus (A), yield stress (B) and yield strain (C).

Table 9: Mechanical properties and degree of acetylation of the different samples (mean and standard deviation).

Sample	DA / %	E / MPa	σ_{yield} / MPa	σ_{max} / MPa	ε_{yield} / %	ε_{max} / %	Work at Yield / mJ·mm^{-3}	Work total / mJ·mm^{-3}
A	89	200 ± 80	13 ± 8	15 ± 3	9.9 ± 0.9	60 ± 10	0.6 ± 0.3	1.5 ± 0.6
B	83	300 ± 100	17 ± 5	17 ± 5	11 ± 1	42 ± 6	0.6 ± 0.2	1.3 ± 0.4
C	80	9 ± 3	5 ± 2	5 ± 1	67 ± 6	90 ± 20	1.3 ± 0.4	1.9 ± 0.7
D	63	21 ± 16	7 ± 3	8 ± 4	70 ± 20	90 ± 30	2.0 ± 0.7	3 ± 1
E	55	17 ± 5	7 ± 3	7 ± 3	57 ± 5	67 ± 7	1.7 ± 0.8	1.4 ± 0.3
F	12	8 ± 2	8 ± 2	9 ± 3	120 ± 20	200 ± 10	4 ± 1	9 ± 3

$3 \cdot 10^{-5}$) and failure ($p = 3 \cdot 10^{-7}$). The E of samples A and B were one order of magnitude higher than that of samples C-F. The σ_{yield} and the σ_{max} drastically decreased from A and B samples to C-F samples. The yield strain, ε_{yield}, and the max strain, ε_{max}, also showed a similar trend: they increased by a factor five from samples A and B to sample C-E, and was about ten times higher from samples A and B to chitosan (F). The work to reach the first failure and the maximum work decreased markedly from the chitosan sample (F) to samples C-E and further decreased for samples A and B.

The E was moderately correlated to the DA ($R^2 = 0.335$); the σ_{yield} and the σ_{max} exhibited a poor correlation with the DA ($R^2 = 0.172$ and $R^2 = 0.124$, respectively).

Conversely, the ε_{yield} and the ε_{max} were highly correlated with the DA ($R^2 = 0.780$ and $R^2 = 0.790$ respectively). The work to yield and to failure was even more linearly correlated with the DA ($R^2 = 0.955$ and $R^2 = 0.825$ respectively).

The observations on mechanical properties could be related to the structural and microfibrillar organization of the chitin molecules. The latter showed a decreasing of inter-

plane regularity, and homogeneity of interactions decreasing the DA. Since the tensile test was carried out applying an uniaxial deformation parallel to the c-axis, the sample deformation requires the breakdown of interactions perpendicular to this axis, i.e. along the b- and a- axis. Since the chitin chain interactions along the a-axis are very strong, those along the b-axis are the sacrificial ones. Among the prepared samples, the weakest were in sample F and the strongest in samples A and B. Samples A and B showed the highest values of E and σ_{max}, while sample F the lowest one. Accordingly, the ε_{max} was expected to be higher in samples with the weaker inter-plain interactions, as effectively observed.

On the base of the results achieved the possibility to customize the material's mechanical properties from a stiff to a more compliant one could lead to a broad range of applications. Samples A and B behaved similarly and find application as chitin films as the ones reported in the introduction. On the other hand, sample F behaved as a chitosan film and could be applied accordingly. Samples C, D, and E, instead, cover a gap that has not been explored yet. Those samples have intermediate properties compared to the previous ones with both moderate mechanical resistance and elasticity. This class of samples also exhibited a higher resistance to dissolution, with respect to high DA chitin or chitosan samples, being insoluble to LiCl 5 wt.% / DMAA, and to acetic acid pH 3 / water. Moreover, the possibility of being able to maintain similar mechanical properties along a wide range of de-acetylation could be intriguing for further functionalization. The higher amino groups available may lead to a different degree of functionalization of the material maintaining mechanical performances common to the chitin sample's family. The different charge of the samples, due to the content of free amino groups, could also be used to study how in composite materials (i.e. dye/metal adsorbed, calcified, blended, etc.) the electrostatic interaction influences the mechanical performances, knowing that the chitinous structure itself does not change its properties.

3.2. Conclusion

This research reports a complete study on the forms of chitin using the same source differently chemically treated. As starting material β-chitin from squid pen was used and the experimental set up was planned with the aim to preserve the microfibrillar organization of the samples having different DA. The obtained results show that the mechanical properties of the chitin do not have a linear dependence from the DA, except for yield and maximum strains. They show also that the structural organization of the chitin macromolecules is affected by the DA mainly in the inter-plane interactions among chitin molecules, while the in-plane interactions remain almost unaffected.

The knowledge from this research may have important implications in the design of new materials based on chitin since it shows that by a simple chemical treatment structural and mechanical properties can be customized on macroscopic samples, but it has also relevance for the understanding of the mechanical properties of chitinous biological samples.

3.3. Materials and methods

Materials All the reagents and solvents were purchased from Sigma Aldrich and utilized without any further purification. Squid pens from the species *Loligo vulgaris* were obtained from a fish market in Bologna Italy.

β-chitin purification Squid pens were washed abundantly with water, then soaked in an HCl solution at pH 3 (20 g of squid pen in 1 L of solution) for 5 h and washed again with water. While hydrated the squid pen where cut to eliminate the central rib. To eliminate the squid pen proteins, the lateral blades collected were set in a boiling solution of NaOH 1M (10 g of squid pen in 250 mL of solution) and stirred for 1 h. After this time, the solution was eliminated, replaced with new clean NaOH solution, and stirred at 100 °C for one hour more. The β-chitin obtained was washed two times with 100 mL of warm NaOH 1M and then with distilled water until neutral pH. The chitin purified was stirred two times in ethanol (100 mL) for 30 min each, to eliminate eventual lipid contents, then two times in distilled water. Finally, the sample was conserved dried in a desiccator.

Sample preparation The β-chitin (or chitosan) samples were de-acetylated by treating 0.5 g of β-chitin in 40 mL of NaOH solution (5 or 10 M) at different times and temperatures, accordingly with reported procedures.[32][33] Then, the samples were washed two times with 10 mL of NaOH solution, and with distilled water until neutral pH. The samples were conserved dried in a desiccator.

Nuclear magnetic resonance measurements The NMR experiments were performed on a Bruker Advance spectrometer operating at the frequency of 300 MHz for proton (equipped with a 4mm MAS BB probe) using the combined techniques of cross polarization and magic angle spinning. Field strengths corresponding to 90° pulses of 4.5 μs were used for the matched spinlock cross-polarization transfer ^{1}H to ^{13}C. The contact time was 1 ms, and the recycle delay 10 s. A typical number of 500–3000 scans were acquired for each spectrum. The chemical shifts were externally referred by setting the carbonyl resonance of glycine to 176.03 ppm. Glycine full width at half-height better than 27 Hz. The spinning speed was set at 8000 Hz for all samples. The assignment of the NMR signals was done according to literature.[37][38]

Molecular weight measurement A solution 0.1 wt.% of sample in N,N-dimethylacetamide, LiCl 5 wt.% was obtained after a two hour reflux. The solution was successively stirred at room temperature for 24 hours and then centrifuged 90 minutes at 8000 rpm. The solution on top was collected from the centrifuge tube and analyzed using dynamic light scattering using a Zetasizer Nano ZS, Malvern. The measure was performed five times using a refractive index of 1.56 for chitin. The molecular weight was extrapolated correlating it with the hydrodynamic radius as reported by Terbojevich, Carraro, & Cosàgi, 1988.[39]

Thermal and calorimetric analysis TGA were performed on a SDT Q900 simultaneous thermal analysis instrument (TA instrument). DSC were performed on a DSC Q100 simultaneous thermal analysis instrument (TA instrument). The analysis were both performed under nitrogen flow from 25 to 450 °C, with a pre-equilibration at 25 °C, and a heating rate of 10 °C·min^{-1}.

Scanning Electron microscopy images SEM imaging was performed on uncoated samples using a Phenom G2 Pure with an energy of 3 Kv. Gold coated (2 nm) samples were observed using a Hitachi SEM 6400 operating at 15 kV.

Fourier transform infrared spectroscopy The infrared spectra were registered in an FTIR Nicolet Magna (Nicolet Analytical Instruments, Madison, WI) connected to a PC with Omnic software (Thermo Electron Corp., Woburn, MA) for data processing and baseline correction. The samples were prepared in KBr pellets at a concentration of 2 wt.%. The spectra were obtained with 4 cm^{-1} resolution and 64 scans. Peak assignment was done according to literature, Table 10.

X-ray diffraction analysis X-ray fiber diffraction diagrams were collected at XRD1 beamline, Elettra, Trieste, Italy. Each frame was collected at the peak wavelength (0.9999 Å) using an exposure of 60 s. The X-ray diffraction diagrams were analyzed using Fit2D software.[46]

Table 10: Assignment of the vibration bands of chitin samples.[47]

Vibration modes	**A**	**B**	**C**	**D**	**E**	**F**
OH out-of-plane bending	690		687	669		
Ring stretching	899	898	899	898	892	898
CH_3 wagging	944	945	945	945	945	944
CO stretching	1034	1033	1032	1036	1035	1134
CO stretching	1068	1072	1066	1069	1068	1169
Asymmetric in-phase ring stretching mode	1111	1115	1110	1112	1111	
Asymmetric bridge oxygen stretching	1155	1156	1155	1155	1156	1154
Amide III	1202	1201	1202		1202	
band and CH_2 wagging	1313	1312	1315	1315	1315	1315
CH bending and symmetric CH_3 deformation	1377	1375	1377	1377	1377	1377
CH_2 bending and CH_3 deformation	1421	1435	1421	1420	1427	1424
Amide II band	1555	1558	1555	1555	1556	1556
Amide I band	1654	1653	1654	1654	1648	1648
CH stretching		2851	2857	2855	2851	2852
Symmetric and asymmetric CH_3 stretching	2884	2872	2878		2878	2877
CH_3 stretching	2931	2918	2920	2920	2920	2920
NH stretching	3097	3099	3095	3094	3093	
NH stretching	3299	3304	3289	3287		
OH stretching	3406	3398	3421	3427	3434	

Uniaxial traction testing Monotonic uniaxial tensile tests were performed using a universal testing machine (Mod. 4465 with Series IX software, Instron) and dedicated grips. The tests were performed with an actuator speed of 5 mm·min^{-1} (resulting in a strain rate of about 0.3 %·sec^{-1}) at room temperature. Each sample was hydrated for 24 h in deionized water and then cut in a proper dimension using scissors. The actual width and thickness of each hydrated sample were measured using a SM-LUX POL microscope collecting images with a 5.0 MP digital camera (Motic Moticam 5+). The images were analyzed using ImageJ. Each sample was about 30 mm long, 5 mm wide, and 0.15 - 0.30 mm thick (the thickness varied between samples, because of the intrinsic variability of the initial biological samples). The samples were connected at the instrument, leaving a free length of 20 mm between the

clamps. As the curves were rather linear until failure started, the following parameters could be calculated, taking into account the actual dimensions of each specimen:

- The Young modulus of elasticity;
- The stress and strain when specimen failure started (yield, detected as a drop of the force by 1 %);
- The maximum stress, and strain;
- The work per unit volume required to reach yield and final failure (in $J \cdot mm^{-3}$).

At least five specimens were tested for each group. The Peirce criterion was adopted to detect and exclude outliers (15 % of the data had to be excluded).[48]

4. Hierarchically organized catechol-functionalized chitinous matrices

4.1. Results

In this work the chitinous architecture of the squid pen of *Loligo vulgaris* was functionalized on the free amino groups with catechols to obtain a functional material. A schematic of the different matrices prepared is reported in Figure 81.

The squid pen from *L. vulgaris* is a chitin based matrix composed of about 40 wt.% of proteins.[49] As in the previous section, the proteins were eliminated from the matrix using a 1 M NaOH solution treatment under reflux for 2 h. This occurs without inducing any change in the morphology and crystal structure of the chitinous matrix in the pen.[50] After this first alkaline treatment the DA of the chitin obtained was about 88 %.[50]

On the base of the data collected in the previous section, a second alkaline treatment was performed using a NaOH 5 M solution under reflux, see Figure 82 step 1, to increase the number of amino moieties in the matrix. In section 3 of this chapter was observed how this NaOH concentration gave the best results in preserving the overall structure of the matrix. The treatment was carried out for 2 h, 8 h, and 24 h obtaining a respective DA of 76.9 ± 0.6 %, 56 ± 1 %, and 32 ± 1 %. The 24 h treated matrix appeared curly and not uniform, we chose not to work with that almost chitosan matrix for practical reasons.

The two deacetylated chitin (DC) samples had a swelling higher than 200 %, Table 11, reached in less than 15 minutes.

The second step of the synthesis was the insertion of the catechol group, Figure 82 step 2. The reaction was performed applying a standard protein coupling in water. Different pHs were tested to prevent the catechol oxidation, Figure 83. Among them, pH 4 was the highest pH that prevents the oxidation in the reaction time (Figure 83). The proceeding of the reaction was checked monitoring the absorption peak of the catechol at 280 nm in the DC along the time, prior washing of the samples using a HCl solution at pH 4. As shown in Figure 83 the reaction appeared to reach a plateau in about 24 h.

After this synthetic step, the catechol-functionalized DC (C_f-DC) obtained from the chitin deacetylated for 8 h was in a gel state with swelling of 3000 ± 700 %, Table 11. Despite the birefringence of the matrix appeared intact, it was impossible to perform uniaxial tensile tests on this set of samples, even after metal insertion or crosslinking.

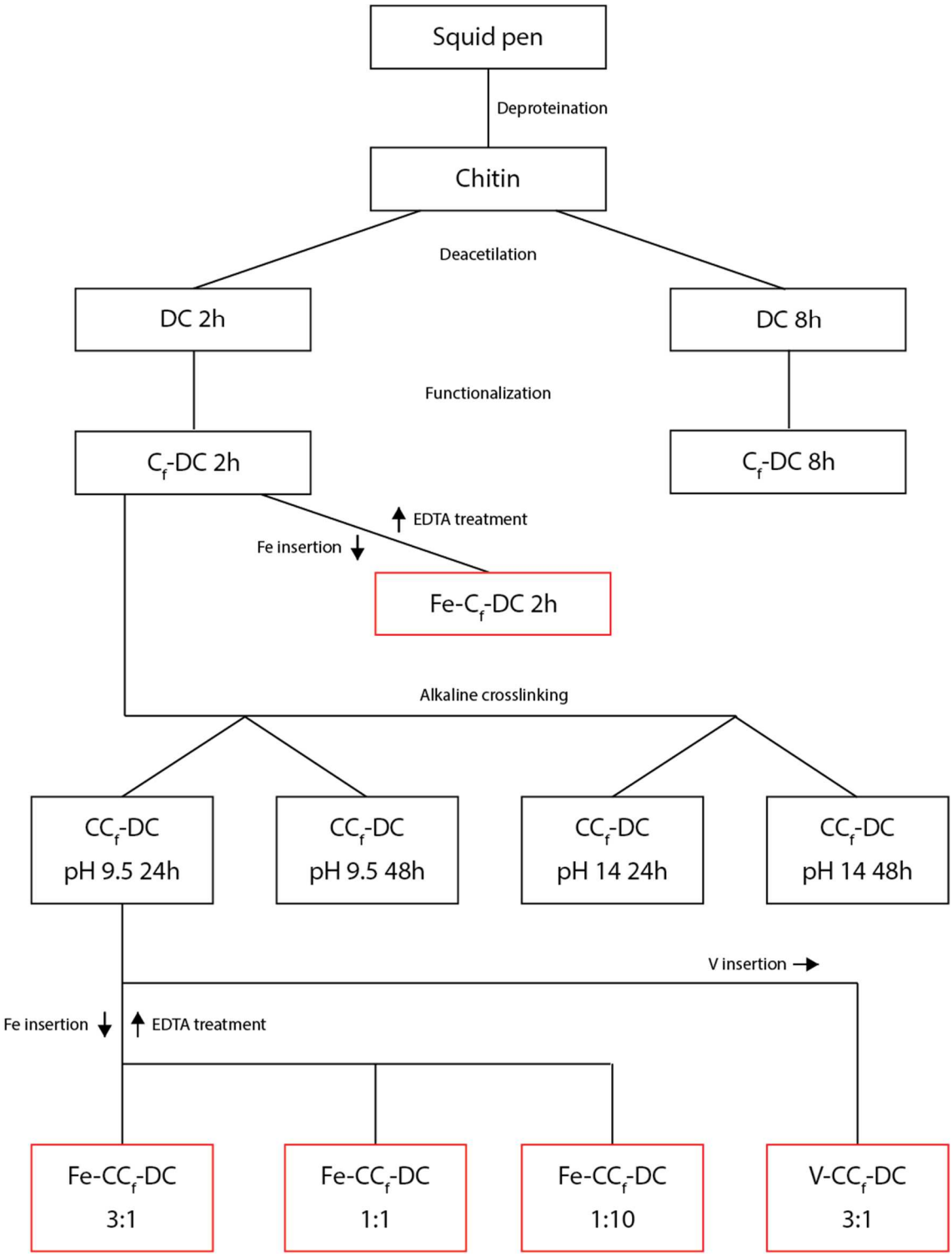

Figure 81: Scheme of the matrices tested in this work. In red the ones containing a metal.

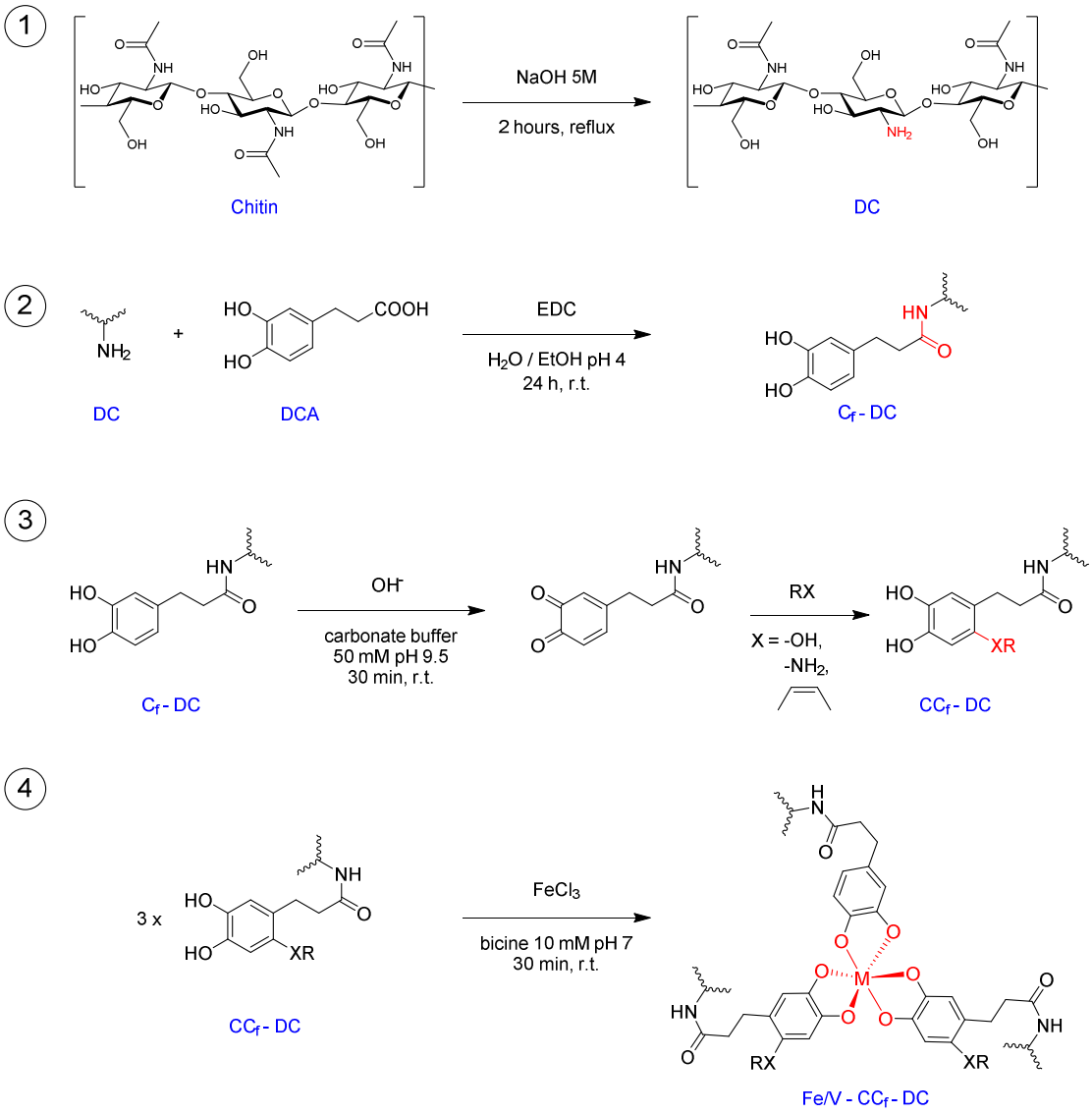

Figure 82: Scheme of the synthetic steps to functionalize the matrix. 1) Chitin partial de-acetylation. 2) Deacetylated chitin functionalization with catechols. 3) Catechol functionalized deacetylated chitin basic crosslinking. 4) Metal insertion in the matrix.

The metal insertion was optimized on the C_f-DC testing different pH of the bicine buffer, see Figure 84. An almost neutral buffered environment was necessary because trivalent iron ions in acidic environment catalyze catechol oxidation.[20] The metal insertion appeared to occur properly between pH 6 and 7.5. No pHs over 7.5 were tested to avoid iron precipitation or catechol oxidation due to the basic environment. Since no differences were observed in the pH 6-7.5 range, pH 7 was defined as pH for the metal insertion because in the optimal buffering range of the bicine buffer. UV-Vis spectra of the C_f-DC before and after metal insertion showed a typical broad catechol–iron peak appearing between 500 and 700 nm[20] in the metal treated matrices. These peaks came along with a

shift of the catechol signal from 280 to 288 nm. Only a weak signal of the o-quinone (oxidized catechol) at 400 nm was observed.[20] After metal insertion, the matrices appeared of a bright blue. The coloration disappeared after treatment with EDTA and the UV-Vis spectra were restored as the C_f-DC one. The presence of catechol-iron complexes was also confirmed using Raman spectroscopy, Figure 85.[20] No significant change in the swelling was observed after metal insertion, Table 11.

The mechanical properties of the samples were tested, Figure 86. The C_f-DC showed lower maximum and first failure stress (σ_{max}, $\sigma_{1st\ failure}$), total and first failure work ($Work_{Tot}$, $Work_{1st\ failure}$), and Young's modulus (E) and an increase in the maximum and first failure elongation (ε_{max}, $\varepsilon_{1st\ failure}$) in comparison to the DC. The Fe-C_f-DC showed a slight increase in the properties compared to the C_f-DC having a: comparable E to the DC, σ_{max} and $\sigma_{1st\ failure}$ intermediate between the C_f-DC and the DC, $Work_{Tot}$ and $Work_{1st\ failure}$ comparable to the C_f-DC, and a lower ε_{max}, $\varepsilon_{1st\ failure}$ compared to the DC.

Table 11: Swelling (%) of the different matrices in water, pH 7, or in HCl solution at pH 4.

Sample	***pH 7***	***pH 4***
DC (2h)	240 ± 10	230 ± 20
DC (8h)	220 ± 10	285 ± 8
C_f-DC (2h)	-	570 ± 40
C_f-DC (8h)	-	2900 ± 700
Fe-C_f-DC (2h)	500 ± 200	-
CC_f-DC (pH 9.5, 24h)	300 ± 100	-
CC_f-DC (pH 9.5, 48h)	500 ± 200	-
CC_f-DC (pH 14, 24h)	500 ± 100	-
CC_f-DC (pH 14, 48h)	400 ± 200	-
3:1 Fe-CCf-DC	260 ± 40	-
1:1 Fe-CCf-DC	280 ± 10	-
1:10 Fe-CCf-DC	320 ± 10	-
3:1 V-CCf-DC	230 ±10	-

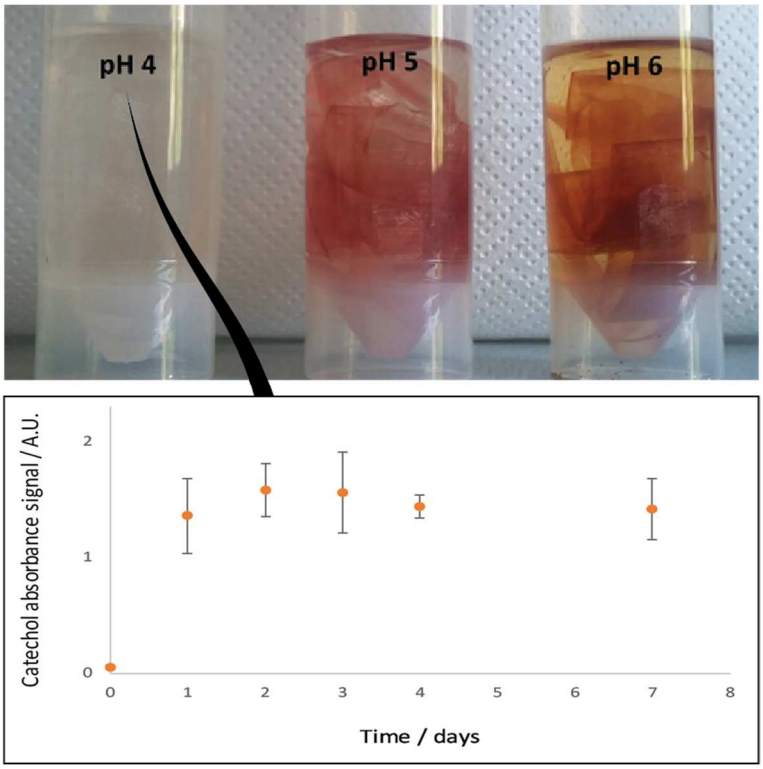

Figure 83: (top) Test of coupling reaction at different pHs. After 24h only pH 4 did not show the reddish coloration typical of oxidized catechols. (bottom) A kinetic of functionalization at pH 4 showing how the 280 nm signal of the catechol stabilize after 24 h of treatment.

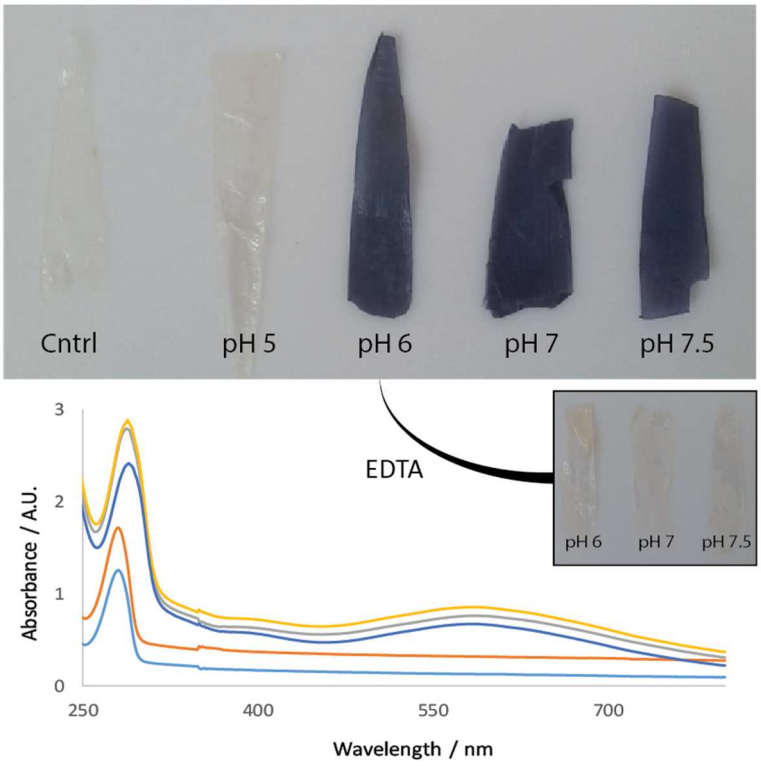

Figure 84: UV-Vis spectra and pictures of the C_f-DC treated with iron (III) at different pHs: 4 (blue), 5 (orange), 6 (grey), 7 (yellow), and 7.5 (blue). An insight shows the metaled matrices after EDTA treatment.

Catechols can also undergo to covalent crosslinking throw oxidation, Figure 82 step 3. The C_f-DC was covalently cross-linked using a basic environment as an alternative way to tune its mechanical properties. A basic environment was chosen instead of stronger oxidative conditions to get a slow oxidation that would allow the matrix to reorganize avoiding, as much as possible, to re-oxidize the catechols after the crosslinking.

Three different pHs were tested, pH 7, 9.5 and 14, for two different times, 24 h and 48 h. The UV-Vis absorption spectra showed no relevant crosslinking at pH 7. The pH 9.5, instead, showed the quinone peak at about 400 nm and an increase of the absorption below 400 nm due to the formation of diverse aromatic species. pH 14 showed a similar pattern of signals as at pH 9.5 but a more intense signal of the quinone was observed, see Figure 87. Only the matrix treated at pH 9.5 for 24 h showed a decrease in the swelling, Table 11.

Except for pH 7, the mechanical properties were tested for all the different cross-linked C_f-DC (CC_f-DC). The different conditions appeared rather similar one to the other but the one at pH 9.5 for 24h showed a higher σ_{max} and E compared to the other conditions. The values were comparable with those of DC except for the lower ε_{max} and $Work_{Tot}$. The mechanical data of the matrices are all reported in Figure 86. With CC_f-DC, when not specified differently, we will refer to the samples treated at pH 9.5 for 24 h.

The metal was inserted in a 3:1 ratio between the free amine groups and iron (Fe-CC_f-DC) or vanadium (V-CC_f-DC), Figure 82 step 4. The iron was also studied with a 1:1 and 1:10 ratio. The UV-Vis absorption peak for iron-catechol was observed in Fe-CC_f-DC. Similarly, the V-CC_f-DC showed a broad peak at about 550 nm (Figure 88). The Raman spectra also showed signals of iron-catechol complexes but no signals of the vanadium-catechol complex were detected, Figure 85. The 3:1 Fe-CC_f-DC was then treated using EDTA inducing a loss of the UV-Vis absorption band of the catechol-iron complex and a change in the coloration, Figure 93.

The structural integrity of the matrices was investigated by XRD using synchrotron radiation, Figure 89 and Figure 90. The diffraction images show how all samples maintained a comparable fibril alignment, with only a few exceptions. The CC_f-DC (pH 14, 48h) showed a loss of anisotropy in the diffraction image compared to the other samples, and a shift of the (100) peak in the diffraction pattern. A slight shift of the (010) peak was also observed in the C_f-DC sample. Finally, the Fe-CC_f-DC showed a broader pattern in the diffraction image, which was not observed as pronounced after EDTA treatment.

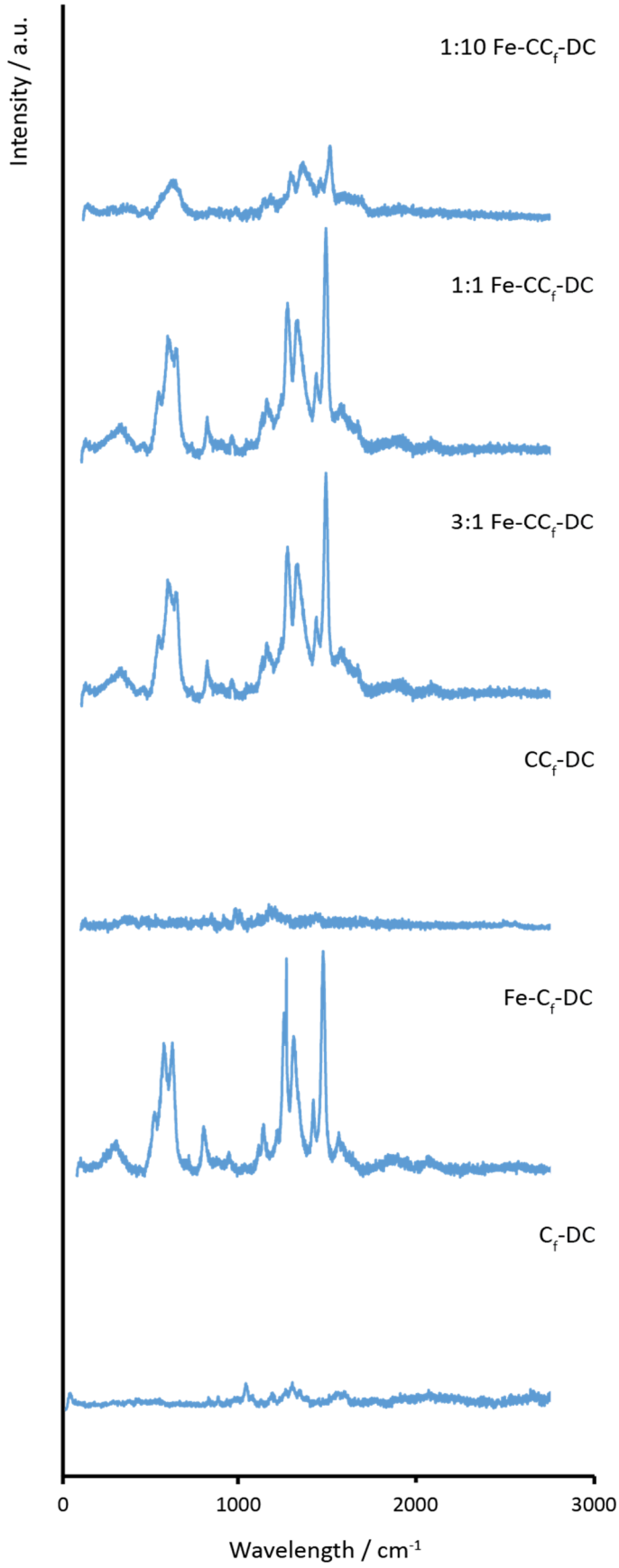

Figure 85: Raman spectra of the different matrices. According to literature, all the samples containing iron show only catechol-Fe signals, as the Fe-O bond vibrations in the 500–700 cm^{-1},[20] *chitin signals were observed in all the samples.*[51]

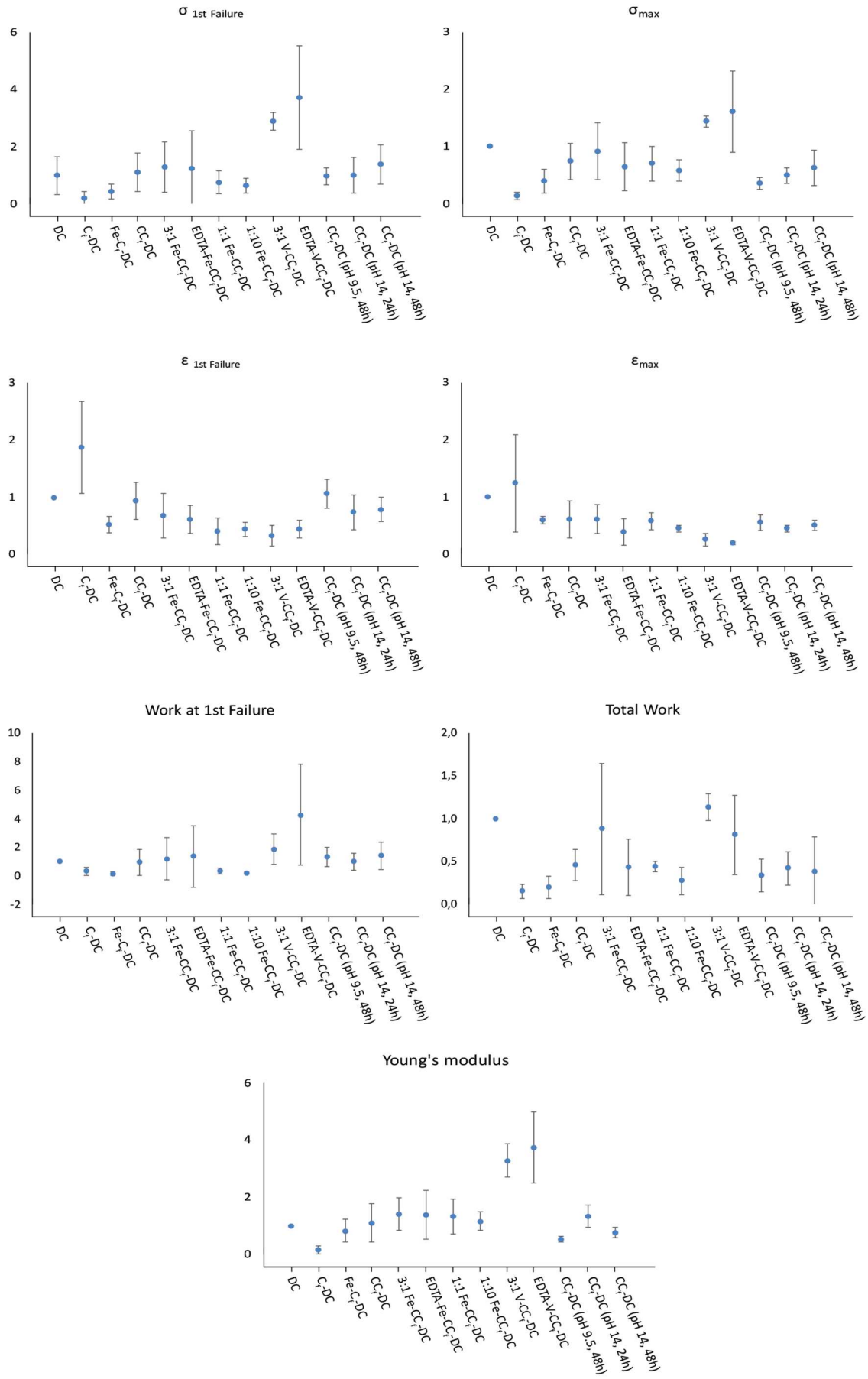

Figure 86: Mechanical data of the different matrices synthetized, normalized on the DC value.

Table 12: Mechanical parameters of the matrices studied normalized on the DC values.

	E	$Work_{Tot}$	ε_{max}	σ_{max}	$Work_{1st\ Failure}$	$\varepsilon_{1st\ Failure}$	$\sigma_{1st\ Failure}$
DC	1	1	1	1	1	1	1
C_f-CD	0.2 ± 0.1	0.15 ± 0.08	1.2 ± 0.8	0.14 ± 0.06	0.3 ± 0.3	1.9 ± 0.8	0.2 ± 0.2
3:1 Fe-C_f-CD	0.8 ± 0.4	0.2 ± 0.1	0.61 ± 0.07	0.4 ± 0.2	0.2 ± 0.1	0.5 ± 0.1	0.5 ± 0.3
CC_f-CD	1.1 ± 0.7	0.5 ± 0.2	0.6 ± 0.3	0.7 ± 0.3	0.9 ± 0.9	0.9 ± 0.3	1.1 ± 0.7
3:1 Fe-CC_f-CD	1.4 ± 0.6	0.9 ± 0.8	0.6 ± 0.2	0.9 ± 0.5	1 ± 1	0.7 ± 0.4	1.3 ± 0.9
EDTA-Fe-CCf-CD	1.4 ± 0.8	0.4 ± 0.3	0.4 ± 0.2	0.6 ± 0.4	1 ± 2	0.6 ± 0.3	1 ± 1
1:1 Fe-CCf-CD	1.3 ± 0.6	0.44 ± 0.06	0.6 ± 0.1	0.7 ± 0.3	0.3 ± 0.2	0.4 ± 0.2	0.8 ± 0.4
1:10 Fe-CCf-CD	1.2 ± 0.3	0.3 ± 0.2	0.46 ± 0.06	0.6 ± 0.2	0.20 ± 0.07	0.5 ± 0.1	0.7 ± 0.2
3:1 V-CCf-CD	3.3 ± 0.6	1.1 ± 0.2	0.3 ± 0.1	1.4 ± 0.1	2 ± 1	0.3 ± 0.2	2.9 ± 0.3
EDTA-V-CCf-CD	4 ± 1	0.8 ± 0.5	0.21 ± 0.03	1.6 ± 0.7	4 ± 4	0.4 ± 0.2	4 ± 2
CC_f-CD (pH 9.5, 24h)	0.5 ± 0.1	0.3 ± 0.2	0.6 ± 0.1	0.4 ± 0.1	1.3 ± 0.7	1.1 ± 0.3	1.0 ± 0.3
CC_f-CD (pH 14, 24h)	1.3 ± 0.4	0.4 ± 0.2	0.46 ± 0.06	0.5 ± 0.1	1 ± 0.6	0.7 ± 0.1	1.0 ± 0.6
CC_f-CD (pH 14, 48h)	0.8 ± 0.2	0.4 ± 0.4	0.52 ± 0.09	0.6 ± 0.3	1.4 ± 0.9	0.8 ± 0.2	1.4 ± 0.7

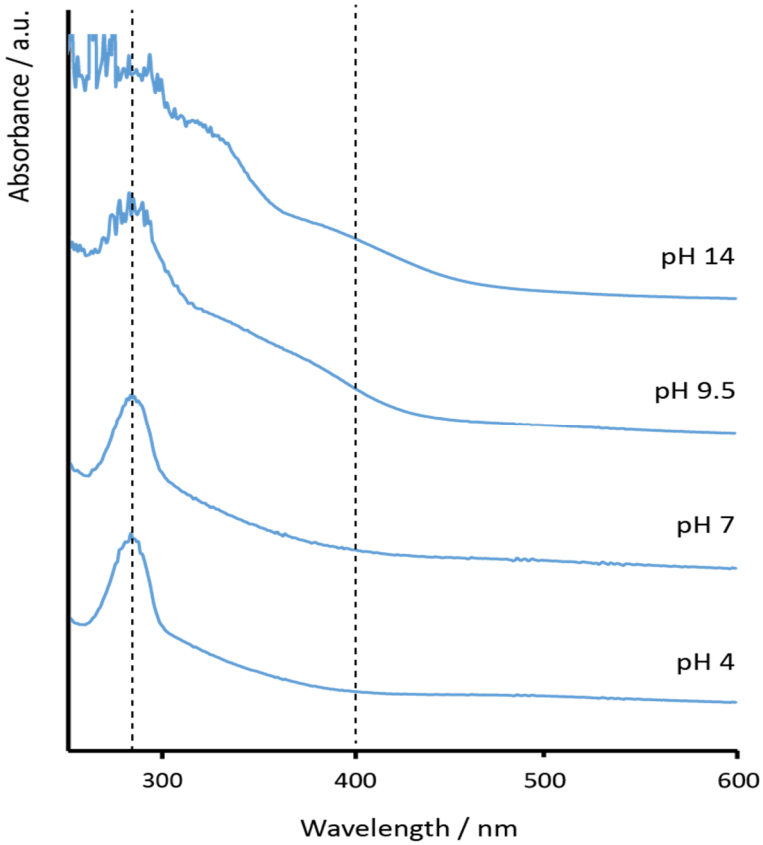

Figure 87: UV-Vis spectra of the matrices cross-linked at different pHs after 24 h. No differences in the spectra were observed at 48 h. Dashes lines refer to the catechol signal at 280 nm and the o-quinone signal at about 400 nm.

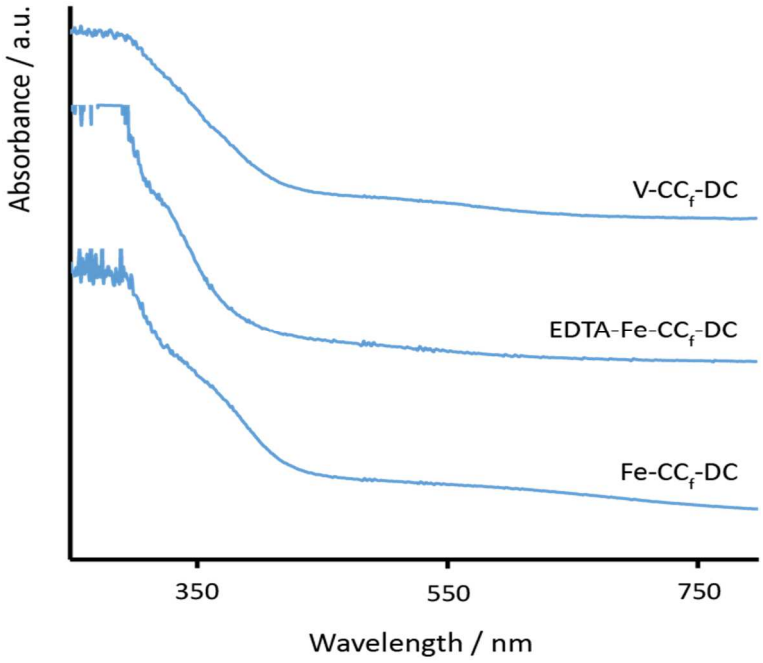

Figure 88: UV-Vis spectra of metaled matrices, both the iron and vanadium treated matrices show a broad signal between 500 and 700 nm. No differences in the spectra were observed using different ratio of iron (here the 3:1 is reported).

The morphology and organization of the sample was examined using SEM, observing the sample longitudinal section and external surface. The initial DC scaffold presented an almost homogenous surface with a parallel fibrous organization and a lamellar structure in the section. The sample surface was almost unaltered in all the samples examined becoming a little more homogenous compared to the DC but still showing an aligned fibrous arrangement. A difference in morphology was observed in sample C_f-DC where it was not possible to observe the lamellar structure in the section, which appeared in a foam-like state. This structure was restored after the cross-linking in sample CC_f-DC and was maintained after metal treatment and metal removal. A clustering of the layers was observed after Fe^{3+} and V^{3+} treatment. This clustering disappeared after EDTA treatment in sample Fe-CC_f-DC (EDTA-Fe-CC_f-DC) but not in sample V-CC_f-DC (EDTA-V-CC_f-DC). The SEM images are reported in Figure 91, and Figure 92.

As observed in Figure 93 the overall structure of the squid pen was conserved along all the synthetic steps.

The metaled CC_f-DC were tested in uniaxial traction as reported in Figure 86 and Table 12. The 3:1 Fe-CC_f-DC showed a slight improvement of the E, σ_{max} and $Work_{Tot}$, and a decrease in the $\varepsilon_{1st\ failure}$ compared to the CC_f-DC. Once treated with EDTA the parameters became

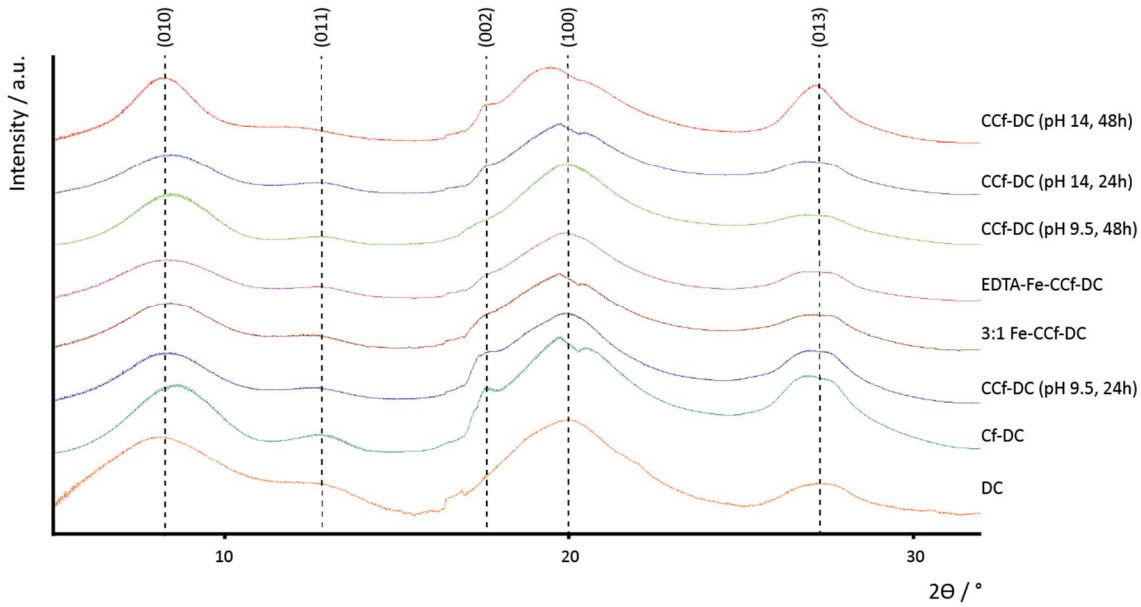

Figure 89: Synchrotron X-ray diffraction pattern of different dry samples. The diffraction pattern were obtained carrying out an integration of the diffracted intensity in the X-ray fiber diffraction images along the 2Θ angle. The diffraction peaks were indexed according to the monoclinic unit cell of β-chitin.[45]

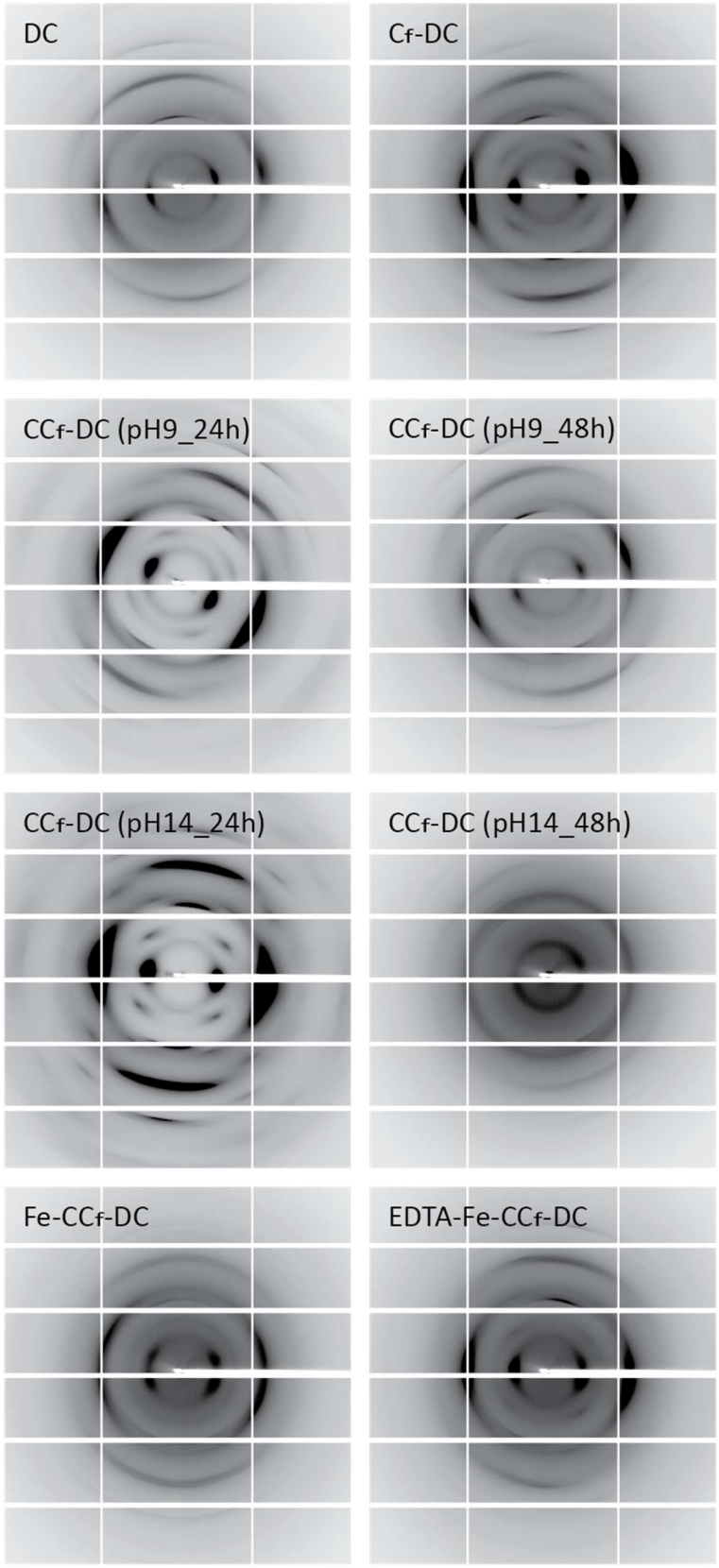

Figure 90: Synchrotron X-ray fiber diffraction images of the samples leading to the sample, 3:1 Fe-CC_f-DC.

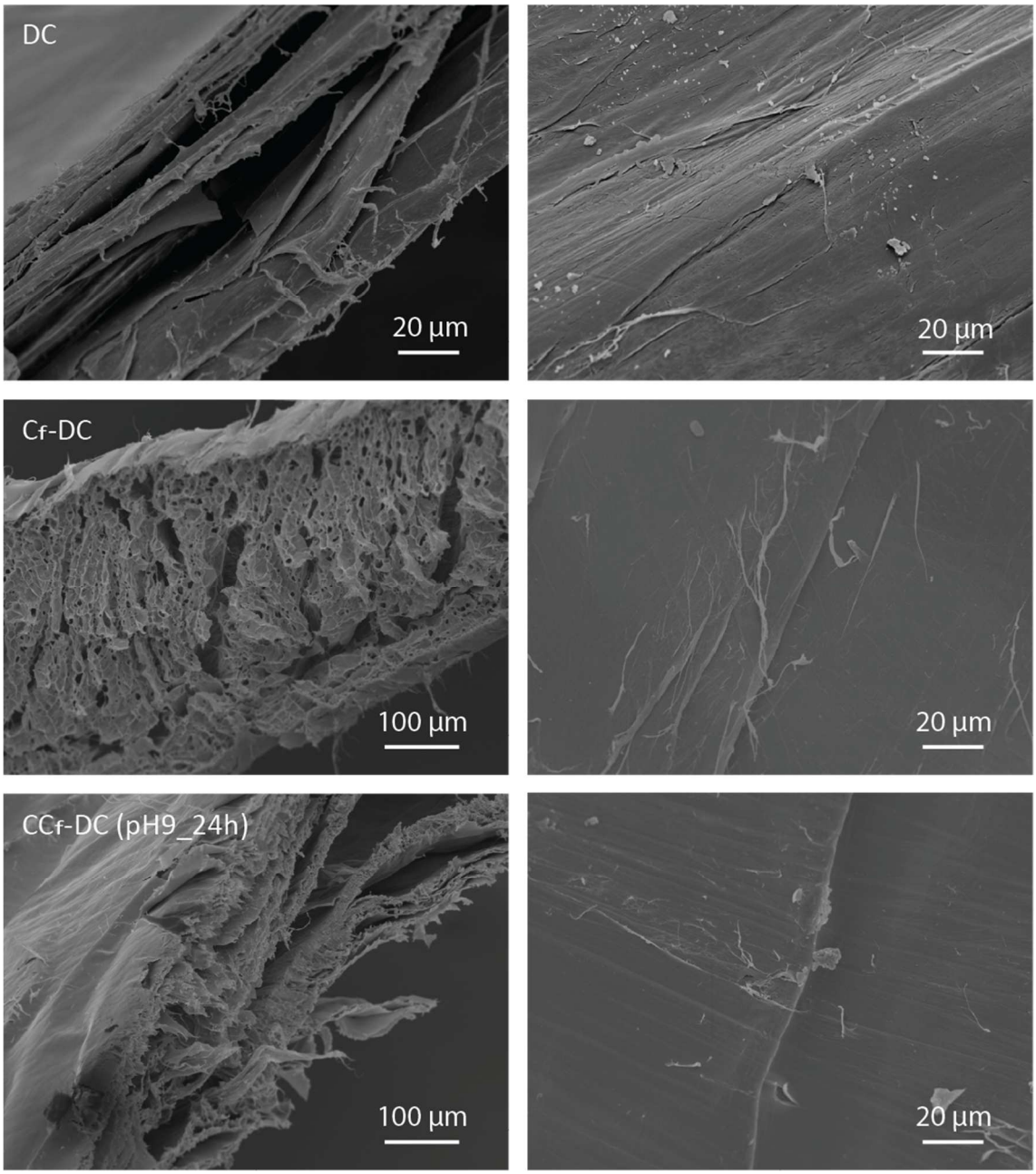

Figure 91: SEM images of matrices without metal. On the left, image of a section showing the lamellar structure of the chitinous matrix. On the right, an image of the sample surface.

more similar to the one of CC_f-DC. A general slightly more brittle behavior was observed increasing the iron ratio. The V-CC_f-DC, instead, showed a huge increase in their mechanical properties compare to all the other samples and a marked decrease in the swelling. Compared to the DC this matrix has almost 3 times the $\sigma_{1st\ Failure}$ and E, 1.5 times the σ_{max}, and 2 times the $Work_{1st\ failure}$. On the other hand, the elongation appear to be 3 times lower than the DC. Contrary to the iron treated sample, the V-CC_f-DC, when treated with EDTA, seems to not change, or even increase, its mechanical resistance.

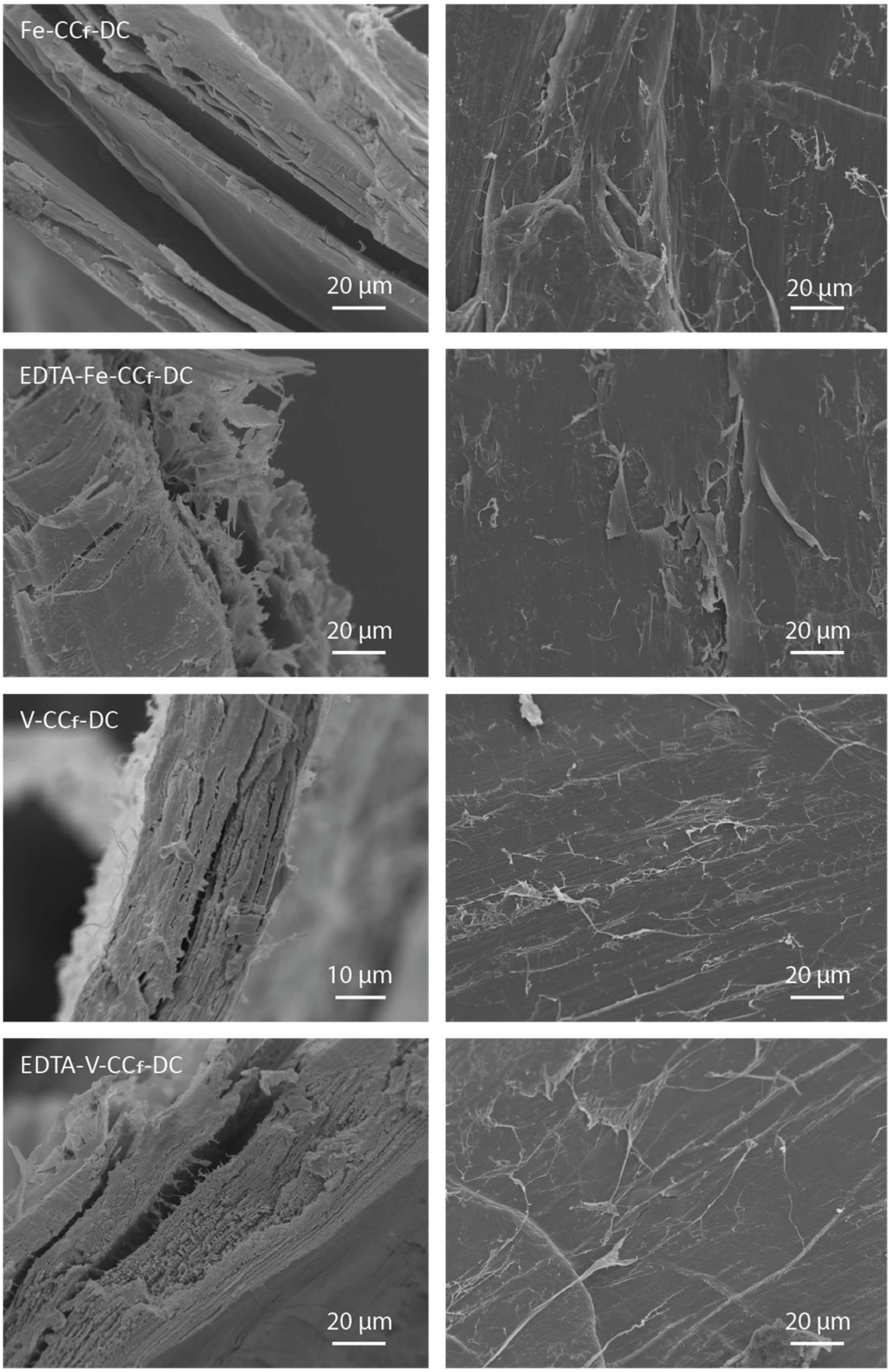

Figure 92: SEM images of cross-linked matrices after metal insertion and removal with EDTA. On the left, images of the sample section. On the right, images of the sample surface.

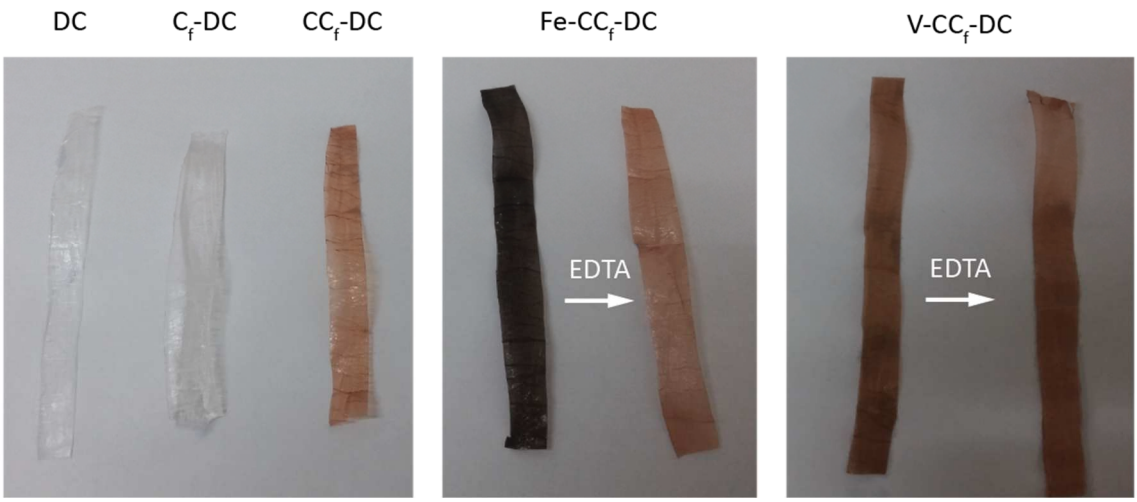

Figure 93: Picture of different matrices obtained in different stages of the synthesis, the iron treated sample showed is the 3:1.

4.2. Discussion

This work investigates the synthesis of different matrices using consecutive synthetic steps, reported in Figure 81, optimized along the study. The final goal was to obtain a chelating and/or cross-linked material bioinspired to mussel's byssus cuticle.

The spectroscopic data collected confirmed the actual functionalization of the DC with catechol moieties, showing how this matrix was able to bind reversibly trivalent iron ions. Despite this new property introduced in the matrix, the materials obtained were softer compared to the initial DC. Considering that no changes between the C_f-DC and the Fe-C_f-DC were observed in the swelling, probably the catechol groups were too distant to induce a proper cross-linking in the matrix.

Successively, the catechols in the matrix were oxidized to induce a covalent cross-linking. In this reaction, the catechols oxidize to o-quinone, and then react with heteroatoms throw a Michael addition reducing back to their initial dihydroxy form. This further functionalization was verified by UV-Vis spectroscopy. The materials obtained from different treatments showed comparable mechanical parameters to that of DC, except for the maximum elongation. This result is coherent with that of cross-linked materials. The condition at pH 9.5 for 24 h was considered the one giving the best mechanical results. This might be due to a lower stabilization of the oxidized form and a slower kinetic of oxidation compared to the pH 14 samples. In fact, samples at pH 14 quickly turn yellow once in solution, meaning that the catechols were oxidized, and maintained this coloration until

the final washing with water. Probably the cross-linking of the matrices occurred all at once when the pH was decreased leading to short-range linkages. At pH 9.5, instead, the matrix changed color along the time fading from colorless to reddish, suggesting a slow oxidation took place without any accumulation of oxidized catechols in the matrix. The decrease in swelling observed is a validation that a proper cross-linking occurred. Raman and UV-Vis spectroscopy confirmed the CC_f-DC as a chelating matrix.

The CC_f-DC treated with iron in a 3:1 ratio showed a slight increase in the stress, work, and E maintaining a similar elongation. The other ratios of metal did not show differences compared to the CC_f-DC. This result might imply that mainly 1:1 Fe-catechol complexes were formed in these last conditions, inducing no cross-linking in the matrix. Once treated with EDTA the matrix showed a change back to the CC_f-DC. This conversion was not completely observed, probably because a further cross-linking was induced by free iron ions in solution during the metalation and de-metalation treatments.

Despite the similar chemical behavior of iron and vanadium, the V-CC_f-DC showed completely different results. The vanadium-catechol complexes should give a higher Raman signal compared to iron complexes[10] but no signals were detected. Moreover, the UV-Vis signal observed might be attributed to the presence of V (II).[52][53] This would mean that the color change was induced by the adsorption of V (II) on the matrix rather than V (III) complexation. In fact, contrary to iron addition the matrix mechanical properties, morphological, and coloration changes induced by the vanadium were not restore after metal removal using EDTA. The results suggest that V (III) works as oxidative agent reducing to V (II) and inducing a massive oxidation of the catechols. This hypothesis is coherent with the increase in hardness and the decrease in the elongation observed.

The overall structure was maintained in all the matrices obtained. The XRD pattern was examined for all the matrices leading to the 3:1 Fe-CC_f-DC and the crystalline structure appeared mostly unaltered. The change observed in the C_f-DC, was probably induced by the highly swelled state when hydrated, in fact it was not detected in secondary matrices. This change occurred along a morphological change, observed using SEM. In fact, the high swelled state of the C_f-DC induce a complete loss of the lamellar structure of the chitinous matrix. Despite this relevant change in morphology, the structure maintained a memory of its original organization, restoring it after the cross-linking. In CC_f-DC (pH 14, 48 h) a loss in fibrils alignment, along with an expansion along the (100) plane, was observed. Probably

the long exposure to a highly alkaline pH induced solubilization/re-precipitation processes in the matrix, leading to a loss of crystallinity. Observing the diffraction image the fibril alignment of the structure was maintained in all the synthetic steps but slightly dropped when iron was added. This last difference might be due to a reorganization or bending of the polymeric chains due to the introduction of new bonds among them. After iron insertion a clustering of the lamellas was observed, supporting the hypothesis of a metal-induced cross-linking. The hypothesis is also supported by the partial recovery of the anisotropy and the separation of the lamellas after metal removal with EDTA.

4.3. Conclusion

We successfully synthetized different functional materials using a top-up approach on a hierarchically organized chitin-based matrix, the pen of *L. vulgaris*.

The matrix mechanical properties were tunable based on the level of cross-linking induced, moving from stiffer to softer materials. All the matrices synthetized have chelating properties on iron ions. Among the matrices chelating metals, an increment of about 30 % of the $\sigma_{1st\ Failure}$ and 40 % of the E compared to the initial chitin scaffold was observed in the 3:1 Fe-CC_f-DC. A different result was obtained exposing the matrix to vanadium (III), resulting in a significant increment in hardness (over 300 % in E and $\sigma_{1st\ Failure}$) probably due to high oxidative cross-linking. These results show how the matrix can actually change its mechanical resistance when exposed to different metals, being a stimuli responsive material.

These chelating tunable matrices might find application in: medicine, as grafts or wound healing materials (being catechols a mucoadhesive enhancing group); water remediation, as chelating matrices; sensors, as metal-responsive materials; etc.

In conclusion, we were able to prove that hierarchically organized chitin-based matrices can be functionalized without altering the chitinous scaffold organization, to get organized functional materials. This approach could lead to new advanced materials combining nature's precisely controlled structure and human's chemistry expertise.

4.4. Materials and methods

Materials All reagents and solvents were purchased from Sigma Aldrich and utilized without any further purification. Squid pens from Loligo vulgaris were collected from a local market. Once hydrated, the lateral blades were isolated, cleaned with abundant distilled water (carefully eliminating eventual residual tissues) and ethanol 70 vol.%, cleaned again using distilled water, and then stored dry in a desiccator.

Matrix synthesis The squid pen was initially deproteinized[54] inserting 2.5 g of squid pens, previously washed as described, in 100 mL of a boiling NaOH 1 M solution and stirring gently for 1 h. After that, the solution was changed with clean NaOH 1 M and refluxed for 1 h more. The chitin films obtained were cleaned once with room temperature NaOH 1 M, and then with distilled water until a neutral pH was observed in the cleavage water. The films were conserved dry in a desiccator.

The chitin was successively deacetylated[50] adding 400 mg of the deproteinized chitin in 20 mL of boiling NaOH 5 M for 2 h while stirring gently. The chitin obtained was cleaned once with room temperature NaOH 5 M, and then with distilled water until a neutral pH was observed in the cleavage water. The deacetylated chitin (DC) was conserved dry in a desiccator.

The DC (800 mg) was then soaked in 90 mL of an HCl pH 4.0 solution until completely hydrated. In 45 mL of a 1:1 mixture of ethanol and water, acidified to pH 4.0, were solubilized 466 mg (2.5 eq. respect to the deacetylated glucosamine units) of 1-ethyl-3-(3-dimethylaminopropyl)carbodiimide and 266 mg (1.5 eq. respect to the deacetylated glucosamine units) of 3,4-dihydroxyhydrocinnamic acid and stirred for one minute. The ethanol/water solution was slowly dropped on the former one under stirring. The reaction mixture was set on a rocking table in a dark room at 25 °C for 24 h. The catechol-functionalized deacetylated chitin matrices (C_f-DC) were washed soaking them three times in an HCl pH 4 solution for 10 minutes. The matrices were conserved wet in the pH 4 solution at 4 °C in the dark.

The crosslinking of the C_f-DC was induced soaking the previously prepared matrices in 200 mL of a carbonate buffer 50 mM pH 9.5 for 24 h on a rocking table. The cross-linked C_f-DC (CC_f-DC), were conserved dry in a desiccator.

A 10 mM bicine buffer at pH 7 containing $FeCl_3$ or VCl_3 in a 1:3 ratio between the deacetylated units and the metal ions was prepared. The appropriate amount of matrices were then soaked in the metal solution to get a 10 mg mL^{-1} dispersion of matrix in the solution and set on a rocking table for 30 minutes. The samples were then washed four times in water soaking the samples for 5 minutes each time.

The metal removal was performed soaking 10 mg mL^{-1} of sample in an EDTA 10 mM and setting the solution on a rocking table for 30 minutes. The samples were then washed four times in water soaking the samples for 5 minutes each time, and conserved in PremilliQ water.

Determination of the degree of acetylation The DA of the chitin was determined using solid-state nuclear magnetic resonance (NMR). The NMR experiments were performed on a Bruker Advance spectrometer operating at the frequency of 300 MHz for proton (equipped with a 4 mm MAS BB probe) using the combined techniques of cross-polarization (CP) and magic angle spinning (MAS). Field strengths corresponding to 90° pulses of 4.5 µs were used for the matched spinlock cross-polarization transfer ^{1}H to ^{13}C. The contact time was 1 ms, and the recycle delay 10 s. A typical number of 500–3000 scans were acquired for each spectrum. The chemical shifts were externally referred by setting the carbonyl resonance of glycine to 176.03 ppm. Glycine full width at half-height better than 27 Hz. The spinning speed was set at 8000 Hz for all samples.

The assignment of NMR signals and the DA calculation was done according to literature.[55]

Spectroscopic analysis

UV spectra were collected between 250 and 800 nm with a 1 nm resolution, and an average time of 0.1 s using a Varian Cary 300 Bio spectrophotometer.

Swelling measurement The measure of the chitin sample swelling in water was carried out first weighting a dry sample, conserved overnight in a desiccator under vacuum, and secondly weighting it after soaking in water overnight, prior blotting it on a paper towel. The measures at pH 4 were performed using a HCl solution at pH 4. Mass measurements were performed using a Sartorius CP225D (± 0.01 mg) on at least 50 mg of initial dry sample. The swelling measurements were performed at least on three independent samples.

Spectroscopic analysis UV-Vis spectra were collected in transmission acquiring between 240 and 800 nm with a 1 nm resolution, and an average time of 0.1 s using a Varian Cary 300 Bio spectrophotometer.

Raman spectra were acquired using a Renishaw Raman Invia spectrophotometer interfaced with a Leica DMLM optical microscope. The spectrophotometer was equipped with a diode laser (780.0 nm, P_{max} = 300 mW), an edge filter to remove the Rayleigh scattering, a monochromator (1200 lines·mm^{-1}), and a CCD detector. The instrument was calibrated using a silicon wafer (520 cm^{-1}). The spectra were acquired summing three spectra using a 1% power and 10 s of acquisition.

Synchrotron X-ray diffraction X-ray fiber diffraction diagrams were collected at XRD1 beamline, Elettra, Trieste, Italy. Each frame was collected at the peak wavelength (0.9999 Å) using an exposure of 60 s. The X-ray diffraction diagrams were analyzed using Fit2D software.

Scanning electron microscopy SEM images were acquired with a Philips SEM 515 using 15 eV. The wet samples were lyophilized, eventually cut with a scalpel to expose the section, glued on carbon tape, dried overnight in a desiccator, and coated with 20 nm of gold prior to image them.

Uniaxial tensile test Monotonic uniaxial tensile tests were performed using a universal testing machine (Mod. 4465 with Series IX software, Instron) and dedicated grips. The tests were performed with an actuator speed of 5 mm·min^{-1} (resulting in a strain rate of about 0.3 %·sec^{-1}) at room temperature. Each sample was cut in a proper dimension using scissors before the de-proteination, maintained hydrated after the synthesis and tested hydrated. The actual width and thickness of each hydrated sample were measured after the de-proteination using a SM-LUX POL microscope collecting images with a 5.0 MP digital camera (Motic Moticam 5+). The images were analyzed using ImageJ. Each sample was about 30 mm long, 5 mm wide, and 0.15-0.30 mm thick (the thickness varied between samples, because of the intrinsic variability of the initial biological samples). The samples were connected at the instrument, leaving a free length of 20 mm between the clamps. As the

curves were rather linear until failure started, the following parameters could be calculated, taking into account the actual dimensions of each specimen:

- The Young modulus of elasticity;
- The stress and strain when specimen failure started (yield, detected as a drop of the force by 1 %);
- The maximum stress, and strain;
- The work per unit volume required to reach yield and final failure (in $J \cdot mm^{-3}$).

At least five specimens were tested for each group. The Peirce criterion was adopted to detect and exclude outliers (15 % of the data had to be excluded).[48]

5. References

[1] H. Sashiwa, S. I. Aiba, *Prog. Polym. Sci.* **2004**, *29*, 887.

[2] K. Kurita, *Prog. Polym. Sci.* **2001**, *26*, 1921.

[3] L. Martin, C. G. Wilson, F. Koosha, L. Tetley, A. I. Gray, S. Senel, I. F. Uchegbu, *J. Control. Release* **2002**, *80*, 87.

[4] F. L. Mi, S. S. Shyu, C. T. Chen, J. Y. Lai, *Polymer (Guildf).* **2002**, *43*, 757.

[5] D. J. Macquarrie, J. J. E. Hardy, *Ind. Eng. Chem. Res.* **2005**, *44*, 8499.

[6] R. Jayakumar, M. Prabaharan, S. V. Nair, S. Tokura, H. Tamura, N. Selvamurugan, *Prog. Mater. Sci.* **2010**, *55*, 675.

[7] M. J. Harrington, A. Masic, N. Holten-andersen, J. H. Waite, P. Fratzl, *Science (80-.).* **2010**, *328*, 216.

[8] D. S. Hwang, M. J. Harrington, Q. Lu, A. Masic, H. Zeng, J. H. Waite, *J. Mater. Chem.* **2012**, *22*, 15530.

[9] S. C. T. Nicklisch, J. H. Waite, *Biofouling* **2012**, *28*, 865.

[10] D. Montroni, F. Valle, S. Rapino, S. Fermani, M. Calvaresi, M. J. Harrington, G. Falini, *ACS Biomater. Sci. Eng.* **2018**, *4*, 57.

[11] E. Filippidi, T. R. Cristiani, C. D. Eisenbach, J. H. Waite, J. N. Israelachvili, B. K. Ahn, M. T. Valentine, *Science (80-.).* **2017**, *358*, 502.

[12] B. Wang, Y. S. Jeon, H. S. Park, J. Kim, **2016**, *69*, 160.

[13] J. Xue, T. Wang, J. Nie, D. Yang, *J. Photochem. Photobiol. B Biol.* **2013**, *119*, 31.

[14] A. Masic, D. K. Han, H. J. Cha, **2014**.

[15] K. Kim, J. H. Ryu, D. Y. Lee, H. Lee, *Biomater. Sci.* **2013**, *1*, 783.

[16] J. H. Ryu, Y. Lee, W. H. Kong, T. G. Kim, T. G. Park, H. Lee, **2011**, 2653.

[17] W. Chen, X. Shen, Y. Hu, K. Xu, Q. Ran, Y. Yu, L. Dai, Z. Yuan, L. Huang, T. Shen, K. Cai, *Biomaterials* **2017**, *114*, 82.

[18] S. M. M. Hydrogels, M. Krogsgaard, M. A. Behrens, J. S. Pedersen, H. Birkedal, **2013**.

[19] Z. Xu, *Sci. Rep.* **2013**, *3*, 2914.

[20] Z. Guo, K. Ni, D. Wei, Y. Ren, *RSC Adv.* **2015**, *5*, 37377.

[21] H. Xu, J. Nishida, H. Wu, M. Kobayashi, H. Otsuka, A. Takahara, *ACS Macro Lett.* **2012**, *1*, 457.

[22] Y. Li, J. Wen, M. Qin, Y. Cao, W. Wang, *ACS Biomater. Sci. Eng.* **2017**, *3*, 979.

[23] A. Asghari, M. Ameri, B. Baraee, M. Rajabi, M. Bakherad, A. Amoozadeh, *Prog. React. Kinet. Mech.* **2015**, *40*, 77.

[24] L. Li, W. Smitthipong, H. Zeng, *Polym. Chem.* **2015**, *6*, 353.

[25] J. Xu, S. Strandman, J. X. X. Zhu, J. Barralet, M. Cerruti, *Biomaterials* **2015**, *37*, 395.

[26] K. Kim, K. Kim, J. Hyun, H. Lee, *Biomaterials* **2015**, *52*, 161.

[27] H. Qiao, M. Sun, Z. Su, Y. Xie, M. Chen, L. Zong, Y. Gao, H. Li, J. Qi, Q. Zhao, X. Gu, Q. Ping, *Biomaterials* **2014**, *35*, 7157.

[28] D. Montroni, C. Piccinetti, S. Fermani, M. Calvaresi, M. J. Harrington, G. Falini, *RSC Adv.* **2017**, *7*, 36605.

[29] B. Wang, J. G. Torres-Rendon, J. Yu, Y. Zhang, A. Walther, *ACS Appl. Mater. Interfaces* **2015**, *7*, 4595.

[30] W. R. Kennedy, N. Dubey, X. Navarro, G. Wendelschafer-Crabb, D. Ceballos, R. T. Tranquillo, *Exp. Neurol.* **1999**, *158*, 290.

[31] O. Zvarec, S. Purushotham, A. Masic, R. V Ramanujan, A. Miserez, **2013**.

[32] G. Chaussard, A. Domard, *Biomacromolecules* **2004**, *5*, 559.

[33] P. Methacanon, M. Prasitsilp, T. Pothsree, J. Pattaraarchachai, *Carbohydr. Polym.* **2003**, *52*, 119.

[34] O. I. Bogdanova, D. K. Polyakov, D. R. Streltsov, A. V. Bakirov, J. Blackwell, S. N. Chvalun, *Carbohydr. Polym.* **2016**, *137*, 678.

[35] G. A. Roberts, *Chitin chemistry*; Macmillan International Higher Education, 1992.

[36] A. Percot, C. Viton, A. Domard, *Biomacromolecules* **2003**, *4*, 1380.

[37] B. Focher, A. Naggi, G. Torri, A. Cosani, M. Terbojevich, *Carbohydr. Polym.* **1992**, *17*, 97.

[38] R. A. Muzzarelli, *Chitin*; Elsevier, 2013.

[39] M. Terbojevich, C. Carraro, A. Cosani, E. Marsano, *Carbohydr. Res.* **1988**, *180*, 73.

[40] Y. Saito, H. Kumagai, M. Wada, S. Kuga, *Biomacromolecules* **2002**, *3*, 407.

[41] L. S. Guinesi, E. T. G. Cavalheiro, *Thermochim. Acta* **2006**, *444*, 128.

[42] M. R. Kasaai, *Carbohydr. Polym.* **2010**, *79*, 801.

[43] K. Van De Velde, P. Kiekens, *Carbohydr. Polym.* **2004**, *58*, 409.

[44] Y. Noishiki, H. Takami, Y. Nishiyama, M. Wada, S. Okada, S. Kuga, *Biomacromolecules* **2003**, *4*, 896.

[45] K. H. Gardner, J. Blackwell, *Biopolymers* **1975**, *14*, 1581.

[46] A. Hammersley, *FIT2D V9. 129 Ref. Man. V3. 1. Inter Rep ESRF98HA01, ESRF, Grenoble.* **1998**.

[47] R. H. Marchessault, F. G. Pearson, C. Y. Liang, *J. Polym. Sciece* **1960**, *43*, 101.

[48] S. M. Ross, *J. Eng. Technol.* **2003**, *20*, 38.

[49] D. Montroni, B. Marzec, F. Valle, F. Nudelman, G. Falini, *Biomacromolecules* **2019**, *20*, 2421.

[50] D. Montroni, S. Fermani, K. Morellato, G. Torri, A. Naggi, L. Cristofolini, G. Falini, *Carbohydr. Polym.* **2019**, *207*, 26.

[51] M. Kaya, M. Mujtaba, H. Ehrlich, A. M. Salaberria, T. Baran, C. T. Amemiya, R. Galli, L. Akyuz, I. Sargin, J. Labidi, *Carbohydr. Polym.* **2017**, *176*, 177.

[52] C. Choi, S. Kim, R. Kim, Y. Choi, S. Kim, H. young Jung, J. H. Yang, H. T. Kim, *Renew. Sustain. Energy Rev.* **2017**, *69*, 263.

[53] N. H. Choi, S. K. Kwon, H. Kim, *J. Electrochem. Soc.* **2013**, *160*, A973.

[54] A. Ianiro, M. Giosia, S. Fermani, C. Samorì, M. Barbalinardo, F. Valle, G. Pellegrini, F. Biscarini, F. Zerbetto, M. Calvaresi, G. Falini, *Mar. Drugs* **2014**, *12*, 5979.

[55] L. Heux, J. Brugnerotto, J. Desbriéres, M. F. Versali, M. Rinaudo, *Biomacromolecules* **2000**, *1*, 746.

Chapter 5:
Conclusion

1. Summary

Nature observation represents an important pool of knowledge and technology evolved and refined over millions of years. Among the information hidden in nature, chitin-based matrices represent an enormous source in material science. Over 70 % of the known species produce chitin, each of them in different forms (cuticles, peritrophic membranes, wings, shells, claws, beaks, etc.) contributing to a massive amount of diversified systems.
In this thesis, chitin-based systems were investigated, at different levels of complexity and molecular heterogeneity.

In chapter 2, we reported an *in vitro* system to study the self-assembly of β-chitin nano-fibrils. In this study hundreds nanometers lengths fibrils self-assembled into almost millimetric length fibers. This system aims to mimic, as much as possible, the conditions where chitin fibrils assemble and study how the interaction with other molecules affect chitin assembly. A second study was performed assembling together chitin and collagen to get new materials for medical applications. In this last study a better understanding of the composition and assembly influence of chitin/collagen materials on cell viability was obtained.

From the nano-level of the self-assembly we moved to the macroscale studying the structure of different chitin-based matrices in chapter 3. We started investigating how molecular interactions between structural proteins and chitin fibrils influence the mechanical properties of the gladius of *Loligo vulgaris*. The results showed how the interaction between the two components of this binary material is crucial for the overall material properties. Successively, different matrices in *Ariolimax californicus* were analyzed to study how materials with completely different functions (compression resistance, protection, mineralization, etc.) evolved using chitin as a versatile building block.

Finally, in chapter 4 a further step in exploiting natural matrices was achieved. In this project a chitinous hierarchically organized matrix, the squid pen of *L. vulgaris*, was

successfully functionalized without altering its structural features. In this last work, the bioinspired chemistry of mussel byssus was applied binding catechol moieties to the free amino groups of chitin to obtain a range of different functional materials with tunable mechanical properties and iron chelating abilities.

In conclusion, this thesis explored different chitin-based systems and developed new approaches on how to study and exploit them in future studies. We hope this work will help shading a bit of light on the unknown secrets hidden in nature complexity.

2. Outlooks

The work done in this thesis explored only a tiny part of its potential possibilities.

The development of a system able to mimic chitin self-assembly in water at the fibril stage opens the possibility to study chitin/protein interaction at both molecular level, using NMR or TEM, and macroscale level, observing how chitin-binding proteins can drive chitin self-assembly.

The characterization of the matrices in chapter 3 could be further investigated. First, an overall mechanical characterization should be performed on all the matrices in the buccal mass. Second, we plan to analyze the composition of the odontophore, the exact mineral composition of radular teeth, or the component/s responsible for the jaw's toughness and coloration. Moreover, a deeper study on the different composition of the organic matrix on the two faces of the internal shell should be done. Solubility tests and in vivo studies are also planned in future studies to validate our theory on this matrix function as calcium storage.

Finally, the knowledge obtained functionalizing a relatively simple system, as the squid pen, could be exploited to target specific highly organized matrices adding functionalities to get advanced functional materials. Considering the amount of chitin-based systems existing and the possible functionalization the existing combinations are almost limitless.

Side projects:
Byssus vs. water pollution

1. Introduction

Water remediation is the process of treating polluted water by removing pollutants or converting them into innocuous products.

A major problem in water pollution are dyes and pigments. Colored molecules are widely used with more than ten thousand dyes commercially available. In total, over $7 \cdot 10^5$ tons per year of dyed materials are produced[1] and about 2 wt.% are discharged in water.[2] One of the main sources for this kind of pollution is the textile sector, with an estimated 1 ktones per year of dye discharged as wastewater.[2][3] Due to a general lack of environmental law limits for dye concentration in effluvial waters, these waters are often colored.[4] In these waters, the dyes adsorb and reflect sunlight, interfering with the ecology of photosynthetic organisms and leading to a reduction of oxygen concentration.[2] In addition, many dyes are toxic, or even carcinogenic, and their aromatic structures make their biological degradation inefficient, extending their persistence time in the environment.[5]

In today's society, metal ions cover a crucial role in every field, from constructions to medicine, and from electronics to agriculture. The intensive use of those cations led, of course, to a wide dispersion of them in the environment. Some important sources of metal ions pollution in aquatic streams are mining refining ores, fertilizer industries, tanneries, batteries, paper industries, pesticides, etc.[6][7][8] Those industries introduce in the environment major toxic metal ions like Cd^{2+}, Co^{2+}, Cr^{3+}, Cu^{2+}, Fe^{3+}, Hg^{2+}, Ni^{2+}, Pb^{2+}, V^{3+}, Zn^{2+}, etc. which are of specific concern due to their toxicity,[9] carcinogenicity,[10] bio-accumulation tendency,[11][12] and persistence in nature (due to lack of biodegradation pathways when compared to organic pollutants).

Effluents treatment processes have been designed to avoid pollutants dispersion in wastewater, reducing any adverse effects.[13] Some conventional effluent treatment for metal ions removal include precipitation, cementation, filtration, coagulation, flotation, complexing, solvent extraction, membrane separation, electrochemical technique, biological process, reverse osmosis, ion exchange, and adsorption.[14][15] Many of these

methods have also been applied to remove dyes from wastewaters. Unfortunately, each method has its limitations such as less efficiency, expensiveness, sensitive operating conditions, incomplete removal, high-energy requirements, and production of toxic sludge or waste products that also require disposal.[6][7][13][16]

Since 1990's the adsorption of pollutants by low cost renewable organic materials has gained importance because of its high efficiency, easy handling, avoiding of byproducts, availability of different adsorbents, and cost-effectiveness.[17] Among adsorbing matrices good results were gained using agricultural wastes[6][18][19] as cheap disposable adsorbent which also guarantee reuse of wastes. For metal pollution a more efficient, but expensive option, was given by synthetic chelating polymer as material developed and synthesized to accomplish this task.[20][21][22][23][24][25][26]

Another important environmental issue is related to mussel processing in fishery industries. Every year 0.5 Mtons of solid residues from mussel fishery industry are discarded.[27][28] Those residues are constituted mainly of shells and minor amounts of soft tissue and byssus. Many researchers have investigated how to recover these solid residues[29] focusing mainly on shells to remedy to anion pollution,[30][31] as a substrate for heterogeneous catalysts,[32][33] or as $CaCO_3$ source;[34] very few studies focused on the recovery of byssus.[35][36][37]

The byssus is a protein-based fibrous holdfast utilized by mussels to anchor to different substrates in marine environments and avoid being dislodged by currents and waves.[38][39] This material is very rich in potential binding sites for aromatic compounds and metal ions based on its unique structure and chemistry. The byssus ultra-structure organization is generally split in four regions (Figure 94), namely: A) the stem; B) the thread core; C) the thread cuticle, and D) the plaque.[40][41] Each different region has a diverse purpose, which will not be described, associated to very diverse structure and chemical composition. The plaque and cuticle are composed of proteins rich in dihydroxyphenylalanine (DOPA) residues,[42] which naturally are coordinated to Fe^{3+} in very stable complexes.[42] The thread core and stem, instead, are mainly composed of proteins called PreCols,[43] which are collagen-based proteins having terminal histidine (His)-rich domains able to bind mainly Cu^{2+} and Zn^{2+}.[44] Those metal-binding sites have a crucial role in the mechanical and self-healing properties of the byssus. In this natural matrix His makes up 2 mol.% of PreCols composition while DOPA content reaches 10-15 mol% in mussel foot protein-1 (mfp-1).[45]

Mfp-1 is the only protein composing the cuticle while one of the five different mfps composing the plaque. Among them mfp-2 is the most abundant (25 wt.% of the plaque) and is characterized by a relatively low percentage of DOPA content, from 3 to 5 mol.%.[46] The remaining 75 wt.% of the plaque is composed of proteins with a higher amount of DOPA residues (e.g. mfp-3 and mfp-5 have DOPA contents higher than 20 mol.%).[47] Notably, polymers having poly-DOPA regions have been used for water remediation,[48] collagen based matrices have been tested for water remediation from anionic dyes,[49][50] and poly-His has been utilized specifically for metal ion removal.[51]

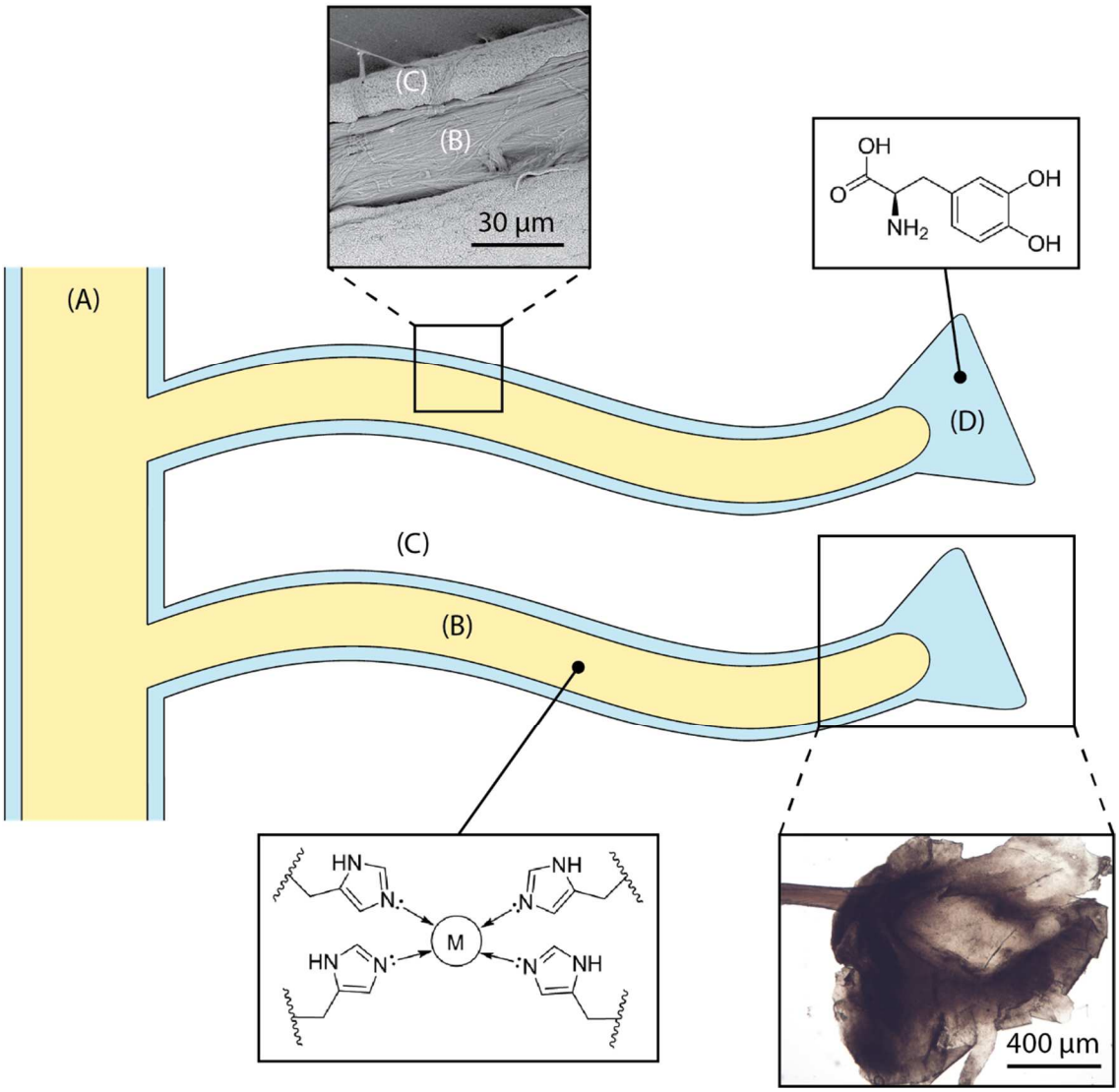

Figure 94: Schematic representation of the byssus. (A) The stem, (B) the thread core, (C) the cuticle, and (D) the plaque. An optical image of a plaque and a SEM image of a byssal thread with a broken cuticle, where the fibrous internal core is visible, are reported. In yellow, the His-rich regions; in blue, the DOPA-rich regions.

2. Aim of the chapter

In this research, we aim to exploit the unique composition and structure of the byssus, due to co-presence of DOPA-rich and His-rich proteins, together with collagen, as potential adsorbent matrix for water remediation for binding a range of different dyes. Moreover, this unique structure, evolved to bind metal ions, will also be studied as material for metal ions removal from polluted waters.

To test the capability of byssus threads as a bio-renewable adsorption matrix for dyes, we tested this material on Methylene Blue (MB) as a test molecule for cationic dyes, and on Eosin Y (EosY), as test molecule for anionic dyes. These test molecules were chosen because of their easy detectability using UV-Vis spectroscopy and their low toxicity. In this work both the native byssus (Figure 95 A), with its native metal ion content, and a de-metaled byssus (Figure 95 B) were used. This comparison was done to understand how the diverse coordination state of the metal binding functional groups affects the performance of this matrix in the removal of dye from wastewater.

As metal ions absorbent matrix only the de-metaled matrix was tested on both metal ions naturally present in the native byssus (Fe^{3+}, Zn^{2+}, and Cu^{2+}) and metal ions of environmental interest (Al^{3+}, Cd^{2+}, Co^{2+}, Ni^{2+}, Mn^{2+}, and V^{3+}). In literature is already known that the byssus can be metaled and de-metaled[39][42][52] making this matrix both a possible disposable or reusable adsorbent.

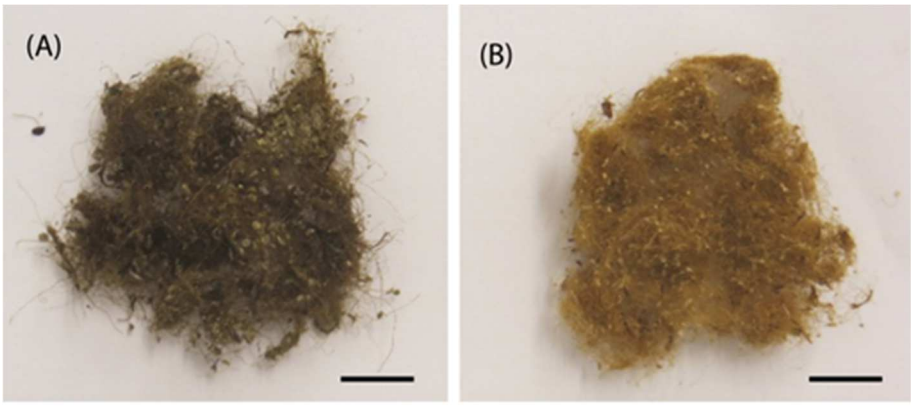

Figure 95: Photographs of the native metaled byssus (A) and of the de-metaled one (B). The color of the material change according to the metal content. In the presence of Fe^{3+} the byssus appears brown-black, while when it is almost metal free its color is gold-like. Scale bar of 10 mm. Figure from Montroni et al. (2017).[53]

3. Water remediation from charged aromatic dyes

3.1. Results

The adsorption kinetics of the byssus was evaluated by incubating a defined mass of byssus into a dye reference solution (0.01 mM). The kinetic data showed that the two dyes interacted differently with the native byssus. While MB was completely adsorbed from the solution in the matrix in less than 24 h, EosY required more time and after 72 h was almost completely removed from the solution. The de-metaled byssus, instead, behaved differently with respect to the two dyes. When these adsorption data were compared to those on the native ones, EosY exhibited a similar kinetic of adsorption, while MB a slower one (Figure 96). Following the information from these preliminary experiments, 48 h for MB and 72 h for EosY were chosen as the incubation times for the byssus in the different dye solutions during removal experiments, assuming that these times ensured the maximum dye loading into the byssus threads, independently from the starting dye concentration.

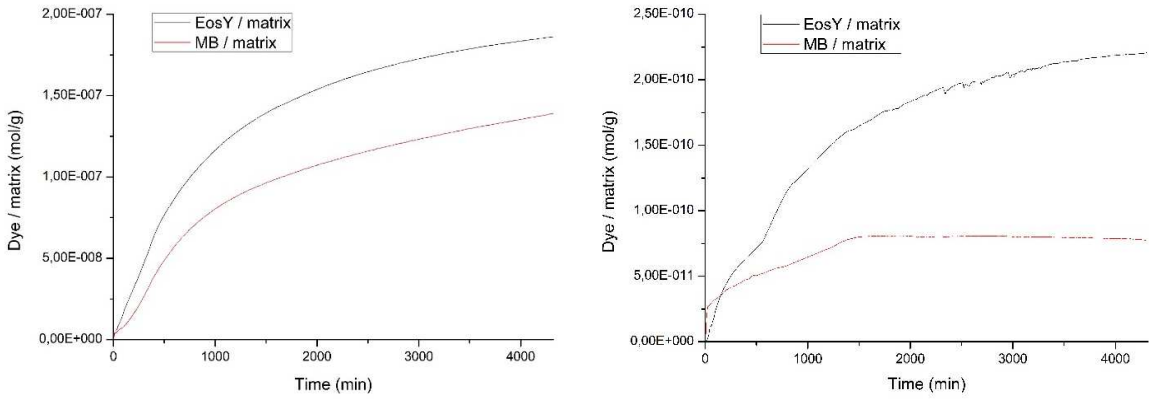

Figure 96: Adsorption kinetic of the de-metaled (left) and pristine (right) byssus in a 0.01 mM solution of dye. Figure from Montroni et al. (2017).[53]

The results of the dye removal experiments are reported in Figure 97 and Table 13, while an optical view of experiments is shown in Figure 98. EosY presented a higher affinity for the de-metaled byssus, while the MB appeared to have a higher affinity to the native one. The analysis of the results reported in Table 13 shows that the 50 mg of byssal threads were able to remove completely the dye from solutions having a dye concentration below or equal to 0.5 mM. Above this concentration different trends were observed. EosY was

removed from solutions more efficiently by using de-metaled byssus than the native one. Indeed, when a 5 mM EosY solution was used, a loading of EosY equal to 117 ± 2 $mg \cdot g^{-1}$ and 56 ± 10 $mg \cdot g^{-1}$ was obtained on de-metaled and native byssus, respectively. MB was more efficiently removed from solution by the native byssus than the de-metaled one. In this case the MB loading from a 5 mM MB solution was equal to 38 ± 1 $mg \cdot g^{-1}$ and 72 ± 17 $mg \cdot g^{-1}$ on de-metaled and native byssus, respectively.

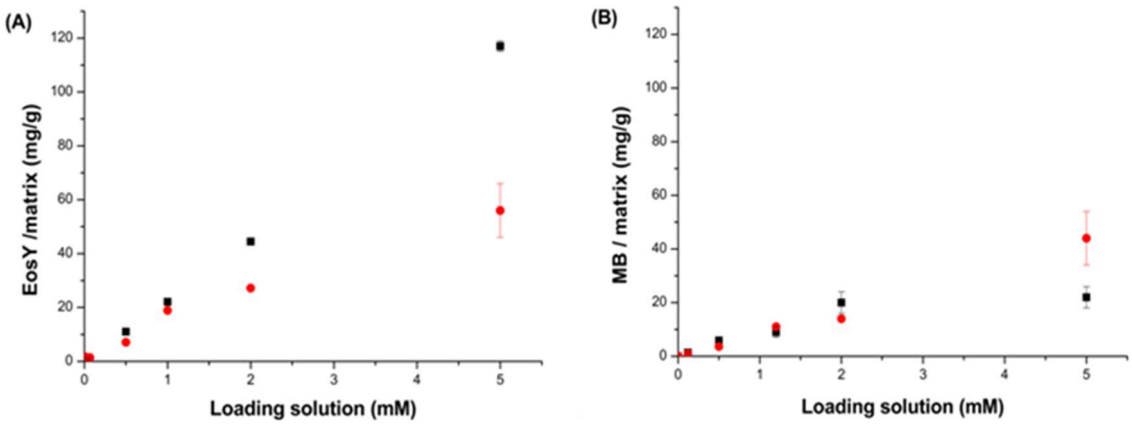

Figure 97: Dye removal of (A) EosY from 1.5 mL of dye solution and (B) MB in the same experimental conditions. In red are reported the data collected using native byssus and in black those using de-metaled byssus. Figure from Montroni et al. (2017).[53]

Table 13: Concentration of dye in the matrix ($mg \cdot g^{-1}$) with the percentage of dye adsorbed from the solution (wt.%) shown in parentheses for removal experiments starting from different loading solution using native byssus and de-metaled byssus. Table from Montroni et al. (2017).[53]

Loading solution (mM)	EosY solution ($mg \cdot L^{-1}$)	Eosin Y		MB solution ($mg \cdot L^{-1}$)	Methylene Blue	
		native byssus ($mg \cdot g^{-1}$)	de-metal. byssus ($mg \cdot g^{-1}$)		native byssus ($mg \cdot g^{-1}$)	de-metal. byssus ($mg \cdot g^{-1}$)
0.01	6.9×10^{-3}	$1.668 \pm 0.004 \times 10^{-1}$ (100)*	$1.41 \pm 0.01 \times 10^{-1}$ (100)*	3.2×10^{-3}	$8.4 \pm 0.1 \times 10^{-1}$ (100)*	$8.13 \pm 0.07 \times 10^{-1}$ (100)*
0.1	6.9×10^{-2}	1.393 ± 0.06 (100)*	1.20 ± 0.01 (100)*	3.2×10^{-2}	1.004 ± 0.009 (100)*	1.36 ± 0.01 (100)*
0.5	0.35	(7.1 ± 0.01) (100)*	(11.02 ± 0.03) (100)*	0.16	(3.61 ± 0.04) (100)*	5.9 ± 0.1 (100)*
1	0.69	18.9 ± 0.1 (99.31 ± 0.03)	(22.1 ± 0.4) (100)*	3.2	11.0 ± 0.2 (96 ± 2)	9 ± 2 (79 ± 13)
2	1.4	27.2 ± 0.9 (97 ± 3)	(44.5 ± 0.4) (100)*	6.4	14.0 ± 0.2 (92 ± 5)	20 ± 4 (81 ± 18)
5	3.5	56 ± 10 (60 ± 8)	117 ± 2 (96 ± 2)	1.6	44 ± 10 (72 ± 17)	22 ± 4 (38 ± 1)

* refers to samples with an after treatment concentration in solution lower than the detectable limit of the instrument (2 µM for EosY and 5 µM for MB), so the dye removal was assumed to be quantitative.

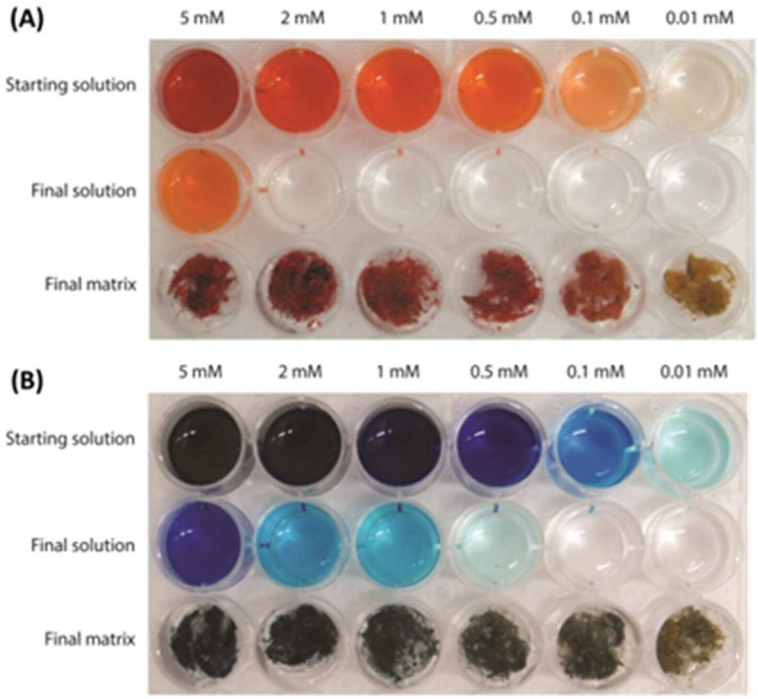

Figure 98: Camera photographs illustrating the dye removal experiments using (A) de-metaled byssus on EosY solutions, and (B) native byssus on MB solutions. Figure from Montroni et al. (2017).[53]

Adsorption isotherm models provide useful data in order to understand the mechanisms of the adsorption process, to describe how an adsorbate interacts with a substrate and to evaluate the applicability of the process. The Langmuir, Freundlich, and Dubinin Radushkevich (D-R) isotherm models were used to describe the relationship between the amount of dye adsorbed onto the byssus thread matrices and their equilibrium concentrations in aqueous solution. The experimental equilibrium data of EosY and MB on native and de-metaled byssus were compared with the theoretical equilibrium data obtained from the Langmuir, Freundlich, and D-R isotherm models. The isotherm constants were calculated by evaluating the linearized form of the models (see Materials and methods for more details). All of the isotherm constants and correlation coefficients are given in Table 14. The adsorption capacity (q_m) of EosY was found to be 46.7 $mg \cdot g^{-1}$ and 85.5 $mg \cdot g^{-1}$ and that of MB was 22.6 $mg \cdot g^{-1}$ and 16.3 $mg \cdot g^{-1}$ on native and de-metaled byssus, respectively, by using the Langmuir model equation. The R_L values were below 1, indicating a favorable adsorption of EosY and MB on the byssus substrates under the studied conditions. The Freundlich isotherm constant, n, gives an idea for the favorability of the adsorption process. The value of n should be less than 10 and higher than unity for

favorable adsorption conditions. As can be seen from Table 14, the n values for EosY and MB were in the range of 3.8 – 5.7. By evaluating the D-R isotherm model, a rough estimation of the mean adsorption energy (E) values were found to be 0.21 $kJ \cdot mol^{-1}$ and 0.79 $kJ \cdot mol^{-1}$ for EosY and those for MB were 0.38 $kJ \cdot mol^{-1}$ and 2.0 $kJ \cdot mol^{-1}$ on native and de-metaled byssus, respectively. If the value of E lies between 8 and 16 $kJ \cdot mol^{-1}$, the adsorption process takes place chemically, whereas when $E < 8$ $kJ \cdot mol^{-1}$, the adsorption process proceeds physically. By comparing the correlation coefficient values obtained from the isotherm models, it can be concluded that the Freundlich isotherm model is the more suitable to describe the experimental data.

Threads treated with 1 mM solutions were cut in sections and observed using an optical microscope to investigate the dye distribution into the external cuticle and inner fibrous core of the byssus. The images (Figure 99) showed that the dyes were homogeneously distributed in the threads in all the conditions examined except for MB uptake into de-metaled byssus. In this matrix a selective uptake of MB for cuticles was observed.

Table 14: Langmuir, Freundlich and Dubinin Radushkevich (D-R) isotherm parameters for the adsorption of MB and EosY on byssus threads (see Materials and methods for more details). Table from Montroni et al. (2017).[53]

	Eosin Y		Methylene Blue	
	native byssus	de-met. byssus *	native byssus	de-met. byssus
Langmuir isotherm model				
q_m / $mg \cdot g^{-1}$	46.7	85.5	22.6	16.3
b / $L \cdot g^{-1}$	0.003	0.0001	0.022	0.012
R_L	0.084	0.65	0.021	0.040
R^2	0.79	0.84	0.66	0.84
Freundlich isotherm model				
K_F / $mg \cdot g^{-1}$	15.7	34	5.7	5.2
n	5.7	3.9	3.8	4.8
R^2	0.88	0.95	0.95	0.98
D-R isotherm model				
q_D / $mg \cdot g^{-1}$	47.3	85.0	11.6	16.7
K_D / $kJ^2 \cdot mol^{-2}$	3.5	0.12	12	0.80
E / $kJ \cdot mol^{-1}$	0.38	2.0	0.21	0.79
R^2	0.68	0.70	0.39	0.65

* This substrate shows a high adsorption capacity for EosY that prevents for low initial concentrations an accurate evaluation of the equilibrium concentrations.

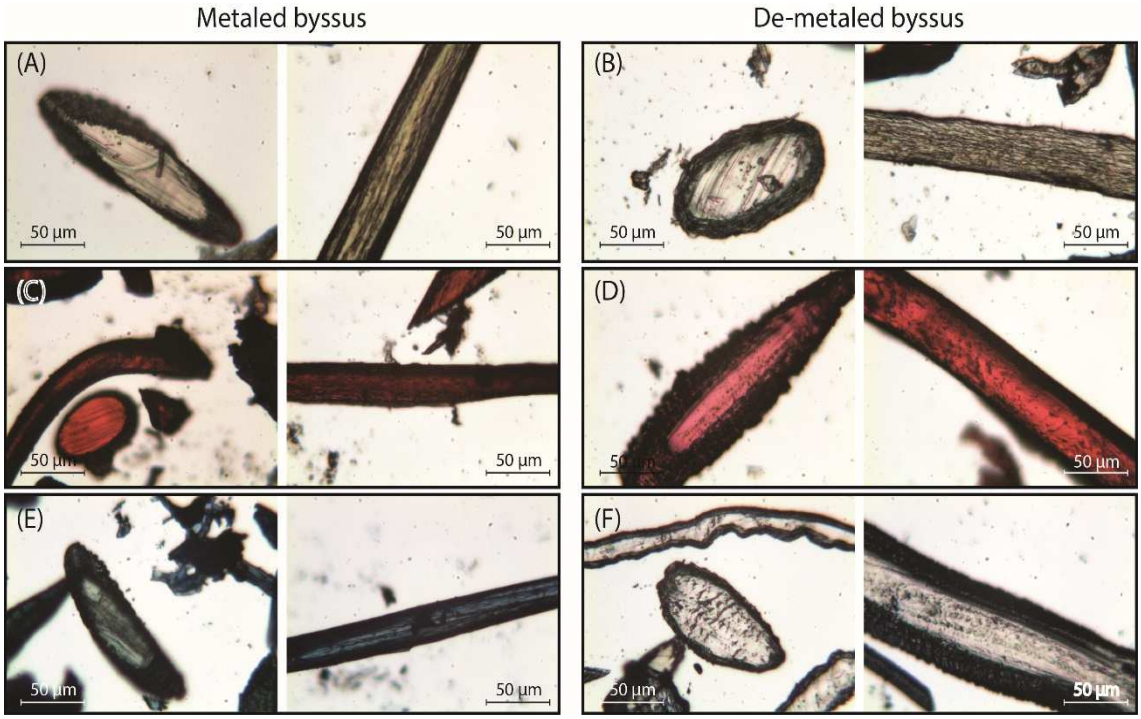

Figure 99: Optical microscopy images of byssus thread section of 40 µm. On the left, metaled byssus threads, on the right, de-metaled byssus threads. (A) and (B) were control samples, (C) and (D) were treated with EosY 1 mM and (E) and (F) were treated with MB 1 mM. For each condition is present a longitudinal section of the thread and a transversal one. Figure from Montroni et al. (2017).[53]

To investigate the dye desorption from the byssus, the byssal samples treated with 0.01, 0.1 and 1 mM dye solutions were immersed in 1.5 mL of water. The results are reported inTable 15. The only two conditions releasing dye after 72 h were MB/de-metaled byssus and EosY/native byssus treated with 1 mM solutions, consistently with all the previous experiments. However, for EosY, desorption was very small, while for MB desorption, it was around 6 %.

Table 15: Percentage (wt.%) of dye desorbed from the matrix in 1.5 mL of water after 72 h from byssal threads dye loaded using different starting concentrations of dye. Table from Montroni et al. (2017).[53]

Loading solution (mM)	Eosin Y		Methylene Blue	
	native byssus (wt.%)	de-met. byssus (wt.%)	native byssus (wt.%)	de-met. byssus (wt.%)
0.01	-*	-	-	-
0.1	-	-	-	-
1	0.18 ± 0.01	-	-	6 ± 1

* The data not reported have a concentration lower than the detection limit (2 µM for EosY and 5 µM for MB).

3.2. Discussion

The experimental results showed that the byssal threads, both in the metaled native state and in the de-metaled state, act efficiently in removing charged aromatic dyes from water. The loading capacity of these materials, up to more than 10 wt.% of the starting mass, are of the same order of magnitude of other waste materials.[54][55][56] In addition, it has to be considered mussel mariculture wastes annual production[27][28] that lead to a potential capability of dye removal of about 0.5 ktones per year. This value represents about 50 wt.% of the of dye pollution per year in waste waters from textile sector.[2] In addition the byssal threads offer the possibility to be tunable with respect positive or negative charged aromatic dyes. This can be done controlling the metal ions content in the byssus threads via chelation treatment with EDTA, which may reflect the diverse possible chemical interactions by the DOPA and His residues in the byssus proteins. Also the pH is a parameter that could possibly be used to control the adsorption capability of byssus, since the functional groups, which are likely responsible for interaction between dye molecules and adsorbent, can be protonated or deprotonated to produce different surface charges in solution having different pH values. This parameter has not been investigated in the present research. However, it has been proved that the byssus is stable in a range of pH from 2 to 10.[37] It can be considered that at acidic pH values the histidine groups of byssus become protonated and this changes their uptake capability of charged dyes. On the other hand, basic pH values induce the deprotonation of cuticle localized DOPA residues, affecting the dye uptake for both a change in the interactions and a potential shielding effect of the negatively charged cuticle. In addition to these general considerations, the byssus in acidic environment will bind metal ions less tightly. In this study, the experiments were carried out at ambient temperature. The byssus is a material that is very stable with the temperature, experimental data indicate that its structure remains unaffected up to a temperature of at least 80 °C.[37] Thus, it can be reasonably supposed that byssus adsorption capability should not be drastically affected by the temperature.

The two dyes used represents model molecules that differ mostly for the ionic charge. The native byssus showed a high affinity for a cationic dye, i.e. MB, as illustrated by the adsorption kinetics, which showed that the dye was completely absorbed in less than 24 h. Furthermore, the experiments of dye removal from solutions exhibited an almost complete removal of the dye up to a starting concentration of 2 mM, with EosY showing similar

behavior in loading. The desorption kinetics confirmed this affinity data, showing no desorption for MB and only a very low desorption of EosY. In other words, the dyes bind quite strongly to the byssus material. Both dyes appeared to be absorbed homogeneously along the different parts of the byssus suggesting no selective interactions with the diverse molecules and functional groups of the native byssus.

De-metaled byssus, on the other hand, appeared to prefer anionic dyes, i.e. EosY. As for the native one, the dye removal experiments showed an almost complete removal of EosY in all the concentrations studied. This is different from MB, which showed saturation in the dye uptake for concentrations higher than 0.5 mM.

These considerations are supported by the adsorption isotherm model results, which show that the best experimental data fitting occurs using the Freundlich isotherm model. This model assumes that the adsorption takes place on heterogeneous surface sites, which have different adsorption energies. The analysis of mean adsorption energy values (from the D-R isotherm model) may suggest physical interactions. This fits with wide variety of interactions offered by the byssus structural complexity and richness of molecular moieties and functional groups.

The desorption kinetics were in line with the uptake data and, while EosY was not desorbed, MB was desorbed when loaded from a 1 mM solution. This last result was different from the one obtained with the EosY/native byssus. A reasonable explanation is given by the observation of optical images, which exhibited a selective binding of the MB in cuticle and plaques, which are the most exposed regions of the byssus and the ones richer in DOPA, while under all other conditions the dyes accumulated homogeneously in the diverse byssus regions. These results show that the anionic EosY was more adsorbed from the de-metaled byssus than the metaled one, in which localized positive regions should be present due to the coordinated metallic cations. This may suggest that electrostatic interactions are not the driving force for adsorption and that other interactions may be more prominent. It is important to note that in the experimental conditions used in the adsorbing experiments, the imidazole group of His residue is not protonated. According to literature collagen domains are the binding site for EosY,[48][43] and this may explain the homogeneous adsorption of EosY in the thread also in presence of metals. Dye and byssus aromatic functional groups (e.g. His and DOPA) may also interact through π-staking. The later require specific geometries according to molecular charge distributions of the aromatic regions.[57]

The EosY electron-rich aromatic structure may interact with His residues, which have an electron-poor aromatic structure, preferentially when His is not coordinating metal ions and has higher mobility (Figure 100). However, this possibility must be further examined. MB uptake from the byssal threads, instead, requires different hypotheses of interaction. No studies have been reported showing MB staining of collagen. Thus, electrostatic and π-staking interactions should govern the MB uptake by the byssus. The presence of MB into the core the His rich region of the metaled byssus suggests that the electrostatic repulsion between metal ion and cationic MB does not affect the uptake. This agrees with the observation that into the de-metaled byssus core, free of localized positive charges, the dye is not up-taken. Indeed, in this condition the MB concentrates into the cuticle, suggesting a repulsion from the core region or a preferential uptake in the cuticle region. We can suppose that also in the case the different efficiencies of the π-staking interactions, due to the diverse mobility of the imidazole group of His as function of metalation, may control the dye uptake. However, His makes up 2 mol.% of the total preCol composition (localized at the ends), and it is plausible that the functional groups of other amino acids also play an important role in interacting with dyes. Thus, additional focused experiments will be necessary to understand at molecular level the mechanism of dye uptake by the byssus. Nonetheless, a strong and tunable absorption effect of byssus as a dye remediation material is demonstrated and this represents the main goal of this research.

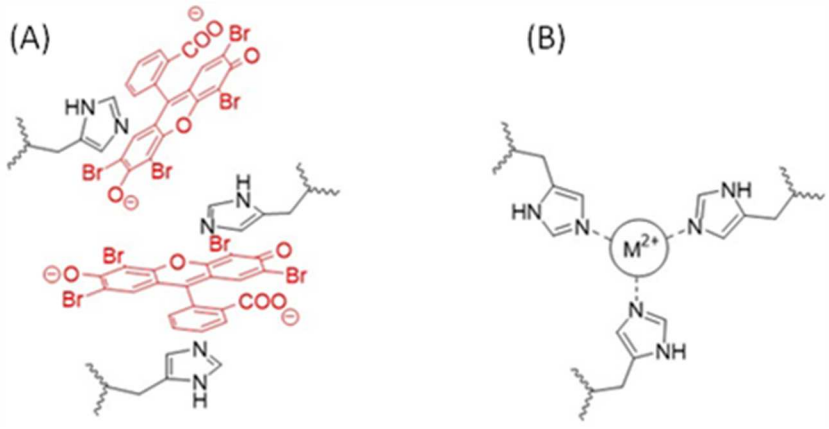

Figure 100: Schematic representation of a hypothesis of EosY interaction with His into the byssus in the absence of metal ions (A) in the metal coordination site His_3-M^{2+} of the byssus (B).[58] *The presence of the metal ion reduced the mobility of the imidazole of the His residues and prevents the establishing of π-staking interactions. Figure from Montroni et al. (2017).*[53]

Neutral dyes were not used in the current study. Nevertheless, it can be supposed that they can be removed by the byssus. Indeed, in the mechanism proposed, the byssus material is likely to be capable of a number of different interactions besides the electrostatic interaction, including as π-stacking and hydrophobic interactions that could favor neutral dye removal. Another important point to consider is that the solubility of uncharged dyes in water is likely to be quite low. However, as the byssus is organic and insoluble in most solvents, it could be used as well for the removal of dyes from not water solvents as long as it solvates in them.

3.3. Conclusion

In this work we demonstrated the easy applicability of the byssus as a substrate for dye removal from wastewater of both anionic and cationic aromatic dyes. The byssus showed the peculiar ability to switch its affinity for cationic or anionic dyes depending on the presence of metal ions coordinated by its residues. The de-metaled byssus appeared to have a higher affinity for anionic dyes, while the native one binds more efficiently the cationic one. Beside this observation, this research demonstrated that the byssus can absorb in a tunable way up to 10 wt.% of its own weight in dye. In conclusion, the byssus is proposed as a cheap, efficient, and tunable solution to fight industrial dye pollution in water using a biorenewable waste product. The high capability of the byssus to absorb dyes stably is also supported by the parameters obtained by the adsorption isotherm models, offering the perspective to use it as an environmental marker of dye pollution in waters. Moreover, the study of the different interactions between dyes and byssus has provided useful information for byssus future applications in different fields as sensoristics o material science.

3.4. Materials and methods

Materials Reagents and solvents were purchased from Sigma Aldrich and utilized without any further purification. EosY and MB daily fresh solutions were prepared for each experiment. The byssus was collected from a mussel-breeding farm close to Fano (Italy).

Byssus pre-treatment The byssus was mechanically collected from the mussels by hand and rinsed with water and detergent until the washing water was completely clear. Afterwards, it was washed again with de-ionized water to remove the detergent, stirred twice in ethanol for 30 minutes and finally washed again twice with deionized water for 15 minutes to rehydrate the threads and remove the ethanol. The clean air-dried byssus was stored in a desiccator under vacuum (Figure 95 A).

Byssus de-metalation The de-metalation process was carried out following the procedure reported by Schmitt et al.,[52] in which EDTA was used as a chelating agent. The protocol was modified using 0.1 M TRIS buffer and adding two more 1 h wash in milliQ water at the end of the procedure to ensure full removal of EDTA. The air dried sample was conserved in a desiccator under vacuum (Figure 95 B).

Optical microscope images Optical microscope images were collected using a SM-LUX POL microscope and a Leica EC3 camera. When thread cross sections were analyzed 40 µm samples were cut using a Cryo-microtome (Cryostat Microm HM560).

Dye removal experiments Dye removal experiments were carried out inserting 50 mg of byssus in 1.5 mL of solution having different concentrations of dye. The byssus incubation time was of 48 and 72 h for MB and EosY solutions, respectively. The dye concentration in solution was measured before and after the byssus insertion by using a UV-Vis spectrophotometer (Cary60, Agilent Technologies) using a spectral range of 600 – 810 nm for MB and 450 – 810 for EosY. The MB and EosY starting concentrations used were 0.01, 0.1, 0.5, 1, 2, and 5 mM. Each incubation experiment was carried out in double at 22 °C. The 5 mM starting solution of EosY and MB had a pH of 7.1 and 8.2, respectively.

Adsorption and desorption kinetics Adsorption kinetics experiments were carried out using 50 mg of byssus in 1.5 mL of a 0.01 mM solution of dye and recording the spectra every 10 minutes for the first 300 minutes and then every 15 minutes until 72 h. The desorption kinetics were done using the same parameters by inserting samples from the dye removal experiments in 1.5 mL of Pre-milliQ water (resistivity 18.2 MΩ cm at 25 °C; filtered through a 0.22 µm membrane) for 72 h. All the kinetics experiments were carried out using a Cary60 from Agilent Technologies equipped with an 18-cell holder at 22 °C.

Adsorption isotherms The data were fitted using three adsorption isotherm models.

Langmuir adsorption isotherm[59] describes quantitatively the formation of an adsorbed monolayer on the outer surface of the adsorbent, and after that no further adsorption takes place. The Langmuir isotherm is valid for monolayer adsorption onto a surface containing a finite number of identical sites. The model assumes uniform energies of adsorption onto the surface and no transmigration of adsorbate in the plane of the surface.

$$q_e = \frac{q_m\, b\, C_e}{1 + b\, C_e}$$

$$\frac{1}{q_e} = \frac{1}{q_m} + \frac{1}{q_m\, b\, C_e}$$

where C_e is the equilibrium concentration of adsorbate (mg·L^{-1}); q_e is the amount of dye adsorbed per gram of the adsorbent at equilibrium (mg·g^{-1}); q_m is maximum monolayer coverage capacity (mg g^{-1}); b is Langmuir isotherm constant (L·mg^{-1}). K_L is an important tool in the calculation of the dimensionless equilibrium parameters (R_L) that explains the favourability of adsorption process; R_L is calculated using

$$R_L = \frac{1}{1 + b\, C_o}$$

where C_0 is the highest initial dye concentration (mg·L^{-1}) There are four possibilities for the R_L value: for favourable sorption $0 < R_L < 1$; for unfavourable sorption $R_L > 1$; for linear sorption $R_L = 1$; for irreversible sorption $R_L = 0$.

Freundlich adsorption isotherm[60] is commonly used to describe the adsorption characteristics for the heterogeneous surface sites.

$$q_e = K_F\, C_e^{1/n}$$

$$ln\, q_e = ln\, K_F + \frac{1}{n}\, lnC_e$$

where C_e is the equilibrium concentration of adsorbate (mg·L^{-1}); q_e is the amount of dye adsorbed per gram of the adsorbent at equilibrium (mg·g^{-1}); n is adsorption intensity; K_F is Freundlich isotherm constant (mg·g^{-1}). The value of 1/n indicates the type of isotherm. If the value of 1/n lies in between (0 < 1/n < 1) it showed that isotherm is favourable, if 1/n = 0, it indicates isotherm is irreversible and if 1/n > 1, it is unfavourable.

Dubinin–Radushkevich isotherm[61] is generally applied to express the adsorption mechanism with a Gaussian energy distribution on a heterogeneous surface. This model is successfully fitted high solute activities at different concentration ranges. This approach was implied to distinguish the chemical and physical adsorption. This isotherm is temperature dependent and assumes that there is no homogenous surface on the adsorbent and the equation is expressed as follows.

$$q_e = \; q_D\, e^{-K_D \varepsilon^2}$$

$$ln\, q_e = ln\, q_D - K_D\, \varepsilon^2$$

$$\varepsilon = RT\, ln(1 + 1/C_e)$$

where K_D and ε are D-R constant (mol^2·kJ^{-2}) and D-R isotherm constant, respectively; R and T are the gas constant (8.314 × 10^{-3} kJ·mol^{-1}·K^{-1}) and temperature (K), and q_D is the saturation capacity (mg·g^{-1}). The parameters are obtained by the linear plot of ln q_e vs. ε^2. K_D is the activity coefficient useful in obtaining the mean sorption energy E (kJ·mol^{-1}).

4. Water remediation from metal ions

4.1. Results

The pristine byssus was digested and its metal composition was analyzed (Table 16). The matrix had a 0.5 ± 0.2 wt.% metal content, the major metals were Al, Cu, Fe, and Zn. After the de-metalation process, the metal content dropped to 0.122 ± 0.006 wt.% (80 ± 10 % less than the pristine), and the main metal left were Al and Fe.

Table 16: Metal content, reported in $\mu g \cdot g^{-1}$, of the native byssus and the de-metaled byssus.

Metal	Native byssus	De-metaled byssus
Al	2300 ± 900	1200 ± 900
As	0.3 ± 0.4	0
B	20 ± 20	0
Ba	30 ± 20	8 ± 8
Be	0.01 ± 0.02	0
Ca	10 ± 8	1 ± 1
Cd	1 ± 1	0
Co	4 ± 3	0.5 ± 0.7
Cr	5 ± 1	1 ± 1
Cu	200 ± 200	40 ± 50
Fe	2000 ± 1000	1100 ± 900
K	1.5 ± 0.6	0.9 ± 0.8
Li	3.8 ± 0.6	1.3 ± 0.9
Mn	200 ± 100	1.94 ± 0.02
Mo	20 ± 20	30 ± 30
Ni	20 ± 20	8 ±10
P	0.3 ± 0.2	0.4 ± 0.4
Pb	0.4 ± 0.6	0
S	3 ± 3	6 ± 5
Se	4 ± 5	10 ± 10
Si	0.05 ± 0.07	0.2 ± 0.2
Sn	0.5 ± 0.5	1 ± 1
Sr	90 ± 70	20 ± 20
Ti	20 ± 10	20 ± 10
V	30 ± 30	6 ± 4
Zn	200 ± 200	20 ± 10

Five different loading concentrations were tested for each metal ion studied: 0.01, 0.1, 0.5, 1, and 10 mM. The amount of adsorbed metal ion was measured as the difference in concentration between the loading and the final solution, after being exposed to the byssus for 72 h. After this time, the system was assumed to have reached equilibrium.

The results of the metal ion removal at pH 7 are reported in Table 17, and the discoloration of three colored metal solutions, i.e. Mn^{2+}, Fe^{3+}, and Cu^{2+}, due to the byssus' metal adsorption are reported in Figure 101. The system was studied in a buffered environment using 2,2-bis(hydroxymethyl)-2,2',2''-nitrilotriethanol (bis-TRIS), a non-chelating buffer, at pH 7. For Fe^{3+} N,N-bis(2-hydroxyethyl)glycine (bicine) was used, since a precipitate formed in bis-TRIS.

The analysis of each 2 mL metal ion solution after the byssus treatment revealed the presence of trace metal ions released from the byssus, most of them were largely below 20 ppb. Only three metal ions were desorbed in large quantity from the matrix, Al (~0.1 mM in solution), Fe (~0.04 mM), and Zn (~0.01 mM). For this reason, it was not possible to collect reliable data for Al^{3+} and at low concentration of Fe^{3+} and Zn^{2+}. It was also difficult to determine in accurate way the uptake of Mn^{2+} at a concentration lower than 0.1 mM because of partial overlap of the Fe and Mn emission bands that affected the measure of the concentration difference (anyway small) of the final solution compared to the loading one. A similar effect might have also affected the Cd measure when using a 0.01 mM solution.

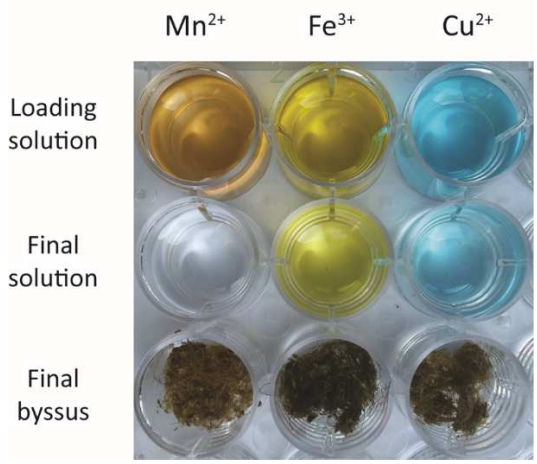

Figure 101: Camera picture of the 10 mM Mn^{2+}, Fe^{3+}, or Cu^{2+} solution before and after being in contact with the byssus. After the treatment, a decrease in the color intensity of the solution can be observed. The byssus exposed to Fe^{3+} assumed a darker coloration.

The byssus matrix was also tested at pH 4, where the His residues are protonated and no more able to chelate metals.[62][63][64] Four metal ions were tested at this pH: Ni^{2+} and Cu^{2+} as ions with a high affinity to His, V^{3+} as an ion with a high DOPA affinity, and Mn^{2+} as metal with no preferential binding sites. The acetate buffer was used, considering that most of the buffers at pH 4 act also as chelating agents. The results of the metal ion removal at pH 4 are reported in

Table 18. Also at pH 4 desorption of metal ions from the byssus matrix was observed, as occurred at pH 7. In this case, a minor number of metals were detected at a concentration lower than 20 ppb, but as observed at pH 7 higher concentration of Al (~50 µM), Fe (~50 µM), and Zn (~5 µM) were released.

As in the previous study on dye uptake, the data collected were interpolated using three different isotherm models: Langmuir, Freundlich, and D-R. The results of the interpolations are reported in Table 19. More details about the interpolation using these models can be found in this chapter section 3.4.

To compare the behavior of the byssus matrix with the different metal ions the uptakes (reported in $mol \cdot g^{-1}$) from the 10 mM solutions were compared using a T-test ($v \geq 2$, $p = 0.05$). The T-test showed that the value of Cd^{2+}, Co^{2+}, Cu^{2+}, Ni^{2+}, and Zn^{2+} at pH 7 were significantly equal. This occurred also for Mn^{2+}, at both the pH, and V^{3+}, at pH 4.

The metal ions adsorbed in the byssus was also determined digesting few representative matrices and quantifying the metal content present in them. The results are reported in Table 20.

To discover if the metal ion presence induces morphological changes on the surface of the byssus matrix, SEM images were acquired. The byssus matrices treated with the 10 mM solution and with the 0.5 mM solution were investigated. Two cases were observed. Case 1: No morphological differences were observed in the surfaces of the samples treated at the two concentrations examined. Case 2: The byssus thread treated using the 10 mM solution had a more homogenous surface where the globular structures were not visible. The metal ions inducing this last behavior were Co^{2+}, Cu^{2+}, Fe^{3+}, and Mn^{2+} at pH 7. For Cu^{2+} and Mn^{2+} this difference was not observed as clearly at pH 4. Representative images of the byssus surface are reported in Figure 102.

Table 17: Metal ion adsorption at pH 7 calculated as the difference between the initial and final concentration of the loading solution. For each condition, the results are reported in mg·g^{-1} of the byssus matrix above and the percentage below. The results not reported gave problems due to ion desorption from the matrix. (*) No difference was observed with the loading solution.

	0.01 mM	0.1 mM	0.5 mM	1 mM	10 mM
Cd^{2+}	0*	$(3 \pm 1) \times 10^{-2}$	0.4 ± 0.1	0.66 ± 0.02	21.7 ± 0.3
	0*	9 ± 3	18 ± 6	15.7 ± 6	49.6 ± 0.4
Co^{2+}	$(5.4 \pm 0.1) \times 10^{-3}$	$(5.0 \pm 0.6) \times 10^{-2}$	0.25 ± 0.2	0.43 ± 0.02	9.2 ± 0.1
	26 ± 1	20 ± 2	19 ± 1	16.4 ± 0.7	34 ± 5
Cu^{2+}	$(6 \pm 6) \times 10^{-3}$	$(12 \pm 2) \times 10^{-2}$	0.63 ± 0.03	0.85 ± 0.07	14 ± 2
	30 ± 30	56 ± 7	52 ± 2	35 ± 3	55 ± 6
Fe^{3+}	-	-	-	0.24 ± 0.09	7.5 ± 0.4
	-	-	-	10 ± 4	33 ± 2
Mn^{2+}	0*	0*	0.07 ± 0.05	0.47 ± 0.03	16,66 ± 0.01
	0*	0*	6 ± 4	17 ± 1	66.29 ± 0.01
Ni^{2+}	$(1.3 \pm 0.1) \times 10^{-3}$	$(6.8 \pm 0.5) \times 10^{-2}$	0.399 ± 0.003	0.71 ± 0.09	10.2 ± 0.5
	8 ± 1	29 ± 2	31.6 ± 0.2	29 ± 3	39 ± 2
V^{3+}	$(2.0 \pm 0.2) \times 10^{-3}$	$(3.8 \pm 0.1) \times 10^{-2}$	0.21 ± 0.02	0.58 ± 0.02	1.3 ± 0.1
	11.4 ± 0.8	21.0 ± 0.6	24 ± 2	26 ± 1	7.5 ± 0.6
Zn^{2+}	-	$(0.20 \pm 0.05) \times 10^{-2}$	0.10 ± 0.01	0.33 ± 0.01	12.8 ± 0.7
	-	1.0 ± 0.3	9 ± 2	14.6 ± 0.6	55 ± 3

Table 18: Metal adsorption at pH 4 calculated as the difference between the initial and final concentration of the loading solution. For each condition, the results are reported in mg·g^{-1} of the matrix above and the percentage below.

	0.01 mM	0.1 mM	0.5 mM	1 mM	10 mM
Cu^{2+}	$(2.55 \pm 0.03) \times 10^{-3}$	$(22.34 \pm 0.06) \times 10^{-2}$	1.079 ± 0.002	2.12 ± 0.03	10.4 ± 0.6
	93.6 ± 0.8	93.92 ± 0.06	89.9 ± 0.4	88 ± 1	44 ± 3
Mn^{2+}	$(2.26 \pm 0.08) \times 10^{-3}$	$(19.4 \pm 0.1) \times 10^{-2}$	0.93 ± 0.02	2.04 ± 0.05	16.96 ± 0.01
	80 ± 3	77.1 ± 0.4	75 ± 1	78 ± 2	66.46 ± 0.01
Ni^{2+}	$(25.1 \pm 0.5) \times 10^{-3}$	$(19.7 \pm 0.2) \times 10^{-2}$	0.97 ± 0.03	1.92± 0.01	4.5 ± 0.2
	89 ± 2	87 ± 1	84 ± 2	82.2 ± 0.2	21.2 ± 0.8
V^{3+}	$(1.03 \pm 0.01) \times 10^{-3}$	$(14.6 \pm 0.3) \times 10^{-2}$	0.878 ± 0.001	1.76 ± 0.01	15.51 ± 0.07
	82.9 ± 0.3	85 ± 1	96.46 ± 0.03	96.6 ± 0.2	87.8 ± 0.3

Table 19: Calculated parameters from the fitting of the adsorption isotherms with different models. In blue are highlighted the R^2 values from the isotherm model(s) that showed the best fitting. For some fitting with the Langmuir model, no valid values (n.v.) of K_L and q_m were obtained.

	Metal	Langmuir model			Freundlich			Dubinin–Radushkevich		
		R^2	K_L	q_m	R^2	K_F	n	R^2	K_D	q_D
pH 7	Cd^{2+}	0.915	n.v.	n.v.	0.978	0.00107	0.652	0.566	53.3	1.90
	Co^{2+}	0.998	0.0279	0.494	0.976	0.00909	0.938	0.399	0.472	0.485
	Cu^{2+}	0.298	0.259	0.0723	0.912	0.0267	0.922	0.544	0.304	0.585
	Mn^{2+}	0.593	n.v.	n.v.	0.975	$7.53 \cdot 10^{-6}$	0.365	0.805	695	7.13
	Ni^{2+}	0.987	n.v.	n.v.	0.984	0.00755	0.813	0.552	0.658	0.574
	V^{3+}	0.993	n.v.	n.v.	0.937	0.00905	1.05	0.766	0.507	0.286
	Zn^{2+}	0.925	n.v.	n.v.	0.993	$6.16 \cdot 10^{-5}$	0.450	0.709	32.1	0.895
pH 4	Cu^{2+}	0.989	0.135	4.43	0.955	0.356	1.50	0.756	0.0741	1.99
	Ni^{2+}	0.984	0.182	1.83	0.902	0.224	1.64	0.764	0.0964	1.32
	Mn^{2+}	0.979	0.0755	2.19	0.997	0.144	1.10	0.621	0.164	1.74
	V^{3+}	0.613	n.v.	n.v.	0.832	0.622	1.18	0.918	0.730	10.6

Table 20: Analyses of the metal content into the byssus matrices treated using 10 mM solutions at pH 7. The metal content ($mg \cdot g^{-1}$) was measured after digesting the byssus matrices and is reported in the column labelled matrix. The one calculated as the difference of metal ion content in solution before and after the treatment is reported in the column marked solution. The percentage of metal retained in the matrix compared to the one lost from the solution is reported in the last column.

	matrix	solution	% retained
V	0.90 ± 0.06	1.3 ± 0.1	69
Ni	2.1 ± 0.1	10.2 ± 0.5	21
Cu	8.2 ± 0.5	14 ± 2	58

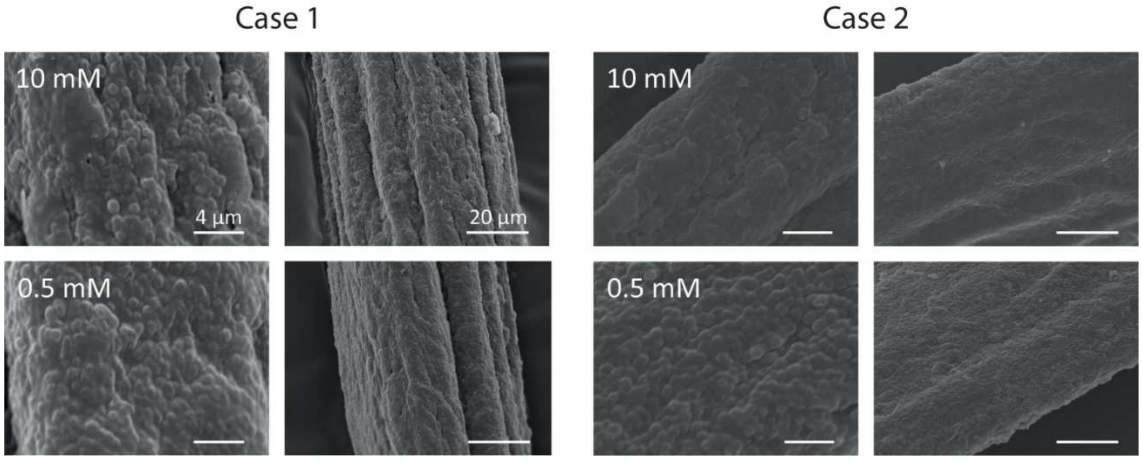

Figure 102: SEM images of the byssus surface. Case 1: Zn^{2+} treated sample at pH 7 where no difference was observed between the two concentrations examined. Case 2: Mn^{2+} at pH 7 where the 10 mM solution treated sample showed a more smooth surface than those treated with the 0.5 mM solution. For each condition, two different magnifications are reported.

4.2. Discussion

The byssus is a protein filament that can chelate metal ions mainly thanks to the presence of DOPA and His residues. However, proteins are complex matrices that can interact in many different ways with cation and anions. For this reason, to minimize interference from counter ions only chloride salts were used for the different metals studied. pH is also a crucial factor that influences the protonation of different residues and alters the environment where metal ions are dispersed.

The analysis of the digested native and de-metaled byssus, used as an adsorbing substrate, showed how the byssus decreases its metal content of 80 ± 10 % with the de-metalation treatment. This allows considering the byssus as de-metaled and available to bind additional metal ions. Indeed, the removal experiments have shown how the byssus is an efficient matrix for metal ions removal, even without being fully de-metaled.

The results showed how at pH 7 the matrix adsorbed a high amount of metal ions when exposed to high concentration as the 10 mM one (up to 22 $mg \cdot g^{-1}$ for Cd, equal to 2 wt.%). The contaminants observed being desorbed by the byssus in the experimental conditions were Al, Fe, and Zn. All those three elements have also been detected in relatively high amount in the de-metaled matrix (Al 0.063 ± 0.009 wt.%, Fe 0.052 ± 0.001 wt.%, and Al 0.00085 ± 0.00003 wt.%), despite their amount was strongly reduced with the de-metalation (respectively: Al 73%, Fe 74%, and Zn 96%). The Al contamination might be due

to residual sediments of the sea bed which were still glued to the plaques. Fe and Zn, instead, are well known major components of the metal composition of natural byssus.[42][44] Those metals might have been weakly re-adsorbed in the matrix during the de-metalation process to be slowly released in the buffer during the 72 h of the experiment. The minor contaminant observed might be due to residues of sediments as suggested for Al, or being due to overlap of adsorption bands of other elements in solution (coming both from the byssus or the buffer). Anyway, the desorption of metal ions might be a problem to apply this matrix in water remediation but could be easily solved pre-desorbing the matrix in water before the usage or applying a better de-metalation protocol.

From the T-test, it was possible to define a family of metal ions behaving similarly, namely Cd^{2+}, Co^{2+}, Ni^{2+}, and Zn^{2+}. Those metal ions share the same uptake (as $mol \cdot g^{-1}$) by the byssus matrix in the 10 mM condition, a similar isotherm of adsorbed metal ($mol \cdot g^{-1}$) vs. loading concentration (mM) (Figure 103), and a best-fitting with the Freundlich model. It can be supposed that those metals share the same binding sites (we will refer to this group as the Ni family). Among these metal ions, the Co^{2+} showed a better fitting with the Langmuir model, compared to the other members of the group. The Co^{2+} also showed a morphological difference between the 0.5 mM and the 10 mM conditions as observed using SEM. This metal ion might have a higher affinity for binding sites on the surface, compared with the other metal ions of the Ni family. Those binding sites might interact with the metal ion preferentially at high metal concentration. Thus, Co^{2+} behaves slightly different in the Ni family.

In the Ni family, Ni^{2+} was chosen to study as model to study the byssus matrix uptake at pH 4, where His residues are completely protonated[62][63] and no more able to bind metal ions.[64] Along with it, V^{3+} was tested as a metal ion representative with a high affinity for DOPA residues, Cu^{2+} as a metal ion with high His affinity that behaving differently from the Ni family, and Mn^{2+} as metal with no specific interaction with both the binding site's type. V^{3+} was chosen instead of Fe^{3+} because the byssus matrix desorbed the latter.

Comparing the pH 7 and the pH 4 adsorption data, the byssus matrix showed a higher metal ion uptake at pH 4, for concentrations lower than 10 mM. In those conditions, the lowest percentage of adsorption was 75 % despite His-based binding sites are not available at this pH. This matrix behavior at pH 4 represents a benefit for metal ions removal, considering that most of the metal ions are acids. This higher uptake might be due to the speciation of

metal ions, the change of buffer molecule, or the protonation of the matrix. Collagen is known to protonate and swells in acid pHs,[65] despite no higher swelling of the matrix was measured at pH 4. The swelled state of the collagenous thread core may favors the metal ion diffusion process and makes the binding sites more accessible. Accordingly, a Langmuir model described the adsorption isotherms better than a Freundlich model.

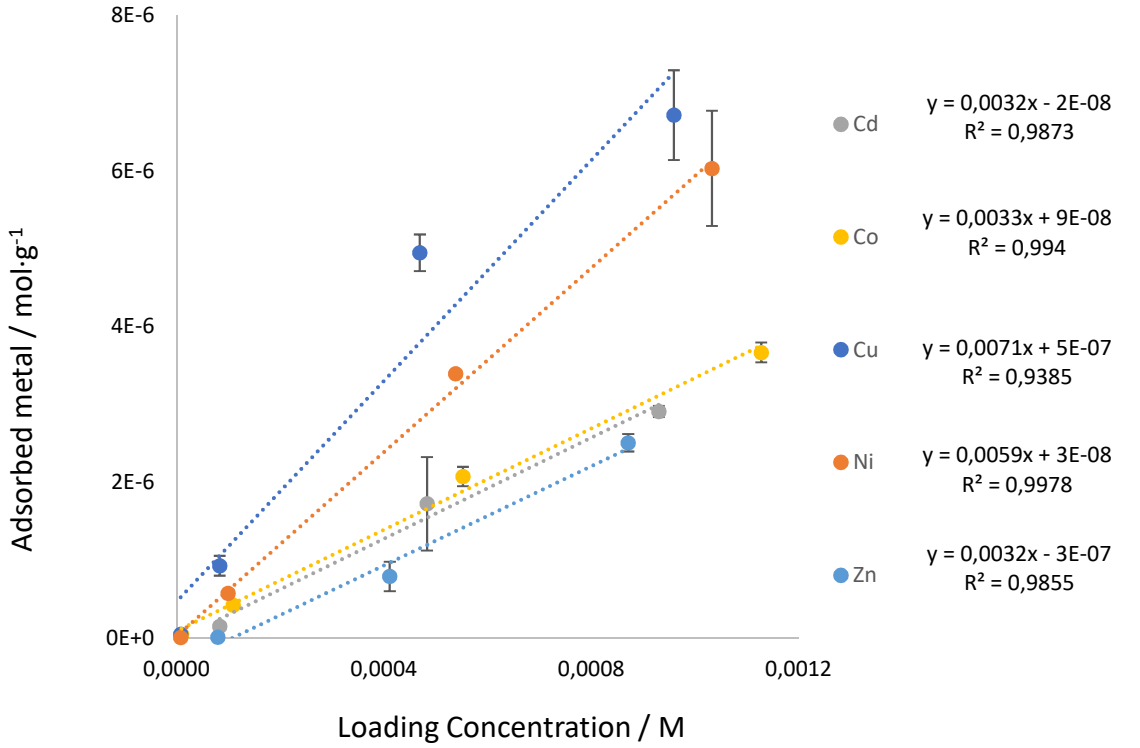

Figure 103: Graph of the adsorbed metal ion, reported in mol·g^{-1}, in the Ni family excluding the 10 mM loading concentration to avoid artifact due to the saturation of the binding sites.

When the 10 mM solutions were used, Ni^{2+} and Cu^{2+} reduced their maximum uptake passing from pH 7 to pH 4 (55 ± 5 % and 23 ± 4 % less metal respectively). This reduction was the same in mol·g^{-1}, suggesting that the same number of binding sites (~7 x 10^{-5} mol·g^{-1}) were lost, which are probably His-based.

At pH 4 the byssus showed a higher uptake for Cu^{2+} than the Ni family and showed a quite different adsorption isotherm (Figure 103). Despite those differences, Cu^{2+} best fitted the same models as the Ni family. Cu^{2+} and the Ni^{2+} family were described properly by a Freundlich model at pH 7 and by a Langmuir/Freundlich model at pH 4. The observed differences can indicate that Cu^{2+} have access to the same binding sites of the Ni family with a higher affinity or a higher number of non-pH dependent binding sites. The latter

could be sulfur ligands or, considering the high amount of Cu^{2+} adsorbed, additional specific binding sites. The presence of non-pH dependent binding sites could justify the best fitting using Langmuir/Freundlich model instead of the Freundlich one. The different morphology, case 2 observed in the Cu^{2+} at pH 7, was not observed as clearly at pH 4. This observation strengths the hypothesis of the collagen swelling at pH 4, which would allow the Cu^{2+} to diffuse more homogenously inside the thread, while at pH 7 it mainly relies on external binding sites.

Ion manganese (II), instead, showed no difference in the uptake using the 10 mM solution in both pHs, relying probably on non-pH-dependent binding sites. As the other metal ions tested, an increase in the uptake at lower concentration was observed at pH 4. As Cu^{2+}, Mn^{2+} showed different morphologies in the 10 mM condition at pH 4 and 7 and their isotherms could be better described with a Langmuir model. Considering that Mn^{2+} seemed to rely on different binding sites compare to Cu^{2+} or Ni^{2+}, this similar behavior recalls for the collagen swelling or, at least, of changing in the matrix behavior passing from pH 7 to pH 4 rather than changing in the metal ion speciation in solution.

The V^{3+} uptake was higher at pH 4 than pH 7 (from 1.3 to 15.5 $mg \cdot g^{-1}$) and the adsorption isotherms were described by Freundlich model and D-R model, respectively. This higher uptake at pH 4 can be due, among other factors, to better availability of the DOPA residues at pH 4. Dopamine, the decarboxylated form of DOPA, is known to undergo oxidation at pH > 5.[66] During the byssus matrix preparation and the 72 h of incubation the DOPA could convert in their oxidized state. This form does not chelate metal ions, this would explain the low V^{3+} and Fe^{3+} uptake compared to the other metal ions. At a pH below 5 dopamine converts to trihydroxylate form, which coordinates metal ions.[67] This change in the redox state of the DOPA can explain why the matrix was able to chelate over 10 times more V^{3+} at pH 4. Differently to the other metals tested, V^{3+} did not fit the Langmuir model at pH 4. Thus, we can assume that this metal ion does not rely on non-pH dependent binding sites. Considering the similar behavior of V^{3+} and Fe^{3+}, it is possible that the byssus matrix, evolved to chelate Fe^{3+} when still inside the organism in a controlled environment,[68] may better chelate them in a slightly acid pH range where iron does not induce DOPA crosslinking[69] and DOPA does not undergo oxidation.[66] Considering the low adsorption of V^{3+} at pH 7 and the high affinity of Fe^{3+} for DOPA, mostly localized in the external cuticle,

the morphological change of the thread treated with Fe^{3+} is explained by a selective surface interaction of the metal ion.

As a final test, the metal ions contained in the byssus matrix samples treated in 10 mM solutions of V^{3+}, Ni^{2+}, and Cu^{2+} at pH 7 were quantified digesting the matrix with an acid/oxidative treatment. The byssus matrix contained less metal ions than the quantity expected from the loading measurements. This can imply the desorption metal ions during the water washing of the byssus matrix, considering the high solubility of these metal ions in pure water.[70]

4.3. Conclusion

In this research is shown that the byssus matrix removes metal ions from water solutions. It adsorbs high amounts of metal ions at pH 7 from concentrated solution (from 1.3 $mg \cdot g^{-1}$ of V^{3+} to 22 $mg \cdot g^{-1}$ of Cd^{2+}). At this pH, Cd^{2+}, Co^{2+}, Ni^{2+}, and Zn^{2+} mainly linked to the same binding sites.

At pH 4 the byssus matrix increased uptake of the metal ions, probably due to the swelling of the collagenous thread core. In this condition, the metal ions were almost completely adsorbed at loading concentration ≤ 1 mM. At a 10 mM loading concentration, Cu^{2+} and Ni^{2+} lost their His-based binding sites (being adsorbed 10.4 and 4.5 $mg \cdot g^{-1}$, respectively), while Mn^{2+} was not affected by the pH change (~17 $mg \cdot g^{-1}$). Contrary, V^{3+} largely increases its adsorption at acid pH (from 1.3 to 15.5 $mg \cdot g^{-1}$).

The ability to chelate metals ions acid pH makes the byssus matrix a promising substrate for metal ion removal from industrial wastewaters, which usually have an acid pH, especially for metals like V^{3+} and Fe^{3+}. On the contrary, the byssus matrix could be utilized in polluted waters with a high concentration of metal ions. This because a neutral buffered environment reduces its ability to adsorb metal ions at concentrations lower than 1 mM.

In conclusion, the byssus, a waste material from seafood, was is an excellent metal chelating matrix, especially at pH 4, being suitable and promising for applications, as both disposable and reusable cheap matrix, in wastewaters.

Besides, the results gained in this research, combined with the previously reported adsorbing capability for aromatic dyes.[53][37], make the byssus a very promising cheap matrix to treat wastewaters from tanneries and paper industries, which usually combine dyes and metal ions to get colored compounds.

4.4. Materials and methods

Materials Reagents and solvents were purchased from Sigma Aldrich and utilized without any further purification. Metal daily fresh solutions were prepared for each experiment. The byssus was collected from a mussel-breeding farm close to Fano (Italy).

Byssus pre-treatment The byssus was collected by hand from the mussels and rinsed, with water and detergent, to remove sand and mud. Afterward, it was washed with de-ionized water to remove the detergent, stirred twice in ethanol for 30 minutes, and washed again twice with de-ionized water for 15 minutes to rehydrate the threads and remove the ethanol. The clean air-dried byssus was stored in a desiccator under vacuum.

Byssus de-metalation The de-metalation process was carried out following the procedure reported by Schmitt et al,[52] in which EDTA was used as a chelating agent in the acid environment. The protocol was modified using 0.1 M TRIS buffer to remove better the shell contaminants, and adding two more 1 h wash in milliQ water at the end of the procedure to ensure full removal of EDTA. The air-dried sample was conserved in a plastic Petri dish in a desiccator under vacuum.

Metal ions removal experiments Metal removal experiments were carried out inserting 50 mg of byssus in 2 mL of the buffered solution having different metal ion concentrations, Figure 104. The incubation time was 72 h, afterward, the metal solution was collected. The byssus was then washed twice with 100 µL of the buffer. The latter buffer and the metal ion solution were collected together and diluted to 5 mL using the experimental buffer. The metal ion concentration in solution was measured using induced coupling plasma optical emission spectroscopy (ICP-OES) in the final 5 mL solutions and in the loading solutions. The metal ion loading concentrations used were 0, 0.01, 0.1, 0.5, 1, and 10 mM. Each incubation experiment was performed in double at 25 °C. The buffer used was 50 mM bis-TRIS for the pH 7 solutions, except for iron (III) solution where 50 mM bicine was used. A 50 mM acetate solution was used for the buffer at pH 4.

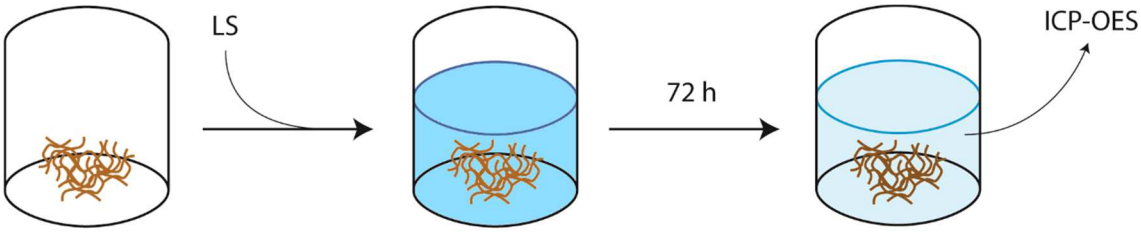

Figure 104: Schematic representation of the experimental setting in the water remediation experiments. I) 50 mg of byssus were set in a well of a 24 well plate; ii) 2 mL of loading solution (LS) was added; ii) after 72 h the solution was collected and analyzed using ICP-OES.

Induced coupling plasma-optical emission spectroscopy (ICP-OES) measures All the samples obtained from the metal removal experiments were measured three times, 12 s each, with 60 s of prerunning, using an ICP-OES, Spectro Arcos-Ametek, Inductive Coupled Plasma Optical Emission Spectroscopy with an axial torch and high salinity kit. The Al signal was measured at 117 nm, the Cd at 229 nm, the Co signal at 229 nm, the Cu signal at 325 nm, the Fe signal was measured at 232 nm, the Ni at 232.0 nm, the Mn at 258 nm, the V signal at 293 nm, and the Zn signal at 214 nm. The calibrating curve was done using certified standards in the experimental buffer.

Metal quantification in the byssus matrix The byssus from the metal removal experiments was washed three times using 1 mL of Pre-milliQ water to remove experimental buffer traces. The metal inside the byssus was quantified digesting 50 mg of sample. The sample was set in a Teflon holder with 0.5 mL of H_2O_2 (30% Carlo Erba, for electronic applications) and 6 mL of nitric acid (65% Honeywell). The holder was set in a microwave over, Milestone, programmed to operate as follows: 2 min at 250 Watt, 2 min at 400 Watt, 1 min at 0 Watt, and 3 min at 750 Watt. The digested sample was quantitatively collected and diluted to 10 mL with water, filtered on paper, and analyzed as described in the ICP-OES section. The measure was carried out in duplicate for each sample type.

Scanning electron microscopy SEM images were acquired with a Philips SEM 515 using a tension of 15 kV. The wet samples were glued on carbon tape, dried in a desiccator, and coated with 20 nm of gold prior image them.

5. References

[1] K. S. Ramesh, S. T. Bharathi, *Appll Water Sci* **2013**, *3*, 773.

[2] S. J. Allen, B. Koumanova, *J. Univ. Chem. Technol. Metall.* **2005**, *40*, 175.

[3] Y. Hu, H. Cheng, *Environ. Dev.* **2013**, *8*, 57.

[4] T. Ito, Y. Adachi, Y. Yamanashi, Y. Shimada, *Water Res.* **2016**, *100*, 458.

[5] C. I. Pearce, J. R. Lloyd, J. T. Guthrie, *Dye. Pigment.* **2003**, *58*, 179.

[6] D. Sud, G. Mahajan, M. P. Kaur, *Bioresour. Technol.* **2008**, *99*, 6017.

[7] A. Celik, A. Demirbaş, *Energy Sources* **2005**, *27*, 1167.

[8] K. Pastircakova, *Energy Edu. Sci. Technol* **2004**, *13*, 97.

[9] J. O. Duruibe, M. O. C. Ogwuegbu, J. N. Egwurugwu, *Int. J. Phys. Sci.* **2007**, *2*, 112.

[10] R. B. Hayes, *Cancer Causes Control* **1997**, *8*, 371.

[11] I. S. Eneji, R. Sha'Ato, P. a Annune, *Pakistan J. Anal. Environ. Chem.* **2011**, *12*, 25.

[12] A. Jakimska, P. Konieczka, K. Skora, J. Namiesnik, *Pol. J. Environ. Stud.* **2011**, *20*, 1117.

[13] B. W. Atkinson, F. Bux, H. C. Kasan, *Water SA* **1998**, *24*, 129.

[14] A. Aklil, M. Mouflih, S. Sebti, *J. Hazard. Mater.* **2004**, *112*, 183.

[15] F. Fu, Q. Wang, *J. Environ. Manage.* **2011**, *92*, 407.

[16] S. S. Ahluwalia, D. Goyal, *Eng. Life Sci.* **2005**, *5*, 158.

[17] A. Kara, L. Uzun, N. Beşirli, A. Denizli, *J. Hazard. Mater.* **2004**, *106B*, 93.

[18] A. Bhatnagar, M. Sillanpää, *Chem. Eng. J.* **2010**, *157*, 277.

[19] N. Meunier, J. Laroulandie, J. F. Blais, R. D. Tyagi, *Bioresour. Technol.* **2003**, *90*, 255.

[20] W. Li, H. Zhao, P. R. Teasdale, R. John, S. Zhang, *React. Funct. Polym.* **2002**, *52*, 31.

[21] A. Denizli, K. Kesenci, Y. Arica, E. Pişkin, *React. Funct. Polym.* **2000**, *44*, 235.

[22] C. C. Wang, C. Y. Chang, C. Y. Chen, *Macromol. Chem. Phys.* **2001**, *202*, 882.

[23] R. R. Navarro, K. Sumi, N. Fujii, M. Matsumura, *Wat. Res.* **1996**, *30*, 2488.

[24] A. Sağlam, S. Bektaş, S. Patir, Ö. Genç, A. Denizli, *React. Funct. Polym.* **2001**, *47*, 185.

[25] W. Li, H. Zhao, P. R. Teasdale, R. John, *Polymer (Guildf).* **2002**, *43*, 4803.

[26] K. Kesenci, R. Say, A. Denizli, *Eur. Polym. J.* **2002**, *38*, 1443.

[27] FAO Yearbook: Fishery and Aquaculture Statistics (Statistics and Information Service of the Fisheries and Aquaculture Department) **2014**.

[28] N. Vallejos, G. González, E. Troncoso, R. N. Zúñiga, *Food Biophys.* **2014**, *9*, 322.

[29] D. Iribarren, M. T. Moreira, G. Feijoo, *Resour. Conserv. Recycl.* **2010**, *54*, 1219.

[30] J. Xiong, Y. Qin, E. Islam, M. Yue, W. Wang, *Desalination* **2011**, *276*, 317.

[31] G. Ferreira-coelho, R. Paradelo-nú, A. Quint, M. J. Fern, J. C. N, *J. Clean. Prod.* **2016**, *131*, 485.

[32] R. Rezaei, M. Mohadesi, G. R. Moradi, *Fuel* **2013**, *109*, 534.

[33] S. Hu, Y. Wang, H. Han, *Biomass and Bioenergy* **2011**, *35*, 3627.

[34] M. I. Jones, H. Barakat, D. A. Patterson, In *IOP Conference Series: Materials Science and Engineering*; 2011; Vol. 18.

[35] F. Byette, C. Pellerin, I. Marcotte, *J. Mater. Chem. B* **2014**, *2*, 6378.

[36] F. Byette, A. Laventure, I. Marcotte, C. Pellerin, *Biomacromolecules* **2016**, *17*, 3277.

[37] D. Montroni, F. Valle, S. Rapino, S. Fermani, M. Calvaresi, M. J. Harrington, G. Falini, *ACS Biomater. Sci. Eng.* **2018**, *4*, 57.

[38] M. J. Harrington, J. Herbert Waite, *Adv. Mater.* **2009**, *21*, 440.

[39] E. Vaccaro, J. H. Waite, *Biomacromolecules* **2001**, *2*, 906.

[40] Y. Fan, T. Saito, A. Isogai, *Biomacromolecules* **2008**, *9*, 1919.

[41] M. H. Suhre, M. Gertz, C. Steegborn, T. Scheibel, *Nat. Commun.* **2014**, *5*, 3392.

[42] M. J. Harrington, A. Masic, N. Holten-andersen, J. H. Waite, P. Fratzl, *Science (80-.).* **2010**, *328*, 216.

[43] J. H. Waite, X. X. Qin, K. J. Coyne, *Matrix Biol.* **1998**, *17*, 93.

[44] T. Hassenkam, T. Gutsmann, P. Hansma, J. Sagert, J. H. Waite, *Biomacromolecules* **2004**, *5*, 1351.

[45] N. Holten-Andersen, J. H. Waite, *J Dent Res* **2008**, *87*, 701.

[46] D. S. Hwang, H. Zeng, A. Masic, M. J. Harrington, J. N. Israelachvili, J. H. Waite, *J. Biol. Chem.* **2010**, *285*, 25850.

[47] J. H. Waite, X. Qin, *Biochemistry* **2001**, *40*, 2887.

[48] L. Yu, X. Liu, W. Yuan, L. J. Brown, D. Wang, *Langmuir* **2015**, *31*, 6351−6366.

[49] M. V. Tuttolomondo, J. M. Galdopórpora, L. Trichet, H. Voisin, T. Coradin, M. F. Desimone, *RSC Adv.* **2015**, *5*, 57395.

[50] T. Qiang, M. Luo, Q. Bu, X. Wang, *Chem. Eng. J.* **2012**, *197*, 343.

[51] D. L. Callahan, A. J. M. Baker, S. D. Kolev, A. G. Wedd, *J. Biol. Inorg. Chem.* **2006**, *11*, 2.

[52] C. N. Z. Schmitt, A. Winter, L. Bertinetti, A. Masic, P. Strauch, M. J. Harrington, *J. R. Soc. Interface* **2015**, *12*, 466.

[53] D. Montroni, C. Piccinetti, S. Fermani, M. Calvaresi, M. J. Harrington, G. Falini, *RSC Adv.* **2017**, *7*, 36605.

[54] G. Annadurai, R. S. Juang, D. J. Lee, *J. Hazard. Mater. B* **2002**, *92*, 263.

[55] C. Duran, D. Ozdes, A. Gundogdu, H. B. Senturk, *J. Chem. Eng. Data* **2011**, *56*, 2136.

[56] V. Vadivelan, K. Vasanth Kumar, *J. Colloid Interface Sci.* **2005**, *286*, 90.

[57] C. A. Hunter, J. K. M. Sanders, *J. Am. Chem. Soc.* **1990**, *112*, 5525.

[58] S. Schmidt, A. Reinecke, F. Wojcik, D. Pussak, L. Hartmann, M. J. Harrington, *Biomacromolecules* **2014**, *15*, 1644.

[59] I. Langmuir, *J. Am. Chem. Soc.* **1918**, *40*, 1361.

[60] H. Freundlich, *Zeitschrift für Phys. Chemie* **1906**, *57*, 385.

[61] M. M. Dubinin, L. V. Radushkevich, *Chem. Zent.* **1947**, *1*, 875.

[62] S. P. Edgcomb, K. P. Murphy, *Proteins Struct. Funct. Genet.* **2002**, *49*, 1.

[63] R. Loewenthal, J. Sancho, A. R. Fersht, *J. Mol. Biol.* **1992**, *224*, 759.

[64] E. Degtyar, M. J. Harrington, Y. Politi, P. Fratzl, *Angew. Chem. Int. Ed. Engl.* **2014**, *53*, 12026.

[65] D. J. LLOYD, R. H. MARRIOTT, W. B. PLEA, *Trans. Faraday Soc.* **1933**, 554.

[66] K. Kim, J. H. Ryu, D. Y. Lee, H. Lee, *Biomater. Sci.* **2013**, *1*, 783.

[67] J. Li, B. M. Christensen, *J. Electroanal. Chem.* **1994**, *375*, 219.

[68] T. Priemel, E. Degtyar, M. N. Dean, M. J. Harrington, *Nat. Commun.* **2017**, *8*, 14539.

[69] Z. Guo, K. Ni, D. Wei, Y. Ren, *RSC Adv.* **2015**, *5*, 37377.

[70] J. Speight, *Lange's Handbook Of Chemistry, Sixteenth Edition*; 2005.

Acknowledgements

Dear reader,

I hope you enjoyed this thesis, or at least part of it. I started this thesis with a citation “Logic will get you from A to B. Imagination will take you everywhere”. After these three years I still think this citation encases the heart of research itself. Only imagination can give us targets that logic can help us accomplish. In these last few lines I would like to share with you a bit of my life thanking most of the people who helped me in these years and kept this statement in my mind in good and bad moments.

I would like to thank my supervisor Giuseppe and of course all the people who actively collaborated to the works reported in the thesis and the one that are not. A special thank goes to Francesco Valle and Marianna Barbalinardo who were always available and encouraged me in all the experiments I asked for. I also would like to thank Fabio Nudelman and Matthew Harrington who both welcomed me in their group for a short period. Of course I would like to thank Marco Rolandi’s group where I have worked for over six months. Among all the people I got in touch during this experience a special thank goes to Giulia who has been my lab buddy for over three years, sharing lots of funny moments and little drama together; to Matteo, Tainah, Cante and Sofia with which I spent most of my not research related time at the university; to Jack, Xeno, and Kostas who have been of great support in and outside the lab in Santa Cruz; to Delphine, and Giorgia who shared with me all the byssus related experience.

Outside the academia I truly want to thank my family who helped and supported me, mentally, emotionally, and occasionally economically. Alberto who have always been there for me and Claudia, who showed me how far my imagination could go. All of my friends and all the people from my theatre group for all the good moments we had.

Last but not least, I would like to thank you for reading at least this, hopefully giving importance to something that was important to me.

Thanks.

Thesis reviews

1. Reviewer 1

To whom it may concern,

the PhD Thesis entitled “Hierarchically organized chitin-based matrices” presented by Mr. Devis Montroni and supervised by Prof. Giuseppe Falini describes the study and characterization of chitin organization (self-assembly) in relation with relevant molecules of the natural environment and the application of this know-how to designed top-up production of functional materials using the squid pen of *Loligo vulgaris* as proof of concept. The originality of the work arises from the combination of innovative methodologies inspired by nature coupled with their application in preparing new materials. This thesis opens new perspectives for the application of natural material in many biotechnological applications.

In the first chapters it is discuss a bottom-up approach to study chitin (β-CnFs into β-chitin fibers) self-assembled *in vitro* and its interaction with other biomacromolecules. The novelty of this study could be exploited in composition of chitin/collagen blend mixtures in which biocompatible route to obtain a micro-homogenous blend of two distinct pH-responsive biomacromolecules could be use for example in medical application.

The second topic examined the organized chitin-based matrices in nature, in *Ariolimax californicus* and *Loligo vulgaris*, in order to gain new information on natural structures. The study concluded that the proteins in the squid pen act as a stiff matrix that link crystalline chitin fibrils avoiding sliding.

In the last chapter the top-up approach is used to exploit the natural hierarchically organized chitinous matrices from the squid pen of *L. Vulgaris*. The bioinspired chemistry of mussel byssus was used for the binding of catechol moieties to the free amino groups of chitin obtaining functional materials of tunable mechanical properties.

The work is topped with a last chapter on the use of the byssus matrix, a waste material from seafood, as a promising and cheap matrix for the cleaning of wastewaters due to its potent metal chelating capacity.

The Thesis is well structure and the results are clearly presented facilitating the reading and comprehension. The language is also clear and I have no detected many typos. The

candidate has already published six articles in well recognized SCI Journals, being first authors in 5 of them, with two more manuscripts already submitted proving the high quality of the work summarized in this Thesis.

Overall, the work presented in the thesis combined with the academic activities, three conferences (two of them international) and five specialized courses carried out during the PhD program has completed his formation and worth a PhD award.

Dr. José A. Gavira Gallardo

Tenure Scientist at CSIC

Relevance with the PhD topic:	4/5
Originality:	5/5
Quality:	5/5
Scientific relevance:	5/5
Presentation:	5/5

2. Reviewer 2

The PhD thesis by Devis Montroni, "Hierarchically organized chitin-based matrices" describes one of the most abundant biopolymer on the Earth, the chitin-based systems at different level of hierarchy, from nano-fibrils to highly organized structures. The thesis is organized in a form of several sections: Thesis summary, five Chapters and Side projects. Of these, three main chapters are logically connected one to the other, depending on the level of organization studied. Specifically, in chapter 2 a study of the self-assembly of beta-chitin nano-fibrils is reported. The developed model system is particularly appreciated and can be considered as a major achievement of the present work, especially considering the further studies that will be carried out. In chapter 3 a study of different composite biogenic matrices is reported. A deep investigation on their structure and composition and their influence on the properties of the material is described. The outputs from these studies are significant achievements in the field and show new possibilities for bioinspired materials preparation. In chapter 4 a new top-up approach for the exploitation of organized chitinous matrices is suggested. The obtained results are significant novelty in the use of natural organized structures, available in a wide range of different morphologies, with the aim to prepare new functional materials. Finally, in the section “Side projects”, two possible applications of the byssus in water remediation are reported. Indeed, despite their simplicity, both side projects are well described and their methodologies have been properly carried out end tested on suitable model systems, with statistical analysis.

Overall, the thesis is very well written, demonstrating a proper use of the English language by the author. In addition, layout and figure composition are very well formatted and certainly above the average I found in similar PhD thesis.

The author considered and appropriately quoted number of bibliographic sources, demonstrated deep theoretical knowledge and very good understanding of the problems discussed in this work. The results are well presented and analyzed in details without ignoring or hiding the weak points and limitations of the methods applied, or the hypothesis made in the discussion.

As a summary, I can state that PhD candidate, Devis Montroni carried out excellent research in different laboratories. He is already a well-trained researcher, capable to carry out scientific activity on his own. He studied important scientific problems, explored new

branches of animal matrices and developed novel methods for treatment of the chitin-based systems. To accomplish those tasks, the proper methods were used, as well as some new and reliable approaches based on simple laboratory techniques. As a consequence, the results of Devis Montroni's research are already published in several top scientific international journals. Therefore, I am happy to be able to recommend the promotion of Devis Montroni to PhD degree, without any reserve.

Best regards,

Damir Kralj, Senior scientist

Ruđer Bošković Institute, Zagreb, Croatia

Relevance with the PhD topic:	5/5
Originality:	5/5
Quality:	5/5
Scientific relevance:	5/5
Presentation:	5/5